NONDESTRUCTIVE DAMAGE DETECTION IN GENERAL BEAMS

A Dissertation

by

SELCUK DINCAL

Submitted to the Office of Graduate Studies of
Texas A&M University
in partial fulfillment of the requirements for the degree of

DOCTOR OF PHILOSOPHY

December 2010

Major Subject: Civil Engineering

NONDESTRUCTIVE DAMAGE DETECTION IN GENERAL BEAMS

A Dissertation

by

SELCUK DINCAL

Submitted to the Office of Graduate Studies of
Texas A&M University
in partial fulfillment of the requirements for the degree of

DOCTOR OF PHILOSOPHY

Approved by:

Chair of Committee,	Norris Stubbs
Committee Members,	Luciana R. Barroso
	Stefan Hurlebaus
	Alan B. Palazzolo
Head of Department,	John Niedzwecki

December 2010

Major Subject: Civil Engineering

ABSTRACT

Nondestructive Damage Detection in General Beams. (December 2010)
Selcuk Dincal, B.S., Eskisehir Osmangazi University;
M.S., Texas A&M University
Chair of Advisory Committee: Dr. Norris Stubbs

Monitoring the integrity of civil engineering structures is an imperative aspect of public safety, since structural failures can pose serious threats to life and property. Periodic inspection performed throughout the life span of these structures is also vital for a nation's economy. Substantial sums of money may be saved upon detecting structural deterioration in a timely manner.

Nondestructive damage evaluation (NDE) offers effective and economically feasible solutions to perform such tasks. Better predictions can be made regarding the current state of structures, and structurally deficient regions that need immediate attention may successfully be narrowed down by utilizing NDE. For these reasons, a considerable amount of research has been conducted in the field of NDE over the past few decades. As a result, many different methodologies are now available, and many new ones continue to emerge as the need for better evaluation techniques prevails.

Upon reviewing the NDE methodologies proposed to date, it may be concluded that theories based on the fundamental equations of mechanics and mathematics in conjunction with justifiable assumptions provided the best results compared to the algorithms developed pragmatically. The goal of this study is to provide NDE methodologies that simultaneously identify the location, the extent, and the severity of damage in general beams. By general beams, we mean beyond Euler-Bernoulli beams (i.e. slender beams) to deep beams and stubby beams whose response may be based on the Timoshenko beam theory, and the Theory of Elasticity.

After presenting the governing equations of equilibrium and stress-displacement relations of the fundamental beam theories including the Euler-Bernoulli Beam theory, the Timoshenko beam theory, and the beam theory based on linear Elasticity Theory, mathematical expressions which relate physical properties (e.g. stiffness) of the undamaged and damaged structure to measurable response quantities (e.g. displacement, strains, etc.) are developed.

We believe that these algorithms will lead to earlier and more accurate prediction of damage in critical structures. The findings of this work will also lead to a better understanding of the limitations of the currently proposed NDE techniques. In addition, it is anticipated that by incorporating the methodologies proposed in this study to the continuous health monitoring of structural systems could reduce the cost of maintenance and offer safer infrastructure networks.

DEDICATION

To my parents Ayla and Sevki Dincal, and to my dear Paolita

ACKNOWLEDGEMENTS

I would like to express my most sincere gratitude to my advisor and the chairman of my advisory committee, Dr. Norris Stubbs, for all his guidance, invaluable help and encouragement throughout my studies at Texas A&M University. I can only dream of being as smart and intelligent as he is. Without his help, his support, and without his brilliant ideas, this dissertation would not have become a reality.

I am grateful to my advisory committee, Dr. Luciana Barroso, Dr. Stefan Hurlebaus, and Dr. Alan Palazzolo for their guidance and advise not only during the completion of this document, but also throughout my studies at Texas A&M University. I was very fortunate to have had them as instructors and some of the ideas presented in this study had bits and pieces of information gathered in their classes.

I would like to take this opportunity to thank to Dr. Harry Jones, whom I worked for as a teaching assistant during my final semesters at Texas A&M University, for his encouragement, attention and the wealth of knowledge that he has shared in his classes. I would also like to express my deepest gratitude to Dr. Anne Raich, who served as the chairman of my advisory committee in my Master's Degree, for introducing me to this line of research.

I am grateful to have had many good friends during my studies at Texas A&M University. I would like to thank all of them for making College Station home for me. They will never be forgotten.

Finally, my deepest appreciation goes to my parents, and to my one and only Paolita, without whom none of this would have been accomplished. And without whom, accomplishing anything would not have even mattered. Thank you for supporting me in everything I have done, and the unconditional love you have given. This dissertation is dedicated to you.

TABLE OF CONTENTS

Page

ABSTRACT iii

DEDICATION v

ACKNOWLEDGEMENTS vi

TABLE OF CONTENTS vii

LIST OF FIGURES xii

LIST OF TABLES xxxv

CHAPTER

I INTRODUCTION 1

Problem Statement 1
Background 1
Overview 1
Methods Utilizing Changes in Frequency 3
Methods Utilizing Changes in Mode Shapes 5
Methods Utilizing Changes in Curvature of Mode Shapes 6
Methods Utilizing Changes in Strain Energy 6
Methods Utilizing Changes Dynamically Measured Flexibility 9
Methods Utilizing Static Displacement and Static Strain Changes 10
NDE Methods Developed at Texas A&M University 11
Shortcomings of the Current NDE Techniques 14
Outstanding Needs 16
Dissertation Objectives 16
Scope of This Work 17
Significance of This Work 17
Organization of the Dissertation 18

TABLE OF CONTENTS (Continued)

CHAPTER		Page
II	A REVIEW OF THE ELEMENTARY BEAM THEORIES AND THE CONCEPT OF DISCONTINUITY IN BEAM-TYPE STRUCTURES	19
	Introduction	19
	A Review of the Elementary Beam Theories	19
	The Euler-Bernoulli Beam Theory	19
	The Timoshenko Beam Theory	22
	The Concept of Discontinuity in Beam-type Structures	26
	Summary	29
III	DESCRIPTION OF THE SELECTED NUMERICAL EXPERIMENTS	31
	Introduction	31
	Description of the Test Structures	31
	The Slender Beam	32
	The Intermediate Beam	35
	The Deep Beam	37
	Damage Scenarios Applied to the Beam Models	40
	The Slender Beam	41
	The Intermediate Beam	47
	The Deep Beam	52
	Assessment of Damage Detection Accuracy	59
	Summary	60
IV	DAMAGE INDEX USING THE PRINCIPLE OF INVARIANT STRESS RESULTANTS AND EULER-BERNOULLI BEAM THEORY	61
	Introduction	61
	Proposed Methodology	61
	Proposed Experimental Arrangement and Basic Measurements Required by Theory	64
	Assessment of the Proposed Methodologies via Numerical Experiments	66
	The Slender Beam	76
	The Intermediate Beam	90
	The Deep Beam	103
	Discussion of Results	116

TABLE OF CONTENTS (Continued)

CHAPTER		Page
	Summary and Conclusions	119
V	DAMAGE INDICES BASED ON NODAL CURVATURES	120
	Introduction	120
	Proposed Methodology	120
	Nodal Flexural Stiffness Based on the Average of Curvatures at the Point of Flexural Discontinuity	121
	Nodal Flexural Stiffness Based on the Average of Flexural Stiffnesses at the Point of Flexural Discontinuity	125
	Proposed Experimental Arrangement and Basic Measurements Required by Theory	128
	Assessment of the Proposed Methodologies via Numerical Experiments	128
	The Slender Beam	128
	The Intermediate Beam	151
	The Deep Beam	163
	Discussion of Results	176
	Summary and Conclusions	177
VI	DAMAGE INDEX USING THE PRINCIPLE OF INVARIANT STRESS RESULTANTS AND TIMOSHENKO BEAM THEORY	178
	Introduction	178
	Proposed Methodology	178
	Proposed Experimental Arrangement and Basic Measurements Required by Theory	184
	Assessment of the Proposed Methodologies via Numerical Experiments	187
	The Slender Beam	188
	The Intermediate Beam	202
	The Deep Beam	221
	Discussion of Results	240
	Summary and Conclusions	243
VII	DAMAGE INDICES BASED ON NODAL ROTATIONS	245
	Introduction	245
	Proposed Methodology	245

TABLE OF CONTENTS (Continued)

CHAPTER		Page
	Nodal Flexural Stiffness Based on the Average of the First Derivative of Rotation at the Point of Flexural Discontinuity	246
	Nodal Flexural Stiffness Based on the Average of Flexural Stiffnesses at the Point of Flexural Discontinuity	250
	Proposed Experimental Arrangement and Basic Measurements Required by Theory	253
	Assessment of the Proposed Methodologies via Numerical Experiments	253
	The Slender Beam	253
	The Intermediate Beam	266
	The Deep Beam	278
	Discussion of Results	291
	Summary and Conclusions	292
VIII	DAMAGE INDICES DERIVED FROM LINEAR ELASTICITY THEORY	293
	Introduction	293
	Proposed Methodology	293
	Damage Indices for a Cantilever Beam Loaded at its Free End	294
	Damage Indices for a Simply Supported Beam Subjected to Uniform Loading	299
	Proposed Experimental Arrangement and Basic Measurements Required by Theory	304
	Assessment of the Proposed Methodologies via Numerical Experiments	306
	The Slender Beam	307
	The Intermediate Beam	326
	The Deep Beam	345
	Discussion of Results	367
	Summary and Conclusions	368
IX	DAMAGE DETECTION RESULTS USING FIELD MEASUREMENTS	369
	Introduction	369
	Description of the Structure	369
	Inflicted Damage Scenarios	371
	Response Parameters Utilized for Damage Detection	373

TABLE OF CONTENTS (Continued)

CHAPTER Page

Summary of the Previous NDD Algorithms Utilized for Damage Detection 375
The Damage Index Method 375
The Mode Shape Curvature Method 376
The Change in Flexibility Method 377
The Change in Uniform Load Surface Curvature Method (Uniform Flexibility) 378
The Change in Stiffness Method 378
Performance of the EB Pseudo Method on Los Alamos Data 380
Damage Scenario 1 380
Damage Scenario 2 383
Damage Scenario 3 385
Damage Scenario 4 387
Discussion of Results 389
Summary and Conclusions 391

X SUMMARY AND CONCLUSIONS 392

Summary and Major Findings 392
Originality of the Work 397
Conclusions 398
Future Work 398

REFERENCES 399

APPENDIX A APPROXIMATION OF THE DEFLECTION PROFILES USING MODAL FLEXIBILITY 404

VITA 414

LIST OF FIGURES

Page

Figure 2.1 Displacement Components of the Euler-Bernoulli Beam Model 20

Figure 2.2 Displacement Components of the Timoshenko Beam Model 23

Figure 2.3 Beam Model Comprised of Several Beam Elements..... 26

Figure 3.1 Schematic of Slender Cantilever Beam 32

Figure 3.2 Bilinear Quadrilateral Element and Nodal DOF..... 33

Figure 3.3 Convergence of the FEM Compared with the Solution from the Theory of Elasticity – Slender Beam..... 34

Figure 3.4 Finite Element Mesh of the Slender Beam 35

Figure 3.5 Schematic of Intermediate Cantilever Beam 35

Figure 3.6 Convergence of the FEM Compared with the Solution from the Theory of Elasticity – Intermediate Beam..... 37

Figure 3.7 Finite Element Mesh of the Intermediate Beam 37

Figure 3.8 Schematic of Deep Cantilever Beam..... 38

Figure 3.9 Convergence of the FEM Compared with the Solution from the Theory of Elasticity – Deep Beam..... 39

Figure 3.10 Finite Element Mesh of the Deep Beam..... 40

Figure 3.11 Schematic Representation of the First Damage Case on the Finite Element Mesh of the Slender Beam 41

Figure 3.12 Schematic Representation of the Second Damage Case on the Finite Element Mesh of the Slender Beam 42

Figure 3.13 Schematic Representation of the Third Damage Case on the Finite Element Mesh of the Slender Beam 44

Figure 3.14 Schematic Representation of the Fourth Damage Case on the Finite Element Mesh of the Slender Beam 45

LIST OF FIGURES (Continued)

Page

Figure 3.15 Schematic Representation of the Fifth Damage Case on the Finite Element Mesh of the Slender Beam 46

Figure 3.16 Schematic Representation of the First Damage Case on the Finite Element Mesh of the Intermediate Beam 47

Figure 3.17 Schematic Representation of the Second Damage Case on the Finite Element Mesh of the Intermediate Beam 48

Figure 3.18 Schematic Representation of the Third Damage Case on the Finite Element Mesh of the Intermediate Beam 49

Figure 3.19 Schematic Representation of the Fourth Damage Case on the Finite Element Mesh of the Intermediate Beam 50

Figure 3.20 Schematic Representation of the Fifth Damage Case on the Finite Element Mesh of the Intermediate Beam 51

Figure 3.21 Schematic Representation of the First Damage Case on the Finite Element Mesh of the Deep Beam 53

Figure 3.22 Schematic Representation of the Second Damage Case on the Finite Element Mesh of the Deep Beam 54

Figure 3.23 Schematic Representation of the Third Damage Case on the Finite Element Mesh of the Deep Beam 55

Figure 3.24 Schematic Representation of the Fourth Damage Case on the Finite Element Mesh of the Deep Beam 56

Figure 3.25 Schematic Representation of the Fifth Damage Case on the Finite Element Mesh of the Deep Beam 58

Figure 4.1 Damage Detection Model Utilized to Predict Local Changes in the Flexural Stiffness Distribution via the Principle of Invariant Stress Resultants and the Euler-Bernoulli Beam Theory 62

Figure 4.2 Sensor Layout for the Slender Beam 64

LIST OF FIGURES (Continued)

Page

Figure 4.3 Sensor Layout for the Intermediate Beam 64

Figure 4.4 Sensor Layout for the Deep Beam 65

Figure 4.5 The Linear Springs Model Utilized to Estimate the Lower Bound Damage Severity 69

Figure 4.6 Plane Elements Centered at the Distance x_0 72

Figure 4.7 The Linear Springs Model Utilized to Estimate the Equivalent One-dimensional Bending Stiffness 72

Figure 4.8 The Deformed Shape of the Linear Springs Model Subjected to Bending 73

Figure 4.9 The Linear Springs Model Utilized to Estimate the Equivalent One-dimensional Shear Stiffness 75

Figure 4.10 Vertical Displacement of the Beam Axis of the Slender Beam Approximated by the 15^{th} Modal Flexibility 77

Figure 4.11 Damage Localization Result for Damage Case SB 1 Using EB Direct β_j 78

Figure 4.12 Damage Extent and Severity Estimate for Damage Case SB 1 Using EB Direct β_j 79

Figure 4.13 Damage Localization Result for Damage Case SB 2 Using EB Direct β_j 81

Figure 4.14 Damage Extent and Severity Estimate for Damage Case SB 2 Using EB Direct β_j 82

Figure 4.15 Damage Localization Result for Damage Case SB 3 Using EB Direct β_j 83

LIST OF FIGURES (Continued)

Page

Figure 4.16 Damage Extent and Severity Estimate for Damage Case SB 3 Using EB Direct β_j 84

Figure 4.17 Damage Localization Result for Damage Case SB 4 Using EB Direct β_j 86

Figure 4.18 Damage Extent and Severity Estimate for Damage Case SB 4 Using EB Direct β_j 87

Figure 4.19 Damage Localization Result for Damage Case SB 5 Using EB Direct β_j 88

Figure 4.20 Damage Extent and Severity Estimate for Damage Case SB 5 Using EB Direct β_j 89

Figure 4.21 Vertical Displacement of the Beam Axis of the Intermediate Beam Approximated by the 15^{th} Modal Flexibility 91

Figure 4.22 Damage Localization Result for Damage Case IB 1 Using EB Direct β_j 92

Figure 4.23 Damage Extent and Severity Estimate for Damage Case IB 1 Using EB Direct β_j 93

Figure 4.24 Damage Localization Result for Damage Case IB 2 Using EB Direct β_j 94

Figure 4.25 Damage Extent and Severity Estimate for Damage Case IB 2 Using EB Direct β_j 95

Figure 4.26 Damage Localization Result for Damage Case IB 3 Using EB Direct β_j 96

Figure 4.27 Damage Extent and Severity Estimate for Damage Case IB 3 Using EB Direct β_j 97

LIST OF FIGURES (Continued)

Page

Figure 4.28 Damage Localization Result for Damage Case IB 4 Using EB Direct β_j 99

Figure 4.29 Damage Extent and Severity Estimate for Damage Case IB 4 Using EB Direct β_j 100

Figure 4.30 Damage Localization Result for Damage Case IB 5 Using EB Direct β_j 101

Figure 4.31 Damage Extent and Severity Estimate for Damage Case IB 5 Using EB Direct β_j 102

Figure 4.32 Vertical Displacement of the Beam Axis of the Deep Beam Approximated by the 13^{th} Modal Flexibility 104

Figure 4.33 Damage Localization Result for Damage Case DB 1 Using EB Direct β_j 105

Figure 4.34 Damage Extent and Severity Estimate for Damage Case DB 1 Using EB Direct β_j 106

Figure 4.35 Damage Localization Result for Damage Case DB 2 Using EB Direct β_j 107

Figure 4.36 Damage Extent and Severity Estimate for Damage Case DB 2 Using EB Direct β_j 108

Figure 4.37 Damage Localization Result for Damage Case DB 3 Using EB Direct β_j 109

Figure 4.38 Damage Extent and Severity Estimate for Damage Case DB 3 Using EB Direct β_j 110

Figure 4.39 Damage Localization Result for Damage Case DB 4 Using EB Direct β_j 112

LIST OF FIGURES (Continued)

Page

Figure 4.40 Damage Extent and Severity Estimate for Damage Case DB 4 Using EB Direct β_j 113

Figure 4.41 Damage Localization Result for Damage Case DB 5 Using EB Direct β_j 114

Figure 4.42 Damage Extent and Severity Estimate for Damage Case DB 5 Using EB Direct β_j 115

Figure 5.1 Damage Detection Model Utilized to Predict Local Changes in the Flexural Stiffness Distribution via Nodal Curvatures..... 121

Figure 5.2 Damage Localization Result for Damage Case SB 1 Using EB Pseudo β_j 130

Figure 5.3 Damage Extent and Severity Estimate for Damage Case SB 1 Using EB Pseudo β_j 131

Figure 5.4 Damage Localization Result for Damage Case SB 1 Using EB Pseudo γ_j 132

Figure 5.5 Damage Extent and Severity Estimate for Damage Case SB 1 Using EB Pseudo γ_j 133

Figure 5.6 Damage Localization Result for Damage Case SB 2 Using EB Pseudo β_j 134

Figure 5.7 Damage Extent and Severity Estimate for Damage Case SB 2 Using EB Pseudo β_j 135

Figure 5.8 Damage Localization Result for Damage Case SB 2 Using EB Pseudo γ_j 136

Figure 5.9 Damage Extent and Severity Estimate for Damage Case SB 2 Using EB Pseudo γ_j 137

LIST OF FIGURES (Continued)

Page

Figure 5.10 Damage Localization Result for Damage Case SB 3 Using EB Pseudo β_j 138

Figure 5.11 Damage Extent and Severity Estimate for Damage Case SB 3 Using EB Pseudo β_j 139

Figure 5.12 Damage Localization Result for Damage Case SB 3 Using EB Pseudo γ_j 140

Figure 5.13 Damage Extent and Severity Estimate for Damage Case SB 3 Using EB Pseudo γ_j 141

Figure 5.14 Damage Localization Result for Damage Case SB 4 Using EB Pseudo β_j 143

Figure 5.15 Damage Extent and Severity Estimate for Damage Case SB 4 Using EB Pseudo β_j 144

Figure 5.16 Damage Localization Result for Damage Case SB 4 Using EB Pseudo γ_j 145

Figure 5.17 Damage Extent and Severity Estimate for Damage Case SB 4 Using EB Pseudo γ_j 146

Figure 5.18 Damage Localization Result for Damage Case SB 5 Using EB Pseudo β_j 147

Figure 5.19 Damage Extent and Severity Estimate for Damage Case SB 5 Using EB Pseudo β_j 148

Figure 5.20 Damage Localization Result for Damage Case SB 5 Using EB Pseudo γ_j 149

Figure 5.21 Damage Extent and Severity Estimate for Damage Case SB 5 Using EB Pseudo γ_j 150

LIST OF FIGURES (Continued)

Page

Figure 5.22 Damage Localization Result for Damage Case IB 1 Using EB Pseudo β_j 152

Figure 5.23 Damage Extent and Severity Estimate for Damage Case IB 1 Using EB Pseudo β_j 153

Figure 5.24 Damage Localization Result for Damage Case IB 2 Using EB Pseudo β_j 154

Figure 5.25 Damage Extent and Severity Estimate for Damage Case IB 2 Using EB Pseudo β_j 155

Figure 5.26 Damage Localization Result for Damage Case IB 3 Using EB Pseudo β_j 156

Figure 5.27 Damage Extent and Severity Estimate for Damage Case IB 3 Using EB Pseudo β_j 157

Figure 5.28 Damage Localization Result for Damage Case IB 4 Using EB Pseudo β_j 159

Figure 5.29 Damage Extent and Severity Estimate for Damage Case IB 4 Using EB Pseudo β_j 160

Figure 5.30 Damage Localization Result for Damage Case IB 5 Using EB Pseudo β_j 161

Figure 5.31 Damage Extent and Severity Estimate for Damage Case IB 5 Using EB Pseudo β_j 162

Figure 5.32 Damage Localization Result for Damage Case DB 1 Using EB Pseudo β_j 164

Figure 5.33 Damage Extent and Severity Estimate for Damage Case DB 1 Using EB Pseudo β_j 165

LIST OF FIGURES (Continued)

Page

Figure 5.34 Damage Localization Result for Damage Case DB 2 Using EB Pseudo β_j 166

Figure 5.35 Damage Extent and Severity Estimate for Damage Case DB 2 Using EB Pseudo β_j 167

Figure 5.36 Damage Localization Result for Damage Case DB 3 Using EB Pseudo β_j 169

Figure 5.37 Damage Extent and Severity Estimate for Damage Case DB 3 Using EB Pseudo β_j 170

Figure 5.38 Damage Localization Result for Damage Case DB 4 Using EB Pseudo β_j 171

Figure 5.39 Damage Extent and Severity Estimate for Damage Case DB 4 Using EB Pseudo β_j 172

Figure 5.40 Damage Localization Result for Damage Case DB 5 Using EB Pseudo β_j 174

Figure 5.41 Damage Extent and Severity Estimate for Damage Case DB 5 Using EB Pseudo β_j 175

Figure 6.1 Damage Detection Model Utilized to Predict the Changes in Flexural Stiffness Distribution via the Principle of Invariant Stress Resultants and the Timoshenko Beam Theory 179

Figure 6.2 Damage Detection Model Utilized to Predict the Changes in Shear Stiffness Distribution via the Principle of Invariant Stress Resultants and the Timoshenko Beam Theory 179

Figure 6.3 Sensor Layout for the Slender Beam 184

Figure 6.4 Sensor Layout for the Intermediate Beam 185

Figure 6.5 Sensor Layout for the Deep Beam 185

LIST OF FIGURES (Continued)

Page

Figure 6.6 Fraction of the Deflected Shape at the First Bending Mode..... 187

Figure 6.7 Vertical Displacement of the Beam Axis of the Slender Beam Approximated by the 31st Modal Flexibility..... 188

Figure 6.8 Rotation of the Beam Axis of the Slender Beam Approximated by the 32nd Modal Flexibility..... 189

Figure 6.9 Damage Localization Result for Damage Case SB 1 Using TB Direct β_j^M 190

Figure 6.10 Damage Extent and Severity Estimate for Damage Case SB 1 Using TB Direct β_j^M 191

Figure 6.11 Damage Localization Result for Damage Case SB 2 Using TB Direct β_j^M 193

Figure 6.12 Damage Extent and Severity Estimate for Damage Case SB 2 Using TB Direct β_j^M 194

Figure 6.13 Damage Localization Result for Damage Case SB 3 Using TB Direct β_j^M 195

Figure 6.14 Damage Extent and Severity Estimate for Damage Case SB 3 Using TB Direct β_j^M 196

Figure 6.15 Damage Localization Result for Damage Case SB 4 Using TB Direct β_j^M 198

Figure 6.16 Damage Extent and Severity Estimate for Damage Case SB 4 Using TB Direct β_j^M 199

Figure 6.17 Damage Localization Result for Damage Case SB 5 Using TB Direct β_j^M 200

LIST OF FIGURES (Continued)

Page

Figure 6.18 Damage Extent and Severity Estimate for Damage Case SB 5 Using TB Direct β_j^M 201

Figure 6.19 Vertical Displacement of the Beam Axis of the Intermediate Beam Approximated by the 31st Modal Flexibility..... 203

Figure 6.20 Rotation of the Beam Axis of the Intermediate Beam Approximated by the 32nd Modal Flexibility..... 203

Figure 6.21 Damage Localization Result for Damage Case IB 1 Using TB Direct β_j^M 204

Figure 6.22 Damage Extent and Severity Estimate for Damage Case IB 1 Using TB Direct β_j^M 205

Figure 6.23 Damage Localization Result for Damage Case IB 2 Using TB Direct β_j^M 207

Figure 6.24 Damage Extent and Severity Estimate for Damage Case IB 2 Using TB Direct β_j^M 208

Figure 6.25 Damage Localization Result for Damage Case IB 3 Using TB Direct β_j^M 209

Figure 6.26 Damage Extent and Severity Estimate for Damage Case IB 3 Using TB Direct β_j^M 210

Figure 6.27 Damage Localization Result for Damage Case IB 3 Using TB Direct β_j^V 212

Figure 6.28 Damage Extent and Severity Estimate for Damage Case IB 3 Using TB Direct β_j^V 213

Figure 6.29 Damage Localization Result for Damage Case IB 4 Using TB Direct β_j^M 214

LIST OF FIGURES (Continued)

Page

Figure 6.30 Damage Extent and Severity Estimate for Damage Case IB 4 Using TB Direct β_j^M 215

Figure 6.31 Damage Localization Result for Damage Case IB 5 Using TB Direct β_j^M 217

Figure 6.32 Damage Extent and Severity Estimate for Damage Case IB 5 Using TB Direct β_j^M 218

Figure 6.33 Damage Localization Result for Damage Case IB 5 Using TB Direct β_j^V 219

Figure 6.34 Damage Extent and Severity Estimate for Damage Case IB 5 Using TB Direct β_j^V 220

Figure 6.35 Vertical Displacement of the Beam Axis of the Deep Beam Approximated by the 25th Modal Flexibility 222

Figure 6.36 Rotation of the Beam Axis of the Deep Beam Approximated by the 26th Modal Flexibility 222

Figure 6.37 Damage Localization Result for Damage Case DB 1 Using TB Direct β_j^M 223

Figure 6.38 Damage Extent and Severity Estimate for Damage Case DB 1 Using TB Direct β_j^M 224

Figure 6.39 Damage Localization Result for Damage Case DB 2 Using TB Direct β_j^M 226

Figure 6.40 Damage Extent and Severity Estimate for Damage Case DB 2 Using TB Direct β_j^M 227

Figure 6.41 Damage Localization Result for Damage Case DB 3 Using TB Direct β_j^M 228

LIST OF FIGURES (Continued)

Page

Figure 6.42 Damage Extent and Severity Estimate for Damage Case DB 3 Using TB Direct β_j^M 229

Figure 6.43 Damage Localization Result for Damage Case DB 3 Using TB Direct β_j^V 230

Figure 6.44 Damage Extent and Severity Estimate for Damage Case DB 3 Using TB Direct β_j^V 231

Figure 6.45 Damage Localization Result for Damage Case DB 4 Using TB Direct β_j^M 233

Figure 6.46 Damage Extent and Severity Estimate for Damage Case DB 4 Using TB Direct β_j^M 234

Figure 6.47 Damage Localization Result for Damage Case DB 5 Using TB Direct β_j^M 235

Figure 6.48 Damage Extent and Severity Estimate for Damage Case DB 5 Using TB Direct β_j^M 236

Figure 6.49 Damage Localization Result for Damage Case DB 5 Using TB Direct β_j^V 238

Figure 6.50 Damage Extent and Severity Estimate for Damage Case DB 5 Using TB Direct β_j^V 239

Figure 7.1 Damage Detection Model Utilized to Predict Local Changes in the Flexural Stiffness Distribution via Nodal Rotations..... 247

Figure 7.2 Damage Localization Result for Damage Case SB 1 Using TB Pseudo β_j 255

LIST OF FIGURES (Continued)

Page

Figure 7.3 Damage Extent and Severity Estimate for Damage Case SB 1 Using TB Pseudo β_j 256

Figure 7.4 Damage Localization Result for Damage Case SB 2 Using TB Pseudo β_j 257

Figure 7.5 Damage Extent and Severity Estimate for Damage Case SB 2 Using TB Pseudo β_j 258

Figure 7.6 Damage Localization Result for Damage Case SB 3 Using TB Pseudo β_j 259

Figure 7.7 Damage Extent and Severity Estimate for Damage Case SB 3 Using TB Pseudo β_j 260

Figure 7.8 Damage Localization Result for Damage Case SB 4 Using TB Pseudo β_j 262

Figure 7.9 Damage Extent and Severity Estimate for Damage Case SB 4 Using TB Pseudo β_j 263

Figure 7.10 Damage Localization Result for Damage Case SB 5 Using TB Pseudo β_j 264

Figure 7.11 Damage Extent and Severity Estimate for Damage Case SB 5 Using TB Pseudo β_j 265

Figure 7.12 Damage Localization Result for Damage Case IB 1 Using TB Pseudo β_j 267

Figure 7.13 Damage Extent and Severity Estimate for Damage Case IB 1 Using TB Pseudo β_j 268

Figure 7.14 Damage Localization Result for Damage Case IB 2 Using TB Pseudo β_j 269

LIST OF FIGURES (Continued)

Page

Figure 7.15 Damage Extent and Severity Estimate for Damage Case IB 2 Using TB Pseudo β_j 270

Figure 7.16 Damage Localization Result for Damage Case IB 3 Using TB Pseudo β_j 271

Figure 7.17 Damage Extent and Severity Estimate for Damage Case IB 3 Using TB Pseudo β_j 272

Figure 7.18 Damage Localization Result for Damage Case IB 4 Using TB Pseudo β_j 274

Figure 7.19 Damage Extent and Severity Estimate for Damage Case IB 4 Using TB Pseudo β_j 275

Figure 7.20 Damage Localization Result for Damage Case IB 5 Using TB Pseudo β_j 276

Figure 7.21 Damage Extent and Severity Estimate for Damage Case IB 5 Using TB Pseudo β_j 277

Figure 7.22 Damage Localization Result for Damage Case DB 1 Using TB Pseudo β_j 279

Figure 7.23 Damage Extent and Severity Estimate for Damage Case DB 1 Using TB Pseudo β_j 280

Figure 7.24 Damage Localization Result for Damage Case DB 2 Using TB Pseudo β_j 281

Figure 7.25 Damage Extent and Severity Estimate for Damage Case DB 2 Using TB Pseudo β_j 282

Figure 7.26 Damage Localization Result for Damage Case DB 3 Using TB Pseudo β_j 284

LIST OF FIGURES (Continued)

Page

Figure 7.27 Damage Extent and Severity Estimate for Damage Case DB 3 Using TB Pseudo β_j 285

Figure 7.28 Damage Localization Result for Damage Case DB 4 Using TB Pseudo β_j 286

Figure 7.29 Damage Extent and Severity Estimate for Damage Case DB 4 Using TB Pseudo β_j 287

Figure 7.30 Damage Localization Result for Damage Case DB 5 Using TB Pseudo β_j 289

Figure 7.31 Damage Extent and Severity Estimate for Damage Case DB 5 Using TB Pseudo β_j 290

Figure 8.1 Cantilever Beam Loaded at Its Free End 294

Figure 8.2 Simply Supported Beam with a Uniformly Distributed Load 300

Figure 8.3 Ideal Sensor Layout for the Slender Beam 305

Figure 8.4 Ideal Sensor Layout for the Intermediate Beam 305

Figure 8.5 Ideal Sensor Layout for the Deep Beam 305

Figure 8.6 Schematic Representation of Damage Case SB 1 307

Figure 8.7 Damage Localization Result for Damage Case SB 1 Using Elasticity β_j^M 308

Figure 8.8 Damage Severity Estimates for Damage Case SB 1 Using Elasticity β_j^M 308

Figure 8.9 Schematic Representation of Damage Case SB 2 309

LIST OF FIGURES (Continued)

Page

Figure 8.10 Damage Localization Result for Damage Case SB 2 Using Elasticity β_j^M 310

Figure 8.11 Damage Severity Estimates for Damage Case SB 2 Using Elasticity β_j^M 310

Figure 8.12 Schematic Representation of Damage Case SB 3 311

Figure 8.13 Damage Localization Result for Damage Case SB 3 Using Elasticity β_j^M 312

Figure 8.14 Damage Severity Estimates for Damage Case SB 3 Using Elasticity β_j^M 312

Figure 8.15 Damage Localization Result for Damage Case SB 3 Using Elasticity β_j^V 313

Figure 8.16 Damage Severity Estimates for Damage Case SB 3 Using Elasticity β_j^V 314

Figure 8.17 Damage Localization Result for Damage Case SB 3 Using Elasticity β_j^ν 315

Figure 8.18 Damage Severity Estimates for Damage Case SB 3 Using Elasticity β_j^ν 316

Figure 8.19 Schematic Representation of Damage Case SB 4 317

Figure 8.20 Damage Localization Result for Damage Case SB 4 Using Elasticity β_j^M 318

Figure 8.21 Damage Severity Estimates for Damage Case SB 4 Using Elasticity β_j^M 318

Figure 8.22 Schematic Representation of Damage Case SB 5 320

LIST OF FIGURES (Continued)

Page

Figure 8.23 Damage Localization Result for Damage Case SB 5 Using Elasticity β_j^M 320

Figure 8.24 Damage Severity Estimates for Damage Case SB 5 Using Elasticity β_j^M 321

Figure 8.25 Damage Localization Result for Damage Case SB 5 Using Elasticity β_j^V 322

Figure 8.26 Damage Severity Estimates for Damage Case SB 5 Using Elasticity β_j^V 323

Figure 8.27 Damage Localization Result for Damage Case SB 5 Using Elasticity β_j^ν 324

Figure 8.28 Damage Severity Estimates for Damage Case SB 5 Using Elasticity β_j^ν 325

Figure 8.29 Schematic Representation of Damage Case IB 1 326

Figure 8.30 Damage Localization Result for Damage Case IB 1 Using Elasticity β_j^M 327

Figure 8.31 Damage Severity Estimates for Damage Case IB 1 Using Elasticity β_j^M 327

Figure 8.32 Schematic Representation of Damage Case IB 2 328

Figure 8.33 Damage Localization Result for Damage Case IB 2 Using Elasticity β_j^M 329

Figure 8.34 Damage Severity Estimates for Damage Case IB 2 Using Elasticity β_j^M 329

LIST OF FIGURES (Continued)

Page

Figure 8.35 Schematic Representation of Damage Case IB 3 330

Figure 8.36 Damage Localization Result for Damage Case IB 3 Using Elasticity β_j^M 331

Figure 8.37 Damage Severity Estimates for Damage Case IB 3 Using Elasticity β_j^M 331

Figure 8.38 Damage Localization Result for Damage Case IB 3 Using Elasticity β_j^V 333

Figure 8.39 Damage Severity Estimates for Damage Case IB 3 Using Elasticity β_j^V 333

Figure 8.40 Damage Localization Result for Damage Case IB 3 Using Elasticity β_j^v 335

Figure 8.41 Damage Severity Estimates for Damage Case IB 3 Using Elasticity β_j^v 335

Figure 8.42 Schematic Representation of Damage Case IB 4 337

Figure 8.43 Damage Localization Result for Damage Case IB 4 Using Elasticity β_j^M 337

Figure 8.44 Damage Severity Estimates for Damage Case IB 4 Using Elasticity β_j^M 338

Figure 8.45 Schematic Representation of Damage Case IB 5 339

Figure 8.46 Damage Localization Result for Damage Case IB 5 Using Elasticity β_j^M 340

Figure 8.47 Damage Severity Estimates for Damage Case IB 5 Using Elasticity β_j^M 340

LIST OF FIGURES (Continued)

Page

Figure 8.48 Damage Localization Result for Damage Case IB 5 Using Elasticity β_j^V 342

Figure 8.49 Damage Severity Estimates for Damage Case IB 5 Using Elasticity β_j^V 342

Figure 8.50 Damage Localization Result for Damage Case IB 5 Using Elasticity β_j^v 344

Figure 8.51 Damage Severity Estimates for Damage Case IB 5 Using Elasticity β_j^v 344

Figure 8.52 Schematic Representation of Damage Case DB 1 346

Figure 8.53 Damage Localization Result for Damage Case DB 1 Using Elasticity β_j^M 346

Figure 8.54 Damage Severity Estimates for Damage Case DB 1 Using Elasticity β_j^M 347

Figure 8.55 Schematic Representation of Damage Case DB 2 348

Figure 8.56 Damage Localization Result for Damage Case DB 2 Using Elasticity β_j^M 349

Figure 8.57 Damage Severity Estimates for Damage Case DB 2 Using Elasticity β_j^M 349

Figure 8.58 Schematic Representation of Damage Case DB 3 351

Figure 8.59 Damage Localization Result for Damage Case DB 3 Using Elasticity β_j^M 351

Figure 8.60 Damage Severity Estimates for Damage Case DB 3 Using Elasticity β_j^M 352

LIST OF FIGURES (Continued)

Page

Figure 8.61 Damage Localization Result for Damage Case DB 3 Using Elasticity β_j^V 353

Figure 8.62 Damage Severity Estimates for Damage Case DB 3 Using Elasticity β_j^V 354

Figure 8.63 Damage Localization Result for Damage Case DB 3 Using Elasticity β_j^v 356

Figure 8.64 Damage Severity Estimates for Damage Case DB 3 Using Elasticity β_j^v 356

Figure 8.65 Schematic Representation of Damage Case DB 4..... 358

Figure 8.66 Damage Localization Result for Damage Case DB 4 Using Elasticity β_j^M 358

Figure 8.67 Damage Severity Estimates for Damage Case DB 4 Using Elasticity β_j^M 359

Figure 8.68 Schematic Representation of Damage Case DB 5..... 361

Figure 8.69 Damage Localization Result for Damage Case DB 5 Using Elasticity β_j^M 361

Figure 8.70 Damage Severity Estimates for Damage Case DB 5 Using Elasticity β_j^M 362

Figure 8.71 Damage Localization Result for Damage Case DB 5 Using Elasticity β_j^V 363

Figure 8.72 Damage Severity Estimates for Damage Case DB 5 Using Elasticity β_j^V 364

LIST OF FIGURES (Continued)

Page

Figure 8.73 Damage Localization Result for Damage Case DB 5 Using Elasticity β_j^{ν} 365

Figure 8.74 Damage Severity Estimates for Damage Case DB 5 Using Elasticity β_j^{ν} 366

Figure 9.1 Elevation View of the Portion of the Bridge that was Tested 370

Figure 9.2 Typical Cross-section of the Bridge 371

Figure 9.3 Damage Scenarios Inflicted on the North Plate Girder 372

Figure 9.4 Sensor Layout for the North Plate Girder 373

Figure 9.5 Unit-normalized Mode Shapes 374

Figure 9.6 Damage Localization Result for Damage Scenario 1 Using EB Pseudo β_j 381

Figure 9.7 Damage Severity Estimate for Damage Scenario 1 Using EB Pseudo β_j 382

Figure 9.8 Damage Localization Result for Damage Scenario 2 Using EB Pseudo β_j 383

Figure 9.9 Damage Severity Estimate for Damage Scenario 2 Using EB Pseudo β_j 384

Figure 9.10 Damage Localization Result for Damage Scenario 3 Using EB Pseudo β_j 385

Figure 9.11 Damage Severity Estimate for Damage Scenario 3 Using EB Pseudo β_j 386

Figure 9.12 Damage Localization Result for Damage Scenario 4 Using EB Pseudo β_j 388

LIST OF FIGURES (Continued)

Page

Figure 9.13 Damage Severity Estimate for Damage Scenario 4 Using EB Pseudo β_j 389

LIST OF TABLES

Page

Table 3.1 Material and Section Properties of the Slender Cantilever Beam 32

Table 3.2 Material and Section Properties of the Intermediate Cantilever Beam 36

Table 3.3 Material and Section Properties of the Deep Cantilever Beam 38

Table 3.4 Summary of the First Damage Scenario Applied to the Slender Beam..... 42

Table 3.5 Summary of the Second Damage Scenario Applied to the Slender Beam . 43

Table 3.6 Summary of the Third Damage Scenario Applied to the Slender Beam 44

Table 3.7 Summary of the Fourth Damage Scenario Applied to the Slender Beam .. 46

Table 3.8 Summary of the Fifth Damage Scenario Applied to the Slender Beam 47

Table 3.9 Summary of the First Damage Scenario Applied to the Intermediate Beam 48

Table 3.10 Summary of the Second Damage Scenario Applied to the Intermediate Beam 49

Table 3.11 Summary of the Third Damage Scenario Applied to the Intermediate Beam 50

Table 3.12 Summary of the Fourth Damage Scenario Applied to the Intermediate Beam 51

Table 3.13 Summary of the Fifth Damage Scenario Applied to the Intermediate Beam 52

Table 3.14 Summary of the First Damage Scenario Applied to the Deep Beam 53

Table 3.15 Summary of the Second Damage Scenario Applied to the Deep Beam 54

Table 3.16 Summary of the Third Damage Scenario Applied to the Deep Beam..... 55

Table 3.17 Summary of the Fourth Damage Scenario Applied to the Deep Beam..... 57

Table 3.18 Summary of the Fifth Damage Scenario Applied to the Deep Beam..... 58

LIST OF TABLES (Continued)

Page

Table 4.1 Assessment of the Damage Localization Accuracy for Damage Case SB 1 Using EB Direct β_j 79

Table 4.2 Assessment of the Damage Extent and Severity Accuracy for Damage Case SB 1 Using EB Direct β_j 80

Table 4.3 Assessment of the Damage Localization Accuracy for Damage Case SB 2 Using EB Direct β_j 81

Table 4.4 Assessment of the Damage Extent and Severity Accuracy for Damage Case SB 2 Using EB Direct β_j 82

Table 4.5 Assessment of the Damage Localization Accuracy for Damage Case SB 3 Using EB Direct β_j 84

Table 4.6 Assessment of the Damage Extent and Severity Accuracy for Damage Case SB 3 Using EB Direct β_j 85

Table 4.7 Assessment of the Damage Localization Accuracy for Damage Case SB 4 Using EB Direct β_j 86

Table 4.8 Assessment of the Damage Extent and Severity Accuracy for Damage Case SB 4 Using EB Direct β_j 87

Table 4.9 Assessment of the Damage Localization Accuracy for Damage Case SB 5 Using EB Direct β_j 89

Table 4.10 Assessment of the Damage Extent and Severity Accuracy for Damage Case SB 5 Using EB Direct β_j 90

Table 4.11 Assessment of the Damage Localization Accuracy for Damage Case IB 1 Using EB Direct β_j 92

Table 4.12 Assessment of the Damage Extent and Severity Accuracy for Damage Case IB 1 Using EB Direct β_j 93

LIST OF TABLES (Continued)

Page

Table 4.13 Assessment of the Damage Localization Accuracy for Damage Case IB 2 Using EB Direct β_j 94

Table 4.14 Assessment of the Damage Extent and Severity Accuracy for Damage Case IB 2 Using EB Direct β_j 95

Table 4.15 Assessment of the Damage Localization Accuracy for Damage Case IB 3 Using EB Direct β_j 97

Table 4.16 Assessment of the Damage Extent and Severity Accuracy for Damage Case IB 3 Using EB Direct β_j 98

Table 4.17 Assessment of the Damage Localization Accuracy for Damage Case IB 4 Using EB Direct β_j 99

Table 4.18 Assessment of the Damage Extent and Severity Accuracy for Damage Case IB 4 Using EB Direct β_j 100

Table 4.19 Assessment of the Damage Localization Accuracy for Damage Case IB 5 Using EB Direct β_j 102

Table 4.20 Assessment of the Damage Extent and Severity Accuracy for Damage Case IB 5 Using EB Direct β_j 103

Table 4.21 Assessment of the Damage Localization Accuracy for Damage Case DB 1 Using EB Direct β_j 105

Table 4.22 Assessment of the Damage Extent and Severity Accuracy for Damage Case DB 1 Using EB Direct β_j 106

Table 4.23 Assessment of the Damage Localization Accuracy for Damage Case DB 2 Using EB Direct β_j 107

Table 4.24 Assessment of the Damage Extent and Severity Accuracy for Damage Case DB 2 Using EB Direct β_j 108

LIST OF TABLES (Continued)

Page

Table 4.25 Assessment of the Damage Localization Accuracy for Damage Case DB 3 Using EB Direct β_j 110

Table 4.26 Assessment of the Damage Extent and Severity Accuracy for Damage Case DB 3 Using EB Direct β_j 111

Table 4.27 Assessment of the Damage Localization Accuracy for Damage Case DB 4 Using EB Direct β_j 112

Table 4.28 Assessment of the Damage Extent and Severity Accuracy for Damage Case DB 4 Using EB Direct β_j 113

Table 4.29 Assessment of the Damage Localization Accuracy for Damage Case DB 5 Using EB Direct β_j 115

Table 4.30 Assessment of the Damage Extent and Severity Accuracy for Damage Case DB 5 Using EB Direct β_j 116

Table 5.1 Assessment of the Damage Localization Accuracy for Damage Case SB 1 Using EB Pseudo β_j 130

Table 5.2 Assessment of the Damage Extent and Severity Accuracy for Damage Case SB 1 Using EB Pseudo β_j 131

Table 5.3 Assessment of the Damage Localization Accuracy for Damage Case SB 1 Using EB Pseudo γ_j 132

Table 5.4 Assessment of the Damage Extent and Severity Accuracy for Damage Case SB 1 Using EB Pseudo γ_j 133

Table 5.5 Assessment of the Damage Localization Accuracy for Damage Case SB 2 Using EB Pseudo β_j 134

Table 5.6 Assessment of the Damage Extent and Severity Accuracy for Damage Case SB 2 Using EB Pseudo β_j 135

LIST OF TABLES (Continued)

Page

Table 5.7 Assessment of the Damage Localization Accuracy for Damage Case SB 2 Using EB Pseudo γ_j 136

Table 5.8 Assessment of the Damage Extent and Severity Accuracy for Damage Case SB 2 Using EB Pseudo γ_j 137

Table 5.9 Assessment of the Damage Localization Accuracy for Damage Case SB 3 Using EB Pseudo β_j 139

Table 5.10 Assessment of the Damage Extent and Severity Accuracy for Damage Case SB 3 Using EB Pseudo β_j 140

Table 5.11 Assessment of the Damage Localization Accuracy for Damage Case SB 3 Using EB Pseudo γ_j 141

Table 5.12 Assessment of the Damage Extent and Severity Accuracy for Damage Case SB 3 Using EB Pseudo γ_j 142

Table 5.13 Assessment of the Damage Localization Accuracy for Damage Case SB 4 Using EB Pseudo β_j 143

Table 5.14 Assessment of the Damage Extent and Severity Accuracy for Damage Case SB 4 Using EB Pseudo β_j 144

Table 5.15 Assessment of the Damage Localization Accuracy for Damage Case SB 4 Using EB Pseudo γ_j 145

Table 5.16 Assessment of the Damage Extent and Severity Accuracy for Damage Case SB 4 Using EB Pseudo γ_j 146

Table 5.17 Assessment of the Damage Localization Accuracy for Damage Case SB 5 Using EB Pseudo β_j 148

Table 5.18 Assessment of the Damage Extent and Severity Accuracy for Damage Case SB 5 Using EB Pseudo β_j 149

LIST OF TABLES (Continued)

Page

Table 5.19 Assessment of the Damage Localization Accuracy for Damage Case SB 5 Using EB Pseudo γ_j 150

Table 5.20 Assessment of the Damage Extent and Severity Accuracy for Damage Case SB 5 Using EB Pseudo γ_j 151

Table 5.21 Assessment of the Damage Localization Accuracy for Damage Case IB 1 Using EB Pseudo β_j 152

Table 5.22 Assessment of the Damage Extent and Severity Accuracy for Damage Case IB 1 Using EB Pseudo β_j 153

Table 5.23 Assessment of the Damage Localization Accuracy for Damage Case IB 2 Using EB Pseudo β_j 154

Table 5.24 Assessment of the Damage Extent and Severity Accuracy for Damage Case IB 2 Using EB Pseudo β_j 155

Table 5.25 Assessment of the Damage Localization Accuracy for Damage Case IB 3 Using EB Pseudo β_j 157

Table 5.26 Assessment of the Damage Extent and Severity Accuracy for Damage Case IB 3 Using EB Pseudo β_j 158

Table 5.27 Assessment of the Damage Localization Accuracy for Damage Case IB 4 Using EB Pseudo β_j 159

Table 5.28 Assessment of the Damage Extent and Severity Accuracy for Damage Case IB 4 Using EB Pseudo β_j 160

Table 5.29 Assessment of the Damage Localization Accuracy for Damage Case IB 5 Using EB Pseudo β_j 162

Table 5.30 Assessment of the Damage Extent and Severity Accuracy for Damage Case IB 5 Using EB Pseudo β_j 163

LIST OF TABLES (Continued)

Page

Table 5.31 Assessment of the Damage Localization Accuracy for Damage Case DB 1 Using EB Pseudo β_j 164

Table 5.32 Assessment of the Damage Extent and Severity Accuracy for Damage Case DB 1 Using EB Pseudo β_j 165

Table 5.33 Assessment of the Damage Localization Accuracy for Damage Case DB 2 Using EB Pseudo β_j 167

Table 5.34 Assessment of the Damage Extent and Severity Accuracy for Damage Case DB 2 Using EB Pseudo β_j 168

Table 5.35 Assessment of the Damage Localization Accuracy for Damage Case DB 3 Using EB Pseudo β_j 169

Table 5.36 Assessment of the Damage Extent and Severity Accuracy for Damage Case DB 3 Using EB Pseudo β_j 170

Table 5.37 Assessment of the Damage Localization Accuracy for Damage Case DB 4 Using EB Pseudo β_j 172

Table 5.38 Assessment of the Damage Extent and Severity Accuracy for Damage Case DB 4 Using EB Pseudo β_j 173

Table 5.39 Assessment of the Damage Localization Accuracy for Damage Case DB 5 Using EB Pseudo β_j 174

Table 5.40 Assessment of the Damage Extent and Severity Accuracy for Damage Case DB 5 Using EB Pseudo β_j 175

Table 6.1 Assessment of the Damage Localization Accuracy for Damage Case SB 1 Using TB Direct β_j^M 191

Table 6.2 Assessment of the Damage Extent and Severity Accuracy for Damage Case SB 1 Using TB Direct β_j^M 192

LIST OF TABLES (Continued)

Page

Table 6.3 Assessment of the Damage Localization Accuracy for Damage Case SB 2 Using TB Direct β_j^M 193

Table 6.4 Assessment of the Damage Extent and Severity Accuracy for Damage Case SB 2 Using TB Direct β_j^M 194

Table 6.5 Assessment of the Damage Localization Accuracy for Damage Case SB 3 Using TB Direct β_j^M 196

Table 6.6 Assessment of the Damage Extent and Severity Accuracy for Damage Case SB 3 Using TB Direct β_j^M 197

Table 6.7 Assessment of the Damage Localization Accuracy for Damage Case SB 4 Using TB Direct β_j^M 198

Table 6.8 Assessment of the Damage Extent and Severity Accuracy for Damage Case SB 4 Using TB Direct β_j^M 199

Table 6.9 Assessment of the Damage Localization Accuracy for Damage Case SB 5 Using TB Direct β_j^M 201

Table 6.10 Assessment of the Damage Extent and Severity Accuracy for Damage Case SB 5 Using TB Direct β_j^M 202

Table 6.11 Assessment of the Damage Localization Accuracy for Damage Case IB 1 Using TB Direct β_j^M 205

Table 6.12 Assessment of the Damage Extent and Severity Accuracy for Damage Case IB 1 Using TB Direct β_j^M 206

Table 6.13 Assessment of the Damage Localization Accuracy for Damage Case IB 2 Using TB Direct β_j^M 207

LIST OF TABLES (Continued)

Page

Table 6.14 Assessment of the Damage Extent and Severity Accuracy for Damage Case IB 2 Using TB Direct β_j^M 208

Table 6.15 Assessment of the Damage Localization Accuracy for Damage Case IB 3 Using TB Direct β_j^M 210

Table 6.16 Assessment of the Damage Extent and Severity Accuracy for Damage Case IB 3 Using TB Direct β_j^M 211

Table 6.17 Assessment of the Damage Localization Accuracy for Damage Case IB 3 Using TB Direct β_j^V 212

Table 6.18 Assessment of the Damage Extent and Severity Accuracy for Damage Case IB 3 Using TB Direct β_j^V 213

Table 6.19 Assessment of the Damage Localization Accuracy for Damage Case IB 4 Using TB Direct β_j^M 215

Table 6.20 Assessment of the Damage Extent and Severity Accuracy for Damage Case IB 4 Using TB Direct β_j^M 216

Table 6.21 Assessment of the Damage Localization Accuracy for Damage Case IB 5 Using TB Direct β_j^M 217

Table 6.22 Assessment of the Damage Extent and Severity Accuracy for Damage Case IB 5 Using TB Direct β_j^M 218

Table 6.23 Assessment of the Damage Localization Accuracy for Damage Case IB 5 Using TB Direct β_j^V 220

Table 6.24 Assessment of the Damage Extent and Severity Accuracy for Damage Case IB 5 Using TB Direct β_j^V 221

LIST OF TABLES (Continued)

Page

Table 6.25 Assessment of the Damage Localization Accuracy for Damage Case DB 1 Using TB Direct β_j^M 224

Table 6.26 Assessment of the Damage Extent and Severity Accuracy for Damage Case DB 1 Using TB Direct β_j^M 225

Table 6.27 Assessment of the Damage Localization Accuracy for Damage Case DB 2 Using TB Direct β_j^M 226

Table 6.28 Assessment of the Damage Extent and Severity Accuracy for Damage Case DB 2 Using TB Direct β_j^M 227

Table 6.29 Assessment of the Damage Localization Accuracy for Damage Case DB 3 Using TB Direct β_j^M 229

Table 6.30 Assessment of the Damage Extent and Severity Accuracy for Damage Case DB 3 Using TB Direct β_j^M 230

Table 6.31 Assessment of the Damage Localization Accuracy for Damage Case DB 3 Using TB Direct β_j^V 231

Table 6.32 Assessment of the Damage Extent and Severity Accuracy for Damage Case DB 3 Using TB Direct β_j^V 232

Table 6.33 Assessment of the Damage Localization Accuracy for Damage Case DB 4 Using TB Direct β_j^M 233

Table 6.34 Assessment of the Damage Extent and Severity Accuracy for Damage Case DB 4 Using TB Direct β_j^M 234

Table 6.35 Assessment of the Damage Localization Accuracy for Damage Case DB 5 Using TB Direct β_j^M 236

LIST OF TABLES (Continued)

Page

Table 6.36 Assessment of the Damage Extent and Severity Accuracy for Damage Case DB 5 Using TB Direct β_j^M 237

Table 6.37 Assessment of the Damage Localization Accuracy for Damage Case DB 5 Using TB Direct β_j^V 238

Table 6.38 Assessment of the Damage Extent and Severity Accuracy for Damage Case DB 5 Using TB Direct β_j^V 239

Table 7.1 Assessment of the Damage Localization Accuracy for Damage Case SB 1 Using TB Pseudo β_j 255

Table 7.2 Assessment of the Damage Extent and Severity Accuracy for Damage Case SB 1 Using TB Pseudo β_j 256

Table 7.3 Assessment of the Damage Localization Accuracy for Damage Case SB 2 Using TB Pseudo β_j 257

Table 7.4 Assessment of the Damage Extent and Severity Accuracy for Damage Case SB 2 Using TB Pseudo β_j 258

Table 7.5 Assessment of the Damage Localization Accuracy for Damage Case SB 3 Using TB Pseudo β_j 260

Table 7.6 Assessment of the Damage Extent and Severity Accuracy for Damage Case SB 3 Using TB Pseudo β_j 261

Table 7.7 Assessment of the Damage Localization Accuracy for Damage Case SB 4 Using TB Pseudo β_j 262

Table 7.8 Assessment of the Damage Extent and Severity Accuracy for Damage Case SB 4 Using TB Pseudo β_j 263

Table 7.9 Assessment of the Damage Localization Accuracy for Damage Case SB 5 Using TB Pseudo β_j 265

LIST OF TABLES (Continued)

Page

Table 7.10 Assessment of the Damage Extent and Severity Accuracy for Damage Case SB 5 Using TB Pseudo β_j 266

Table 7.11 Assessment of the Damage Localization Accuracy for Damage Case IB 1 Using TB Pseudo β_j 267

Table 7.12 Assessment of the Damage Extent and Severity Accuracy for Damage Case IB 1 Using TB Pseudo β_j 268

Table 7.13 Assessment of the Damage Localization Accuracy for Damage Case IB 2 Using TB Pseudo β_j 269

Table 7.14 Assessment of the Damage Extent and Severity Accuracy for Damage Case IB 2 Using TB Pseudo β_j 270

Table 7.15 Assessment of the Damage Localization Accuracy for Damage Case IB 3 Using TB Pseudo β_j 272

Table 7.16 Assessment of the Damage Extent and Severity Accuracy for Damage Case IB 3 Using TB Pseudo β_j 273

Table 7.17 Assessment of the Damage Localization Accuracy for Damage Case IB 4 Using TB Pseudo β_j 274

Table 7.18 Assessment of the Damage Extent and Severity Accuracy for Damage Case IB 4 Using TB Pseudo β_j 275

Table 7.19 Assessment of the Damage Localization Accuracy for Damage Case IB 5 Using TB Pseudo β_j 277

Table 7.20 Assessment of the Damage Extent and Severity Accuracy for Damage Case IB 5 Using TB Pseudo β_j 278

Table 7.21 Assessment of the Damage Localization Accuracy for Damage Case DB 1 Using TB Pseudo β_j 279

LIST OF TABLES (Continued)

Page

Table 7.22 Assessment of the Damage Extent and Severity Accuracy for Damage Case DB 1 Using TB Pseudo β_j 280

Table 7.23 Assessment of the Damage Localization Accuracy for Damage Case DB 2 Using TB Pseudo β_j 282

Table 7.24 Assessment of the Damage Extent and Severity Accuracy for Damage Case DB 2 Using TB Pseudo β_j 283

Table 7.25 Assessment of the Damage Localization Accuracy for Damage Case DB 3 Using TB Pseudo β_j 284

Table 7.26 Assessment of the Damage Extent and Severity Accuracy for Damage Case DB 3 Using TB Pseudo β_j 285

Table 7.27 Assessment of the Damage Localization Accuracy for Damage Case DB 4 Using TB Pseudo β_j 287

Table 7.28 Assessment of the Damage Extent and Severity Accuracy for Damage Case DB 4 Using TB Pseudo β_j 288

Table 7.29 Assessment of the Damage Localization Accuracy for Damage Case DB 5 Using TB Pseudo β_j 289

Table 7.30 Assessment of the Damage Extent and Severity Accuracy for Damage Case DB 5 Using TB Pseudo β_j 290

Table 8.1 Percent Error in Severity Estimates for Damage Case SB 1 Using Elasticity β_j^M 309

Table 8.2 Percent Error in Severity Estimates for Damage Case SB 2 Using Elasticity β_j^M 311

Table 8.3 Percent Error in Severity Estimates for Damage Case SB 3 Using Elasticity β_j^M 313

LIST OF TABLES (Continued)

Page

Table 8.4 Percent Error in Severity Estimates for Damage Case SB 3 Using Elasticity β_j^V 314

Table 8.5 Percent Error in Severity Estimates for Damage Case SB 3 Using Elasticity β_j^v 316

Table 8.6 Percent Error in Severity Estimates for Damage Case SB 4 Using Elasticity β_j^M 319

Table 8.7 Percent Error in Severity Estimates for Damage Case SB 5 Using Elasticity β_j^M 321

Table 8.8 Percent Error in Severity Estimates for Damage Case SB 5 Using Elasticity β_j^V 323

Table 8.9 Percent Error in Severity Estimates for Damage Case SB 5 Using Elasticity β_j^v 325

Table 8.10 Percent Error in Severity Estimates for Damage Case IB 1 Using Elasticity β_j^M 328

Table 8.11 Percent Error in Severity Estimates for Damage Case IB 2 Using Elasticity β_j^M 330

Table 8.12 Percent Error in Severity Estimates for Damage Case IB 3 Using Elasticity β_j^M 332

Table 8.13 Percent Error in Severity Estimates for Damage Case IB 3 Using Elasticity β_j^V 334

Table 8.14 Percent Error in Severity Estimates for Damage Case IB 3 Using Elasticity β_j^v 336

LIST OF TABLES (Continued)

Page

Table 8.15 Percent Error in Severity Estimates for Damage Case IB 4 Using Elasticity β_j^M 338

Table 8.16 Percent Error in Severity Estimates for Damage Case IB 5 Using Elasticity β_j^M 341

Table 8.17 Percent Error in Severity Estimates for Damage Case IB 5 Using Elasticity β_j^V 343

Table 8.18 Percent Error in Severity Estimates for Damage Case IB 5 Using Elasticity β_j^ν 345

Table 8.19 Percent Error in Severity Estimates for Damage Case DB 1 Using Elasticity β_j^M 347

Table 8.20 Percent Error in Severity Estimates for Damage Case DB 2 Using Elasticity β_j^M 350

Table 8.21 Percent Error in Severity Estimates for Damage Case DB 3 Using Elasticity β_j^M 352

Table 8.22 Percent Error in Severity Estimates for Damage Case DB 3 Using Elasticity β_j^V 355

Table 8.23 Percent Error in Severity Estimates for Damage Case DB 3 Using Elasticity β_j^ν 357

Table 8.24 Percent Error in Severity Estimates for Damage Case DB 4 Using Elasticity β_j^M 360

Table 8.25 Percent Error in Severity Estimates for Damage Case DB 5 Using Elasticity β_j^M 362

LIST OF TABLES (Continued)

Page

Table 8.26 Percent Error in Severity Estimates for Damage Case DB 5 Using Elasticity β_j^V 364

Table 8.27 Percent Error in Severity Estimates for Damage Case DB 5 Using Elasticity β_j^v 366

Table 9.1 Resonant Frequencies for the First Two Bending Modes..... 375

Table 9.2 Summary of Damage Detection Results Using SET 1 Modal Data 379

Table 9.3 Assessment of the Damage Localization Accuracy for Damage Scenario 1 Using EB Pseudo β_j 381

Table 9.4 Assessment of the Damage Severity Accuracy for Damage Scenario 1 Using EB Pseudo β_j 382

Table 9.5 Assessment of the Damage Localization Accuracy for Damage Scenario 2 Using EB Pseudo β_j 383

Table 9.6 Assessment of the Damage Severity Accuracy for Damage Scenario 2 Using EB Pseudo β_j 384

Table 9.7 Assessment of the Damage Localization Accuracy for Damage Scenario 3 Using EB Pseudo β_j 386

Table 9.8 Assessment of the Damage Severity Accuracy for Damage Scenario 3 Using EB Pseudo β_j 387

Table 9.9 Assessment of the Damage Localization Accuracy for Damage Scenario 4 Using EB Pseudo β_j 388

Table 9.10 Assessment of the Damage Severity Accuracy for Damage Scenario 4 Using EB Pseudo β_j 389

CHAPTER I

INTRODUCTION

PROBLEM STATEMENT

This dissertation deals with the problem of nondestructively detecting, locating, and quantifying damage in civil engineering structures.

Monitoring the integrity of civil engineering structures is an imperative aspect of public safety, since structural failures can pose serious threats to life and property. Periodic inspection performed throughout the life span of these structures is also vital for a nation's economy. Substantial sums of money may be saved upon detecting structural deterioration in a timely manner.

Nondestructive damage evaluation (NDE) offers effective and economically feasible solutions to perform such tasks. Better predictions can be made regarding the current state of structures, and structurally deficient regions that need immediate attention may successfully be narrowed down by utilizing NDE. Due to these reasons, a considerable amount of research has been conducted in the field of NDE over the past few decades. As a result, many different methodologies are now available, and many new ones continue to emerge as the need for better evaluation techniques prevails.

BACKGROUND

Overview

NDE methodologies may be classified into two main groups, namely local and global. Current local damage evaluation methods consists of visual inspection or localized experimental methods such as eddy current, radiography, magnetic particle, etc. (Shull 2002) which require the vicinity of damage to be known *a priori*. In

---

This dissertation follows the style and format of the *Journal of Structural Engineering, ASCE*.

comparison, global NDE techniques such as vibration-based methods have the potential to provide information throughout the life cycle of a structure without requiring access to its main components, which may not be feasible all the time.

Vibration-based NDE methodologies are based on the fact that changes in the physical properties of the structure (mass, damping, and stiffness) alter the response characteristics, which may be used to nondestructively evaluate the current state of the structure. Modal parameters (resonant frequencies, mode shapes, modal damping) and static or dynamic response measurements are some of the response data so far utilized by researchers.

NDE methods may further be classified as either response-based methods or finite element model (FEM) updating based methodologies. Response-based methods utilize structural response directly to identify the current state of a structure. FEM updating based methodologies however, update structural parameters of a preliminary finite element model so that measured responses match the analytical responses in the best possible way. Both methods have shortcomings and advantages. While information regarding the physical properties of the structure may not be adequate to build a detailed FEM (which seemingly makes updating methodologies less desirable), response-based methods normally require the availability of initial (prior to damage) measurements in order to detect damage.

Rytter (1993) further classified the NDE methodologies on the basis of information provided regarding the damage. Four possible levels of information are identified:

1. Level I – Detection of Damage: A quantitative indication regarding the presence of damage in the structure.

2. Level II – Localization of Damage: A quantitative indication regarding the location of damage in the structure.

3. Level III – Assessment of the Severity of Damage: A quantitative indication regarding the severity of damage previously located in the structure.

4. Level IV – Performance Evaluation after Damage: A quantitative indication regarding the impact of damage on the performance of the structure and remaining useful life at the damaged state.

A summary of existing research on Level I, II, and III NDE algorithms is presented below. Methods are classified in accordance with the response characteristics used for damage evaluation. These include changes in frequencies, changes in mode shapes, changes in curvature of mode shapes, changes in strain energy, changes in dynamically measured flexibility, methods utilizing static displacement and static strain changes, and so on.

A significant amount of research in the field NDE has been performed at Texas A&M University (TAMU) over the past three decades. Thus, after providing a more general review of the current methodologies, the author felt obliged to summarize some of the research performed at TAMU.

Methods Utilizing Changes in Frequency

The fundamental concept behind detecting damage using the changes in frequency is that a local change in stiffness also alters the natural frequency of the structure.

Adams et al. (1978) located damage in a straight bar by measuring the resonant frequencies with progressing damage. The proposed method utilized the axial receptance of the bar, which varies with frequency and indicates the possible damaged site(s) as the intersection(s) of the receptance curves computed for different modes of vibration after damage.

Cawley and Adams (1979) later extended this method to two-dimensional structures by replacing the receptance technique with finite element (FE) analysis. The basic idea

behind the theory is that the ratio of the frequency changes in two modes is only a function of damage location and the positions where the theoretically determined ratios equals to the experimentally measured ones are the possible damage sites. Sensitivity analysis was used to compute the changes in the natural frequencies instead of repeating a full dynamic analysis.

Stubbs, et al. (1990) and Stubbs and Osegueda (1990a, 1990b) further extended Cawley and Adams' (1979) work by introducing first-order sensitivity equations relating the measured change in the natural damped frequency of a dynamical system, to the changes in modal mass, stiffness and damping. The authors stated that to ensure numerical stability the number of frequencies required for NDE should be at least as many as the number of damage locations.

Kim and Stubbs (2003) attempted to overcome the problem of numerical instability by introducing an error index that locates damage by utilizing the error between the ratio of fractional changes in eigenvalues and the ratio of sensitivities computed for different modes of vibration. One false-positive prediction has been made in localization due to symmetry. Damage severity was obtained by a crack sizing algorithm based on work done by Gudmundson (1982) and by implementing the principles of linear elastic fracture mechanics. Although NDE using eigenfrequencies has many advantages (such as easy implementation to any of kind of structural system and relatively simple measurement scheme), unfortunately its application is mostly limited to controlled experiments.

As Salawu (1997) mentioned, frequency changes vary proportionally with the square root of the stiffness change, and particularly for large structures, moderate local stiffness changes may produce negligible detectable changes in eigenfrequencies. Existing literature on nondestructive damage detection using resonant frequencies is quite large. Doebling et al. (1996) and Salawu et al. (1997) have provided comprehensive reviews.

Methods Utilizing Changes in Mode Shapes

One of the earlier works utilizing the changes in mode shapes to detect structural damage was performed by West (1984). Modal Assurance Criterion (MAC) was used to localize damage in the Orbiter fuselage aft bulkhead. Comparing MAC values obtained from the baseline structure to the ones computed after acoustic loading indicated that the largest disparity between them occurs in areas where damage is visible using conventional inspection methods. It was concluded that the process was able to isolate the change in structural properties to a particular locale when these changes are significant.

Fox (1992) reported that natural frequency is a better indicator for the presence of damage than the MAC, however Nodal Line MAC (MAC values corresponding to selected measurements points which are close to nodes of a particular mode) proved to be more sensitive to the existence of damage by showing relatively small correlation between the modes that are affected to a greater extent by the defect. Graphical comparisons performed on these mode shapes exhibited constant patterns from which the location of defect may be determined.

Osegueda, et al. (1992) stated the importance of associating a resonant frequency with a mode shape in order to track the changes in resonant frequencies properly. However, based on laboratory tests performed on a typical jacket-type offshore platform, it was concluded that differences in mode shapes do not indicate the location of damage.

Mazurek and DeWolf (1990) performed vibration tests on a bridge girder and attempted to detect structural deterioration using the data obtained during these tests. Deterioration was created via inflicting support failure (by removing one of the two through-pin bearing blocks) and crack propagation (by reducing the overall bridge vertical bending inertia to amounts of about 81%, 68%, and 67% of the original cross-section) on the girder. Results indicated that the greatest changes in mode shapes occur

in the vicinity of the structural defect and that the mode shapes can be used for detecting the location of the defect, although substantial degradation was introduced to generate such results.

Methods Utilizing Changes in Curvature of Mode Shapes

Pandey et al. (1991) used mode shape curvatures to locate damage in beam-type structures. Modal curvatures were obtained from the displacement mode shapes by using the central difference approximation. An increase in the absolute difference between the curvature mode shapes of the intact and damaged beam was observed as the stiffness of the damaged zone was reduced. No numerical estimates of damage severity were reported.

Wahab and Roeck (1999) employed modes shape curvature method to detect damage in a prestressed concrete bridge. A damage indicator so-called "Curvature Damage Factor (CDF)" was introduced where the mean value of all modal curvature differences were computed. CDF aims to eliminate the ambiguity in the selection of mode shape data used in approximating modal curvatures. Numerical simulations performed on the finite element model of a two-span beam revealed that caution must be exercised while computing modal curvature differences at the nodal points of modes since false-positive indications have been reported at the intermediate support. The importance of fine measurement grid and reliable mode shape data were acknowledged for successful damage detection.

Methods Utilizing Changes in Strain Energy

The Damage Index Method, developed by Stubbs et al. (1992), utilizes the equivalency of the fraction of modal strain energy (also referred to as element sensitivity) before and after damage. Feasibility and practicality of the method have been demonstrated on various structures ranging from offshore platforms (Stubbs et al. (1992)) to beams (Stubbs et al. (1995)), and frames (Park et al. (2006)).

Petro et al. (1997) proposed the Strain Energy Damage Index (SEDI) parameter to detect damage in beam-type structures. SEDI corresponds to the percent change in the strain energy computed in terms of mode shape curvatures between undamaged and damaged structures and attains a larger value in the vicinity of damage.

Nicholson and Alnefaie (2000) defined the Modal Moment Index (MMI) parameter, which utilized the difference in modal strain energies to detect defects in beam structures. The difference in strain energies before and after damage was expressed in terms of modal moments assuming that the modal portion of the bending moment is not changed due to damage. The MMI was shown to have a sharp increase at the damage region.

Kim and Stubbs (2002) proposed an improved damage identification method based on modal information. This new algorithm utilizes the fractional changes in modal parameters in addition to the strain energy stored in the structure. The difference in the modal sensitivities computed before and after damage was approximated by using the fractional changes in eigenvalues and modal mass. The proposed methodology was compared to the earlier formulations of Damage Index Method and based on the results obtained from the FE model of a two-span continuous beam, it was concluded that the accuracy of damage localization and severity estimation was improved.

Later, Kim et al. (2003) compared the performance of the two previously derived NDE algorithms utilizing the modal information obtained from the FE model of a simply-supported prestressed concrete beam. Frequency-based damage detection (FBDD) method was the first algorithm that had been originally proposed by Kim (1993) and Topole (1993) and later modified by Kim and Stubbs (2003) to include a crack sizing methodology based on linear elastic fracture mechanics and the fractional change in modal strain energy. Mode-shape-based damage detection (MBDD) method was the other NDE methodology formerly proposed by Kim and Stubbs (2002). Damage was simulated by eliminating the stiffness of elements at the appropriate crack depth either at

the quarter-span or at the mid-span of the beam. Results obtained from several damage scenarios indicated that both methods were able to localize the damage and accurately estimate the size of the cracks located at the mid-span with relatively small errors. However, accuracy of localization and severity estimation were decreased for the cracks located at the quarter-span.

Shi et al. (1998) proposed Modal Strain Energy Change Ratio (MSECR) to detect damage in structures. Upon computing the modal strain energy utilizing pre- damage and post-damage mode shapes and the elemental stiffness matrices, MSECR were computed as the ratio of the modal strain energy differences obtained before and after damage to the modal strain energies computed before damage. Theoretical derivation of MSECR using mode shape sensitivities revealed that it attains the largest value at the damaged element, relatively smaller values at the adjacent elements and finally very small values at elements located far away from the damage. Numerical studies performed on a cantilever test beam supported these observations.

Later, Shi et al. (2000) added a damage quantification scheme to the MSECR method based on the modal strain energy sensitivity. Improvements in damage quantification were later proposed by Shi et al. (2002) by including the analytical stiffness and mass matrices of the structural system to the modal strain energy sensitivity equations.

Osegueda (1999) utilized the difference in the modal strain energy between the damaged and undamaged structure. Locations that exhibited an increase in the difference designated the areas of possible damage. Modal curvatures required for strain energy computations were obtained by using an iterative curve-fitting algorithm.

Guan and Karbhari (2008) introduced a damage detection method based on modal strain energy. Instead of relying on numerical differentiation methods to obtain modal curvatures, modal displacements and modal rotations in conjunction with Hermite cubic shape functions were used to compute the modal strain energy.

Methods Utilizing Changes in Dynamically Measured Flexibility

The flexibility matrix is the inverse of the stiffness matrix and relates the applied static loads to the resulting structural displacements. Each row of the flexibility matrix may be interpreted as the deformed shape of a structure due to a unit load applied at the corresponding DOF. The modal approximation of the flexibility matrix is called the dynamically measured flexibility or modal flexibility.

The flexibility matrix possesses many advantages over its inverse, the stiffness matrix. Firstly, an accurate representation of modal flexibility can be obtained by using only a few of the lower modes. Secondly, due to being uncoupled with the mass matrix, computation of modal flexibility is much more straightforward compared to the stiffness matrix. Mass-normalized mode shapes are necessary to construct the modal flexibility matrix, which requires the use of forced vibration tests instead of output-only modal analysis techniques.

Various research attempts have been made to utilize the dynamically measured flexibility (modal flexibility) for NDE.

Pandey and Biswas (1994) utilized the change in modal flexibilities before and after damage to locate defects on analytical and experimental case studies. For each DOF, maximum absolute value of the elements in the corresponding column of the flexibility difference was chosen as the damage indicator. No theoretical background was provided regarding the choice of this indicator however. Pandey and Biswas concluded that the proposed method works best when damage is located at a section where high bending moments occur. The authors also performed tests on wide-flanged I-beams to verify the effectiveness of the flexibility difference method (Pandey and Biswas, 1995).

Toksoy and Aktan (1994) examined the change in modal flexibility on a continuous three-span reinforced concrete bridge with and without a set of baseline modal information. Comparing the bridge deflections obtained from modal flexibilities exposed

the possible locations of damage. It was declared that once an indication of damage is obtained, it is possible to load the baseline and post-damage flexibilities load patterns which may better indicate the damage region.

Zhang and Aktan (1995) utilized the curvature of uniform load flexibility (the sum of all columns of the flexibility matrix, which represents the deflected shape of the structure if a unit load is applied at each DOF simultaneously) to detect damage. The largest value of the curvature difference computed before and after damage indicated the location of damage.

Methods Utilizing Static Displacement and Static Strain Changes

Many researchers utilized static displacement measurements to detect structural damage.

Hjelmstad and Shin (1997) brought up the importance of using static data by stating the fact that utilizing static data has the fewest theoretical complications and has the potential to present the clearest view to the problems associated with damage detection. They proposed an adaptive parameter grouping method that separates damaged parts in the FEM by subdividing parameter groups sequentially until all the damaged members are completely extracted. Sparsity of data and the influence of noise over the success of damage identification were addressed in the research.

Hajela and Soeiro (1990) proposed a system identification based method where changes in the analytical model (FEM of the structure) necessary to minimize differences between the measured and predicted response was determined. Considering this approach as an unconstrained optimization problem, iterative nonlinear programming methods were used to find a possible solution. The inclusion of static displacements to the modal data was justified by stating the optimization method's dependency on the number of modes utilized for damage detection. Displacement

profiles obtained via loading schemes that simulate higher modes were utilized in the research.

Sanayei and Saletnik (1996) presented a method for structural parameter identification by utilizing a subset of applied static forces and measured strains. They pointed out that strain measurements are more accurate than ordinary displacement measurements if proper attention is paid to negate possible sources of error such as temperature effects, electronic noise, nonlinearities, etc. To employ strain measurements in the FEM, a mapping model that relates the nodal displacements to elemental strains was established. This led to the development of a matrix containing strain, force and stiffness (parameters to be identified) entries from which a strain error function is defined in conjunction with the measured strains. Iterative methodologies that utilize Gauss-Newton or the steepest descend techniques were employed to minimize the error function for identifying the unknown parameters.

NDE Methods Developed at Texas A&M University

Topole (1993) investigated the applicability of three modal-based nondestructive evaluation (NDE) methods developed at Texas A&M University to nonlinear structures. These included “Stubbs’ Sensitivity Method (based on Stubbs and Osegueda (1990a) - Method A)” that predicts damage from eigenfrequency and mode shape data by solving a system of equations, “Modified Cawley’s Method (built upon the ideas presented by Cawley and Adams (1979) - Method B)” that locates damage by using the ratio of sensitivities (fraction of energy present at an element on a particular mode) and load vectors (that contain information about the change in eigenvalues, modal mass, and so on), and lastly “The Damage Index Method - Method C)”. A new method based on the total energy balance was proposed as a part of the dissertation. All methods were applied to nonlinear elastic structures with and without viscous damping as well as to a linear structure with structural damping for comparison purposes. While modal-based methods

proved to be limited, energy-based method correctly localized and quantified damage on a series of numerical experiments regardless of the degree of nonlinearity.

Kim (1993) investigated the relative impact of model uncertainty on the nondestructive damage detection (NDD) in structures by developing NDD methods first (Stubbs' Sensitivity Method, Modified Cawley's Method and Damage Index Method) and by proposing a methodology to assess the impact on model uncertainty and NDD accuracy later on. Model uncertainty included the uncertainty in the selection of damage detection model (DDM), uncertainty in the DDM parameters (due to inaccurately calibrated measurements or uncertainty in geometry, mass, damping, stiffness parameters) and uncertainty in the input to the DDM (i.e. measurement noise, missing sensor readings, or uncertainty in mode shapes, natural frequencies, and so on).

Maduakolam (1995) extended Damage Index Method to detect structural and mass damage in a class of floating structures. An increase in mass (e.g. flooding) was considered as mass damage.

Park (1997) proposed an NDE method to evaluate the condition of an existing structure and assess the safety of the structure by utilizing structural reliability concepts. The Damage Index equations were modified to include the change in the fraction of modal energy obtained through a first order approximation of the fraction of modal energy of the undamaged structure. Combining this concept with a technique that directly estimates the system structural reliability from element/component reliabilities, a methodology that is able to identify, locate and quantify damage as well as to evaluate its impact on structures was proposed.

Choi (1999) proposed rules for combining multiple damage algorithms to enhance the performance of damage localization and severity estimation. Damage indices using static measures, time and frequency domain response measures and modal parameters were proposed. He concluded that combining multiple damage algorithms improved the

performance of NDD and utilizing dynamic and static responses in addition to mode shapes proved to be valuable in damage detection.

Nam (2001) extended the capabilities of previously proposed systems identification (SID) and nondestructive damage evaluation (NDE) methods. Improvements in the accuracy of sensitivity-based SID (originally presented by Stubbs (1985) and revisited later by Stubbs and Kim (1996)) using additional spectral information (antiresonant and static compliance dominant frequencies) were reported. Extension of the baseline NDE algorithm (The Damage Index Method) resolved problems associated with the baseline method (e.g. shifting the axis of reference due to division-by-zero problem) and offered improvements in the severity estimation.

Kim (2002) developed damage index equations for beam and plate-like structures using the concept of modal flexibility. The proposed NDE method (namely The Flexural Damage Index) required computing the modal flexibilities of the damaged and undamaged beams (or plates) from which curvature profiles of the structures may be obtained. Using these curvatures and upon making the assumption that internal forces remain unaltered before and after damage (in cases where structure experiences small damage), an over-determined system of linear equations were solved to obtain damage indices.

Hyung (2007) developed two NDE methodologies that can identify stiffness and damping changes simultaneously in structures. The first method is an extension of the conservation of total energy technique previously given by Topole (1993) in which an over-determined system of linear equations with element stiffness and damping coefficients as unknowns was formed. The second method builds a sensitivity matrix using accelerations, element stiffnesses, and damping coefficients where stiffness and damping changes were found by utilizing the measured accelerations.

SHORTCOMINGS OF THE CURRENT NDE TECHNIQUES

If the preceding NDE techniques are examined under two main categories, namely the response-based and the model-based methodologies, it is reasonable to state that response-based NDE methodologies offer more straightforward tools for health monitoring compared to model-based techniques. Often times inadequate information regarding the physical properties of the structure may not allow building a detailed FEM. Furthermore, finite element updating algorithms generally are cumbersome when compared to response-based methods.

Upon reviewing the response-based NDE methodologies proposed to date, one may conclude that theories based on the fundamental equations of mechanics and mathematics in conjunction with reasonable (justifiable) assumptions (e.g. The Damage Index Method proposed by Stubbs et al. (1992)), provided the best results compared to the algorithms developed pragmatically (e.g. The Mode Shape Curvature Method proposed by Pandey et al. (1991), the Change in Modal Flexibility proposed by Pandey and Biswas (1994), the Change in Curvature of Uniform Load Flexibility proposed by Zhang and Aktan (1995), etc.).

Due to a lack of fundamental theory for the basis of damage detection, many existing NDE methodologies utilize response data in an *ad-hoc* way to detect structural damage. So far, the problem has been construed as one to identify response characteristics of a structure that are more sensitive to the existence of damage. Considering static (e.g. displacements and strains) and dynamic (e.g. frequencies, mode shapes, modal flexibilities, etc.) measurements as the two types of response data, the common practice is to utilize such measurements to develop NDE methodologies. In reality however, fundamental concepts of mechanics and mathematics on which the NDE methodology is based on, must dictate the response quantities to be measured. Many favorable response-based methodologies were unable to extend their capabilities to a Level III NDE algorithm due to this reason. In fact, many prominent damage detection methodologies

including the Damage Index Method (excluding the works of Kim (1993) and Park (1997)) did not address the damage severity estimations after locating the damage.

The spatial resolution of sensors is another issue that inevitably affects the performance of every single response-based NDE algorithm. Typically, structural response is measured through a limited number of sensors, and interpolation is used to simulate additional measurement locations. This practice leads to biased damage indices, since true local information may be lost. Many previously proposed NDE methodologies are unable to provide satisfactory damage detection (location and severity estimation) results in the absence of a very fine sensor layout. Therefore, current practice is to modify the sensor layout with expectation to obtain better damage predictions. Although this philosophy may lead to more accurate damage prediction results, by measuring fundamental response parameters that theoretically relate response to the damage, in addition to an adequate sensor layout can only provide better damage indicators.

In addition, the few NDE methodologies that are based on fundamental theories of mechanics (i.e. The Damage Index Method) mostly utilize simplified 1-D models such as the Euler-Bernoulli beam theory. Consequently, the applicability of these approaches is limited to structures, which conform to the deformations dictated by the Euler-Bernoulli beam theory.

In the view of the discussion given above, major shortcomings of the reviewed body of response-based NDE algorithms may be listed as follows:

1. There exists a lack of a fundamental theory for NDE;
2. There appears to be mainly *ad hoc* criteria for damage detection;
3. Most approaches are limited to damage detection and localization only (i.e. Level I and Level II);
4. Very few of the methods provide an estimate of damage severity (i.e. Level III);

5. Even fewer methods provide an estimate of the consequence of damage (i.e. Level IV);

6. Most approaches tend to focus on structures that obey the Euler-Bernoulli beam theory.

OUTSTANDING NEEDS

A review of the capabilities and limitations of the existing proposed global NDE methodologies suggests at least four outstanding needs:

1. To develop mathematical expressions based on the fundamental theories of mechanics, which relate physical properties (e.g. stiffness) of the undamaged and damaged structure to measurable response quantities (e.g. displacement, strains, etc.);

2. To develop reliable Level III and Level IV damage detection algorithms;

3. To extend NDE methodologies for damage prediction to general beams beyond Euler-Bernoulli beams (i.e. slender beams) to deep beams and stubby beams whose response may be based on the Timoshenko beam theory, and the Theory of Elasticity.

4. To build more accurate, efficient, and reliable damage indices that may be more suitable for the continuous monitoring of critical structures.

DISSERTATION OBJECTIVES

This dissertation proposes several NDE methods, which are based on fundamental concepts of solid mechanics, and which simultaneously utilize measurable response quantities to detect, locate and quantify damage in beam-type structures. Measurable structural responses may vary from static displacements or strains to dynamic parameters such as mode shapes and frequencies. In order to accomplish the stated objective, the following sub-objectives are anticipated:

1. Present the governing equations of equilibrium and stress-displacement relations of the fundamental beam theories including the Euler-Bernoulli Beam theory, the Timoshenko beam theory, and the beam theory based on linear Elasticity Theory;

2. Introduce a set of 2-D numerical experiments to simulate damage in all categories of beam types (slender, intermediate, and deep);

3. Develop NDE methodologies for all categories of beams based on the Euler-Bernoulli beam theory;

4. Develop NDE methodologies for all categories of beams based on the Timoshenko beam theory;

5. Develop NDE methodologies for all categories of beams based on the linear Elasticity Theory, and

6. Evaluate the performance of the proposed NDE methodologies on the basis of their capability to predict the location, the extent and the severity of damage simulated in the numerical experiments.

SCOPE OF THIS WORK

The scope of this dissertation is limited to general beams. By general beams, we mean a wide range of beams that may be encountered in structural design practice. These can generally be grouped under three main categories, namely: slender, intermediate and deep beams. Slender beams conform to the deformations dictated by the Euler-Bernoulli beam theory. Intermediate and deep beams correspond to structures with relatively higher aspect (depth to length) ratios compared to the case of the slender beams.

SIGNIFICANCE OF THIS WORK

This work outlines a set of rational procedures that can lead to reliable relationships between damage indices and measurable response parameters. The procedures are based

on fundamental mechanics and, therefore, are applicable to arbitrary structures. Utilizing the NDE algorithms presented in this study, a wide variety of structures and sub-systems encountered in practice may be analyzed upon employing the proper response quantities. The findings of this work will also lead to a better understanding of the limitations of the currently proposed NDE techniques. In addition, it is anticipated that by incorporating the methodologies proposed in this study to the continuous health monitoring of structural systems could reduce the cost of maintenance, and offer safer infrastructure networks. Furthermore, the results of this study could provide valuable information regarding the remaining useful life of civil engineering structures. The proposed methods have the potential to be expanded to cover a wider range of structures in the future (e.g. rods, frames and plates).

ORGANIZATION OF THE DISSERTATION

The remaining sections of this document are arranged into nine chapters. In Chapter II, the governing equations of equilibrium and the stress-displacement relations of the Euler-Bernoulli and the Timoshenko beam theories are introduced. In Chapter III, the numerical experiments utilized to evaluate the performances of the individual damage detection algorithms are designed. In Chapter IV, an explicit damage index methodology based on the principle of invariant stress resultants and the Euler-Bernoulli beam theory is developed. In Chapter V, damage index methodologies based on the singularities in the flexural stiffness distribution of the beam and the stress-displacement relations of the Euler-Bernoulli beam theory are developed. In Chapter VI, explicit damage index methodologies based on the principle of invariant stress resultants of the Timoshenko beam theory are developed. In Chapter VII, damage index methodologies based on the derivatives of cross sectional rotations are formulated. In Chapter VIII, explicit damage indices derived from linear elasticity theory are presented. In Chapter IX, the performance of the proposed NDE methodologies is evaluated using field measurements. In Chapter X, summary and major findings of this study are presented.

CHAPTER II

A REVIEW OF THE ELEMENTARY BEAM THEORIES AND THE CONCEPT OF DISCONTINUITY IN BEAM-TYPE STRUCTURES

INTRODUCTION

The objective of this chapter is to introduce the governing equations of equilibrium and the stress-displacement relations of the most commonly encountered beam theories in practice, namely the Euler-Bernoulli beam theory and the Timoshenko beam theory. The concept of flexural discontinuity in beam-type structures is discussed and equivalent flexural stiffness formulations at the point of flexural discontinuity are developed utilizing the fundamental equations of the Euler-Bernoulli and the Timoshenko beam models. This concept will be utilized in the derivation of damage detection algorithms proposed in subsequent chapters.

A REVIEW OF THE ELEMENTARY BEAM THEORIES

Governing equations of equilibrium and the stress-displacement relations of the Euler-Bernoulli and the Timoshenko beam theories are presented in this section.

The Euler-Bernoulli Beam Theory

The Euler-Bernoulli beam model utilizes the following displacement components (Reddy (1997)):

$$u(x,z) = -z\frac{dw}{dx} \tag{2.1}$$

$$v(x,z) = w(x) \tag{2.2}$$

where x and z coordinates are taken along the length and the height of the beam and y axis is along the beam thickness (perpendicular to the x and z axes). Rotation of a

transverse plane about the y axis is denoted by $-\frac{dw}{dx}$ and the transverse deflection on the midplane (at $z = 0$) is shown as w. Figure (2.1) depicts displacement components of the Euler-Bernoulli beam theory.

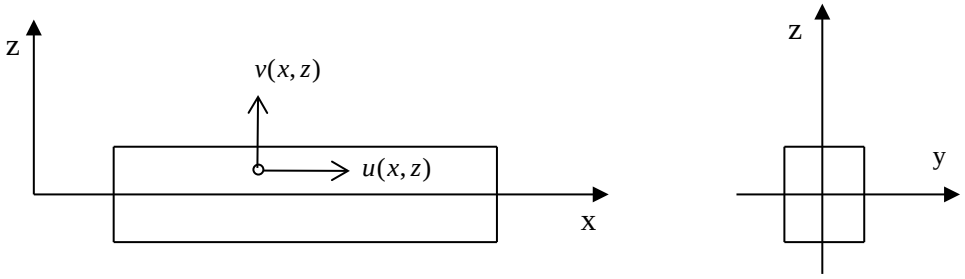

(a)

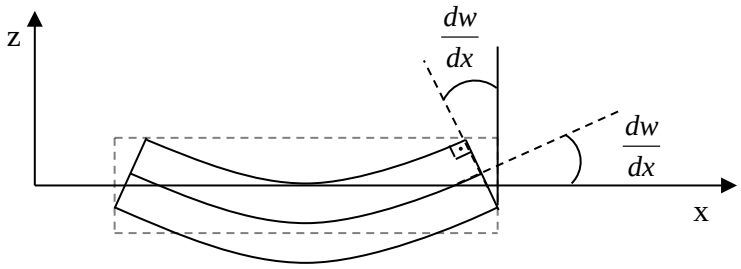

(b)

Figure 2.1 Displacement Components of the Euler-Bernoulli Beam Model.

(a) Horizontal and Vertical Displacement Components and Coordinate Axes

(b) Rotation of the Cross Section about the y axis

Eq. (2.1) and (2.2) imply that the planes that are normal to the beam axis in the undeformed state, remain plane and normal to the beam axis after deformation. This

assumption implies that all transverse shear strains are zero and that the deformation is entirely due to bending and in-plane stretching.

Governing equilibrium equations of the Euler-Bernoulli beam theory may be obtained by utilizing the balance of moments and transverse forces. Utilizing Eq. (2.1) and Eq. (2.2), the normal and shear strains may be written as:

$$\varepsilon_{xx} = \frac{\partial u}{\partial x} = -z\frac{d^2 w}{dx^2} \tag{2.3}$$

$$\gamma_{xz} = \frac{\partial u}{\partial z} + \frac{\partial v}{\partial x} = -\frac{dw}{dx} + \frac{dw}{dx} = 0 \tag{2.4}$$

As shown above, the Euler-Bernoulli beam model is assumed to be rigid with respect to shear deformations. Utilizing the equilibrium of moments and transverse forces gives

$$M(x) = \int_A z\sigma_{xx} dA \tag{2.5}$$

$$\frac{dM}{dx} - V(x) = 0 \tag{2.6}$$

$$\frac{dV}{dx} + q(x) = 0 \tag{2.7}$$

where q is intensity of the external distributed load.

Utilizing Eq. (2.3) and (2.5), assuming linear elastic behavior and setting $\sigma_{yy} = \sigma_{zz} = \tau_{xy} = \tau_{yz} = 0$, give the relation:

$$M(x) = -\int_A z\left(E\, z\frac{d^2 w}{dx^2}\right)dA = -\int_A E\frac{d^2 w}{dx^2} z^2 dA \tag{2.8}$$

where E corresponds to the modulus of elasticity.

Upon defining $I = \int_A z^2 dA$ where I is the moment of inertia, stress resultants given above simplify to:

$$M(x) = -EI\frac{d^2w}{dx^2} \tag{2.9}$$

$$V(x) = -\frac{d}{dx}\left(EI\frac{d^2w}{dx^2}\right) \tag{2.10}$$

Finally, the displacement equation of equilibrium for the Euler-Bernoulli beam theory may be obtained by substituting Eq. (2.10) into Eq. (2.7):

$$-\frac{d^2}{dx^2}\left(EI\frac{d^2w}{dx^2}\right) + q(x) = 0 \tag{2.11}$$

The Timoshenko Beam Theory

The Timoshenko beam theory relaxes the normality assumption of the Euler-Bernoulli beam theory by including a constant state of transverse shear strain throughout the beam thickness (Reddy (1997)). In this beam theory, planes that are normal to the beam axis in the undeformed state, do not necessarily remain normal to the beam axis after deformation. In order to account for the actual quadratic shear stress distribution across the cross section, a shear correction factor is introduced. This factor is commonly defined as the ratio of average shear strain to the shear strain at the centroid of the section (Cowper (1966)). Various methods for determining the shear correction coefficient were presented in existing literature (Kaneko (1975), Jensen (1983), Hutchinson (2001)).

The Timoshenko beam model utilizes the following displacement components:

$$u(x,z) = z\phi(x) \tag{2.12}$$

$$v(x,z) = w(x) \tag{2.13}$$

where x and z coordinates are taken along the length and the height of the beam and y axis is along the beam thickness (perpendicular to the x and z axes). Rotation of a transverse plane about the y axis is denoted by $\phi(x)$ and the transverse deflection on the midplane (at $z = 0$) is shown as w. Figure (2.2) depicts displacement components of the Timoshenko beam theory.

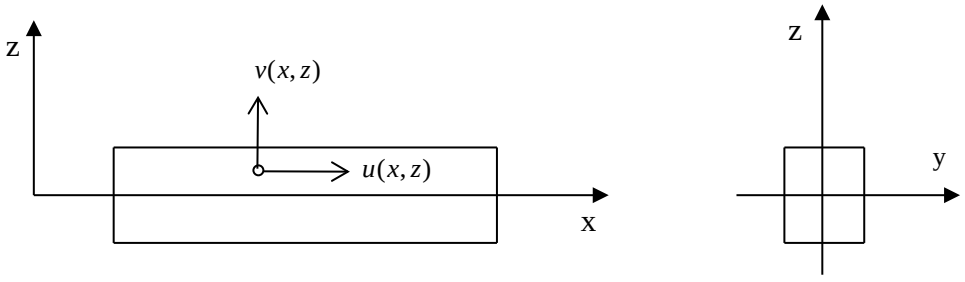

(a)

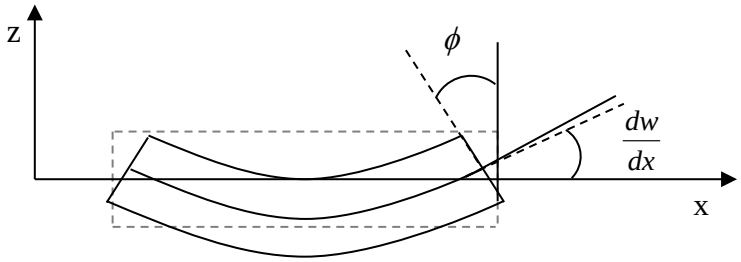

(b)

Figure 2.2 Displacement Components of the Timoshenko Beam Model.

(a) Horizontal and Vertical Displacement Components and Coordinate Axes

(b) Rotation of the Cross Section about the y axis

Governing equilibrium equations of the Timoshenko beam theory may be obtained by utilizing the balance of moments and transverse forces. Utilizing the displacement fields given in Eq. (2.12) and Eq. (2.13), normal and shear strains may be written as

$$\varepsilon_{xx} = \frac{\partial u}{\partial x} = z\frac{d\phi}{dx} \tag{2.14}$$

$$\gamma_{xz} = \frac{\partial u}{\partial z} + \frac{\partial v}{\partial x} = \phi + \frac{dw}{dx} \tag{2.15}$$

As shown above, the Timoshenko beam model admits a nonzero transverse shear strain.

Bending moment and transverse shear force may be defined as:

$$M(x) = \int_A z\sigma_{xx} dA \tag{2.16}$$

$$V(x) = \int_A \tau_{xz} dA \tag{2.17}$$

Utilizing Eq. (2.14) and (2.15), assuming linear elastic behavior and setting $\sigma_{yy} = \sigma_{zz} = \tau_{xy} = \tau_{yz} = 0$, give the relations

$$M(x) = \int_A z\left(E\, z\frac{d\phi}{dx}\right)dA = \int_A E\frac{d\phi}{dx} z^2 dA \tag{2.18}$$

$$V(x) = K_s \int_A G\left(\phi + \frac{dw}{dx}\right)dA \tag{2.19}$$

where E, G and K_s denote modulus of elasticity, shear modulus, and the shear correction factor respectively.

Equations (2.18) and (2.19) may further be simplified by utilizing $A = \int_A dA$ and $I = \int_A z^2 dA$ where I is the moment of inertia of the cross-sectional area A.

$$M(x) = EI\frac{d\phi}{dx} \tag{2.20}$$

$$V(x) = GAK_s\left(\phi + \frac{dw}{dx}\right) \tag{2.21}$$

The equilibrium of moments and transverse forces are written as

$$\frac{dM}{dx} - V(x) = 0 \tag{2.22}$$

$$\frac{dV}{dx} + q(x) = 0 \tag{2.23}$$

where q is intensity of the external distributed load. Substituting Eq. (2.20) and (2.21) back into Eq. (2.22) and (2.23) gives the following equilibrium equations:

$$\frac{d}{dx}\left(EI\frac{d\phi}{dx}\right) - GAK_s\left(\phi + \frac{dw}{dx}\right) = 0 \tag{2.24}$$

$$\frac{d}{dx}\left[GAK_s\left(\phi + \frac{dw}{dx}\right)\right] + q(x) = 0 \tag{2.25}$$

Equations (2.24) and (2.25) are the displacement equations of equilibrium for the Timoshenko beam theory.

The Euler-Bernoulli beam equations may easily be derived from Eq. (2.24) and Eq. (2.25) upon rewriting the former in the following form:

$$GAK_s\left(\phi+\frac{dw}{dx}\right)=\frac{d}{dx}\left(EI\frac{d\phi}{dx}\right) \tag{2.26}$$

Substituting Eq. (2.26) into Eq. (2.25) after replacing the rotation ϕ with $-\frac{dw}{dx}$, yields the previously derived displacement equation of equilibrium of the Euler-Bernoulli beam theory.

$$-\frac{d^2}{dx^2}\left(EI\frac{d^2w}{dx^2}\right)+q(x)=0 \tag{2.27}$$

THE CONCEPT OF DISCONTINUITY IN BEAM-TYPE STRUCTURES

The concept of flexural discontinuity in beam-type structures is discussed and equivalent flexural stiffness formulations at the point of flexural discontinuity are developed utilizing the fundamental equations of the Euler-Bernoulli and the Timoshenko beam theories in this section. This concept will be utilized in the derivation of damage detection algorithms proposed in subsequent chapters.

Consider a beam–type structural member that is comprised of several beam elements with varying flexural stiffnesses. Assume that two beam elements with flexural stiffness values EI_j and EI_{j+1} are connected at a random distance $x=l$ as depicted in Figure 2.3.

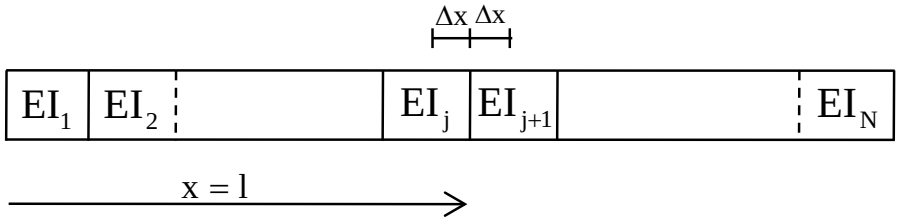

Figure 2.3 Beam Model Comprised of Several Beam Elements

Utilizing Eq. (2.20), bending moment at an infinitesimally small distance Δx before and after l may be written as

$$M(l-\Delta x) = EI_j \frac{d\phi(l-\Delta x)}{dx} \tag{2.28}$$

$$M(l+\Delta x) = EI_{j+1} \frac{d\phi(l+\Delta x)}{dx} \tag{2.29}$$

In the absence of any concentrated bending force, as Δx approaches to zero, bending moment attains a single value. Thus, equating Eq. (2.28) into Eq. (2.29) and using subscripts R and L to represent the derivative of the rotation of the cross-section to the right and left of the distance l gives

$$EI_j \frac{d\phi_L}{dx} = EI_{j+1} \frac{d\phi_R}{dx} \tag{2.30}$$

It is obvious from Eq. (2.30) that distinct values of the flexural stiffnesses EI_j and EI_{j+1} forces the derivative of the rotation to be different as well, thus yielding a discontinuity. If the derivative of the rotational profile is expressed in terms of Fourier series over each sub-element, it is a well-established fact that at a discontinuity Fourier series representation of any function converges to a value that is the average of the values immediately to the left and to right of the discontinuity. This may be written as

$$\frac{d\phi_A}{dx} = \frac{1}{2}\left(\frac{d\phi_L}{dx} + \frac{d\phi_R}{dx}\right) \tag{2.31}$$

The term $\frac{d\phi_A}{dx}$ denotes the average of the derivative of rotation at the point of flexural discontinuity.

Using Eq. (2.31) and (2.20), an average flexural stiffness (EI_A) at the point of flexural discontinuity may now be obtained. At the distance l:

$$M(l) = EI_A \frac{d\phi_A}{dx} \tag{2.32}$$

Substituting Eq. (2.31) back into Eq. (2.32) yields:

$$M(l) = EI_A \frac{1}{2}\left(\frac{d\phi_L}{dx} + \frac{d\phi_R}{dx} \right) \tag{2.33}$$

Expressing the right hand side of Eq. (2.33) in terms of bending moment and flexural stiffnesses of the two adjacent sub-elements gives:

$$M(l) = EI_A \frac{1}{2}\left(\frac{M(l)}{EI_j} + \frac{M(l)}{EI_{j+1}} \right) \tag{2.34}$$

After simplifying like terms on both sides of Eq. (2.34), average flexural stiffness may be expressed as the flexural stiffnesses of adjacent elements.

$$EI_A = 2\left(\frac{EI_j \, EI_{j+1}}{EI_j + EI_{j+1}} \right) \tag{2.35}$$

The discontinuity in the derivative of rotation corresponds to the discontinuity in the curvature profile in Euler-Bernoulli beam theory. This is a natural result of the following identity for Euler-Bernoulli beams

$$\phi = -\frac{dw}{dx} \tag{2.36}$$

Utilizing Eq. (2.9) where $\frac{d^2w}{dx^2}$ represents the curvature of the beam, dividing a continuous bending moment profile into a discontinuous flexural stiffness distribution,

must result in curvature profiles, which are also discontinuous. Biondi and Caddemi (2004 and 2007) observed the same phenomenon by presenting closed form solutions of uniform Euler-Bernoulli beams with flexural stiffness discontinuities and reported continuous deflection and slope functions, whereas curvature profiles showing a discontinuity at the point of flexural singularity.

Thus, Eq. (2.35) is valid both for the Timoshenko and the Euler-Bernoulli beam theories.

Up to this point, stress resultants were utilized to obtain an equivalent flexural stiffness (EI_A) at the point of flexural discontinuity. There is, however a more elementary approach. Since bending stiffness distribution that is nonuniform throughout a beam represents a singularity in the stiffness profile itself, then utilizing Fourier series representation, the following should also be true

$$EI_A = \frac{1}{2}\left(EI_j + EI_{j+1}\right) \tag{2.37}$$

where EI_A represents an average value of the flexural stiffness at the joint where two sub-elements (j and $j+1$) are connected. Eq. (2.37) provides an alternative formulation to Eq. (2.35).

SUMMARY

The governing equations of equilibrium and the stress-displacement relations of the Euler-Bernoulli and the Timoshenko beam theories were presented in this chapter. It was shown that the Euler-Bernoulli beam equations may be conveniently obtained from the more general Timoshenko beam theory upon neglecting the transverse shear deformations. Next, the concept of discontinuity in beam-type structures was introduced. It has been shown that flexural stiffness singularities lead to discontinuities in the derivative of rotation at the point of discontinuity, which more specifically, corresponds

to the discontinuity in the curvature profile in Euler-Bernoulli beams. Finally, utilizing the fundamental equations of solid mechanics and calculus, two equivalent flexural stiffness expressions in terms of the flexural stiffnesses of adjacent elements were obtained at the point of a flexural discontinuity.

CHAPTER III

DESCRIPTION OF THE SELECTED NUMERICAL EXPERIMENTS

INTRODUCTION

The objective of this chapter is to introduce a set of numerical experiments, which will be utilized to evaluate the performances of the individual damage detection algorithms proposed in subsequent chapters. These numerical experiments are intended to simulate the more complex and costly experimental studies. In order to accomplish the stated objective, firstly, an overview of the test structures chosen for the case studies is provided. Secondly, descriptions of the associated finite element (FE) models used in the case studies are given, since the numerical experiments are based on the FE models. The FE models are validated by using solutions from the Elasticity Theory. Thirdly, damage scenarios are simulated by adjusting the elastic modulus and/or Poisson's ratio of individual elements in the FE model. Finally, methodologies to assess the performance of the proposed damage detection algorithms, which are discussed in subsequent chapters, are summarized at the end of this chapter.

DESCRIPTION OF THE TEST STRUCTURES

Three rectangular cantilever beams with varying depth-to-length ratios are chosen as test structures in this study. Each test beam is modeled to simulate the behavior of a different beam-type structure found in engineering practice. As a general rule of thumb, the behavior of a beam with an aspect ratio (depth/length) less than 1/10 may accurately be modeled using the Euler-Bernoulli beam theory, which is pertinent only in the case of slender beams. The selected test structures represent so-called slender, intermediate and deep beams. Following the given rule of thumb, an aspect ratio of 1/12 is deemed appopirate for modeling a slender beam. Aspect ratios of 1/5 and 1/2 are chosen to represent the intermediate and deep beams, respectively. The material properties,

sectional properties, and the finite element models of each test beam are described below.

The Slender Beam

The first test structure represents a slender beam with an aspect ratio of 1/12. The depth and the length of the beam are 12 in. and 144 in., respectively. The beam is made of 2.5 in. thick solid steel. Figure 3.1 shows the elevation and cross-sectional views of the structure and Table 3.1 summarizes the material and sectional properties of the beam.

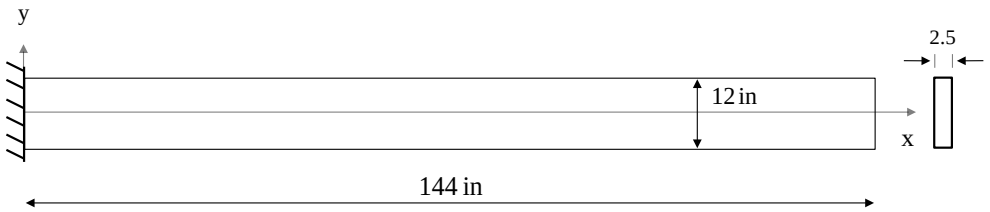

Figure 3.1 Schematic of Slender Cantilever Beam

Table 3.1 Material and Section Properties of the Slender Cantilever Beam

Description	Magnitude
Span Length (in)	144
Beam Thickness (in)	2.5
Beam Depth (in)	12
Cross-sectional Area (in^2)	30
Moment of Inertia (in^4)	360
Mass Density ($kip.sec^2/in^4$)	$7.345x10^{-7}$
Modulus of Elasticity (ksi)	29000
Poisson's ratio	0.30

The finite element (FE) model of the test beam is constructed using bilinear quadrilateral plane elements. Each four-node plane element consists of eight degree of freedoms (DOF). The schematic of a typical element is given in Figure 3.2.

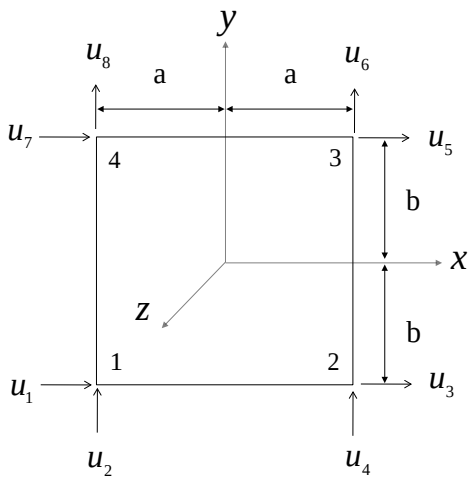

Figure 3.2 Bilinear Quadrilateral Element and Nodal DOF

Conveniently named as Q4, which represents a quadrilateral with four nodes, this element is incapable of representing the pure bending behavior correctly. When subjected to pure bending, it exhibits a shear strain in addition to the anticipated bending strain. This leads to the phenomenon commonly referred to as “shear-locking” and adding quadratic terms to the displacement field of a regular Q4 element has been shown to overcome this problem. Thus, in addition to the physical DOF, each element consists of internal degree of freedoms at the element level that are not associated with any node (nodeless DOF). Additional DOF are appended to the array of nodal DOF and condensed out before elements are assembled to form the global equations. These improved quadrilateral elements are designated as Q6 elements (Cook et al. (2002)).

Convergence tests are performed in order to choose an appropriate finite element mesh for the test structure. The objective of the tests is to identify a relatively simple model that is able to provide a reasonably accurate solution. The free end of the cantilever beam is subjected to a static load of one kip. The vertical displacement at the tip of the beam is computed as 0.096 in. using the theory of elasticity solution given by Ugural and Fenster (2003). Utilizing trial meshes of various sizes, it is concluded that the solution obtained by the FE model converged to the exact solution given by the elastic theory when the beam is subdivided into 120 plane elements. Figure 3.3 depicts the convergence tests performed for the slender beam. The error between the numerical and exact solution is less than 0.5%. Each Q6 element is 4.8 in. wide and 3 in. deep with a 2.5 in. thickness in the perpendicular z direction. The plane stress assumption is adopted in the FE model. Figure 3.4 depicts the selected FE mesh.

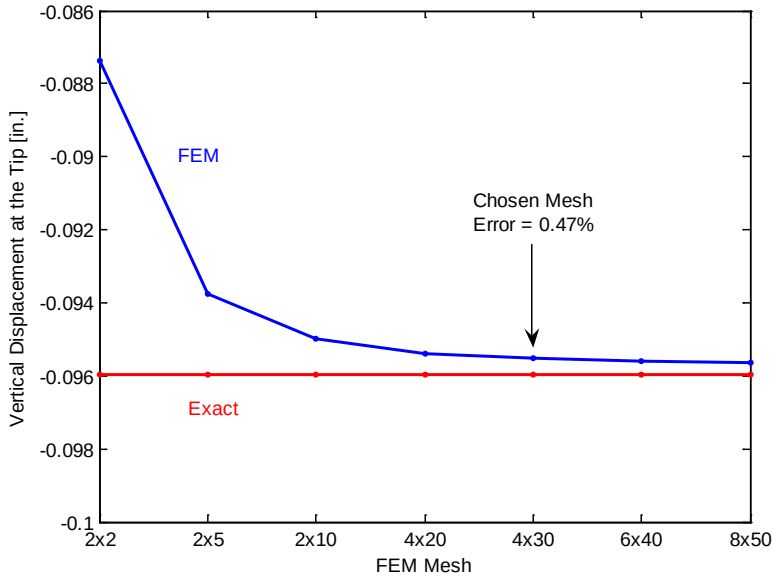

Figure 3.3 Convergence of the FEM Compared with the Solution from the Theory of Elasticity – Slender Beam

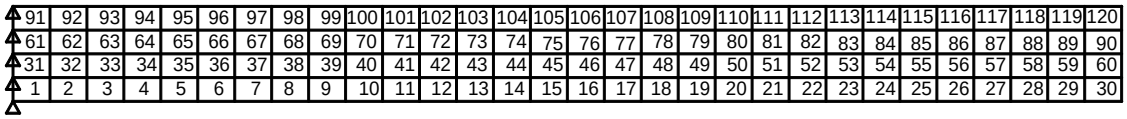

Figure 3.4 Finite Element Mesh of the Slender Beam

The Intermediate Beam

The second test structure represents an intermediate beam with an aspect ratio of 1/5. The length of the beam is 120 in. and the depth of the beam is 24 in. The beam is made of 2.5 in. thick solid steel. The elevation and cross-sectional views of the beam are depicted in Figure 3.5 and the sectional and material properties are listed in Table 3.2.

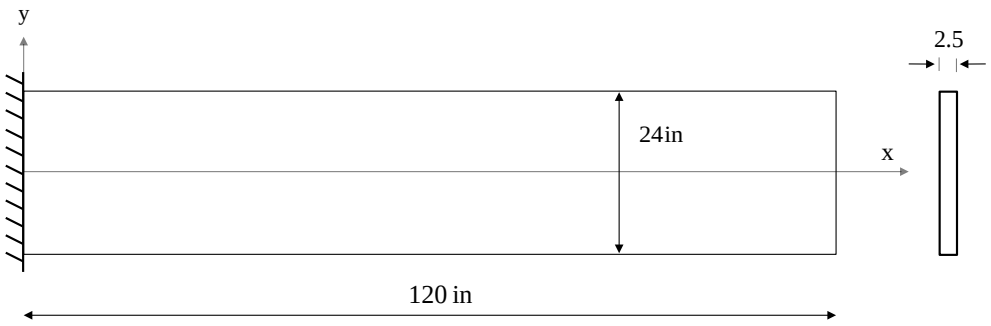

Figure 3.5 Schematic of Intermediate Cantilever Beam

The finite element mesh of the intermediate beam comprises of 180 Q6 elements. As before, convergence tests are performed in order to choose an appropriate finite element mesh for the intermediate beam. The free end of the beam is subjected to a static load of five kips. Using theory of elasticity, the vertical displacement at the free end is found to be 0.0358 in. Utilizing seven different mesh sizes, it is concluded that, any further

refinement in the FE model is not providing any significant improvement in the accuracy of solution. The error between the numerical and exact solution is 1.3 % with the chosen mesh. Each plane element is 4 in. wide and 4 in. deep with 2.5 in. thickness in the perpendicular z direction. Figure 3.6 shows the convergence of the FEM compared with the solution from the theory of elasticity approach. Figure 3.7 depicts the finite element mesh of the beam. The plane stress assumption is used in the FE Model.

Table 3.2 Material and Section Properties of the Intermediate Cantilever Beam

Description	**Magnitude**
Span Length (in)	120
Beam Thickness (in)	2.5
Beam Depth (in)	24
Cross-sectional Area (in^2)	60
Moment of Inertia (in^4)	2880
Mass Density ($kip.sec^2/in^4$)	$7.345x10^{-7}$
Modulus of Elasticity (ksi)	29000
Poisson's ratio	0.30

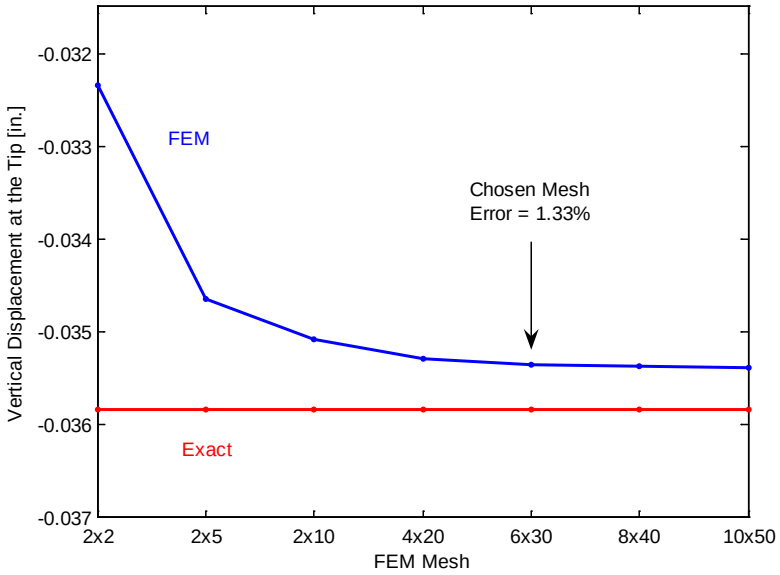

Figure 3.6 Convergence of the FEM Compared with the Solution from the Theory of Elasticity – Intermediate Beam

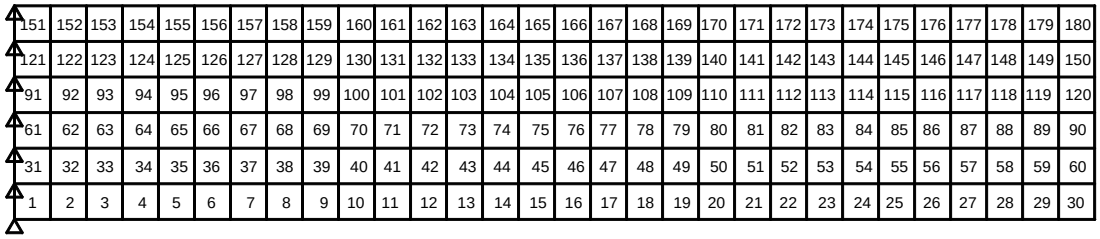

Figure 3.7 Finite Element Mesh of the Intermediate Beam

The Deep Beam

The third structure is a 2.5 in. thick steel beam, which represents the deep beam with an aspect ratio 1/2. The length and the depth of the beam are 60 in. and 30 in.

respectively. Figure 3.8 depicts the elevation and cross-sectional views and Table 3.3 lists the material and sectional properties of the beam.

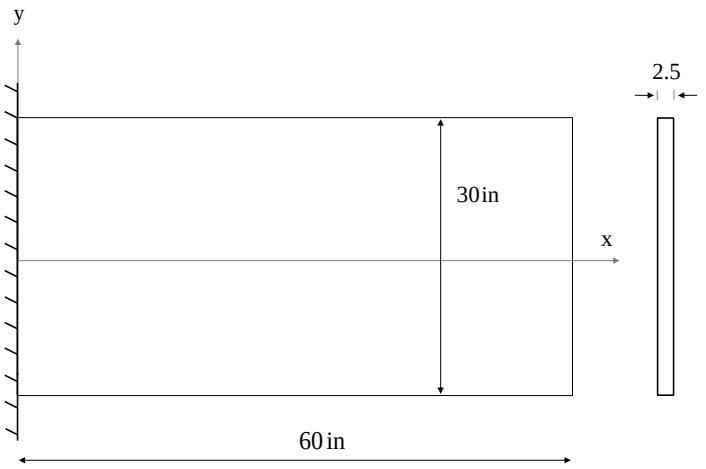

Figure 3.8 Schematic of Deep Cantilever Beam

Table 3.3 Material and Section Properties of the Deep Cantilever Beam

Description	**Magnitude**
Span Length (in)	60
Beam Thickness (in)	2.5
Beam Depth (in)	30
Cross-sectional Area (in^2)	75
Moment of Inertia (in^4)	5625
Mass Density $kip.sec^2/in^4$	$7.345x10^{-7}$
Modulus of Elasticity (ksi)	29000
Poisson's ratio	0.30

The finite element model of the deep beam contains 200 Q6 elements. Eight trial mesh sizes are used in order to choose an appropriate finite element mesh for the test beam. The free end of the deep beam is subjected to a static load of 30 kips. The vertical displacement at the tip of the beam is computed as 0.0165 in. using the theory of elasticity solution. The FE model gives 0.0155 in. with the chosen mesh. Although the error between the two solutions is rather large with 5.6%, any further improvement in the accuracy of solution is deemed not possible with a reasonably simple mesh size. A typical plane element is 2.4 in. wide and 3.75 in. deep with 2.5 in. thickness in the perpendicular z direction. Figure 3.9 depicts the convergence of the FEM with the solution from the elasticity theory. Figure 3.10 depicts the finite element mesh of the deep beam. As before, the plane stress assumption is adopted in the FE Model.

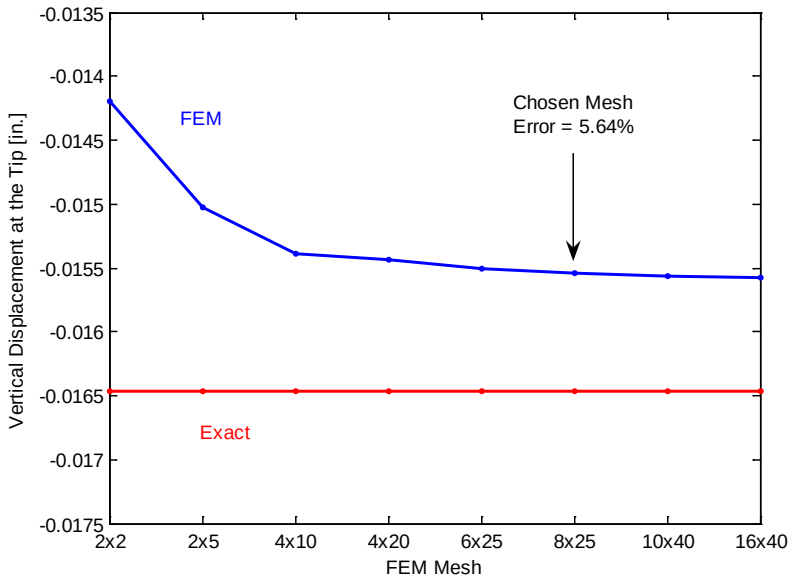

Figure 3.9 Convergence of the FEM Compared with the Solution from the Theory of Elasticity – Deep Beam

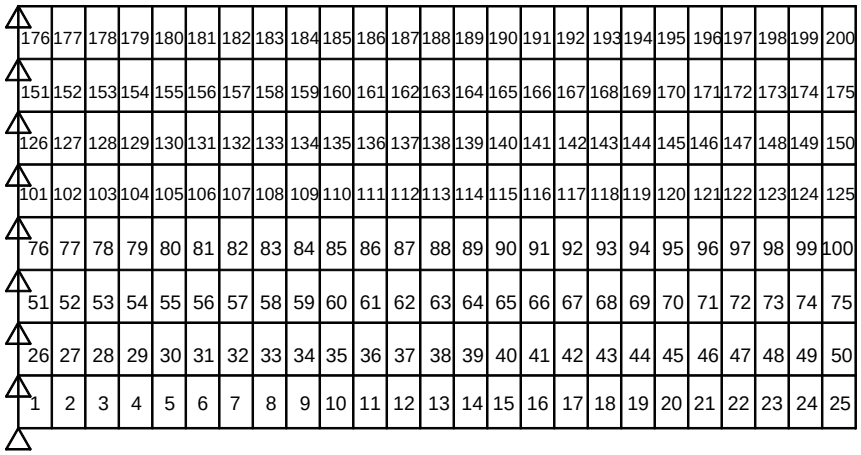

Figure 3.10 Finite Element Mesh of the Deep Beam

DAMAGE SCENARIOS APPLIED TO THE BEAM MODELS

Each test beam is subjected to five different damage scenarios. In order to generate these scenarios, three different parameters are varied: the damage location, the damage extent, and the damage severity. The damage location corresponds to the center of the inflicted damage. Since, 2-D plane elements are used to build the FE model, the damage location is specified by two variables: the x (horizontal) and y (vertical) coordinates. The damage extent signifies the area of the damaged region. It is represented by two variables: Δx (the total length of the damaged region along the x-coordinate) and Δy (the total length of the damaged region along the y-coordinate). The area of an individual damaged zone is the product of these two measures. Finally, the damage severity is defined as the percent reduction in the material properties of individual plane elements within an area defined by the damage extent. Young's modulus and/or Poisson's ratio are adjusted in order to simulate damage in this study. Reducing the elastic modulus solely has been the common practice so far in literature. Since any alteration in the material properties of a structure in real life may also involve a change Poisson's ratio,

here it is deemed appropriate to simulate damage by adjusting the Poisson's ratio in addition to elastic modulus in the FEM of the test structures as well. Simulated damage cases for each beam are summarized below.

The Slender Beam

Damage Case SB 1

This scenario represents a single damage case in which a 5% uniform stiffness reduction is inflicted throughout the depth of the beam in a region centered at 98.4 in. from the clamped end and 6 in. from the bottom of the beam. The extent of damage is 4.8 in. wide and 12 in. deep. This damaged region corresponds to 3.33% of the beam's total surface area. Figure 3.11 shows the first damage case on the FE mesh of the slender beam. Elastic moduli of plane elements 21, 51, 81, and 111 are decreased by 5% to simulate the prescribed damage scenario. Table 3.4 summarizes the details of the inflicted damage. This scenario is intended to simulate local stiffness degradation, which is concentrated along a vertical axis through the depth of the beam.

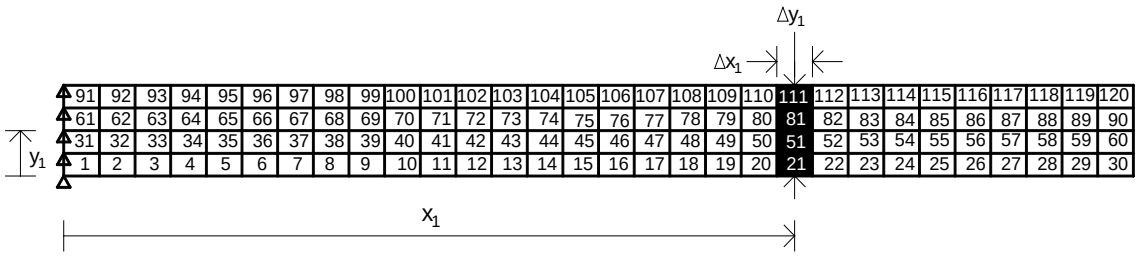

Figure 3.11 Schematic Representation of the First Damage Case on the Finite Element Mesh of the Slender Beam

Table 3.4 Summary of the First Damage Scenario Applied to the Slender Beam

Damage Location		Damage Size			Damage Severity	Damaged Elements
x	y	Δx	Δy	ΔA		
98.4 in.	6 in.	4.8 in.	12 in.	57.6 in^2	-5% of E	21, 51, 81, 111

Damage Case SB 2

This scenario also represents a single damage case in which a 10% stiffness reduction is inflicted in a region centered at 26.4 in. from the clamped end and 3 in. from the bottom of the beam. The extent of damage is 4.8 in. wide and 6 in. deep, which corresponds to 1.67% of the beam's total surface area. The prescribed damage corresponds to plane elements 6 and 36 on the finite element mesh of the beam. Figure 3.12 depicts the location the second damage case and Table 3.5 summarizes the damage parameters. This damage scenario is intended to simulate a localized surface crack.

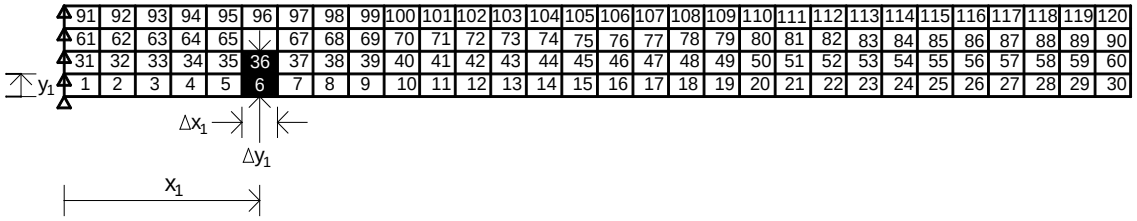

Figure 3.12 Schematic Representation of the Second Damage Case on the Finite Element Mesh of the Slender Beam

Table 3.5 Summary of the Second Damage Scenario Applied to the Slender Beam

Damage Location		Damage Size			Damage Severity	Damaged Elements
x	y	Δx	Δy	ΔA		
26.4 in.	3 in.	4.8 in.	6 in.	28.8 in^2	-10% of E	6, 36

Damage Case SB 3

This damage scenario represents a multiple damage case in which an arbitrary reduction in Poisson's ratio is prescribed in addition to the elastic modulus at the damaged regions.

The first damaged region is centered at 26.4 in. from the clamped end and 4.5 in. from the bottom of the beam. Stiffness of the region is reduced by 10% through altering Young's modulus. The extent of damage is 4.8 in. wide and 9 in. deep, which corresponds to 2.5% of the beam's total surface area. This scenario represents the case in which damage initiated in Damage Case 2 is widened further through the depth of the beam. Poisson's ratio is reduced by 8% at the damaged region. Prescribed damage is represented by plane elements 6, 36 and 66 on the FE mesh of beam.

The second damaged region is centered at 88.8 in. from the clamped end and 3 in. from the bottom of the beam. Stiffness of the region is reduced by 5% through altering Young's modulus. The extent of damage is 4.8 in. wide and 6 in. deep. This corresponds to 1.67% of the beam's total surface area. Poisson's ratio is reduced by 7% at the damaged region. Prescribed damage is represented by plane elements 19 and 49 on the FE mesh of beam.

Figure 3.13 shows the schematic representation of the third damage case and Table 3.6 summarizes the damage related parameters.

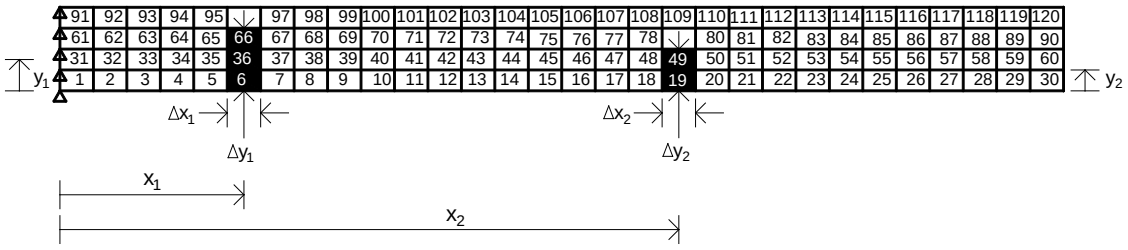

Figure 3.13 Schematic Representation of the Third Damage Case on the Finite Element Mesh of the Slender Beam

Table 3.6 Summary of the Third Damage Scenario Applied to the Slender Beam

Damage Location		Damage Size			Damage Severity	Damaged Elements
x	y	Δx	Δy	ΔA		
26.4 in.	4.5 in.	4.8 in.	9 in.	43.2 in^2	-10% of E	6, 36, 66
26.4 in.	4.5 in.	4.8 in.	9 in.	43.2 in^2	-8% of ν	6, 36, 66
88.8 in.	3 in.	4.8 in.	6 in.	28.8 in^2	-5% of E	19, 49
88.8 in.	3 in.	4.8 in.	6 in.	28.8 in^2	-7% of ν	19, 49

Damage Case SB 4

This damage scenario represents a multiple damage case in which three possible crack locations with varying extents and severities are simulated.

The first damaged region is centered at 33.6 in. from the clamped end and 9 in. from the bottom of the beam. The extent of damage is 9.6 in. wide and 6 in. deep. This damaged region corresponds to 3.33% of the beam's total surface area. Elastic moduli of plane elements 67, 68, 97 and 98 are decreased by 3% in order to simulate the prescribed damage scenario.

The second damaged region is centered at 74.4 in. from the clamped end and 7.5 in. from the bottom of the beam. Stiffness of the region is reduced by 5% through altering Young's modulus. The extent of damage is 4.8 in. wide and 9 in. deep. This corresponds to 2.50% of the beam's total surface area. Prescribed damage is represented by elements 46, 76, 106 on the FE mesh of beam.

The third damaged region simulates an inner crack, which is centered at 112.8 in. from the clamped end and 7.5 in. from the bottom of the beam. The extent of damage is 4.8 in. wide and 3 in. deep and the stiffness of the region is reduced by 6% through altering Young's modulus. Damaged region corresponds to 0.83% of the beam's total surface area. Prescribed damage is represented by the single plane element 84 on the FE mesh of beam.

Figure 3.14 shows the schematic representation of the fourth damage case and Table 3.7 summarizes the damage related parameters.

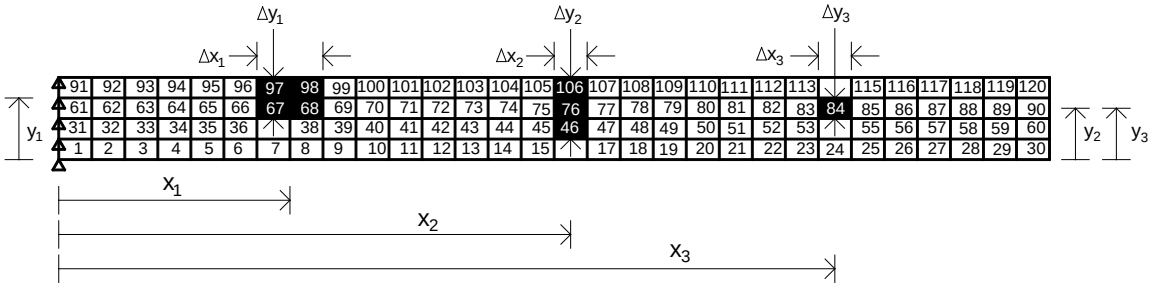

Figure 3.14 Schematic Representation of the Fourth Damage Case on the Finite Element Mesh of the Slender Beam

Table 3.7 Summary of the Fourth Damage Scenario Applied to the Slender Beam

Damage Location		Damage Size			Damage Severity	Damaged Elements
x	y	Δx	Δy	ΔA		
33.6 in.	9 in.	9.6 in.	6 in.	57.6 in^2	-3% of E	67, 68, 97, 98
74.4 in.	7.5 in.	4.8 in.	9 in.	43.2 in^2	-5% of E	46, 76, 106
112.8 in.	7.5 in.	4.8 in.	3 in.	14.4 in^2	-6% of E	84

Damage Case SB 5

This damage scenario introduces a crack at the clamped end of the beam in addition to an inner crack located close to the free end. Figure 3.15 shows the schematic representation of the damage case and Table 3.8 summarizes the damage related parameters. Damage is prescribed by altering Young's modulus and Poisson's ratio of individual plane elements.

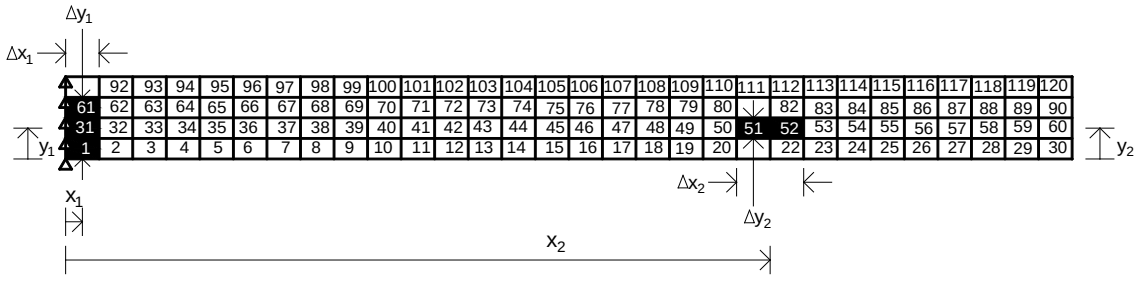

Figure 3.15 Schematic Representation of the Fifth Damage Case on the Finite Element Mesh of the Slender Beam

Table 3.8 Summary of the Fifth Damage Scenario Applied to the Slender Beam

Damage Location		Damage Size			Damage Severity	Damaged Elements
x	y	Δx	Δy	ΔA		
2.4 in.	4.5 in.	4.8 in.	9 in.	43.2 in^2	-11% of E	1, 31, 61
2.4 in.	4.5 in.	4.8 in.	9 in.	43.2 in^2	-6% of ν	1, 31, 61
100.8 in.	4.5 in.	9.6 in.	3 in.	28.8 in^2	-7% of E	51, 52
100.8 in.	4.5 in.	9.6 in.	3 in.	28.8 in^2	-5% of ν	51, 52

The Intermediate Beam

Damage scenarios applied to the intermediate beam follows the same pattern with the ones applied to the slender beam. Each scenario is summarized below.

Damage Case IB 1

Figure 3.16 shows the schematic representation of the first damage case and Table 3.9 summarizes the damage related parameters.

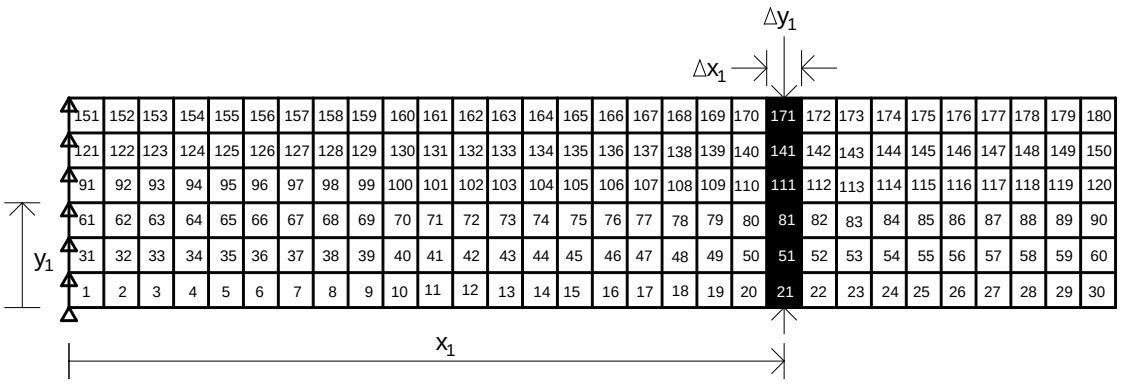

Figure 3.16 Schematic Representation of the First Damage Case on the Finite Element Mesh of the Intermediate Beam

Table 3.9 Summary of the First Damage Scenario Applied to the Intermediate Beam

Damage Location		Damage Size			Damage Severity	Damaged Elements
x	y	Δx	Δy	ΔA		
82 in.	12 in.	4 in.	24 in.	96 in^2	-5% of E	21, 51, 81, 111, 141, 171

Damage Case IB 2

Figure 3.17 shows the schematic representation of the second damage case and Table 3.10 summarizes the damage related parameters.

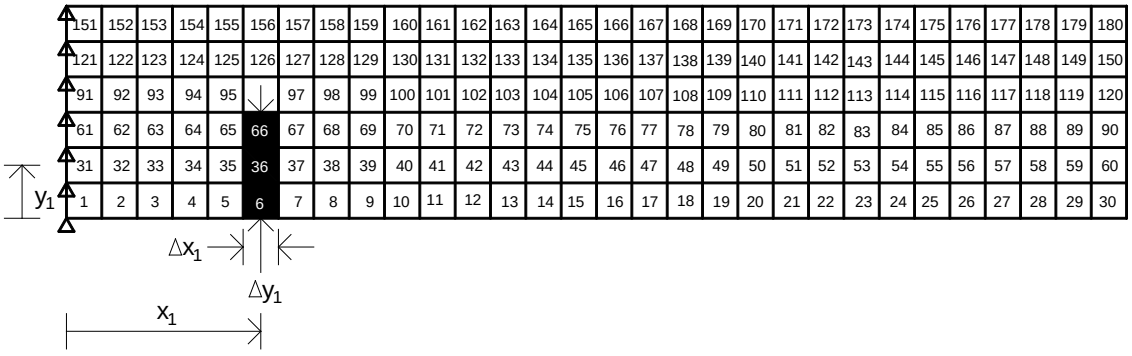

Figure 3.17 Schematic Representation of the Second Damage Case on the Finite Element Mesh of the Intermediate Beam

Table 3.10 Summary of the Second Damage Scenario Applied to the Intermediate Beam

Damage Location		Damage Size			Damage Severity	Damaged Elements
x	y	Δx	Δy	ΔA		
22 in.	6 in.	4 in.	12 in.	48 in^2	-10% of E	6, 36, 66

Damage Case IB 3

Figure 3.18 shows the schematic representation of the third damage case and Table 3.11 summarizes the damage related parameters.

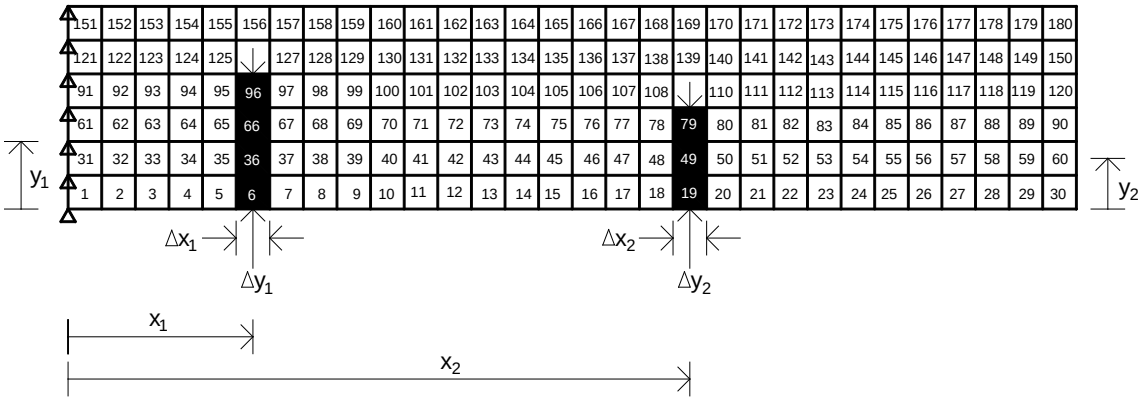

Figure 3.18 Schematic Representation of the Third Damage Case on the Finite Element Mesh of the Intermediate Beam

Table 3.11 Summary of the Third Damage Scenario Applied to the Intermediate Beam

Damage Location		Damage Size			Damage Severity	Damaged Elements
x	y	Δx	Δy	ΔA		
22 in.	8 in.	4 in.	16 in.	64 in^2	-10% of E	6, 36, 66, 96
22 in.	8 in.	4 in.	16 in.	64 in^2	-8% of ν	6, 36, 66, 96
74 in.	6 in.	4 in.	12 in.	48 in^2	-5% of E	19, 49, 79
74 in.	6 in.	4 in.	12 in.	48 in^2	-7% of ν	19, 49, 79

Damage Case IB 4

Figure 3.19 shows the schematic representation of the fourth damage case and Table 3.12 summarizes the damage related parameters.

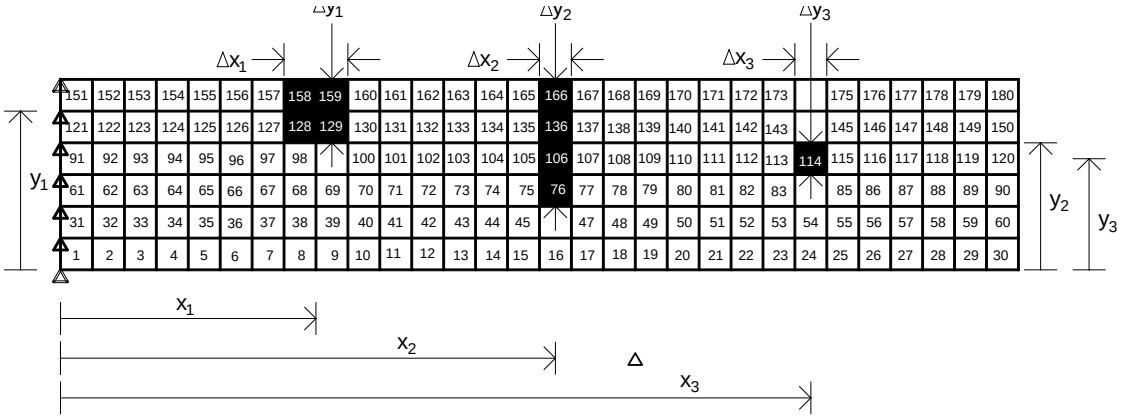

Figure 3.19 Schematic Representation of the Fourth Damage Case on the Finite Element Mesh of the Intermediate Beam

Table 3.12 Summary of the Fourth Damage Scenario Applied to the Intermediate Beam

Damage Location		Damage Size			Damage Severity	Damaged Elements
x	y	Δx	Δy	ΔA		
32 in.	20 in.	8 in.	8 in.	64 in^2	-3% of E	128, 129, 158, 159
62 in.	16 in.	4 in.	16 in.	64 in^2	-5% of E	76, 106, 136, 166
94 in.	14 in.	4 in.	4 in.	16 in^2	-6% of E	114

Damage Case IB 5

Figure 3.20 shows the schematic representation of the fifth damage case and Table 3.13 summarizes the damage related parameters.

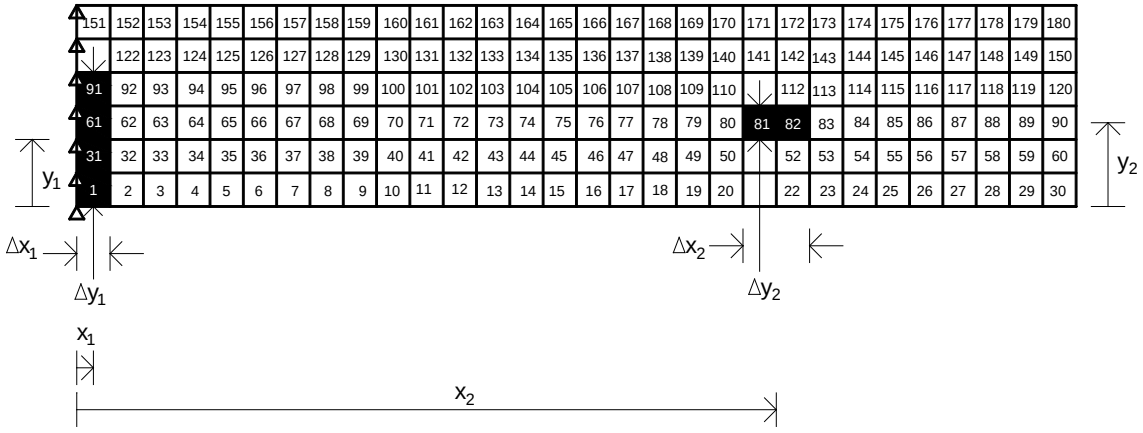

Figure 3.20 Schematic Representation of the Fifth Damage Case on the Finite Element Mesh of the Intermediate Beam

Table 3.13 Summary of the Fifth Damage Scenario Applied to the Intermediate Beam

Damage Location		Damage Size			Damage Severity	Damaged Elements
x	y	Δx	Δy	ΔA		
2 in.	8 in.	4 in.	16 in.	64 in^2	-11% of E	1, 31, 61, 91
2 in.	8 in.	4 in.	16 in.	64 in^2	-6% of ν	1, 31, 61, 91
84 in.	10 in.	8 in.	4 in.	32 in^2	-7% of E	81, 82
84 in.	10 in.	8 in.	4 in.	32 in^2	-5% of ν	81, 82

The Deep Beam

Damage scenarios applied to the deep beam follows the same pattern with the ones applied to the slender beam. Each scenario is summarized below.

Damage Case DB 1

Figure 3.21 shows the schematic representation of the first damage case and Table 3.14 summarizes the damage related parameters.

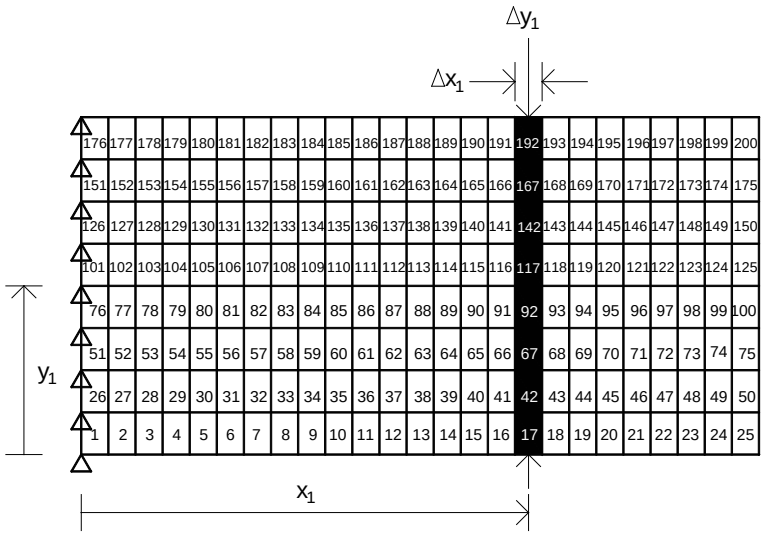

Figure 3.21 Schematic Representation of the First Damage Case on the Finite Element Mesh of the Deep Beam

Table 3.14 Summary of the First Damage Scenario Applied to the Deep Beam

Damage Location		Damage Size			Damage Severity	Damaged Elements
x	y	Δx	Δy	ΔA		
39.6 in.	15 in.	2.4 in.	30 in.	72 in^2	-5% of E	17, 42, 67, 92, 117, 142, 167, 192

Damage Case DB 2

Figure 3.22 shows the schematic representation of the second damage case and Table 3.15 summarizes the damage related parameters.

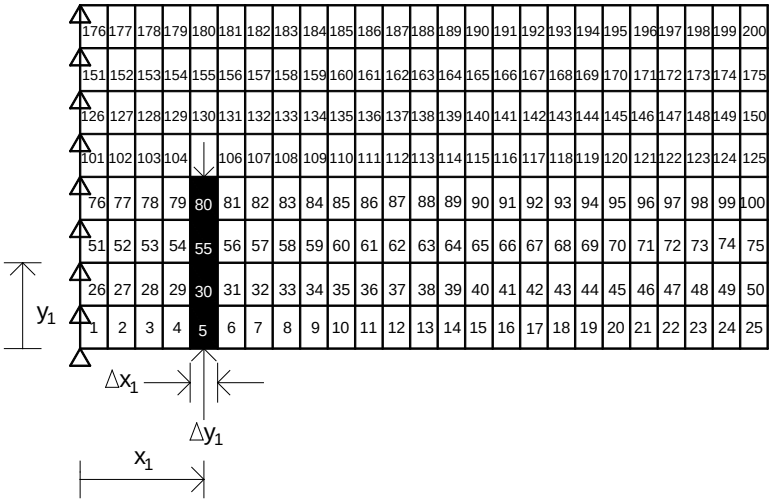

Figure 3.22 Schematic Representation of the Second Damage Case on the Finite Element Mesh of the Deep Beam

Table 3.15 Summary of the Second Damage Scenario Applied to the Deep Beam

Damage Location		Damage Size			Damage Severity	Damaged Elements
x	y	Δx	Δy	ΔA		
10.8 in.	7.5 in.	2.4 in.	15 in.	36 in^2	-10% of E	5, 30, 55, 80

Damage Case DB 3

Figure 3.23 shows the schematic representation of the third damage case and Table 3.16 summarizes the damage related parameters.

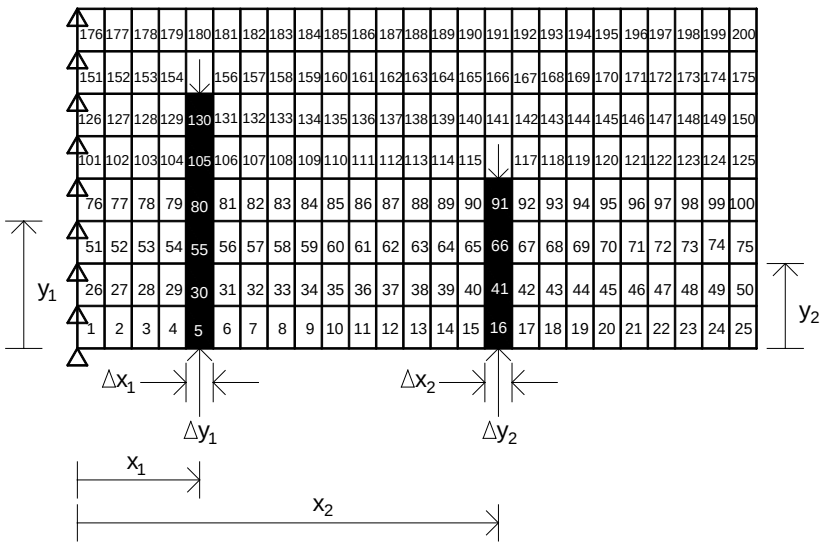

Figure 3.23 Schematic Representation of the Third Damage Case on the Finite Element Mesh of the Deep Beam

Table 3.16 Summary of the Third Damage Scenario Applied to the Deep Beam

Damage Location		Damage Size			Damage Severity	Damaged Elements
x	y	Δx	Δy	ΔA		
10.8 in.	11.25 in.	2.4 in.	22.5 in.	54 in^2	-10% of E	5, 30, 55, 80, 105, 130
10.8 in.	11.25 in.	2.4 in.	22.5 in.	54 in^2	-8% of ν	5, 30, 55, 80, 105, 130
37.2 in.	7.5 in.	2.4 in.	15 in.	36 in^2	-5% of E	16, 41, 66, 91
37.2 in.	7.5 in.	2.4 in.	15 in.	36 in^2	-7% of ν	16, 41, 66, 91

Damage Case DB 4

Figure 3.24 shows the schematic representation of the fourth damage case and Table 3.17 summarizes the damage related parameters.

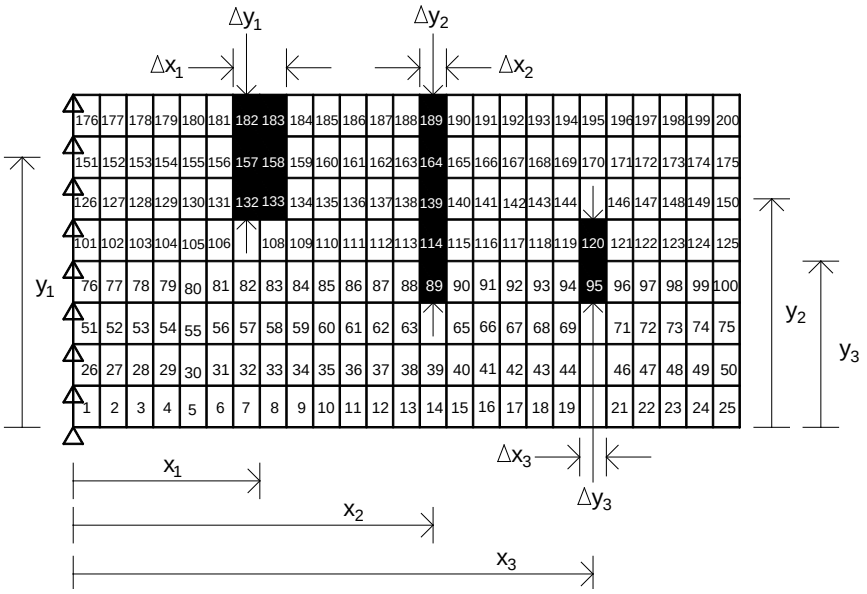

Figure 3.24 Schematic Representation of the Fourth Damage Case on the Finite Element Mesh of the Deep Beam

Table 3.17 Summary of the Fourth Damage Scenario Applied to the Deep Beam

Damage Location		Damage Size			Damage Severity	Damaged Elements
x	y	Δx	Δy	ΔA		
16.8 in.	24.375 in.	4.8 in.	11.25 in.	54 in^2	-3% of E	132, 133, 157, 158, 182, 183
32.4 in.	20.625 in.	2.4 in.	18.75 in.	45 in^2	-5% of E	89, 114, 139, 164, 189
46.8 in.	15 in.	2.4 in.	7.5 in.	18 in^2	-6% of E	95, 120

Damage Case DB 5

Figure 3.25 shows the schematic representation of the fifth damage case and Table 3.18 summarizes the damage related parameters.

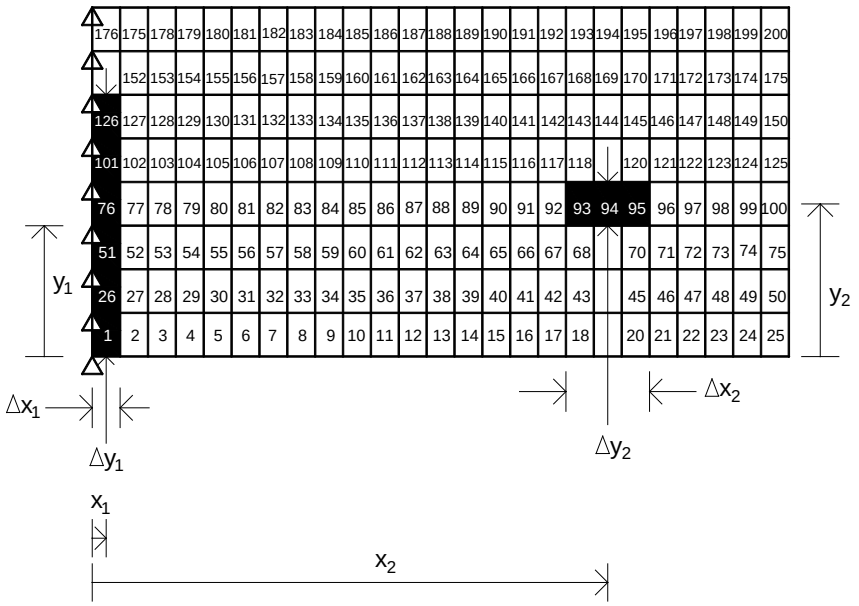

Figure 3.25 Schematic Representation of the Fifth Damage Case on the Finite Element Mesh of the Deep Beam

Table 3.18 Summary of the Fifth Damage Scenario Applied to the Deep Beam

Damage Location		Damage Size			Damage Severity	Damaged Elements
x	y	Δx	Δy	ΔA		
1.2 in.	11.25 in.	2.4 in.	22.5 in.	54 in^2	-11% of E	1, 26, 51, 75, 101, 126
1.2 in.	11.25 in.	2.4 in.	22.5 in.	54 in^2	-6% of ν	1, 26, 51, 75, 101, 126
44.4 in.	13.125 in.	7.2 in.	3.75 in.	27 in^2	-7% of E	93, 94, 95
44.4 in.	13.125 in.	7.2 in.	3.75 in.	27 in^2	-5% of ν	93, 94, 95

ASSESSMENT OF DAMAGE DETECTION ACCURACY

The objective of this section is to present the methodologies to evaluate the accuracy of the damage detection algorithms proposed in subsequent chapters. The accuracy of an NDD algorithm may be evaluated on the basis of at least three criteria: namely; the accuracy of the damage localization, the accuracy of the damage extent and the accuracy of the severity estimation.

In most basic terms, damage localization accuracy is quantified by measuring the distance between the true and predicted damage location. Damage localization error (e_L) may be written in terms of a dimensionless position error, which can be obtained by dividing the distance between the true and predicted damage location to the total length of the beam. This may be expressed in terms of percentage as:

$$e_L = \frac{x_T - x_P}{L} \times 100 \tag{3.1}$$

where x_T and x_P correspond to the true and predicted damage locations and L is the total length of the beam.

Damage extent indicates the area of the damaged region. Thus, damage extent accuracy may be quantified by measuring the difference between the true and predicted damage areas. Damage extent error (e_E) may be written in terms of a dimensionless quantity, which can be obtained by dividing the difference between the true and predicted damage areas to the total surface area of the beam. This may be expressed in terms of percentage as:

$$e_E = \frac{A_T - A_P}{A} \times 100 \tag{3.2}$$

where A_T and A_P correspond to the true and predicted damage areas and A is the total surface area of the beam.

Similarly, the accuracy of the damage severity estimation may be quantified by measuring the difference between the true and predicted damage severities. The error in damage severity estimation (e_α) may be quantified by dividing this difference to the inflicted damage severity. This may be expressed in terms of percentage as:

$$e_\alpha = \frac{\alpha_T - \alpha_P}{\alpha_T} \times 100 \tag{3.3}$$

where α_T and α_P correspond to the true and predicted damage severities respectively.

SUMMARY

This chapter introduced a set of numerical experiments that will be used to assess the performances of the individual damage detection algorithms proposed in the remainder of this document. The numerical experiments were based on the finite element models of the chosen test structures. Various damage scenarios have been simulated by adjusting the material properties of individual elements in these experiments. Methodologies to evaluate the performance of the proposed damage detection methodologies were summarized at the end of the chapter.

CHAPTER IV

DAMAGE INDEX USING THE PRINCIPLE OF INVARIANT STRESS RESULTANTS AND EULER-BERNOULLI BEAM THEORY

INTRODUCTION

The objective of this chapter is to develop an explicit damage index methodology in order to locate and quantify damage in beam-type structures. The proposed methodology is based on the principle of invariant stress resultants and Euler-Bernoulli beam theory. Damage will be expressed in terms of local decreases in the flexural stiffness of structural members. To accomplish the stated objective, this chapter is divided into four major sections: a section articulating the proposed methodology; a section describing specific structural response parameters utilized in the proposed damage detection algorithm; a section evaluating the performance of the methodology using the numerical experiments introduced in Chapter III; and a section discussing the outcomes of the performed case studies.

PROPOSED METHODOLOGY

Assume that a local decrease in the stiffness of a beam-type structure may be expressed in terms of a decrease in the bending stiffness of its sub-element(s). For a beam that is comprised of NE sub-elements and NN nodes (as depicted in Figure 4.1), the pristine and damaged flexural stiffnesses of the j^{th} element may be represented by EI_j and EI_j^*, respectively. The problem here is to identify the location of the damaged sub-elements within the beam and quantify the amount of stiffness degradation inflicted at each damaged region. Using basic principles from solid mechanics, the following approach is taken to address the stated problem.

Assuming that the internal force distribution in the beam is not affected by the inflicted damage (this assumption is true for statically determinate structures and is

approximately true for statically indeterminate structures with low degrees of indeterminacy), the following condition holds for the bending moment along the length of the beam:

$$M(x) = M(x)^{*} \tag{4.1}$$

where the asterisk represents the moment distribution in the damaged beam.

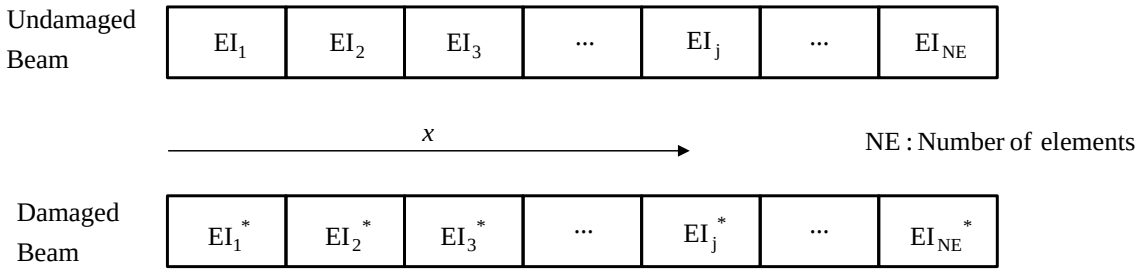

Figure 4.1 Damage Detection Model Utilized to Predict Local Changes in the Flexural Stiffness Distribution via the Principle of Invariant Stress Resultants and the Euler-Bernoulli Beam Theory

Integrating the moment distribution over the j^{th} element using Eq. (4.1) leads to

$$\int_{j} M(x)\,dx = \int_{j} M^{*}(x)\,dx \tag{4.2}$$

Utilizing the fundamental relationship between the curvature and bending moment (Eq. (2.9)), the following result may be obtained from Eq. (4.2):

$$\int_{j} EI_{j}\kappa(x)\,dx = \int_{j} EI_{j}^{*}\kappa^{*}(x)\,dx \tag{4.3}$$

where the curvature at any position along the beam is approximated, according to Euler-Bernoulli beam theory, by the equation:

$$\kappa(x) = \frac{d^2 w(x)}{dx^2} \tag{4.4}$$

Assume that the pristine and damaged flexural stiffnesses, denoted respectively by EI_j and EI_j^*, attain constant values over the j^{th} element. Substituting Eq. (4.4) back into Eq. (4.3) yields the ratio of the flexural stiffnesses before and after damage in terms of curvature profiles:

$$\beta_j = \frac{EI_j}{EI_j^*} = \frac{\int_j \kappa^*(x)\, dx}{\int_j \kappa(x)\, dx} \tag{4.5}$$

Note that the damage indicator, β_j given above, is greater than unity in regions where stiffness degradation has occurred. This damage indicator is designated as "the EB Direct β_j" for identification purposes.

The severity of the inflicted damage for localized damaged regions may now be expressed in terms of the pristine and damaged flexural stiffnesses as:

$$\alpha_j = \frac{\Delta EI_j}{EI_j} = \frac{EI_j^* - EI_j}{EI_j} \tag{4.6}$$

which in turn can be written in terms of the damage indicator β_j given in Eq. (4.5):

$$\alpha_j = \frac{EI_j^*}{EI_j} - 1 = \frac{1}{\beta_j} - 1 \tag{4.7}$$

PROPOSED EXPERIMENTAL ARRANGEMENT AND BASIC MEASUREMENTS REQUIRED BY THEORY

The proposed damage detection methodology utilizes the pre-damaged and post-damaged curvature profiles in order to localize and quantify damage in beam-type structures. Static or dynamic measurements may be used to obtain point curvatures throughout the length of the beam. Although an infinite number of data points are available in theory, only a limited number of sensors can be used to collect data in practice. In order to simulate this more realistic case, the following sensor layouts are utilized in the proposed test beams:

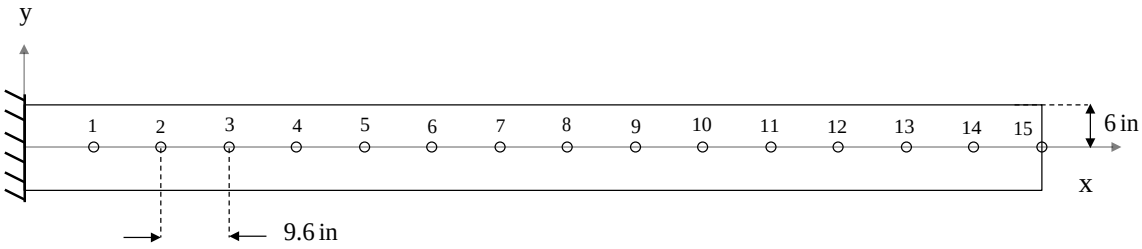

Figure 4.2 Sensor Layout for the Slender Beam

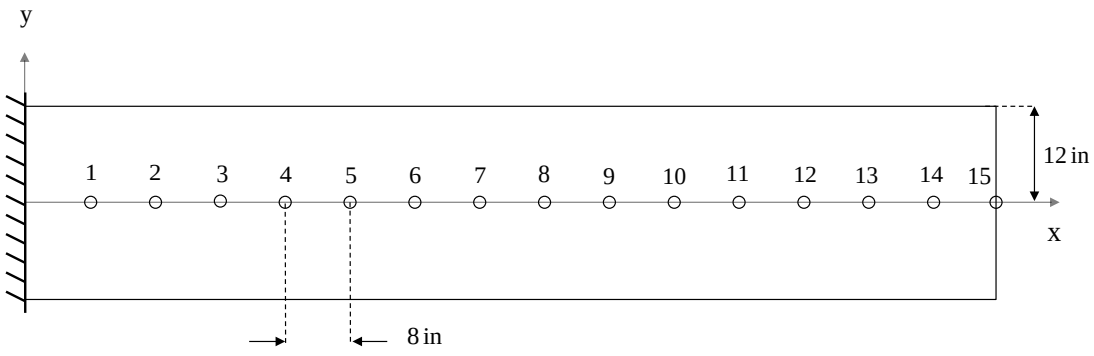

Figure 4.3 Sensor Layout for the Intermediate Beam

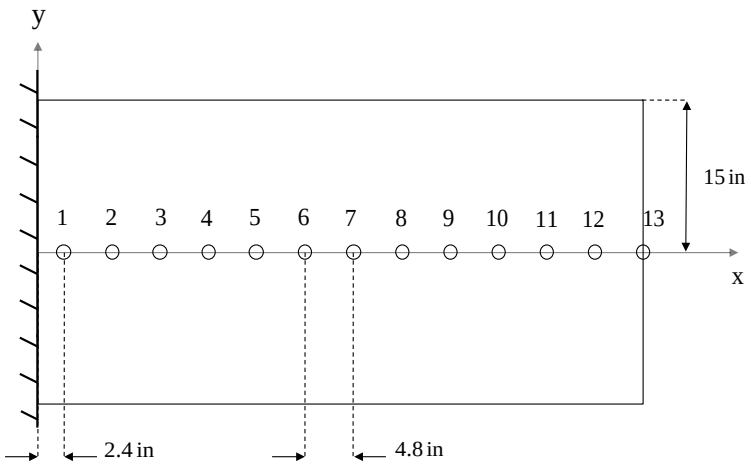

Figure 4.4 Sensor Layout for the Deep Beam

Figures 4.2, 4.3 and 4.4 depict the sensor locations for the slender, intermediate, and deep beam, respectively. Response data are collected from the numerical experiments at the given sensor locations. The recorded response may either be static or dynamic. Static data can directly be utilized to compute the undamaged and damaged curvature profiles. The invariant stress resultant state may be satisfied upon applying the same external load to the pristine and the damaged beams. Alternatively, the flexibility matrix may also be used to estimate the pre- and post-damaged curvature profiles. Note that the flexibility matrix is the inverse of the stiffness matrix and relates the applied static loads to the resulting structural displacements. Each row of the flexibility matrix may be interpreted as the deformed shape of a structure due to a unit load applied at the corresponding DOF.

An alternative to direct static measurements (which may be impractical) is to use the modal approximation of the flexibility matrix, which is called the modal flexibility. Considering the applicability of the proposed methodology to real time health monitoring, it may be more appropriate to use dynamic data in lieu of static tests. Modal flexibility provides the best alternative for static data in damage detection as it offers a

rational means of combining modal information. Furthermore, an accurate representation of modal flexibility can be obtained by using only a few lower modes of vibration. It should be noted that the constant external load required for invariant stress resultants are automatically satisfied when using the modal flexibility.

In order to construct the modal flexibility matrix, it is assumed that an output-only modal testing is performed for both the undamaged and damaged beams. The outcomes of these tests are the first three natural frequencies and transverse degrees of freedom of the mode shapes measured at the given sensor locations. A typical row of the flexibility matrix may be used to compute the pre- and post-damaged curvature profiles required for damage detection. A more concise description of the flexibility computation through output-only modal data is provided in Appendix A.

ASSESSMENT OF THE PROPOSED METHODOLOGIES VIA NUMERICAL EXPERIMENTS

The performance of the proposed damage detection methodology is evaluated in this section. The numerical experiments previously defined in Chapter III are utilized in order to accomplish this assessment. The performance of the method is based on accurately identifying three different damage-related parameters, namely: the location of the damage, the extent of the damage and the severity of the damage. These items are described in Chapter III.

Damage was simulated at various locations within the length and the depth of the two-dimensional beams. The methodology presented here, however, is limited to one-dimensional Euler-Bernoulli Beam Theory. As a result, possible damage can only be localized along the length of the beam and the distribution of damage through the beam depth cannot be addressed.

Once the damage indicator given by Eq. (4.5) is determined, the following statistical criterion utilized by Kim (1993) can be used to identify the location of damage.

Assuming that the collection of the damage indicators for each location is represented by a normally distributed random variable, a normalized damage indicator for each location denoted by Z_j is computed using the equation:

$$Z_j = \frac{(\beta_j - \overline{\beta})}{\sigma_\beta} \tag{4.8}$$

where $\overline{\beta}$ and σ_β represent the mean and standard deviation for the collection of damage indicators for all locations. A statistical-pattern-recognition technique, which utilizes hypothesis testing, is used as the decision rule to determine the location of damage. For instance, let H_o represent the null hypothesis, which suggests that element j is not damaged at the j^{th} location if $Z_j < N$ where N represents some threshold number yet to be determined. Now let the alternate hypothesis H_1 represent the case where element j is damaged at the j^{th} location if $Z_j \geq N$. The center of the predicted damage location is determined by tracing the peak value of Z where H_1 hypothesis applies. Proposed damage localization scheme uses zero as the threshold number. Thus, it is assumed that each element, which possesses a normalized damage indicator greater than zero indicates a possible location of damage. Note that from the statistical point of view, this criterion indicates a confidence level of 50% in a one-tailed test.

Once the location of damage is predicted, the extent and the severity of damage can be identified. The extent of the damage is initially measured by the probability that the true damaged region is a subset of the predicted damaged regions. This measure may be quantified as $P(T \subset P)$. If the extent of damage is within the region where H_1 hypothesis applies, than $P(T \subset P)$ will be 1.0. Damage extent is subsequently quantified by increasing the sensor resolution at the predicted damage location. It was assumed that the extent of damage corresponds to the length of the region where predicted damage severity is less than zero. Note that, the damage extent corresponds to the

footprint of damage severity. Thus, quantifying the extent of damage by means of the estimated damage severity is valid.

Damage extent was defined as the area of the damaged region in Chapter III. In order to be consistent with the one-dimensional damage detection methodology proposed here, it is expressed as the total length of the damaged region. Consequently, damage extent deviation is the difference between the length of the true and predicted damaged regions. Dividing this difference to the total length of the beam leads to a dimensionless quantity, the damage extent error (e_E), which may be expressed in terms of a percentage as:

$$e_E = \frac{L_T - L_P}{L} \times 100 \tag{4.9}$$

where L_T refers to the true length of the inflicted damage and L_P represents the length of the predicted damaged region. L is a metric, which denotes the total length of the beam.

Two different damage severity estimations were identified in this study, namely the upper and lower bound severity estimates. The upper bound severity corresponds to the peak value of damage severity computed directly from Eq. (4.7). The lower bound damage severity is computed by utilizing the contributions of each damaged element within the identified damage extent. A linear springs model connected in series is utilized to estimate the lower bound. The proposed procedure is as follows:

Assume that a single linear spring (with the stiffness K) in Figure 4.5 is subdivided into three linear springs connected in series.

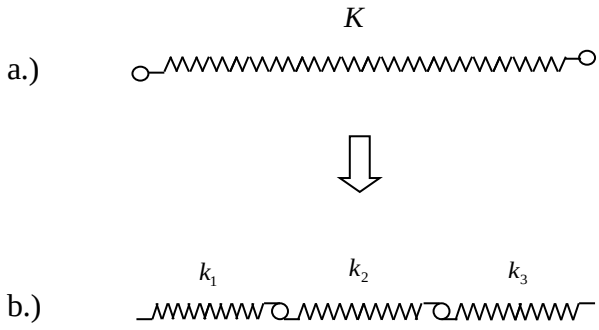

Figure 4.5 The Linear Springs Model Utilized to Estimate the Lower Bound Damage Severity

Let the stiffness of the i^{th} spring be denoted by k_i. An expression for the equivalent stiffness of the system connected in series may be calculated as:

$$\frac{1}{K_{eq}} = \frac{1}{k_1} + \frac{1}{k_2} + \frac{1}{k_3} \tag{4.10}$$

Now assume that a similar model is available for the damaged structure. For this case, the equivalent stiffness of the system a may be written as:

$$\frac{1}{K_{eq}^{*}} = \frac{1}{k_1^{*}} + \frac{1}{k_2^{*}} + \frac{1}{k_3^{*}} \tag{4.11}$$

where the asterisk represents the damaged quantities.

It is assumed that the ratio of the stiffnessess of single spring elements before and after damage (K and K^{*}) is equal to the ratio of the equivalent stiffnesses of the systems connected in series after the subdivision. This ratio is expressed as:

$$\frac{K^{*}}{K} = \frac{K_{eq}^{*}}{K_{eq}} \tag{4.12}$$

Substituting Eq. (4.10) and Eq. (4.11) back into Eq. (4.12) and some algebraic manipulation leads to:

$$\frac{K^*}{K} = \frac{\frac{1}{k_1} + \frac{1}{k_2} + \frac{1}{k_3}}{\frac{1}{k_1^*} + \frac{1}{k_2^*} + \frac{1}{k_3^*}} \tag{4.13}$$

Utilizing Eq. (4.7), K and K^* may be related by the following equation:

$$\frac{K^*}{K} = 1 + \alpha \tag{4.14}$$

where α represents the severity of damage in the single linear spring (Figure 4.5a).

Substituting Eq. (4.14) into Eq. (4.13) gives:

$$1 + \alpha = \frac{\frac{1}{k_1} + \frac{1}{k_2} + \frac{1}{k_3}}{\frac{1}{k_1^*} + \frac{1}{k_2^*} + \frac{1}{k_3^*}} \tag{4.15}$$

Similarly, each damaged spring element connected in series, can be related to their undamaged counterparts by:

$$k_i^* = k_i(1 + \alpha_i) \tag{4.16}$$

Now assume that the following is true for the system:

$$k_1 = k_2 = k_3 = k \tag{4.17}$$

Finally, utilizing Eq. (4.15), Eq. (4.16), and Eq. (4.17), the severity of damage at the single spring element shown in Figure 4.5a may be written in terms of the damage severities inflicted at each linear spring connected in series (Figure 4.5b) as:

$$1+\alpha = \frac{3}{\frac{1}{1+\alpha_1}+\frac{1}{1+\alpha_2}+\frac{1}{1+\alpha_3}} \tag{4.18}$$

For a system where n springs are connected in series, the above expression may be expressed with the aid of summation notation as:

$$1+\alpha = \frac{n}{\sum_{i=1}^{n}\frac{1}{1+\alpha_i}} \tag{4.19}$$

The procedure described above will be utilized to compute an equivalent damage severity within the identified damage extent. Eq. (4.19) represents the lower bound damage severity estimate.

The definition of the true damage severity must also be re-examined here for the following reason: Damage severity is expressed as the percent reduction in the material properties (modulus of elasticity and/or Poisson's ratio) of individual plane elements located within the domain of the damage extent. Note that the true damage severity denoted by α_T will not correspond to the actual reduction imposed on the material properties of the beam elements while using one-dimensional beam theories. For instance, Damage Case 2 represents a damage scenario where 10% stiffness reduction is inflicted by reducing the elastic moduli of the plane elements located below the mid-depth of the test beams. This damage scenario may not manifest a 10% stiffness reduction while using a one-dimensional beam theory since damage can only be detected along the length of the beam and not through its depth. For this reason, equivalent one-dimensional bending and shear stiffnesses must be developed by utilizing the stiffnesses of the individual plane elements located along the depth of the beam. Figure 4.6 shows a schematic of the plane elements centered at a distance x_0 from the origin.

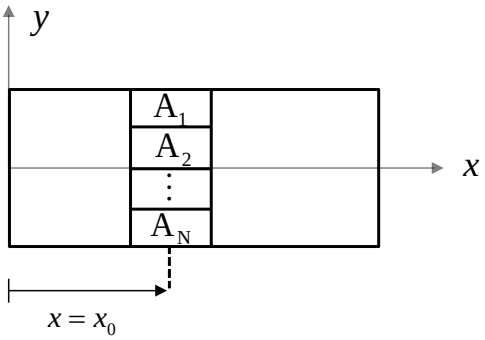

Figure 4.6 Plane Elements Centered at the Distance x_0

In order to obtain an equivalent one-dimensional bending stiffness from the flexural stiffness contributions of the individual plane elements, assume that the plane elements numbered sequentially from one to N are represented by a linear springs model connected in parallel. This is depicted in Figure 4.7.

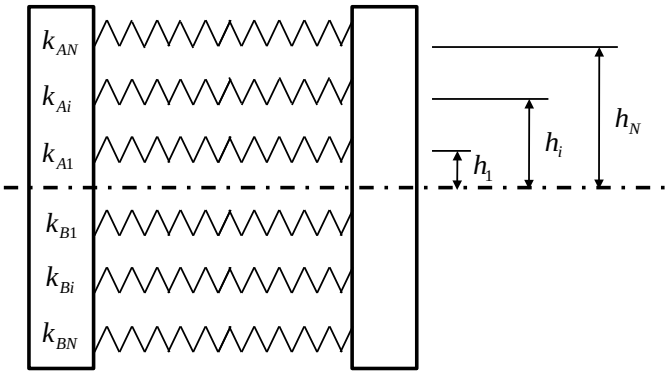

Figure 4.7 The Linear Springs Model Utilized to Estimate the Equivalent One-dimensional Bending Stiffness

If the system shown in Figure 4.7 is subjected to bending, the i^{th} linearly elastic spring experiences a deformation Δ_i. The deformed shape of the system is depicted in Figure 4.8.

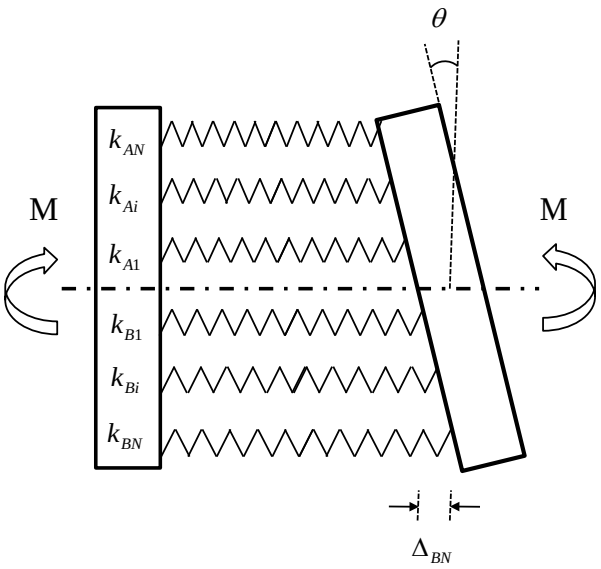

Figure 4.8 The Deformed Shape of the Linear Springs Model Subjected to Bending

The total strain energy of the system depicted above can be written as:

$$U_{total} = \frac{1}{2}\left(k_{BN}\Delta_{BN}{}^2 + k_{Bi}\Delta_{Bi}{}^2 + k_{Ai}\Delta_{Ai}{}^2 + ...k_{AN}\Delta_{AN}{}^2\right) \tag{4.20}$$

If the plane sections remain plane, each deformation Δ_i may be related to the angle of rotation θ and to the height of each spring measured from the neutral axis. Namely:

$$\Delta_i = \theta\, h_i \tag{4.21}$$

Substituting Eq. (4.21) into Eq. (4.20) leads to:

$$U_{total} = \frac{1}{2}\left(k_{BN}\left(h_N\theta\right)^2 + k_{Bi}\left(h_i\theta\right)^2 + k_{Ai}\left(h_i\theta\right)^2 + ...k_{AN}\left(h_N\theta\right)^2\right) \tag{4.22}$$

Utilizing Castigliano's first theorem, $M = \frac{\partial U}{\partial \theta}$, and Eq. (4.22) gives:

$$M = \left(k_{BN}\left(h_N\right)^2 + k_{Bi}\left(h_i\right)^2 + k_{Ai}\left(h_i\right)^2 + ...k_{AN}\left(h_N\right)^2\right)\theta \tag{4.23}$$

where the terms in parenthesis denote the equivalent bending stiffness ($k^{B}{}_{equ}$) of the system.

$$k^{B}{}_{equ} = k_{BN}\left(h_N\right)^2 + k_{Bi}\left(h_i\right)^2 + k_{Ai}\left(h_i\right)^2 + ...k_{AN}\left(h_N\right)^2 \tag{4.24}$$

The stiffness of each spring that appears in the above equation can be estimated from:

$$k_i = \frac{E_i A_i}{l_i} \tag{4.25}$$

The terms E, A and l in Eq. (4.25) denote the elastic modulus, the area, and the length of the individual plane elements, respectively. For the damaged structure (where the moduli of elasticity of one or more plane elements are reduced), the equivalent bending stiffness given in Eq. (4.24) may be written as:

$$k^{B}{}_{equ}{}^{*} = k_{BN}{}^{*}\left(h_N\right)^2 + k_{Bi}{}^{*}\left(h_i\right)^2 + k_{Ai}{}^{*}\left(h_i\right)^2 + ...k_{AN}{}^{*}\left(h_N\right)^2 \tag{4.26}$$

Then, using Eq. (4.26) and Eq. (4.24), the true equivalent damage severity imposed at the flexural stiffness of the system in Figure 4.7 can be computed as:

$$\alpha_T = \frac{k^{B}{}_{equ}{}^{*}}{k^{B}{}_{equ}} - 1 \tag{4.27}$$

Similarly, to obtain an equivalent one-dimensional shear stiffness from the shear stiffnesses of the individual plane elements, the linear springs model depicted in Figure

4.9 is proposed. If the system is subjected to a constant shear force V, each linearly elastic spring experiences the same deformation Δ.

The total strain energy of the system can be written as:

$$U_{total} = \frac{1}{2}\left(k_{BN}\Delta^2 + k_{Bi}\Delta^2 + k_{Ai}\Delta^2 + ...k_{AN}\Delta^2\right) \tag{4.28}$$

Utilizing Castigliano's first theorem, $V = \frac{\partial U}{\partial \Delta}$, and Eq. (4.28) leads to:

$$V = \left(k_{BN} + k_{Bi} + k_{Ai} + ...k_{AN}\right)\Delta \tag{4.29}$$

where the terms in parenthesis denote the equivalent shear stiffness ($k^V{}_{equ}$) of the system.

$$k^V{}_{equ} = k_{BN} + k_{Bi} + k_{Ai} + ...k_{AN} \tag{4.30}$$

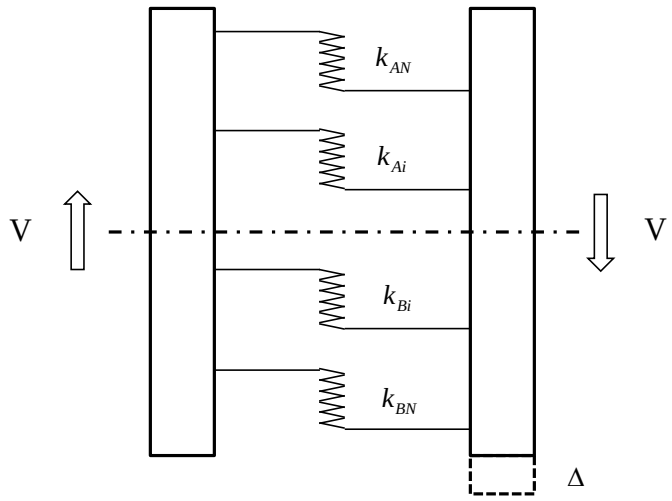

Figure 4.9 The Linear Springs Model Utilized to Estimate the Equivalent One-dimensional Shear Stiffness

The stiffness of each spring that appears in Eq. (4.30) can be estimated from:

$$k_i = \frac{G_i A_i}{l_i} \tag{4.31}$$

The terms G, A and l in Eq. (4.30) denote the shear modulus, the area, and the length of the individual plane elements, respectively.

For the damaged structure (where the shear moduli of one or more plane elements are reduced), the equivalent shear stiffness can be written as:

$$k^{V}{}_{equ}{}^{*} = k_{BN}{}^{*} + k_{Bi}{}^{*} + k_{Ai}{}^{*} + ...k_{AN}{}^{*} \tag{4.32}$$

Then, using Eq. (4.32) and Eq. (4.30), the true equivalent damage severity imposed at the shear stiffness of the system in Figure 4.9 may be computed from:

$$\alpha_T = \frac{k^{V}{}_{equ}{}^{*}}{k^{V}{}_{equ}} - 1 \tag{4.33}$$

The Slender Beam

Damage detection results for the slender beam are presented in this subsection. The first step in the damage detection process is to obtain the deformed shapes of the undamaged and damaged beam using modal flexibility. Utilizing the transverse degrees of freedom of the first three bending modes and corresponding natural frequencies, the modal flexibility of the beam is approximated. Once a deformed shape is available, interpolation is used to generate a finer sensor layout along the length the beam. Cubic spline functions with 0.6 in. uniform intervals are used for interpolation. This process leads to 241 nodal points including the node that corresponds to the clamped support. Ideal supports (exhibiting no settlements) are utilized in this study. Curvature profiles are estimated from the deflected shapes of the undamaged and damaged beams using the central difference approximation.

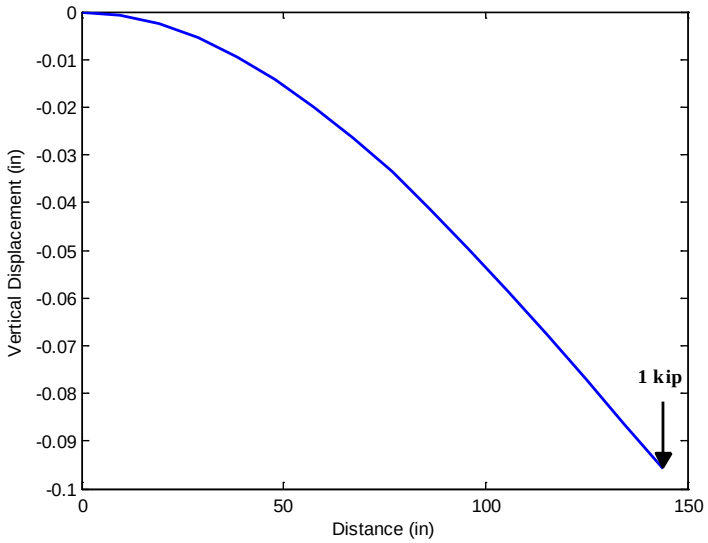

Figure 4.10 Vertical Displacement of the Beam Axis of the Slender Beam Approximated by the 15th Modal Flexibility

The number of degrees of freedom for the modal flexibility is 15 (excluding the support, since the displacement due to a unit load at the support is zero). The curvature profile of the 15th modal flexibility is utilized for damage detection. Note that this loading case corresponds to the deformed shape of the beam due to the unit load applied at the location of sensor 15. Ideally, any row of the flexibility matrix may be used for damage evaluation. In this case, however, unit load applied prior to a damaged region will not provide any useful information regarding damage since the bending moment (and therefore curvature) is zero to the right of the point of excitation. For this reason, it is deemed appropriate to utilize the 15th modal flexibility as it corresponds to the displacement profile caused by a unit load at the tip of the beam. This scenario is depicted in Figure 4.10. Finally, the trapezoidal rule is applied to approximate the integration scheme required by Eq. (4.5).

Damage Case SB 1

Figure 4.11 depicts the damage localization result for Damage Case SB 1 in terms of the normalized damage indicator Z_j. Table 4.1 shows the assessment of damage localization accuracy for the damage case. The error between the central location of the true and the predicted damages is computed by Eq. (3.1). Note that $P(T \subset P)$ indicates the probability that the true damaged region is a subset of the predicted damaged regions.

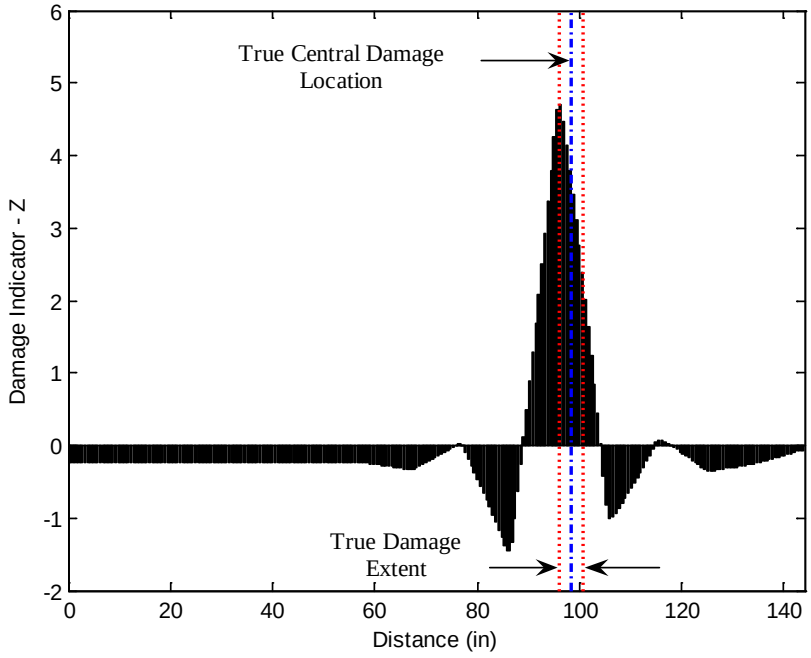

Figure 4.11 Damage Localization Result for Damage Case SB 1 Using EB Direct β_j

Table 4.1 Assessment of the Damage Localization Accuracy for Damage Case SB 1 Using EB Direct β_j

Damage Central Location (in)		Error (%)	$P(T \subset P)$
True	Predicted		
98.4	96.3	1.5	100%

As can be seen in Table 4.1, predicted central damage location is very close to the true central damage location. In addition, the predicted damaged region contains the true damage extent. Thus, $P(T \subset P) = 1.0$.

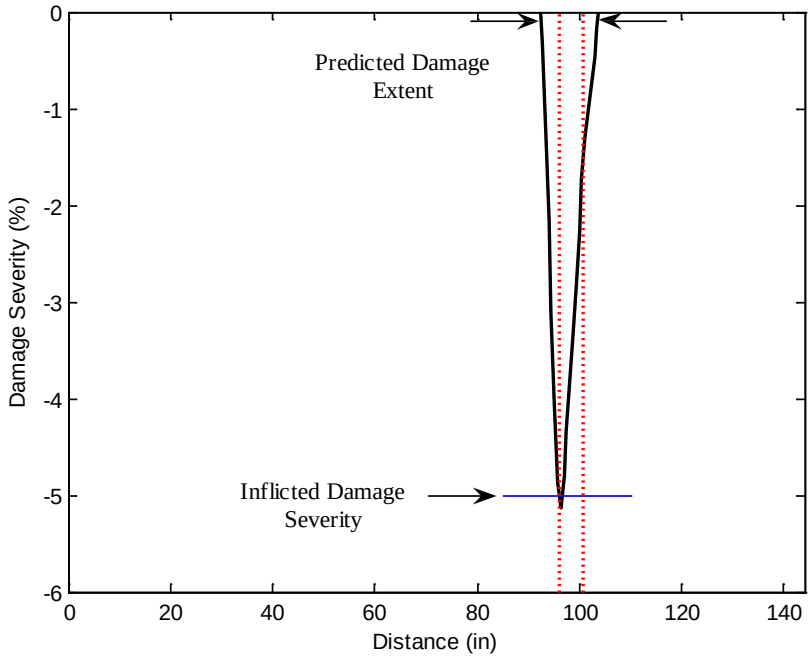

Figure 4.12 Damage Extent and Severity Estimate for Damage Case SB 1 Using EB Direct β_j

Figure 4.12 depicts the damage extent and severity estimate for Damage Case SB 1. Table 4.2 demonstrates the assessment of damage extent and severity accuracy for the damage case. Note that the damage severity and extent estimates are computed by utilizing an improved sensor resolution, which corresponds to the nodes of the finite element mesh at the centerline of the beam. It is assumed that the extent of damage corresponds to the length of the region where predicted damage severity is less than zero. The true damage severity in Table 4.2 is computed by Eq. (4.27). The lower bound and upper bound severity estimates are given by Eq. (4.19) and Eq. (4.7) respectively.

Table 4.2 Assessment of the Damage Extent and Severity Accuracy for Damage Case SB 1 Using EB Direct β_j

Damage Extent (in)		Error (%)	Damage Severity (%)		Error (%)
True	Predicted		True	Predicted Lower Bound/Upper Bound	
4.8	10.8	-4.2	-5.0	-2.5/-5.1	50.0/-2.0

Damage Case SB 2

Figures 4.13 and 4.14 depict the damage prediction results for Damage Case SB 2 using the damage indicator EB Direct β_j. Tables 4.3 and 4.4 tabulate the performance of the damage detection methodology for the damage case.

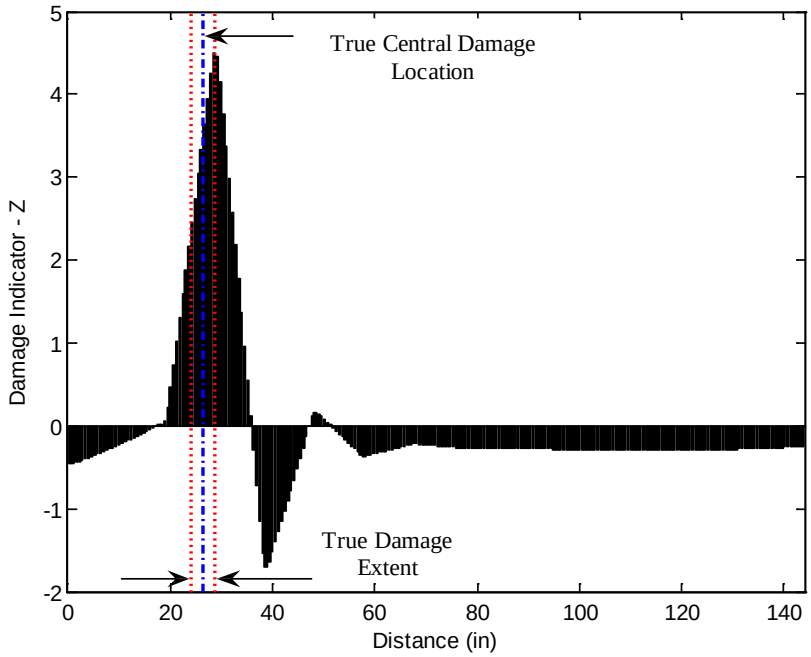

Figure 4.13 Damage Localization Result for Damage Case SB 2 Using EB Direct β_j

Table 4.3 Assessment of the Damage Localization Accuracy for Damage Case SB 2 Using EB Direct β_j

Damage Central Location (in)		Error (%)	$P(T \subset P)$
True	Predicted		
26.4	28.5	-1.5	100%

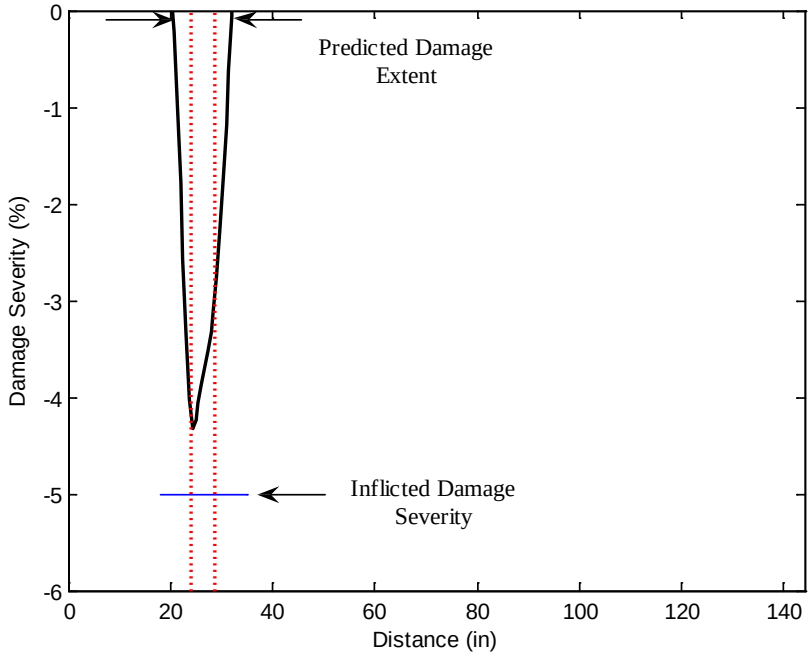

Figure 4.14 Damage Extent and Severity Estimate for Damage Case SB 2 Using EB Direct β_j

Table 4.4 Assessment of the Damage Extent and Severity Accuracy for Damage Case SB 2 Using EB Direct β_j

Damage Extent (in)		Error	Damage Severity (%)		Error (%)
True	Predicted	(%)	True	Predicted Lower Bound/Upper Bound	
4.8	11.4	-4.6	-5.0	-2.6/-4.3	48.0/14.0

Damage Case SB 3

Figures 4.15 and 4.16 depict the damage prediction results for Damage Case SB 3 using the damage indicator EB Direct β_j. Tables 4.5 and 4.6 tabulate the performance of the damage detection methodology for the damage case.

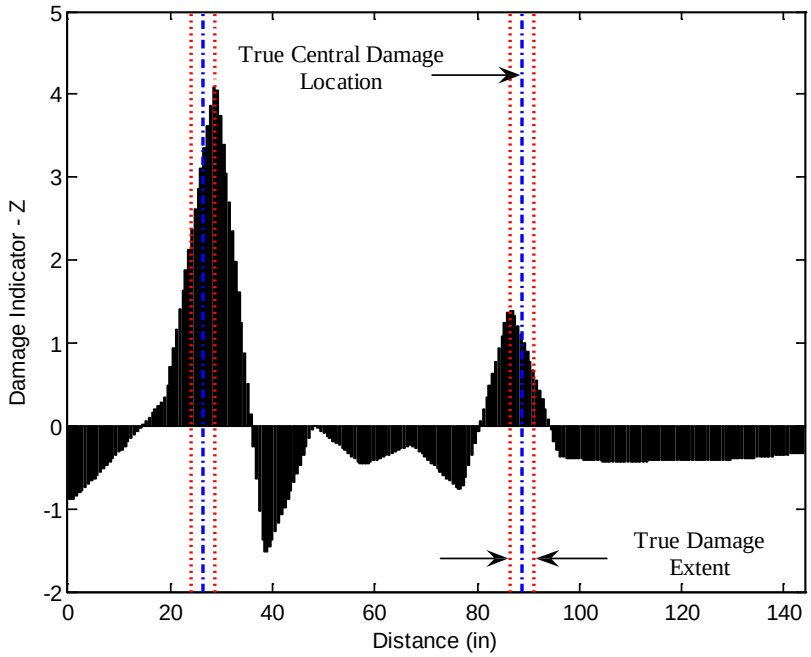

Figure 4.15 Damage Localization Result for Damage Case SB 3 Using EB Direct β_j

Table 4.5 Assessment of the Damage Localization Accuracy for Damage Case SB 3 Using EB Direct β_j

Damage Central Location (in)		Error (%)	$P(T \subset P)$
True	Predicted		
26.4	28.5	-1.5	100%
88.8	86.7	1.5	100%

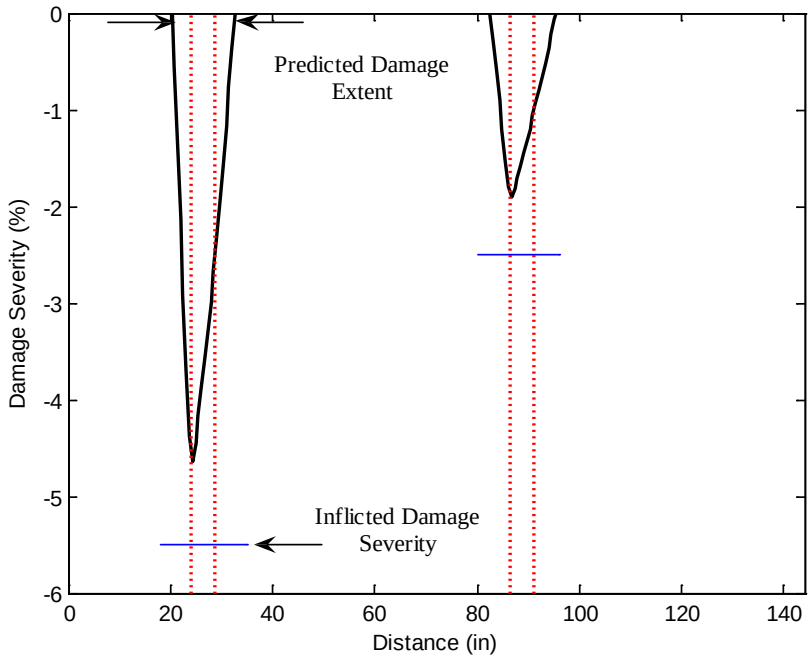

Figure 4.16 Damage Extent and Severity Estimate for Damage Case SB 3 Using EB Direct β_j

Table 4.6 Assessment of the Damage Extent and Severity Accuracy for Damage Case SB 3 Using EB Direct β_j

Damage Extent (in)		Error (%)	Damage Severity (%)		Error (%)
True	Predicted		True	Predicted Lower Bound/Upper Bound	
4.8	11.4	-4.6	-5.5	-2.7/-4.6	50.9/16.4
4.8	12.0	-5.0	-2.5	-1.0/-1.9	60.0/24.0

Damage Case SB 4

Figures 4.17 and 4.18 depict the damage prediction results for Damage Case SB 4 using the damage indicator EB Direct β_j. Tables 4.7 and 4.8 tabulate the performance of the damage detection methodology for the damage case.

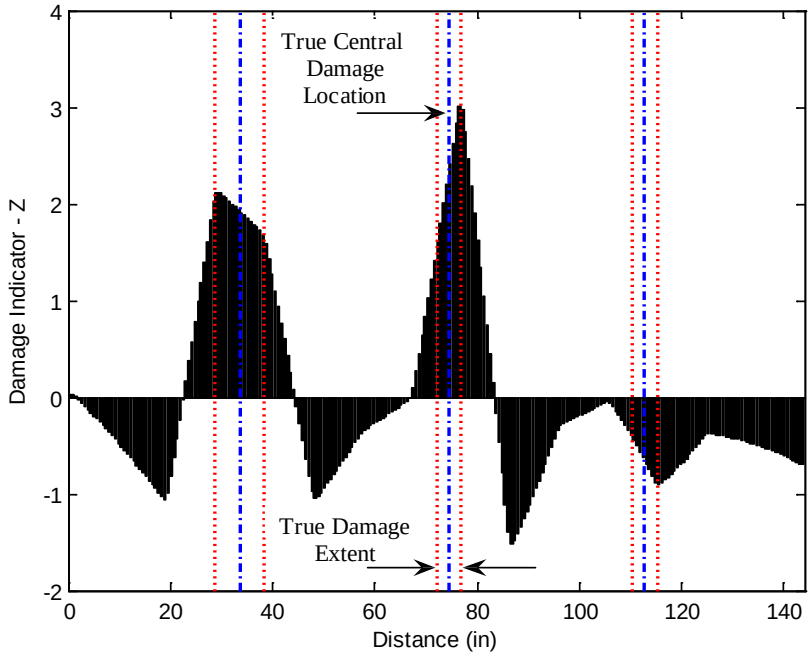

Figure 4.17 Damage Localization Result for Damage Case SB 4 Using EB Direct β_j

Table 4.7 Assessment of the Damage Localization Accuracy for Damage Case SB 4 Using EB Direct β_j

Damage Central Location (in)		Error (%)	$P(T \subset P)$
True	Predicted		
33.6	29.1	3.1	100%
74.4	76.5	-1.5	100%
112.8	No	100.0	0%

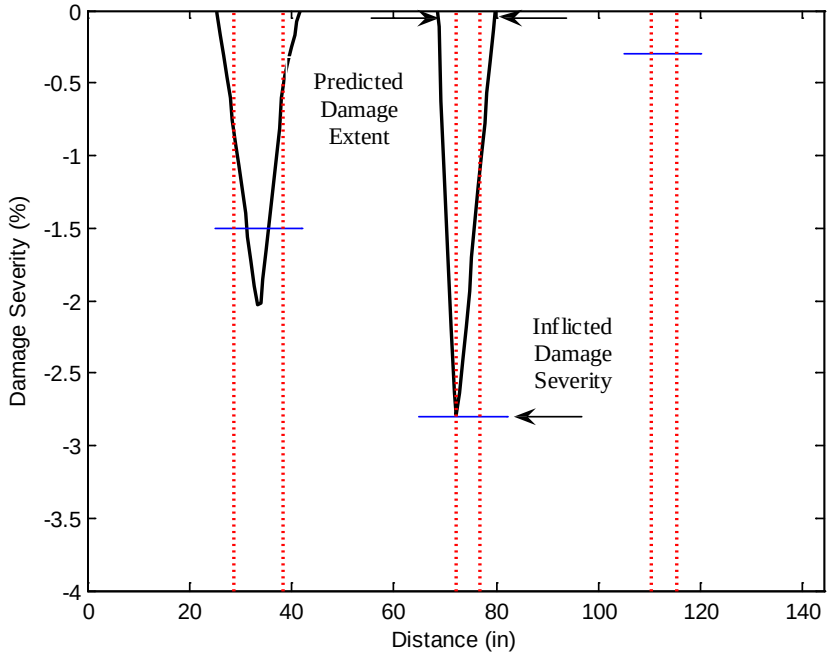

Figure 4.18 Damage Extent and Severity Estimate for Damage Case SB 4 Using EB Direct β_j

Table 4.8 Assessment of the Damage Extent and Severity Accuracy for Damage Case SB 4 Using EB Direct β_j

Damage Extent (in)		Error	Damage Severity (%)		Error (%)
True	Predicted	(%)	True	Predicted Lower Bound/Upper Bound	
9.6	15.6	-4.2	-1.5	-1.0/-2.0	33.3/-33.3
4.8	11.4	-4.6	-2.8	-1.5/-2.8	46.4/0.0
4.8	No	100.0	-0.3	No/No	100.0/100.0

Damage Case SB 5

Figures 4.19 and 4.20 depict the damage prediction results for Damage Case SB 5 using the damage indicator EB Direct β_j. Tables 4.9 and 4.10 tabulate the performance of the damage detection methodology for the damage case.

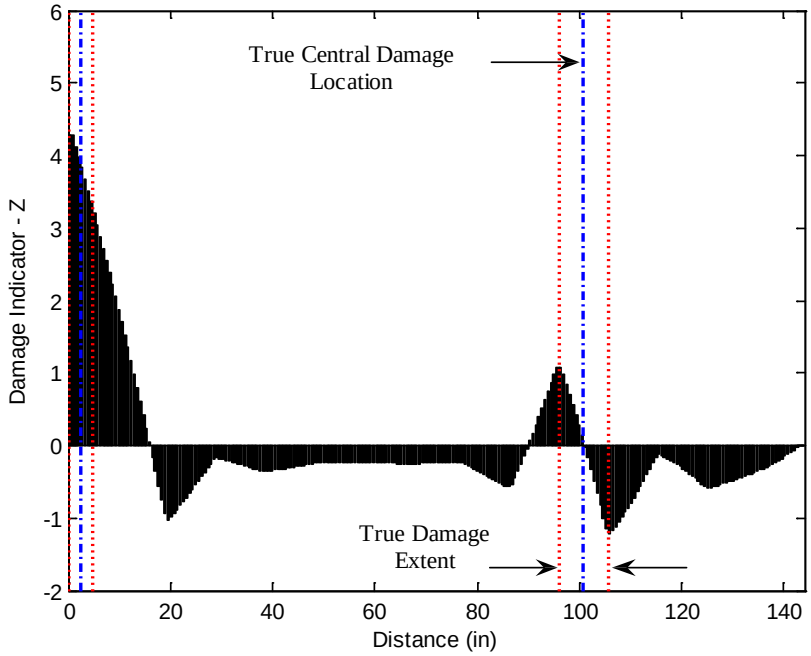

Figure 4.19 Damage Localization Result for Damage Case SB 5 Using EB Direct β_j

Table 4.9 Assessment of the Damage Localization Accuracy for Damage Case SB 5 Using EB Direct β_j

Damage Central Location (in)		Error (%)	$P(T \subset P)$
True	Predicted		
2.4	0.9	1.0	100%
100.8	96.3	3.1	50%

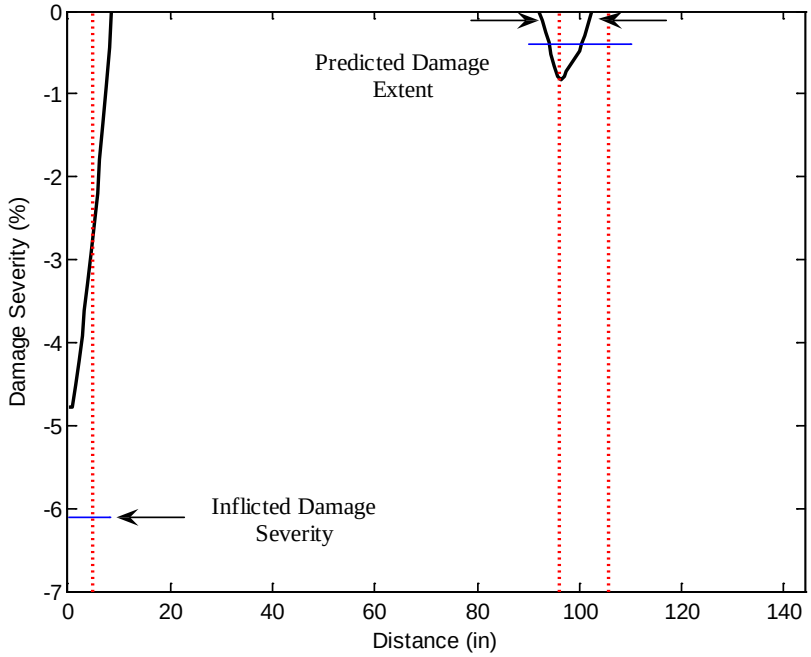

Figure 4.20 Damage Extent and Severity Estimate for Damage Case SB 5 Using EB Direct β_j

Table 4.10 Assessment of the Damage Extent and Severity Accuracy for Damage Case SB 5 Using EB Direct β_j

Damage Extent (in)		Error (%)	Damage Severity (%)		Error (%)
True	Predicted		True	Predicted Lower Bound/Upper Bound	
4.8	8.7	-2.7	-6.1	-2.8/-4.8	54.1/21.3
9.6	10.2	-0.4	-0.4	-0.5/-0.8	-25.0/-100.0

The Intermediate Beam

Damage detection results for the intermediate beam are presented in this subsection. As was done in the slender beam, firstly, the deformed shapes of the undamaged and damaged beam are approximated using modal flexibility. Only the transverse degrees of freedom of the first three bending modes and corresponding natural frequencies are utilized in flexibility calculations. Secondly, interpolation is used to generate a finer sensor layout along the length the beam. Cubic spline functions with 0.5 in. uniform interval are used for interpolation. This leads to 241 nodal points including an ideally assumed zero displacement at the support. Curvature profiles are estimated from the deflected shapes of the undamaged and damaged beams using the central difference approximation. The number of degrees of freedom for the modal flexibility is 15 (excluding the support, since the displacement due to a unit load at the support is zero). The curvature profile of the 15^{th} modal flexibility is utilized for damage detection. This scenario is depicted in Figure 4.21. Finally, the trapezoidal rule is applied to approximate the integration scheme required for damage detection.

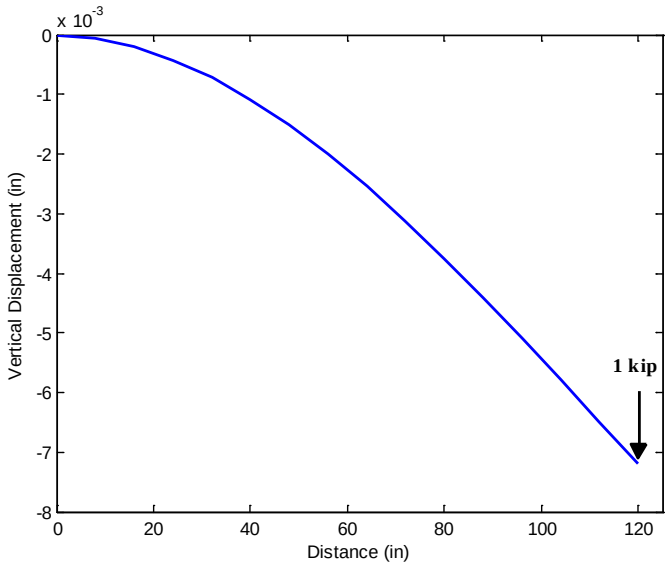

Figure 4.21 Vertical Displacement of the Beam Axis of the Intermediate Beam Approximated by the 15th Modal Flexibility

Damage Case IB 1

Figures 4.22 and 4.23 depict the damage prediction results for Damage Case IB 1 using the damage indicator EB Direct β_j. Tables 4.11 and 4.12 tabulate the performance of the damage detection methodology for the damage case.

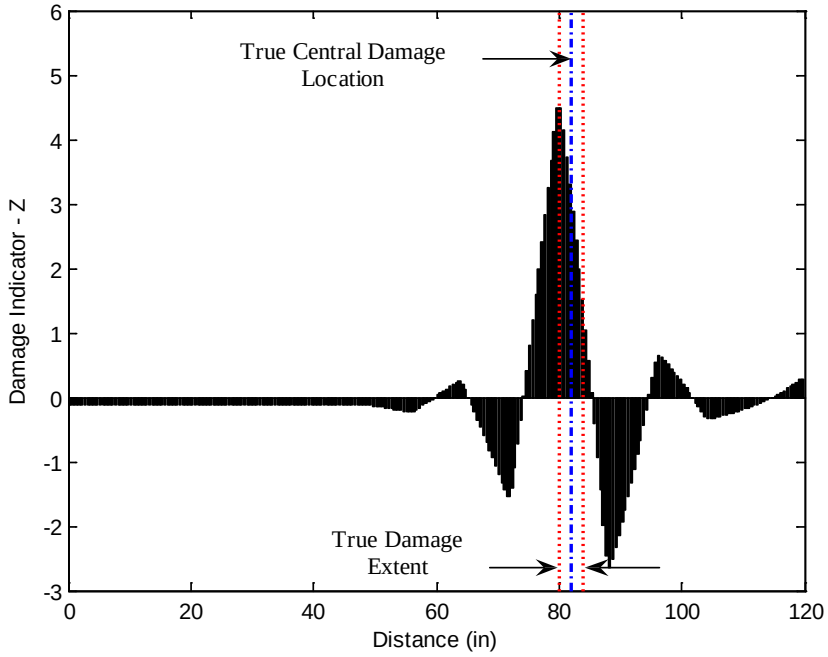

Figure 4.22 Damage Localization Result for Damage Case IB 1 Using EB Direct β_j

Table 4.11 Assessment of the Damage Localization Accuracy for Damage Case IB 1 Using EB Direct β_j

Damage Central Location (in)		Error (%)	$P(T \subset P)$
True	Predicted		
82.0	80.3	1.4	100%

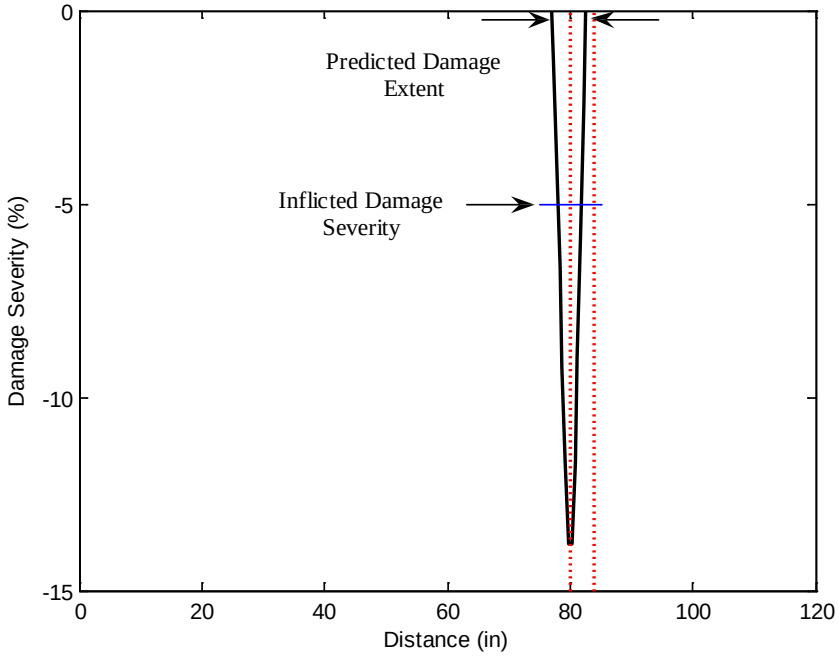

Figure 4.23 Damage Extent and Severity Estimate for Damage Case IB 1 Using EB Direct β_j

Table 4.12 Assessment of the Damage Extent and Severity Accuracy for Damage Case IB 1 Using EB Direct β_j

Damage Extent (in)		Error	Damage Severity (%)		Error (%)
True	Predicted	(%)	True	Predicted Lower Bound/Upper Bound	
4.0	5.5	-1.3	-5.0	-8.3/-13.8	-66.0/-176.0

Damage Case IB 2

Figures 4.24 and 4.25 depict the damage prediction results for Damage Case IB 2 using the damage indicator EB Direct β_j. Tables 4.13 and 4.14 tabulate the performance of the damage detection methodology for the damage case.

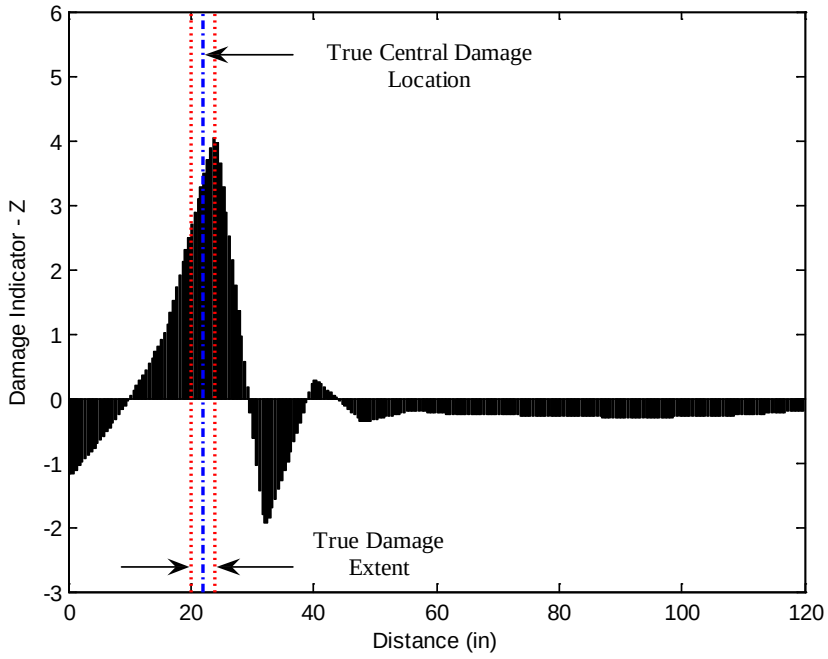

Figure 4.24 Damage Localization Result for Damage Case IB 2 Using EB Direct β_j

Table 4.13 Assessment of the Damage Localization Accuracy for Damage Case IB 2 Using EB Direct β_j

Damage Central Location (in)		Error (%)	$P(T \subset P)$
True	Predicted		
22.0	23.8	-1.5	100%

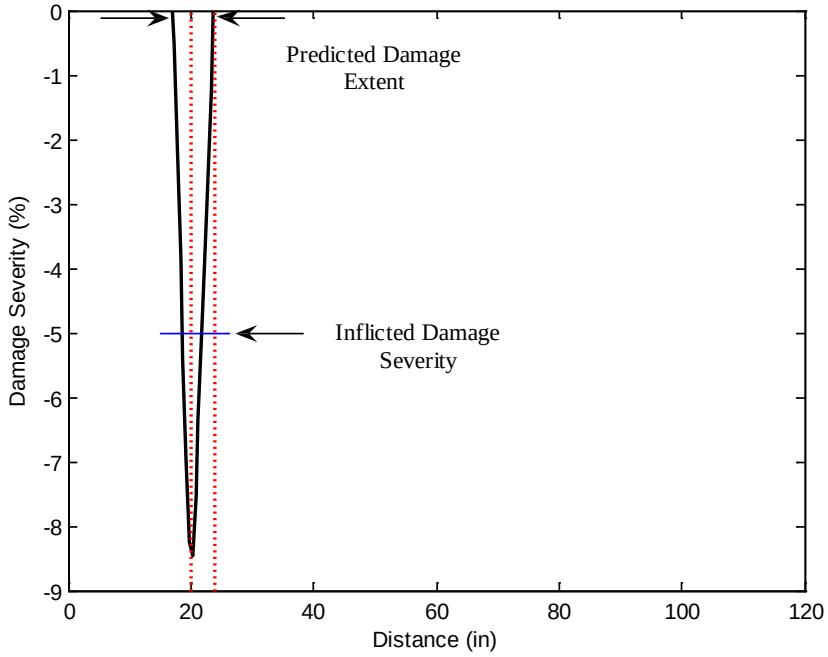

Figure 4.25 Damage Extent and Severity Estimate for Damage Case IB 2 Using EB Direct β_j

Table 4.14 Assessment of the Damage Extent and Severity Accuracy for Damage Case IB 2 Using EB Direct β_j

Damage Extent (in)		Error	Damage Severity (%)		Error (%)
True	Predicted	(%)	True	Predicted Lower Bound/Upper Bound	
4.0	6.5	-2.1	-5.0	-4.5/-8.5	10.0/-70.0

Damage Case IB 3

Figures 4.26 and 4.27 depict the damage prediction results for Damage Case IB 3 using the damage indicator EB Direct β_j. Tables 4.15 and 4.16 tabulate the performance of the damage detection methodology for the damage case.

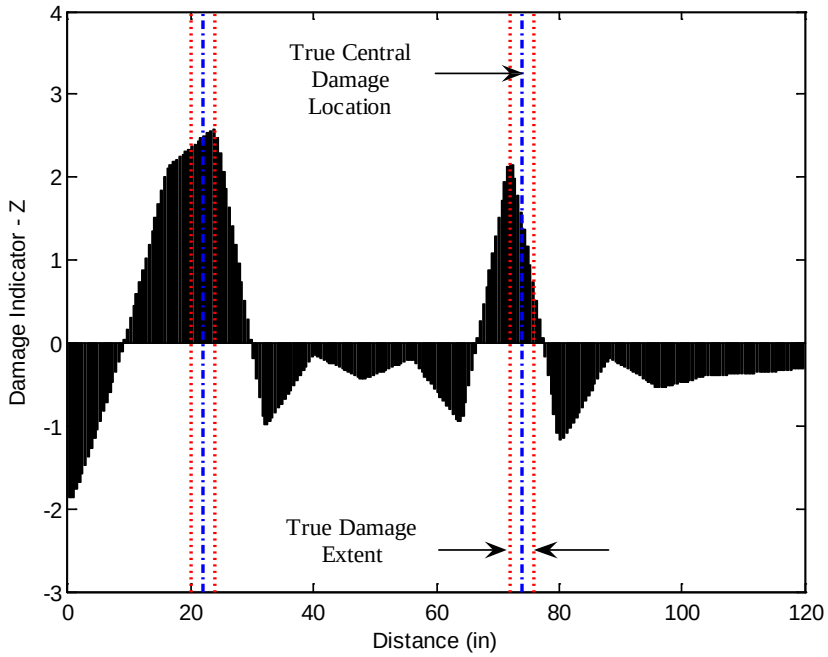

Figure 4.26 Damage Localization Result for Damage Case IB 3 Using EB Direct β_j

Table 4.15 Assessment of the Damage Localization Accuracy for Damage Case IB 3 Using EB Direct β_j

Damage Central Location (in)		Error (%)	$P(T \subset P)$
True	Predicted		
22.0	23.8	-1.5	100%
74.0	72.3	1.4	100%

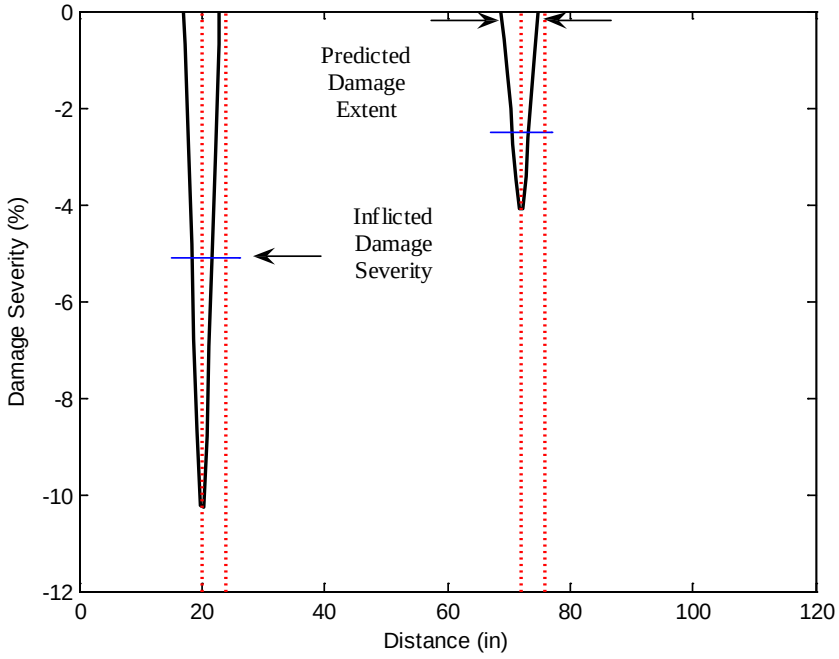

Figure 4.27 Damage Extent and Severity Estimate for Damage Case IB 3 Using EB Direct β_j

Table 4.16 Assessment of the Damage Extent and Severity Accuracy for Damage Case IB 3 Using EB Direct β_j

Damage Extent (in)		Error (%)	Damage Severity (%)		Error (%)
True	Predicted		True	Predicted Lower Bound/Upper Bound	
4.0	6.0	-1.7	-5.1	-5.8/-10.3	-13.7/-102.0
4.0	6.0	-1.7	-2.5	-2.3/-4.1	8.0/-64.0

Damage Case IB 4

Figures 4.28 and 4.29 depict the damage prediction results for Damage Case IB 4 using the damage indicator EB Direct β_j. Tables 4.17 and 4.18 tabulate the performance of the damage detection methodology for the damage case.

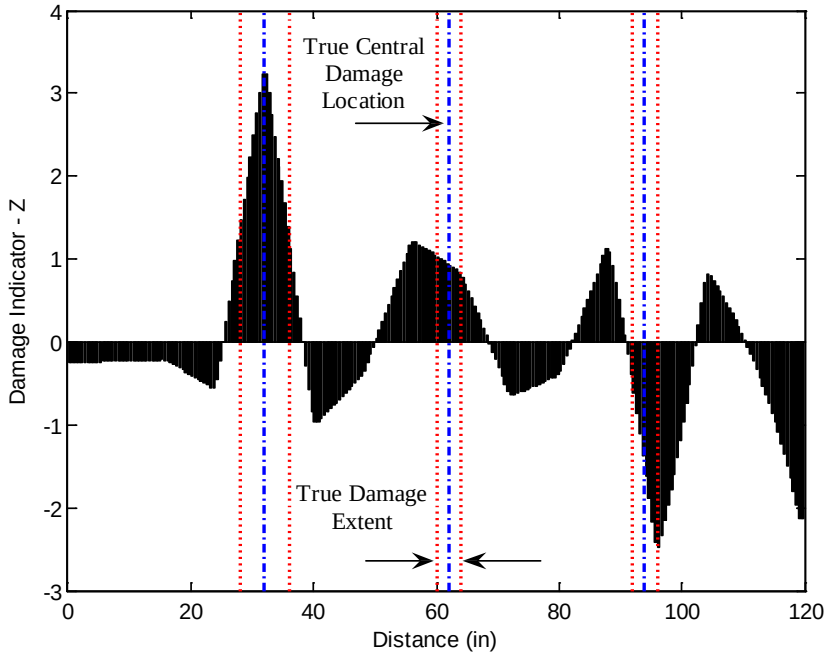

Figure 4.28 Damage Localization Result for Damage Case IB 4 Using EB Direct β_j

Table 4.17 Assessment of the Damage Localization Accuracy for Damage Case IB 4 Using EB Direct β_j

Damage Central Location (in)		Error (%)	$P(T \subset P)$
True	Predicted		
32.0	32.3	-0.2	100%
62.0	56.3	4.8	100%
94.0	No	100.0	0%
FP	87.8	100.0	0%
FP	104.0	100.0	0%

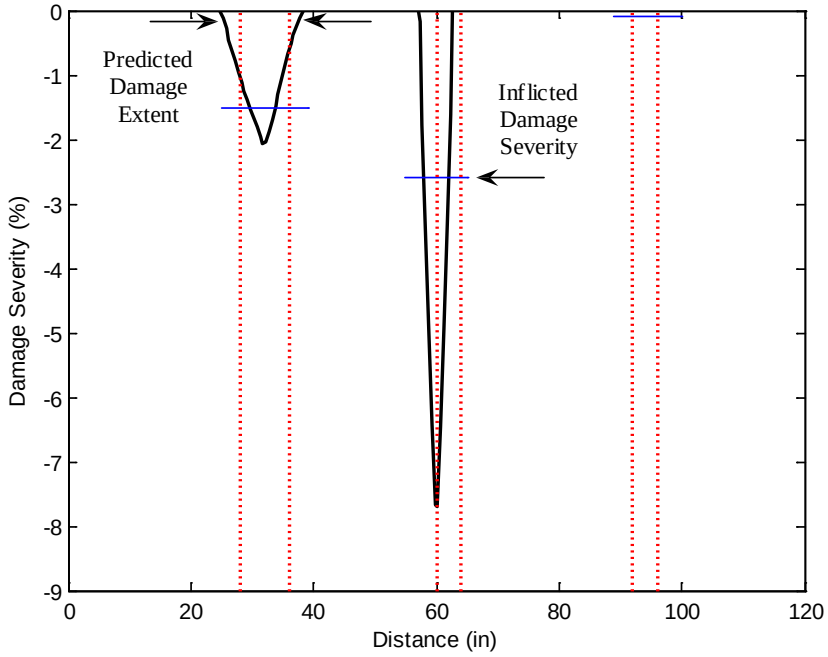

Figure 4.29 Damage Extent and Severity Estimate for Damage Case IB 4 Using EB Direct β_j

Table 4.18 Assessment of the Damage Extent and Severity Accuracy for Damage Case IB 4 Using EB Direct β_j

Damage Extent (in)		Error (%)	Damage Severity (%)		Error (%)
True	Predicted		True	Predicted Lower Bound/Upper Bound	
8.0	13.5	-4.6	-1.5	-1.1/-2.1	26.7/-40.0
4.0	5.5	-1.3	-2.6	-4.5/-7.7	-73.1/-196.2
4.0	No	100.0	-0.1	No	100.0

Damage Case IB 5

Figures 4.30 and 4.31 depict the damage prediction results for Damage Case IB 5 using the damage indicator EB Direct β_j. Tables 4.19 and 4.20 tabulate the performance of the damage detection methodology for the damage case.

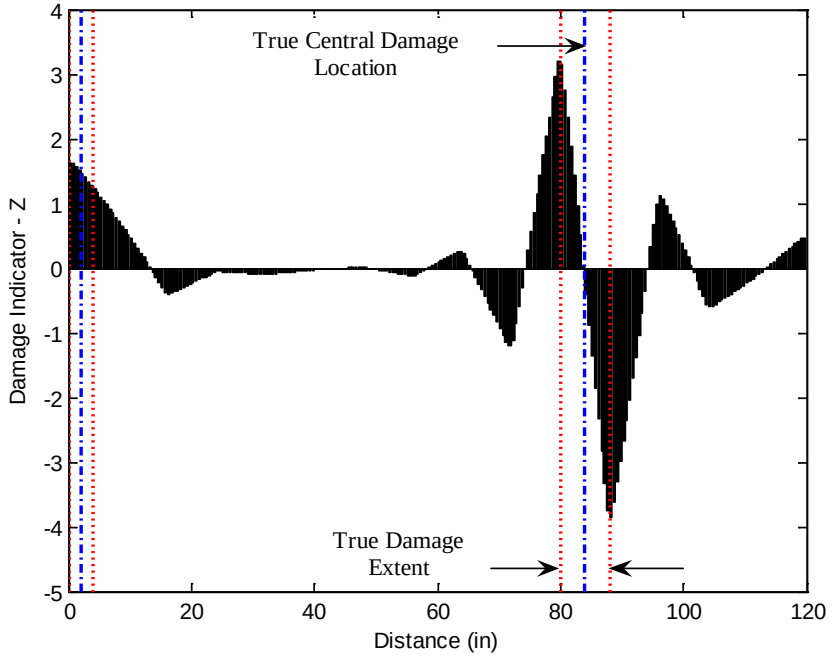

Figure 4.30 Damage Localization Result for Damage Case IB 5 Using EB Direct β_j

Table 4.19 Assessment of the Damage Localization Accuracy for Damage Case IB 5 Using EB Direct β_j

Damage Central Location (in)		Error (%)	$P(T \subset P)$
True	Predicted		
2.0	0.8	1.0	100%
84.0	79.8	3.5	50%
FP	96.3	100.0	0%

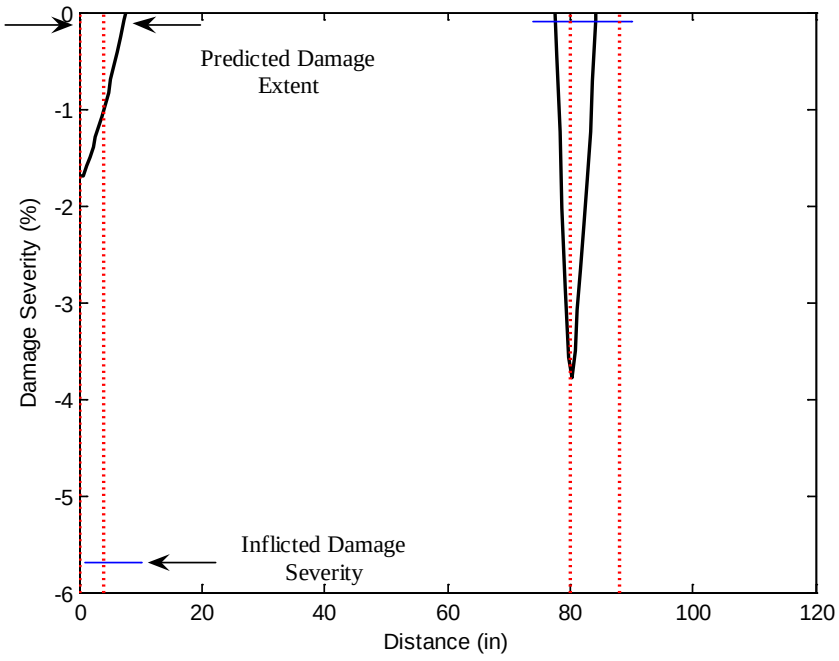

Figure 4.31 Damage Extent and Severity Estimate for Damage Case IB 5 Using EB Direct β_j

Table 4.20 Assessment of the Damage Extent and Severity Accuracy for Damage Case IB 5 Using EB Direct β_j

Damage Extent (in)		Error (%)	Damage Severity (%)		Error (%)
True	Predicted		True	Predicted Lower Bound/Upper Bound	
4.0	7.8	-3.2	-5.7	-1.1/-1.7	80.7/70.2
8.0	7.0	0.8	-0.1	-2.1/-3.8	-2000/-3700

The Deep Beam

Damage detection results for the deep beam are presented in this subsection. As before, the deformed shapes of the undamaged and damaged beam are approximated using modal flexibility. The transverse degrees of freedom of the first three bending modes and pertinent natural frequencies are utilized in flexibility calculations. Cubic spline functions with 0.3 in. uniform interval are used for interpolation in order to generate a finer sensor layout along the length the beam. This leads to 201 nodal points including an ideally assumed zero displacement at the support. Curvature profiles are estimated from the deflected shapes of the undamaged and damaged beams using the central difference approximation.

The number of degrees of freedom for the modal flexibility is 13 (excluding the support, as the displacement due to a unit load at the support is zero). Curvature profile of the 13^{th} modal flexibility is utilized for damage detection. Note that this loading case corresponds to the displacement profile caused by a unit load at the tip of the beam. Figure 4.32 depicts the displacement profile approximated in this manner. The trapezoidal rule is applied to approximate the integration scheme required for damage detection.

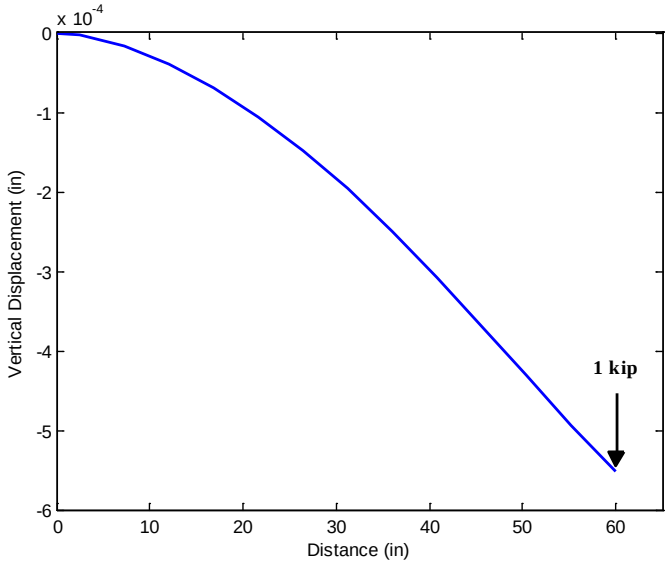

Figure 4.32 Vertical Displacement of the Beam Axis of the Deep Beam Approximated by the 13th Modal Flexibility

Damage Case DB 1

Figures 4.33 and 4.34 depict the damage prediction results for Damage Case DB 1 using the damage indicator EB Direct β_j. Tables 4.21 and 4.22 tabulate the performance of the damage detection methodology for the damage case.

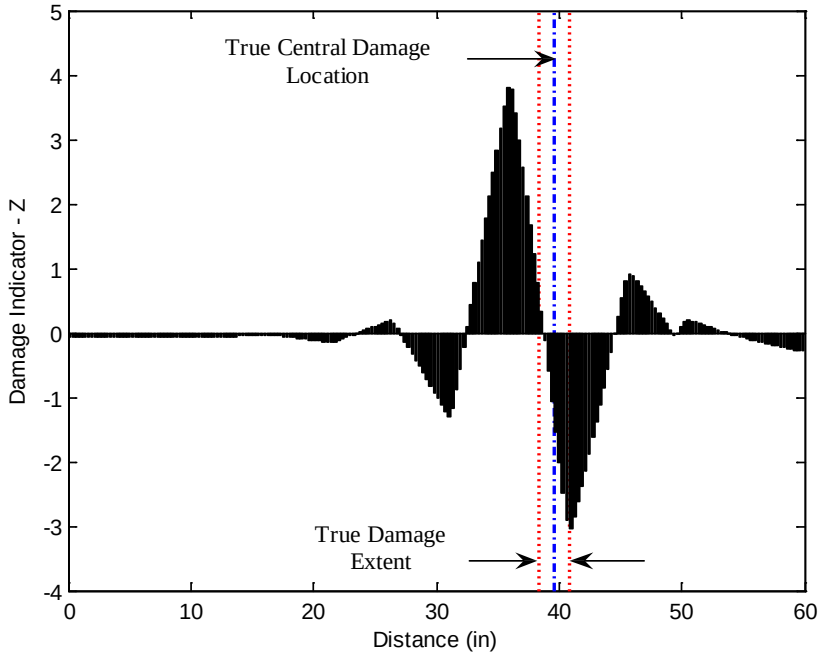

Figure 4.33 Damage Localization Result for Damage Case DB 1 Using EB Direct β_j

Table 4.21 Assessment of the Damage Localization Accuracy for Damage Case DB 1 Using EB Direct β_j

Damage Central Location (in)		Error (%)	$P(T \subset P)$
True	Predicted		
39.6	35.9	6.2	12.5%
FP	45.8	100.0	0%

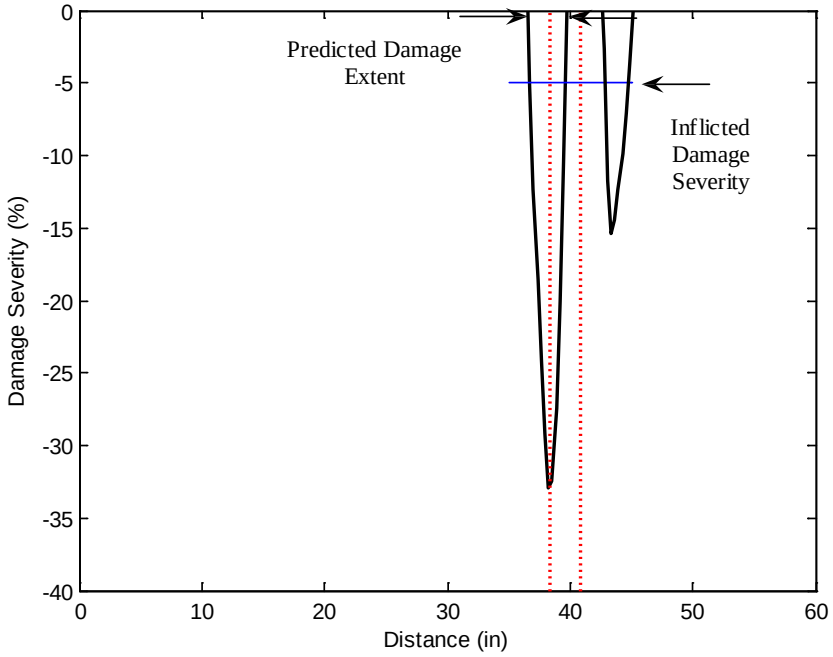

Figure 4.34 Damage Extent and Severity Estimate for Damage Case DB 1 Using EB Direct β_j

Table 4.22 Assessment of the Damage Extent and Severity Accuracy for Damage Case DB 1 Using EB Direct β_j

Damage Extent (in)		Error (%)	Damage Severity (%)		Error (%)
True	Predicted		True	Predicted Lower Bound/Upper Bound	
2.4	3.3	-1.5	-5.0	-20.9/-34.4	-318/-558
FP	2.4	100.0	FP	-9.9/-15.41	100/100

Damage Case DB 2

Figures 4.35 and 4.36 depict the damage prediction results for Damage Case DB 2 using the damage indicator EB Direct β_j. Tables 4.23 and 4.24 tabulate the performance of the damage detection methodology for the damage case.

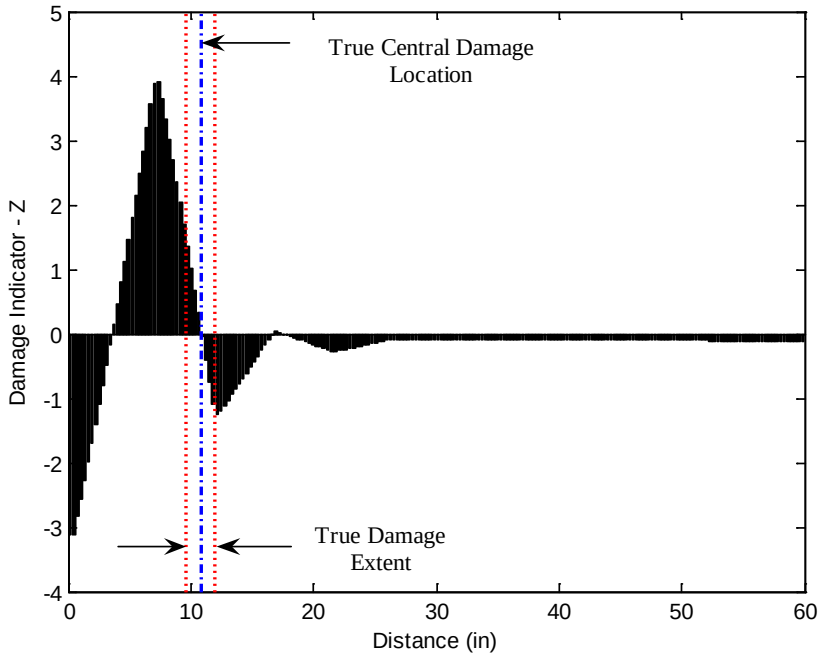

Figure 4.35 Damage Localization Result for Damage Case DB 2 Using EB Direct β_j

Table 4.23 Assessment of the Damage Localization Accuracy for Damage Case DB 2 Using EB Direct β_j

Damage Central Location (in)		Error (%)	$P(T \subset P)$
True	Predicted		
10.8	7.4	5.7	50%

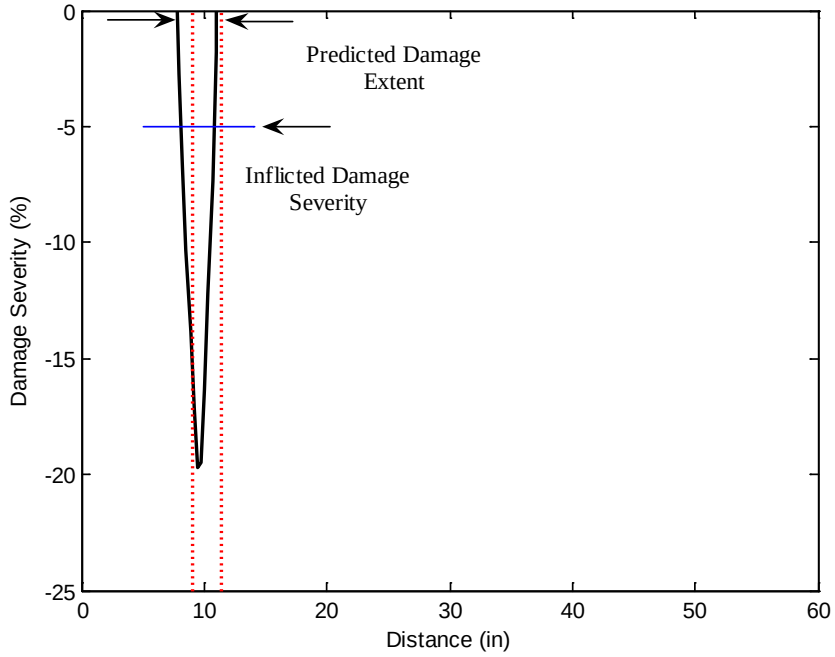

Figure 4.36 Damage Extent and Severity Estimate for Damage Case DB 2 Using EB Direct β_j

Table 4.24 Assessment of the Damage Extent and Severity Accuracy for Damage Case DB 2 Using EB Direct β_j

Damage Extent (in)		Error	Damage Severity (%)		Error (%)
True	Predicted	(%)	True	Predicted Lower Bound/Upper Bound	
2.4	3.3	-1.5	-5.0	-12.0/-19.7	-140/-294

Damage Case DB 3

Figures 4.37 and 4.38 depict the damage prediction results for Damage Case DB 3 using the damage indicator EB Direct β_j. Tables 4.25 and 4.26 tabulate the performance of the damage detection methodology for the damage case.

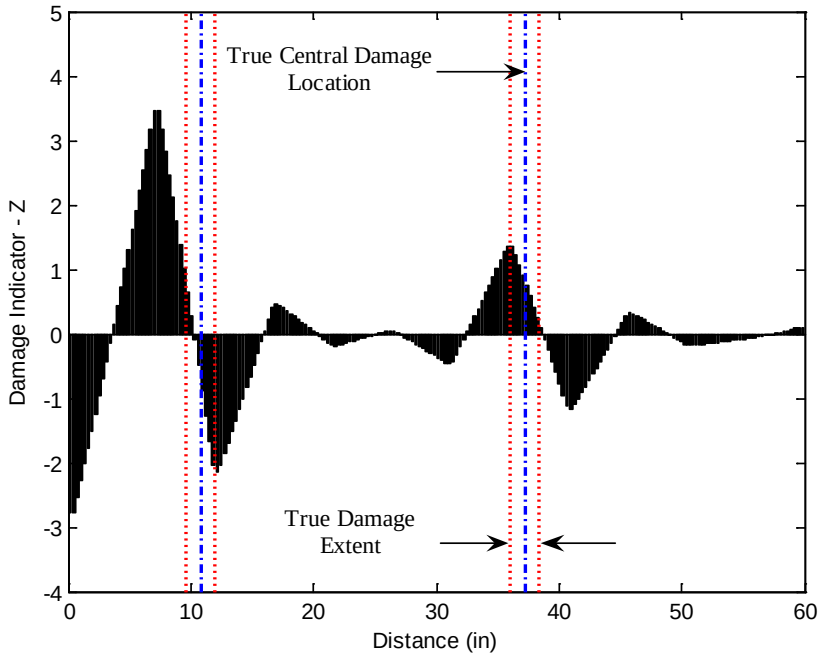

Figure 4.37 Damage Localization Result for Damage Case DB 3 Using EB Direct β_j

Table 4.25 Assessment of the Damage Localization Accuracy for Damage Case DB 3 Using EB Direct β_j

Damage Central Location (in)		Error (%)	$P(T \subset P)$
True	Predicted		
10.8	7.1	6.2	25%
37.2	35.9	2.2	100%

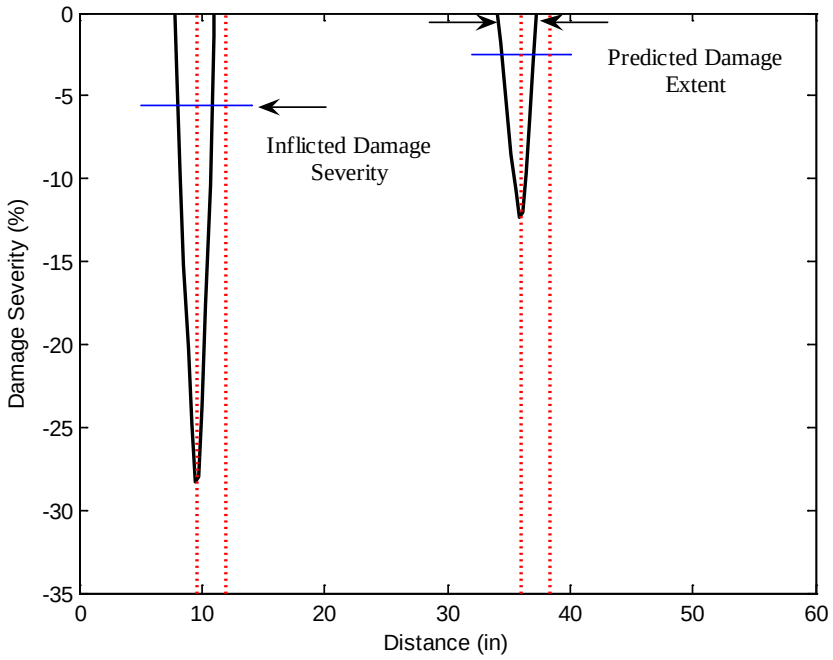

Figure 4.38 Damage Extent and Severity Estimate for Damage Case DB 3 Using EB Direct β_j

Table 4.26 Assessment of the Damage Extent and Severity Accuracy for Damage Case DB 3 Using EB Direct β_j

Damage Extent (in)		Error (%)	Damage Severity (%)		Error (%)
True	Predicted		True	Predicted Lower Bound/Upper Bound	
2.4	3.3	-1.5	-5.6	-17.5/-28.3	-213/-405
2.4	3.3	-1.5	-2.5	-7.6/-12.4	-204/-396

Damage Case DB 4

Figures 4.39 and 4.40 depict the damage prediction results for Damage Case DB 4 using the damage indicator EB Direct β_j. Tables 4.27 and 4.28 tabulate the performance of the damage detection methodology for the damage case.

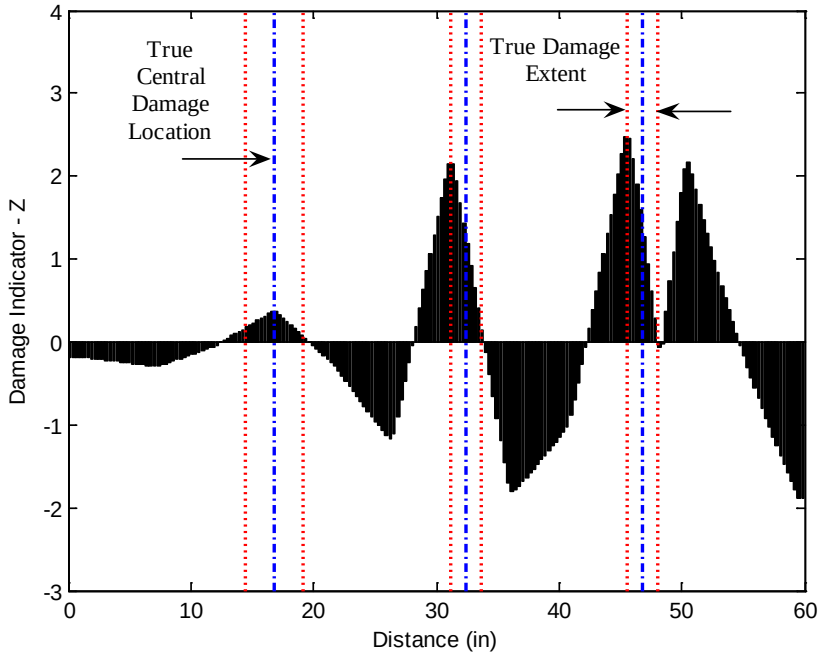

Figure 4.39 Damage Localization Result for Damage Case DB 4 Using EB Direct β_j

Table 4.27 Assessment of the Damage Localization Accuracy for Damage Case DB 4 Using EB Direct β_j

Damage Central Location (in)		Error (%)	$P(T \subset P)$
True	Predicted		
16.8	16.7	0.2	100%
32.4	31.1	2.2	100%
46.8	45.8	1.7	100%
FP	50.6	100.0	0%

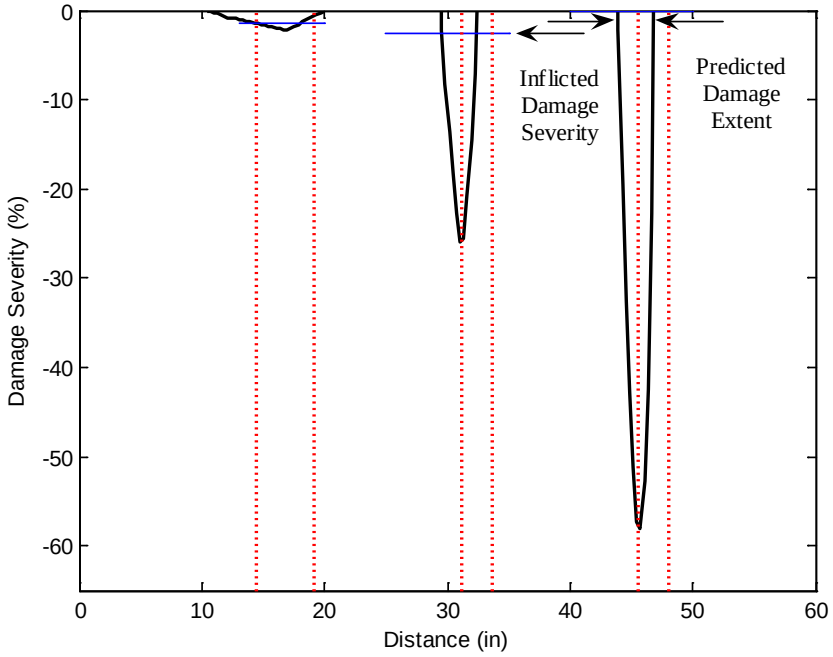

Figure 4.40 Damage Extent and Severity Estimate for Damage Case DB 4 Using EB Direct β_j

Table 4.28 Assessment of the Damage Extent and Severity Accuracy for Damage Case DB 4 Using EB Direct β_j

Damage Extent (in)		Error (%)	Damage Severity (%)		Error (%)
True	Predicted		True	Predicted Lower Bound/Upper Bound	
4.8	9.3	-7.5	-1.5	-1.2/-2.1	20.0/-40.0
2.4	3.0	-1.0	-2.5	-16.6/-26.0	-564/-940
2.4	3.0	-1.0	-0.1	-42.6/-58.0	$(-43/-58)10^3$
FP	3.0	100.0	No	-65.6/-88.7	100/100

Damage Case DB 5

Figures 4.41 and 4.42 depict the damage prediction results for Damage Case DB 5 using the damage indicator EB Direct β_j. Tables 4.29 and 4.30 tabulate the performance of the damage detection methodology for the damage case.

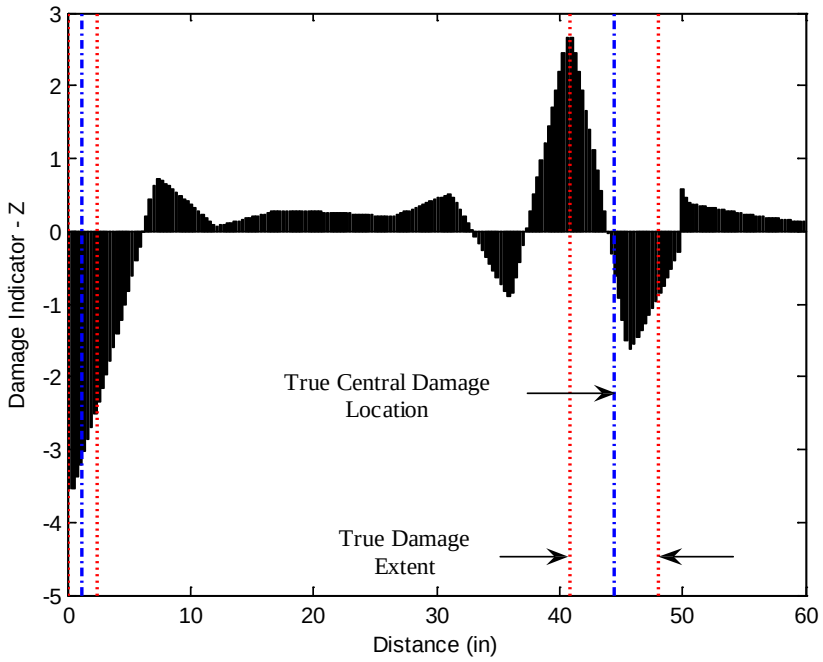

Figure 4.41 Damage Localization Result for Damage Case DB 5 Using EB Direct β_j

Table 4.29 Assessment of the Damage Localization Accuracy for Damage Case DB 5 Using EB Direct β_j

Damage Central Location (in)		Error (%)	$P(T \subset P)$
True	Predicted		
1.2	No	100.0	0%
44.4	41.0	5.7	41.7%

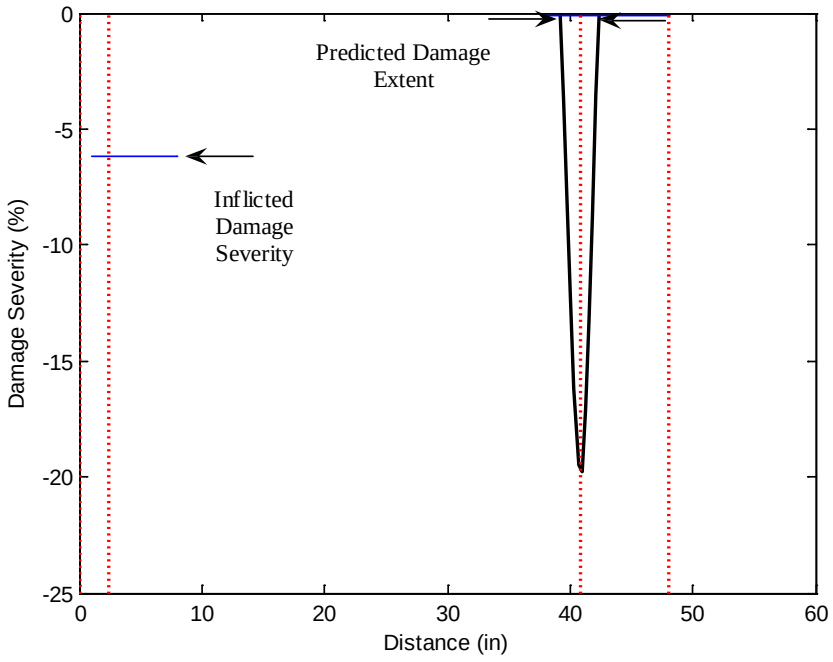

Figure 4.42 Damage Extent and Severity Estimate for Damage Case DB 5 Using EB Direct β_j

Table 4.30 Assessment of the Damage Extent and Severity Accuracy for Damage Case DB 5 Using EB Direct β_j

Damage Extent (in)		Error (%)	Damage Severity (%)		Error (%)
True	Predicted		True	Predicted Lower Bound/Upper Bound	
2.4	No	100.0	-6.2	No/No	100/100
7.2	3.0	7.0	-0.1	-12.6/-19.8	$(-13/-20)10^3$

DISCUSSION OF RESULTS

On reviewing the results, the following observations can be made regarding the accuracy of the proposed localization method.

For damage scenarios SB 1 through SB 5, the error between the central location of the true and the predicted damages, e_L (see Eq. (3.1)) ranged from a minimum of 1.0% in Damage Case SB 5 to a maximum of 3.1% in Damage Case SB 4. Note that there was one false negative (FN) prediction in Damage Case SB 4.

For damage scenarios IB 1 through IB 4, the error between the central location of the true and predicted damages ranged from a minimum of 1.4% in Damage Case IB 1 to a maximum of 4.8% in Damage Case IB 5. There were also three false positive (FP) predictions: Two in Damage Case IB 4 and one in Damage Case IB 5. In addition, one FN prediction was recorded for Damage Case IB 4.

For damage scenarios DB 1 through DB 5, the error between the true central damage and the predicted central damage ranged from a minimum 0.2% in DB 4 to a maximum of 6.2% in DB 1 and DB 3. In addition, two FP were predicted: One in Damage Case DB 1 and the other in DB 4. One FN was recorded for Damage Case DB 5.

From the above observations, the following inferences on the trend of the damage as a function of the type of beam (slender, intermediate, or deep) and the accuracy of damage localization can be made. The magnitude and range for localization errors are smallest for the SB Damage Cases (1.0 % to 3.0 %) and greatest for the DB Damage Cases (0.2 % to 6.2 %). As expected, the range for the localization errors for the IB Damage Cases ranged from 1.4% to 4.8% which falls between the SB and DB Scenarios.

As far as damage localization accuracy is concerned, on the bases of the above observations, at least two conclusions can be made:

1. The EB Direct Method performs the best as it should for slender beams.

2. Even though localization errors increase with the predictions associated with IB and DB, the efficiency of the EB Direct Method appears to be quite remarkable.

On reviewing the results, the following observations can be made with regards to the capability of the EB Direct Method's to monitor the extent of the damage. Note that the capability to monitor the extent of the damage was initially measured by the probability that the true damaged region was a subset of the predicted damaged regions (i.e. $P(T \subset P)$). Also, note that once damage was localized, the damage severity and extent estimates were quantified by utilizing a refined sensor resolution (which corresponds to the nodes of the finite element mesh at the centerline of the beam). It was assumed that the length of the region where predicted damage severity is less than zero indicated the extent of damage.

For the SB Damage Cases, in all damage scenarios except Damage Case SB 4, the probability of zooming in on the damage was 100%. The error between the true and the predicted damage extents, e_E (see Eq. (4.9)) ranged from a minimum 0.4% in SB 5 to a maximum of 5.0% in SB 3. Note that due to the FN prediction in Damage Case SB 4, damage extent at this location was not identified.

For the IB Damage Scenarios, the domain of the damage extent was correctly predicted with 50% to 100% probability in all cases, except for the FP predictions in Damage Case IB 4 and Damage Case IB 5. Damage extent accuracy seems to provide satisfactory results as far as the error estimate is concerned. However, as the predicted damage location diverges from the true damage location, the error between the two quantities becomes of lesser importance.

With respect to the deep beam, the probability of correctly isolating the region of damage was 100% only for the damaged region centered at 37.2 in. at Damage Case DB 3. The rest of the damage cases indicated errors in the accuracy of locating the region of extent of the damage.

From the observations, we conclude that the probability of correctly locating the extent of the damage decreases with the depth to length ratio of the beam when using a damage detection theory that is developed on the basis of the Euler-Bernoulli assumption.

On reviewing the results for the damage predictions using the EB direct approach, the following observations can be made regarding the accuracy of the damage severity results of the EB Direct Method:

Using the upper bound measurement as the damage error indicator, for damage scenarios SB 1 to SB 5, the error between the true bending damage severity and the predicted bending damage severity ranged from a minimum of 0% for Damage Case SB 4 to a maximum of 100% for Damage Case SB 5.

Again, using the upper bound measurement as the estimate of the severity for damage scenarios IB 1 to IB 5, the error between the true damage severity and the damage severity predicted using the EB Direct Method, ranged from a minimum of 40% to a maximum of 3700% in Damage Case IB 5.

Finally, using the upper bound measurement as the damage indicator, for damage scenarios DB 1 to DB 5, the error between the true damage severity and the predicted damage severity, using the EB Direct Method, ranged from a minimum of 40% in Damage Case DB 4 to a maximum of ($-57x10^3$) % in Damage Case DB 4. When using the EB Direct Method, the range and magnitude of the error in the prediction of the accuracy of the damage severity estimate increases as the depth to length ratio of the beam increases.

SUMMARY AND CONCLUSIONS

An explicit damage index methodology based on the principle of invariant stress resultants and the Euler-Bernoulli beam theory was developed. The performance of the proposed damage detection methodology was evaluated by using the response data collected from the numerical experiments of Chapter III. The proposed methodology produced satisfactory damage localization results considering that it is based on the Euler-Bernoulli beam theory, which is pertinent only in the case of slender beams. It was observed that the probability of correctly locating the extent of the damage decreased as the depth to length ratio of the beam increased. Correspondingly, the range and magnitude of the error in damage severity estimation increased as the aspect ratio of the beam increased. Based on the results of the case studies, it can be concluded that damage prediction theories better fit for deeper beams are necessary for improved damage prediction results in the case of deep beams.

CHAPTER V

DAMAGE INDICES BASED ON NODAL CURVATURES

INTRODUCTION

The objective of this chapter is to develop explicit damage index methodologies in order to locate and quantify damage in beam-type structures. The proposed methodology is based on the stress-displacement relations of the Euler-Bernoulli beam theory. Damage is expressed in terms of local decreases in the flexural stiffness of structural members, which in turn is represented as singularities in the flexural stiffness distribution of the beam. Utilizing the concept of discontinuity developed in Chapter II in conjunction with nodal curvatures, the location and magnitude of these local decreases may be identified.

To accomplish the stated objective, this chapter is divided into four major sections: a section articulating the proposed methodology; a section describing specific structural response parameters utilized in the proposed damage detection methodology; a section evaluating the performance of the method using the numerical experiments introduced in Chapter III; and a section discussing the outcomes of the performed case studies.

PROPOSED METHODOLOGY

Assume that a local decrease in the stiffness of a beam-type structure may be expressed in terms of a decrease in the bending stiffness of its sub-element(s). In order to model this, assume that the beam that is comprised of NE sub-elements and NN nodes as depicted in Figure 5.1. The problem here is to identify the location of the damaged sub-elements within the beam and quantify the amount of stiffness degradation inflicted at each damaged region. Following methodologies are proposed in order to address the stated problem.

Nodal Flexural Stiffness Based on the Average of Curvatures at the Point of Flexural Discontinuity

Let the pristine and damaged flexural stiffnesses of the j^{th} element located between the coordinates $x = l_i$ and $x = l_{i+1}$ be represented by EI_j and EI_j^*, respectively. Utilizing the principle of invariant stress resultants, following condition holds at the i^{th} node of the beam:

$$M_i = M_i^* \tag{5.1}$$

where the asterisk represents the moment at $x = l_i$ in the damaged beam.

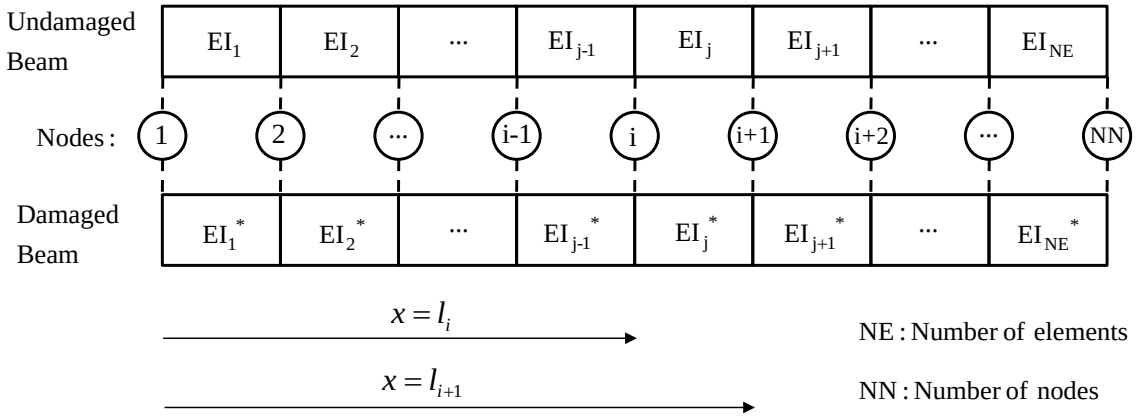

Figure 5.1 Damage Detection Model Utilized to Predict Local Changes in the Flexural Stiffness Distribution via Nodal Curvatures

Utilizing the fundamental relationship between the curvature and bending moment (Eq. (2.9)), Eq. (5.1) may be written in terms of the flexural stiffness and curvature at the i^{th} node before and after damage.

$$EI_i \, \kappa_i = EI_i^* \, \kappa_i^* \tag{5.2}$$

where the curvature at any position along the beam is approximated, according to Euler-Bernoulli beam theory, by the equation:

$$\kappa(x) = \frac{d^2 w(x)}{dx^2} \tag{5.3}$$

At the i^{th} node, discrete values of the flexural stiffnesses EI_{j-1}^* and EI_j^*, leads to a discontinuity in the stiffness distribution of the damaged structure. Utilizing Eq. (2.35), nodal flexural stiffness at the i^{th} node of the damaged beam may be represented by an equivalent flexural stiffness term written in terms of the stiffnesses of the adjacent elements.

$$EI_i^* = 2\left(\frac{EI_{j-1}^* \, EI_j^*}{EI_{j-1}^* + EI_j^*} \right) \tag{5.4}$$

Substituting Eq. (5.4) into Eq. (5.2) yields:

$$EI_i \, \kappa_i = 2\left(\frac{EI_{j-1}^* \, EI_j^*}{EI_{j-1}^* + EI_j^*} \right) \kappa_i^* \tag{5.5}$$

Assuming constant flexural stiffness distribution for the pristine structure (i.e. for $i = 1...NN, EI_i = EI$), Eq. (5.5) may be written as:

$$EI \, \kappa_i = 2\left(\frac{EI_{j-1}^* \, EI_j^*}{EI_{j-1}^* + EI_j^*} \right) \kappa_i^* \tag{5.6}$$

Collecting element stiffnesses at the right hand side of the equation gives:

$$EI\left(\frac{EI_{j-1}^{*}+EI_{j}^{*}}{EI_{j-1}^{*}\,EI_{j}^{*}}\right)\kappa_i = 2\,\kappa_i^{*} \tag{5.7}$$

Factoring out the denominator of the left hand side of Eq. (5.7) yields:

$$EI\left(\frac{EI_{j-1}^{*}}{EI_{j-1}^{*}\,EI_{j}^{*}}+\frac{EI_{j}^{*}}{EI_{j-1}^{*}\,EI_{j}^{*}}\right)\kappa_i = 2\,\kappa_i^{*} \tag{5.8}$$

Cancelling out the like terms within parenthesis leads to the following equation:

$$\left(\frac{EI}{EI_{j}^{*}}+\frac{EI}{EI_{j-1}^{*}}\right)\kappa_i = 2\,\kappa_i^{*} \tag{5.9}$$

This further simplifies into Eq. (5.11) upon introducing the notation:

$$\beta_j = \frac{EI}{EI_{j}^{*}} \tag{5.10}$$

$$\left(\beta_j + \beta_{j-1}\right)\kappa_i = 2\,\kappa_i^{*} \tag{5.11}$$

Similarly, using the recursive scheme established in Eq. (5.11), the relation between the damage indices for the j^{th} and $j+1^{th}$ beam elements at the $(i+1)^{th}$ node become:

$$\left(\beta_{j+1} + \beta_j\right)\kappa_{i+1} = 2\,\kappa_{i+1}^{*} \tag{5.12}$$

For a beam with NN nodes and NE sub-elements, where $NE = NN-1$, $NN-2$ number of linear equations may be written using the procedure described by Eq. (5.11) and Eq. (5.12). This process results in a system of underdetermined linear equations. Singular value decomposition based (SVD) *pseudo-inverse* techniques may then be used to obtain an optimal solution for the values of the element damage indices. The system of equations may be written in the form:

$$A_{(NN-2)x(NE)}\ \beta_{(NEx1)} = B_{(NN-2)x1} \tag{5.13}$$

where the $NEx1$ vector, β, denotes the damage index vector to be evaluated.

$$\beta_{(NEx1)} = \begin{bmatrix} \dots \\ \beta_j \\ \beta_{j+1} \\ \dots \end{bmatrix} \tag{5.14}$$

The $(NN-2)x(NE)$ matrix A represents the curvature sets computed for the undamaged beam. Namely,

$$A_{(NN-2)x(NE)} = \begin{bmatrix} \dots & \dots & \dots & \dots & \dots & \dots & \dots \\ \dots & 0 & \kappa_i & \kappa_i & 0 & \dots & \dots \\ \dots & \dots & 0 & \kappa_{i+1} & \kappa_{i+1} & 0 & \dots \\ \dots & \dots & \dots & \dots & \dots & \dots & \dots \end{bmatrix} \tag{5.15}$$

whereas $(NN-2)x1$ matrix B represents the curvature sets of the damaged beam.

$$B_{(NN-2)x1} = \begin{bmatrix} \dots \\ 2\kappa_i^{\,*} \\ 2\kappa_{i+1}^{\,*} \\ \dots \end{bmatrix} \tag{5.16}$$

The solution to Eq. (5.13) is given by:

$$\beta = A^{-1}B \tag{5.17}$$

where A^{-1} is the *pseudo-inverse* of A.

Note that the damage indicator, β_j, computed above is greater than unity in regions where stiffness degradation has occurred. This damage indicator is designated as "the EB Pseudo β_j" for identification purposes.

The severity of the inflicted damage for localized damaged regions may be expressed in terms of the pristine and damaged flexural stiffnesses:

$$\alpha_j = \frac{\Delta EI_j}{EI_j} = \frac{EI_j^* - EI_j}{EI_j} \tag{5.18}$$

which in turn can be written in terms of the damage indicator β_j computed in Eq. (5.17):

$$\alpha_j = \frac{EI_j^*}{EI_j} - 1 = \frac{1}{\beta_j} - 1 \tag{5.19}$$

Nodal Flexural Stiffness Based on the Average of Flexural Stiffnesses at the Point of Flexural Discontinuity

An analogous formulation to the one given in Eq. (5.13) may be obtained by using Eq. (2.37) in lieu of Eq. (2.35) for expressing the nodal flexural stiffness. Flexural stiffness at the i^{th} node is now represented by the mean value of the flexural stiffnesses of its adjacent elements, namely $j-1$ and j as was shown in Figure 5.1. Thus, at the i^{th} node:

$$EI_i^* = \frac{1}{2}\left(EI_{j-1}^* + EI_j^*\right) \tag{5.20}$$

Substituting Eq. (5.20) for EI_i^* into Eq. (5.2) yields:

$$EI_i\,\kappa_i = \frac{1}{2}\left(EI_{j-1}^* + EI_j^*\right)\kappa_i^* \tag{5.21}$$

As before, assuming constant flexural stiffness distribution for the pristine structure (i.e. for $i = 1...NN, EI_i = EI$), Eq. (5.21) may be written as:

$$EI\,\kappa_i = \frac{1}{2}\left(EI_{j-1}^* + EI_j^*\right)\kappa_i^* \tag{5.22}$$

Next, dividing the right hand side of Eq. (5.22) by the flexural stiffness of the undamaged beam, EI, results in:

$$2\kappa_i = \left(\gamma_{j-1} + \gamma_j\right)\kappa_i^* \tag{5.23}$$

where the equivalent damage index γ_j is now given by:

$$\gamma_j = \frac{EI_j^*}{EI} \tag{5.24}$$

Similarly, using the recursive scheme established in Eq. (5.23), the relation between the damage indices for the j^{th} and $j+1^{th}$ beam elements at the $(i+1)^{th}$ node become:

$$2\kappa_{i+1} = \left(\gamma_j + \gamma_{j+1}\right)\kappa_{i+1}^* \tag{5.25}$$

As before, for a beam with NN nodes and NE sub-elements, where $NE = NN - 1$, $NN - 2$ number of linear equations may be written using the procedure described by Eq. (5.23) and Eq. (5.25). This procedure results in a system of underdetermined linear equations. Singular value decomposition based (SVD) *pseudo-inverse* techniques may then be used to obtain an optimal solution for the values of the element damage indices given in Eq. (5.24). The system of equations may be written in the form:

$$C_{(NN-2)x(NE)}\ \gamma_{(NEx1)} = D_{(NN-2)x1} \tag{5.26}$$

where the $NEx1$ vector, γ, denotes the damage index vector to be evaluated.

$$\gamma_{(NEx1)} = \begin{bmatrix} \cdots \\ \gamma_j \\ \gamma_{j+1} \\ \cdots \end{bmatrix} \tag{5.27}$$

The $(NN-2)x(NE)$ matrix C represents the curvature sets computed for the damaged beam. Namely,

$$C_{(NN-2)x(NE)} = \begin{bmatrix} \dots & \dots & \dots & \dots & \dots & \dots & \dots \\ \dots & 0 & \kappa_i^* & \kappa_i^* & 0 & \dots & \dots \\ \dots & \dots & 0 & \kappa_{i+1}^* & \kappa_{i+1}^* & 0 & \dots \\ \dots & \dots & \dots & \dots & \dots & \dots & \dots \end{bmatrix} \tag{5.28}$$

whereas $(NN-2)x1$ matrix D represents the curvature sets of the undamaged beam.

$$D_{(NN-2)x1} = \begin{bmatrix} \dots \\ 2\kappa_i \\ 2\kappa_{i+1} \\ \dots \end{bmatrix} \tag{5.29}$$

The solution to Eq. (5.26) is given by:

$$\gamma = A^{-1}B \tag{5.30}$$

where A^{-1} is the *pseudo-inverse* of A.

The damage indicator, γ_j, computed above is less than unity in regions where stiffness degradation has occurred. This damage indicator is designated as "the EB Pseudo γ_j" for identification purposes.

The severity of the inflicted damage for localized damaged regions may be expressed in terms of the pristine and damaged flexural stiffnesses:

$$\alpha_j = \frac{\Delta EI_j}{EI_j} = \frac{EI_j^* - EI_j}{EI_j} \tag{5.31}$$

This in turn can be written in terms of the damage indicator γ_j computed in Eq. (5.30):

$$\alpha_j = \frac{EI_j^*}{EI_j} - 1 = \gamma_j - 1 \tag{5.32}$$

PROPOSED EXPERIMENTAL ARRANGEMENT AND BASIC MEASUREMENTS REQUIRED BY THEORY

The proposed NDE methodology utilizes the pre- and post-damaged nodal curvatures for damage detection. The proposed experimental arrangement is identical to the one given in Chapter IV. The pre- and post-damaged nodal curvatures computed previously in Chapter IV are employed in the proposed damage detection methodologies.

ASSESSMENT OF THE PROPOSED METHODOLOGIES VIA NUMERICAL EXPERIMENTS

The performance of the proposed damage detection methodology is evaluated in this section. The numerical experiments previously defined in Chapter III are utilized to evaluate the performance of the NDE methodologies. The performance of the methods is based on accurately identifying the location, the extent, and the severity of the damage as before. These items are described in Chapter IV.

The Slender Beam

Damage detection results for the slender beam are presented in this subsection. The curvature profile of the 15^{th} modal flexibility (note that this corresponds to the deformed shape of the beam due to the unit load applied at the location of sensor 15) is utilized to compute the nodal curvatures of the undamaged and damaged beam.

Cubic spline functions with 0.6 in. uniform intervals are used to generate a finer sensor layout along the length the beam. This procedure leads to 241 nodal points. Curvatures are estimated by the central difference approximation after interpolation.

Damage Case SB 1

Figures 5.2 and 5.3 depict the damage prediction results for Damage Case SB 1 using the damage indicator EB Pseudo β_j. Tables 5.1 and 5.2 tabulate the performance of the damage detection methodology that utilizes EB Pseudo β_j for damage detection. The error between the central location of the true and the predicted damages is computed by Eq. (3.1). Note that $P(T \subset P)$ indicates the probability that the true damaged region is a subset of the predicted damaged regions. The damage severity and extent estimates are computed by utilizing an improved sensor resolution, which corresponds to the nodes of the finite element mesh at the centerline of the beam. It is assumed that only the regions previously identified by the damage localization results are instrumented for predicting the severity and the extent of damage. This process reduces the size of the system of linear equations given by Eq. (5.13). The same approach is utilized while detecting damage with EB Pseudo γ_j.

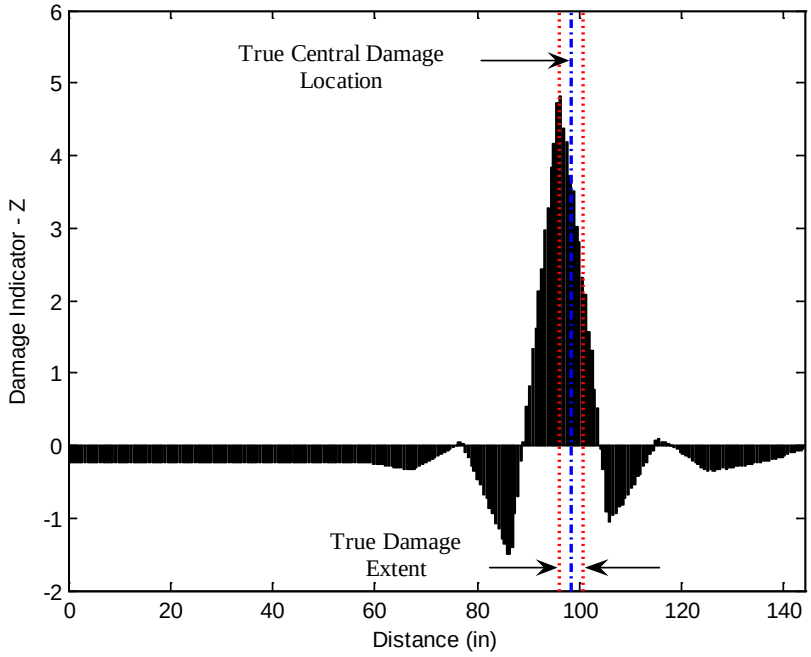

Figure 5.2 Damage Localization Result for Damage Case SB 1 Using EB Pseudo β_j

Table 5.1 Assessment of the Damage Localization Accuracy for Damage Case SB 1 Using EB Pseudo β_j

Damage Central Location (in)		Error (%)	$P(T \subset P)$
True	Predicted		
98.4	96.3	1.5	100%

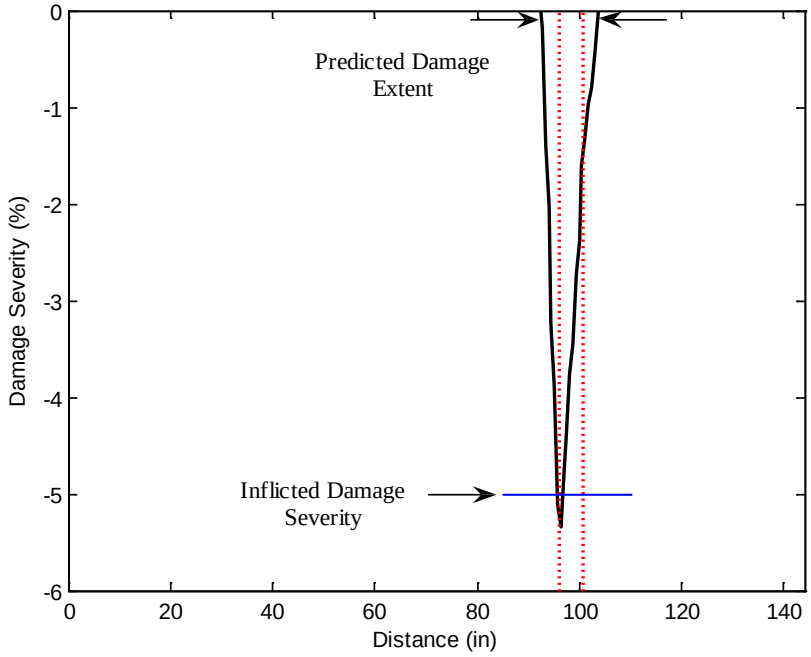

Figure 5.3 Damage Extent and Severity Estimate for Damage Case SB 1 Using EB Pseudo β_j

Table 5.2 Assessment of the Damage Extent and Severity Accuracy for Damage Case SB 1 Using EB Pseudo β_j

Damage Extent (in)		Error	Damage Severity (%)		Error (%)
True	Predicted	(%)	True	Predicted Lower Bound/Upper Bound	
4.8	10.8	-4.2	-5.0	-2.6/-5.3	48.0/-6.0

Figures 5.4 and 5.5 depict the damage prediction results for Damage Case SB 1 using the damage indicator EB Pseudo γ_j. Tables 5.3 and 5.4 tabulate the performance of the damage detection methodology that utilizes EB Pseudo γ_j for damage detection.

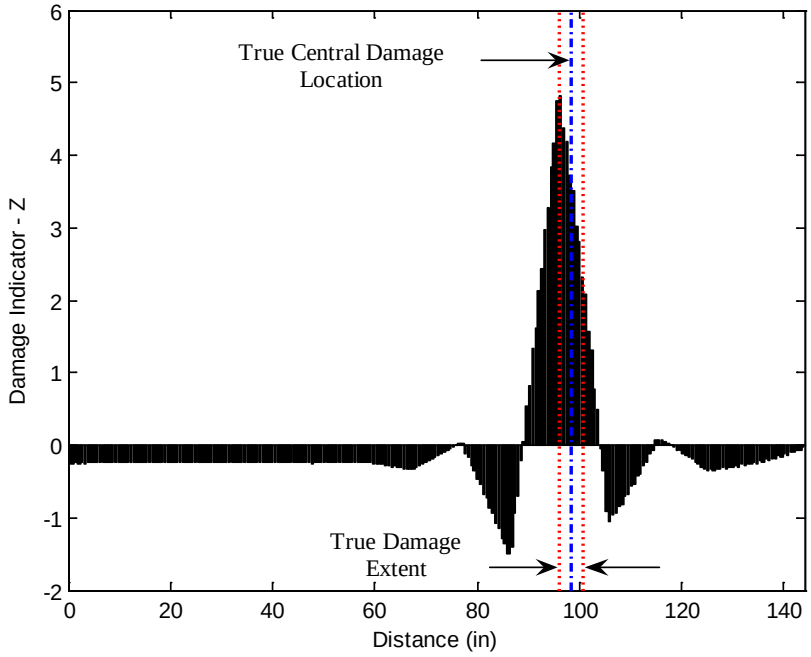

Figure 5.4 Damage Localization Result for Damage Case SB 1 Using EB Pseudo γ_j

Table 5.3 Assessment of the Damage Localization Accuracy for Damage Case SB 1 Using EB Pseudo γ_j

Damage Central Location (in)		Error (%)	$P(T \subset P)$
True	Predicted		
98.4	96.3	1.5	100%

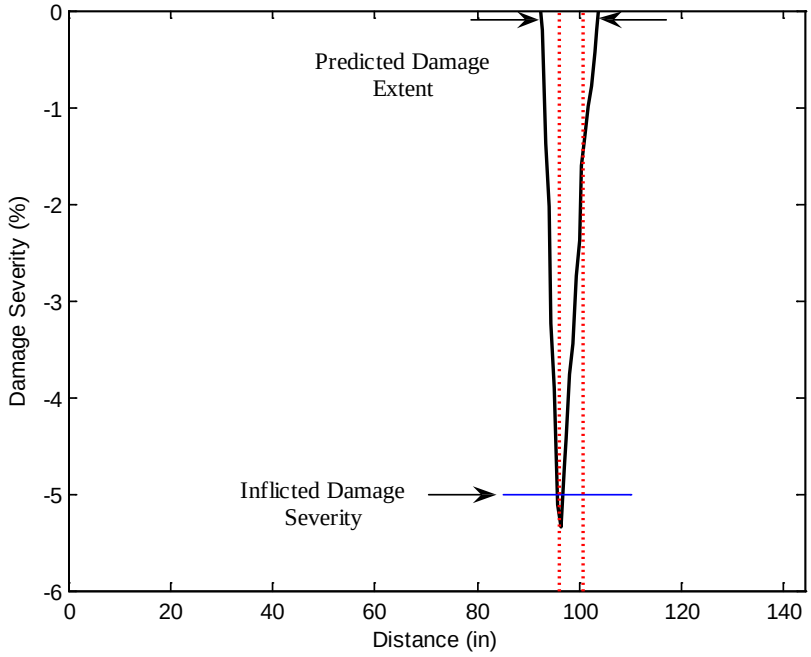

Figure 5.5 Damage Extent and Severity Estimate for Damage Case SB 1 Using EB Pseudo γ_j

Table 5.4 Assessment of the Damage Extent and Severity Accuracy for Damage Case SB 1 Using EB Pseudo γ_j

Damage Extent (in)		Error (%)	Damage Severity (%)		Error (%)
True	Predicted		True	Predicted Lower Bound/Upper Bound	
4.8	10.8	-4.2	-5.0	-2.6/-5.3	48.0/-6.0

Damage Case SB 2

Figures 5.6 and 5.7 depict the damage prediction results for Damage Case SB 2 using the damage indicator EB Pseudo β_j. Tables 5.5 and 5.6 tabulate the performance of the damage detection methodology that utilizes EB Pseudo β_j for damage detection.

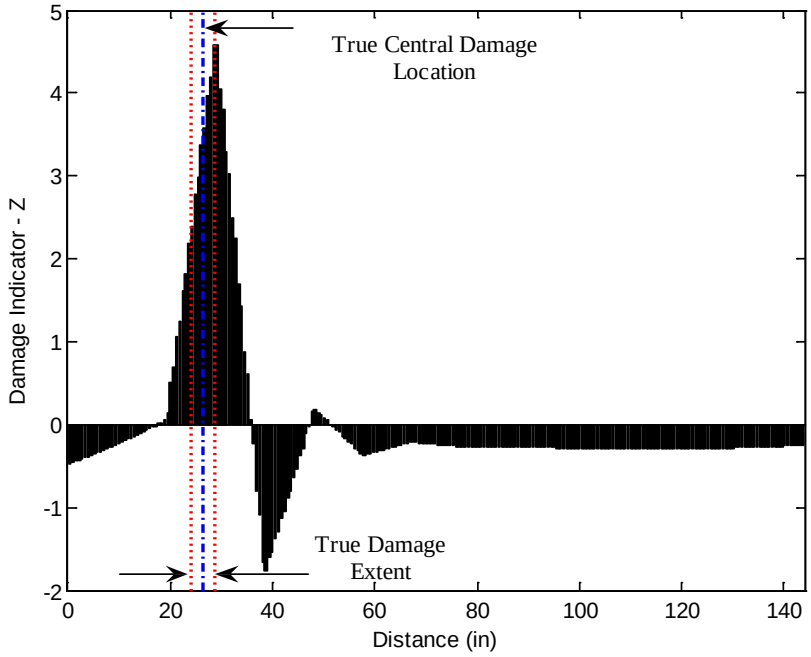

Figure 5.6 Damage Localization Result for Damage Case SB 2 Using EB Pseudo β_j

Table 5.5 Assessment of the Damage Localization Accuracy for Damage Case SB 2 Using EB Pseudo β_j

Damage Central Location (in)		Error (%)	$P(T \subset P)$
True	Predicted		
26.4	28.5	-1.5	100%

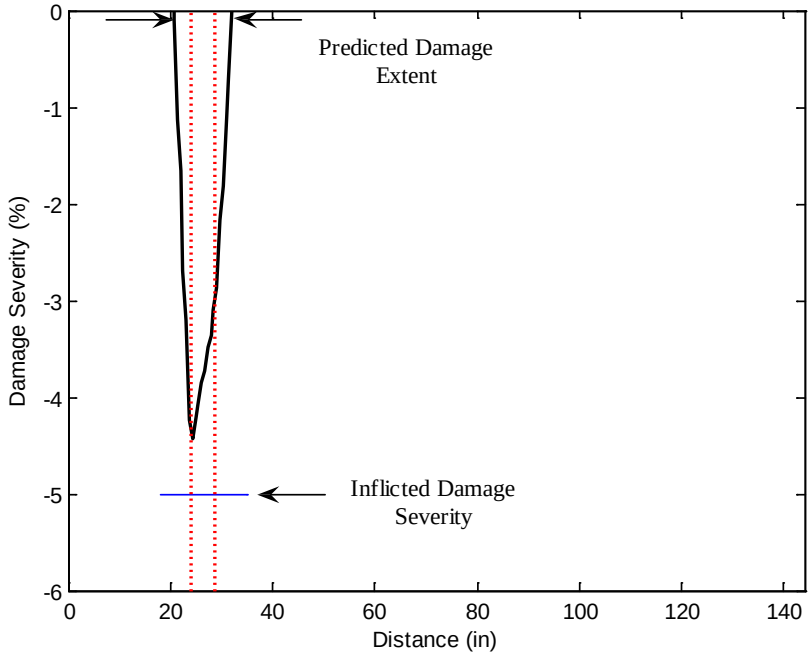

Figure 5.7 Damage Extent and Severity Estimate for Damage Case SB 2 Using EB Pseudo β_j

Table 5.6 Assessment of the Damage Extent and Severity Accuracy for Damage Case SB 2 Using EB Pseudo β_j

Damage Extent (in)		Error	Damage Severity (%)		Error (%)
True	Predicted	(%)	True	Predicted Lower Bound/Upper Bound	
4.8	11.4	-4.6	-5.0	-2.6/-4.4	48.0/12.0

Figures 5.8 and 5.9 depict the damage prediction results for Damage Case SB 2 using the damage indicator EB Pseudo γ_j. Tables 5.7 and 5.8 tabulate the performance of the damage detection methodology that utilizes EB Pseudo γ_j for damage detection.

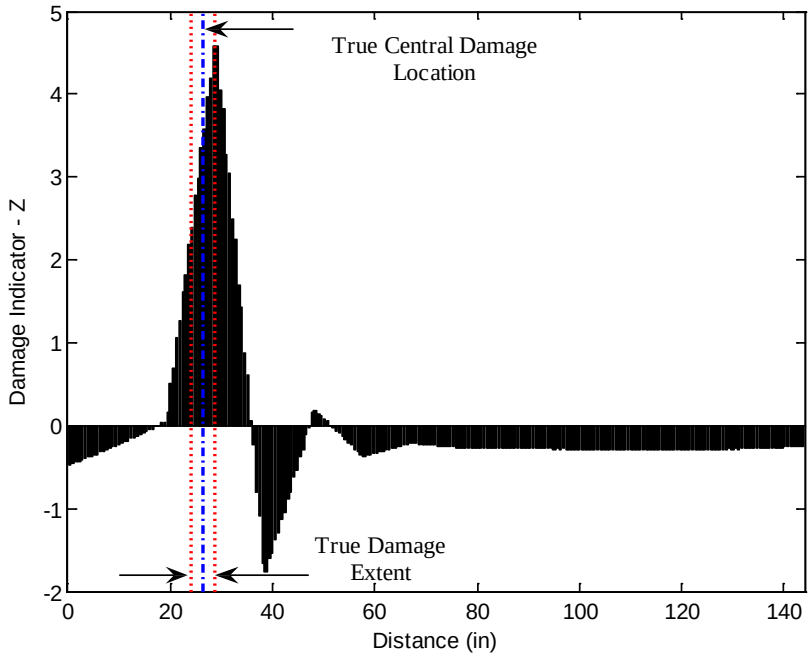

Figure 5.8 Damage Localization Result for Damage Case SB 2 Using EB Pseudo γ_j

Table 5.7 Assessment of the Damage Localization Accuracy for Damage Case SB 2 Using EB Pseudo γ_j

Damage Central Location (in)		Error (%)	$P(T \subset P)$
True	Predicted		
26.4	29.1	-1.9	100%

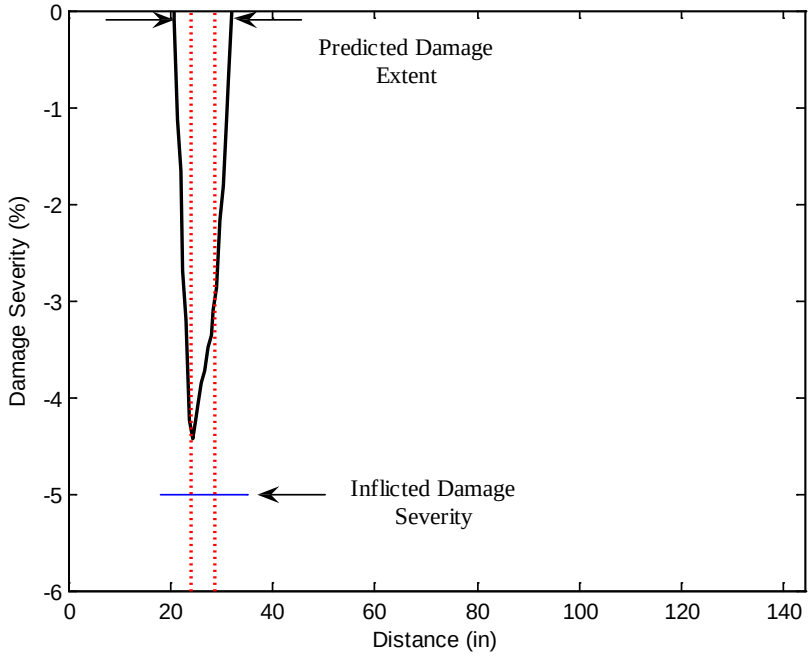

Figure 5.9 Damage Extent and Severity Estimate for Damage Case SB 2 Using EB Pseudo γ_j

Table 5.8 Assessment of the Damage Extent and Severity Accuracy for Damage Case SB 2 Using EB Pseudo γ_j

Damage Extent (in)		Error	Damage Severity (%)		Error (%)
True	Predicted	(%)	True	Predicted Lower Bound/Upper Bound	
4.8	11.4	-4.6	-5.0	-2.6/-4.4	48.0/12.0

Damage Case SB 3

Figures 5.10 and 5.11 depict the damage prediction results for Damage Case SB 3 using the damage indicator EB Pseudo β_j. Tables 5.9 and 5.10 tabulate the performance of the damage detection methodology that utilizes EB Pseudo β_j for damage detection.

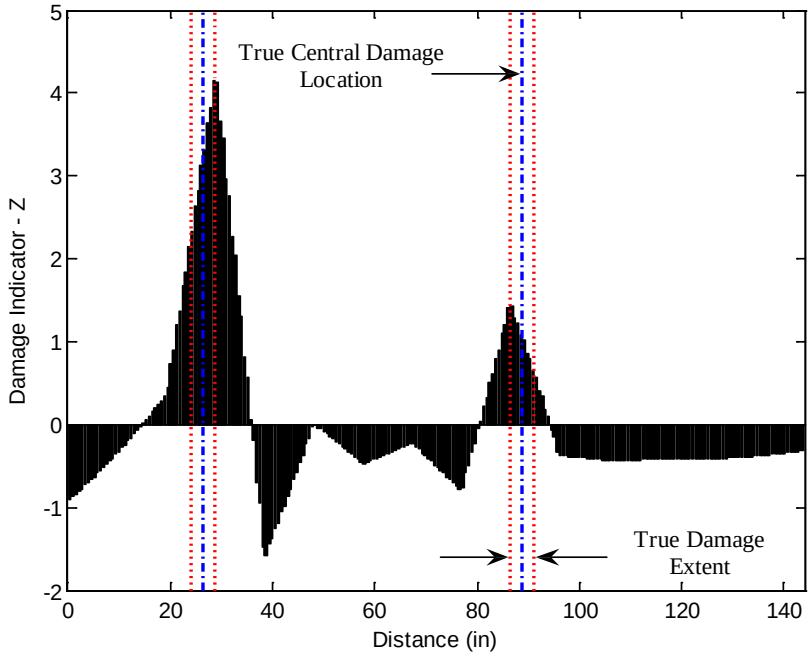

Figure 5.10 Damage Localization Result for Damage Case SB 3 Using EB Pseudo β_j

Table 5.9 Assessment of the Damage Localization Accuracy for Damage Case SB 3 Using EB Pseudo β_j

Damage Central Location (in)		Error (%)	$P(T \subset P)$
True	Predicted		
26.4	28.5	-1.5	100%
88.8	86.7	1.5	100%

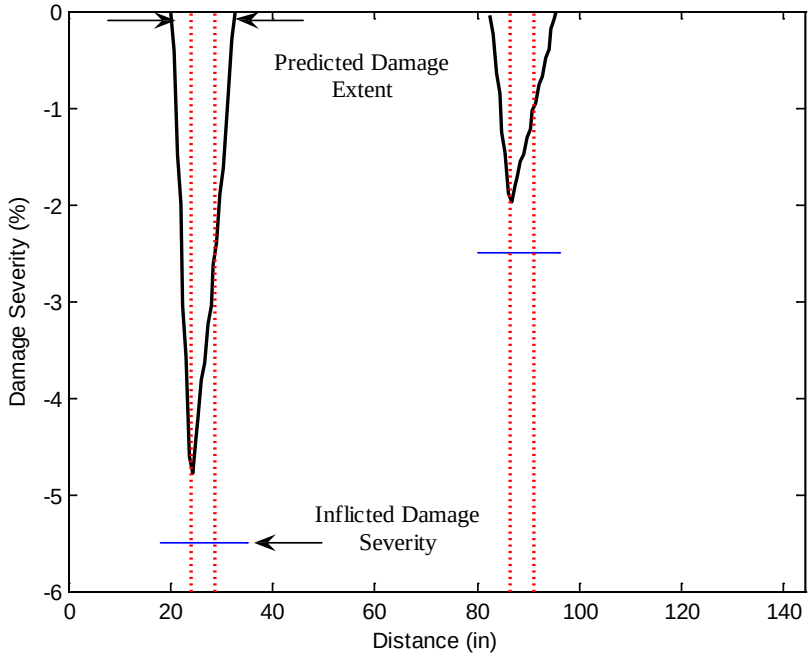

Figure 5.11 Damage Extent and Severity Estimate for Damage Case SB 3 Using EB Pseudo β_j

Table 5.10 Assessment of the Damage Extent and Severity Accuracy for Damage Case SB 3 Using EB Pseudo β_j

Damage Extent (in)		Error (%)	Damage Severity (%)		Error (%)
True	Predicted		True	Predicted Lower Bound/Upper Bound	
4.8	12.6	-5.4	-5.5	-2.5/-4.8	54.5/12.7
4.8	12.6	-5.4	-2.5	-1.0/-2.0	60.0/20.0

Figures 5.12 and 5.13 depict the damage prediction results for Damage Case SB 3 using the damage indicator EB Pseudo γ_j. Tables 5.11 and 5.12 tabulate the performance of the damage detection methodology that utilizes EB Pseudo γ_j for damage detection.

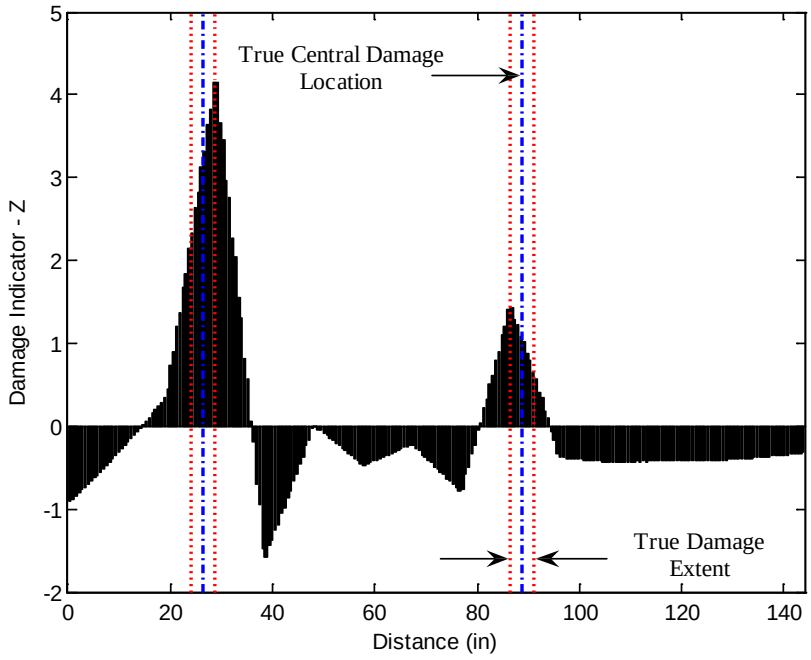

Figure 5.12 Damage Localization Result for Damage Case SB 3 Using EB Pseudo γ_j

Table 5.11 Assessment of the Damage Localization Accuracy for Damage Case SB 3 Using EB Pseudo γ_j

Damage Central Location (in)		Error (%)	$P(T \subset P)$
True	Predicted		
26.4	28.5	-1.5	100%
88.8	86.7	1.5	100%

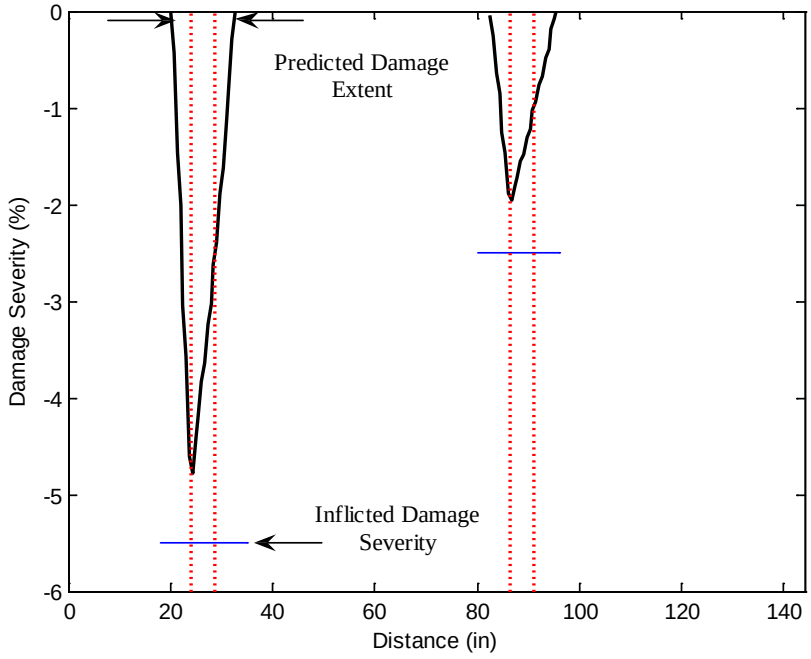

Figure 5.13 Damage Extent and Severity Estimate for Damage Case SB 3 Using EB Pseudo γ_j

Table 5.12 Assessment of the Damage Extent and Severity Accuracy for Damage Case SB 3 Using EB Pseudo γ_j

Damage Extent (in)		Error (%)	Damage Severity (%)		Error (%)
True	Predicted		True	Predicted Lower Bound/Upper Bound	
4.8	12.6	-5.4	-5.5	-2.5/-4.8	54.5/12.7
4.8	12.6	-5.4	-2.5	-1.0/-2.0	60.0/20.0

Damage Case SB 4

Figures 5.14 and 5.15 depict the damage prediction results for Damage Case SB 4 using the damage indicator EB Pseudo β_j. Tables 5.13 and 5.14 tabulate the performance of the damage detection methodology that utilizes EB Pseudo β_j for damage detection.

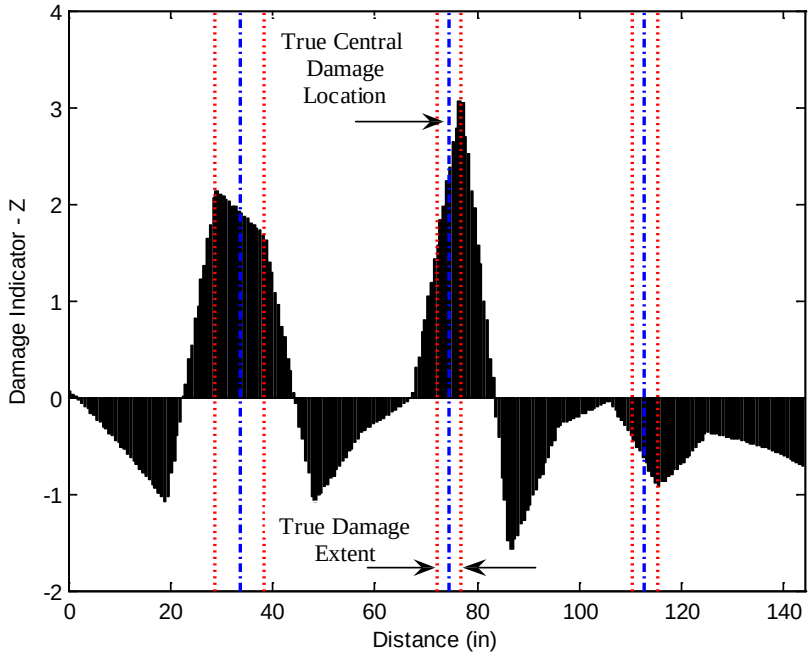

Figure 5.14 Damage Localization Result for Damage Case SB 4 Using EB Pseudo β_j

Table 5.13 Assessment of the Damage Localization Accuracy for Damage Case SB 4 Using EB Pseudo β_j

Damage Central Location (in)		Error (%)	$P(T \subset P)$
True	Predicted		
33.6	29.1	3.1	100%
74.4	76.5	-1.5	100%
112.8	No	100.0	0%

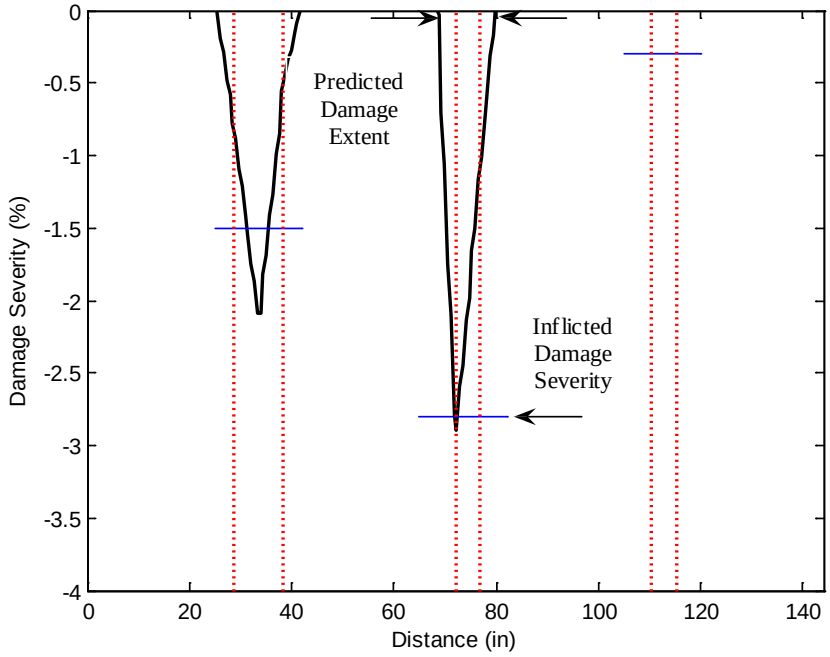

Figure 5.15 Damage Extent and Severity Estimate for Damage Case SB 4 Using EB Pseudo β_j

Table 5.14 Assessment of the Damage Extent and Severity Accuracy for Damage Case SB 4 Using EB Pseudo β_j

Damage Extent (in)		Error (%)	Damage Severity (%)		Error (%)
True	Predicted		True	Predicted Lower Bound/Upper Bound	
9.6	15.6	-4.2	-1.5	-1.0/-2.1	33.3/-40.0
4.8	11.4	-4.6	-2.8	-1.5/-2.9	46.4/-3.6
4.8	No	100.0	-0.3	No/No	100.0/100.0

Figures 5.16 and 5.17 depict the damage prediction results for Damage Case SB 4 using the damage indicator EB Pseudo γ_j. Tables 5.15 and 5.16 tabulate the performance of the damage detection methodology that utilizes EB Pseudo γ_j for damage detection.

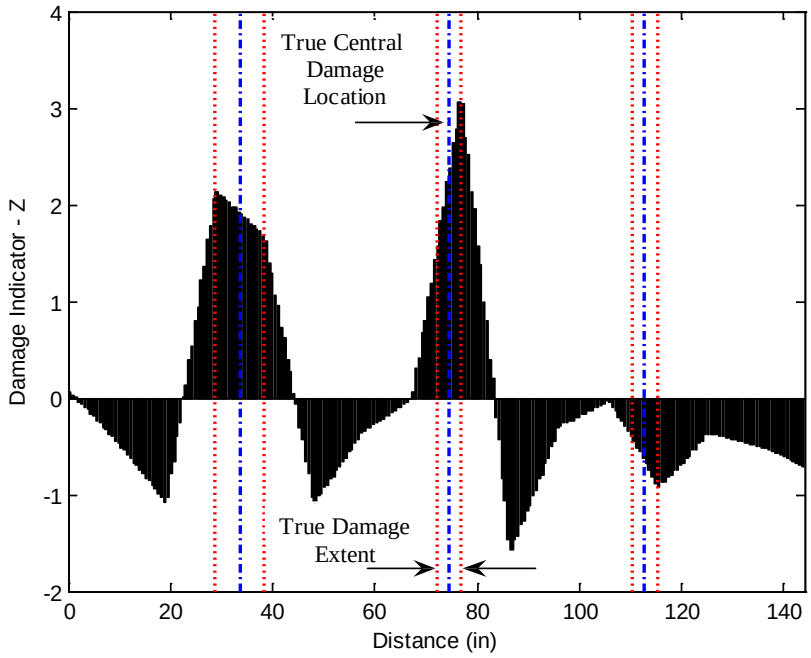

Figure 5.16 Damage Localization Result for Damage Case SB 4 Using EB Pseudo γ_j

Table 5.15 Assessment of the Damage Localization Accuracy for Damage Case SB 4 Using EB Pseudo γ_j

Damage Central Location (in)		Error (%)	$P(T \subset P)$
True	Predicted		
33.6	29.1	3.1	100%
74.4	76.5	-1.5	100%
112.8	No	100.0	0%

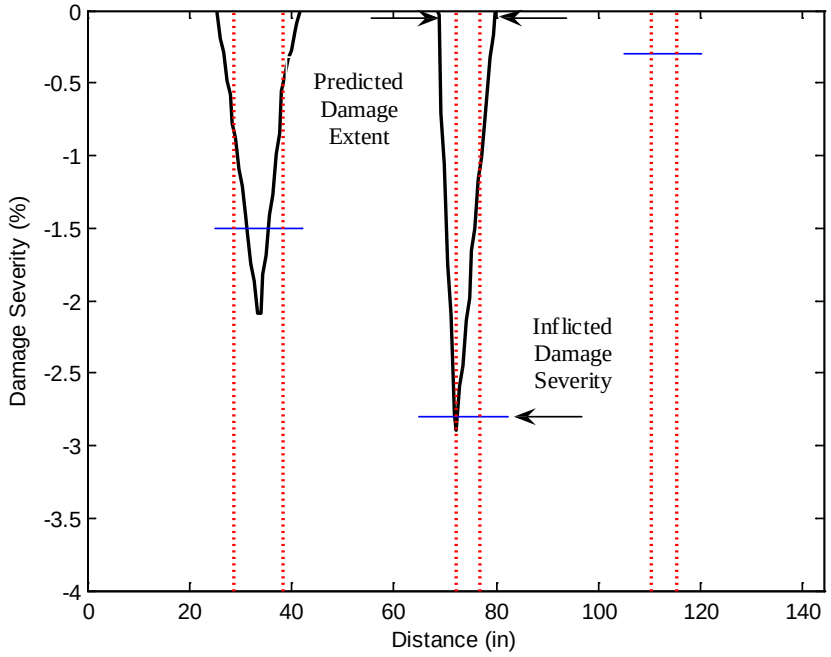

Figure 5.17 Damage Extent and Severity Estimate for Damage Case SB 4 Using EB Pseudo γ_j

Table 5.16 Assessment of the Damage Extent and Severity Accuracy for Damage Case SB 4 Using EB Pseudo γ_j

Damage Extent (in)		Error (%)	Damage Severity (%)		Error (%)
True	Predicted		True	Predicted Lower Bound/Upper Bound	
9.6	15.6	-4.2	-1.5	-1.0/-2.1	33.3/-40.0
4.8	11.4	-4.6	-2.8	-1.5/-2.9	46.4/-3.6
5.8	No	100.0	-0.3	No/No	100.0/100.0

Damage Case SB 5

Figures 5.18 and 5.19 depict the damage prediction results for Damage Case SB 5 using the damage indicator EB Pseudo β_j. Tables 5.17 and 5.18 tabulate the performance of the damage detection methodology that utilizes EB Pseudo β_j for damage detection.

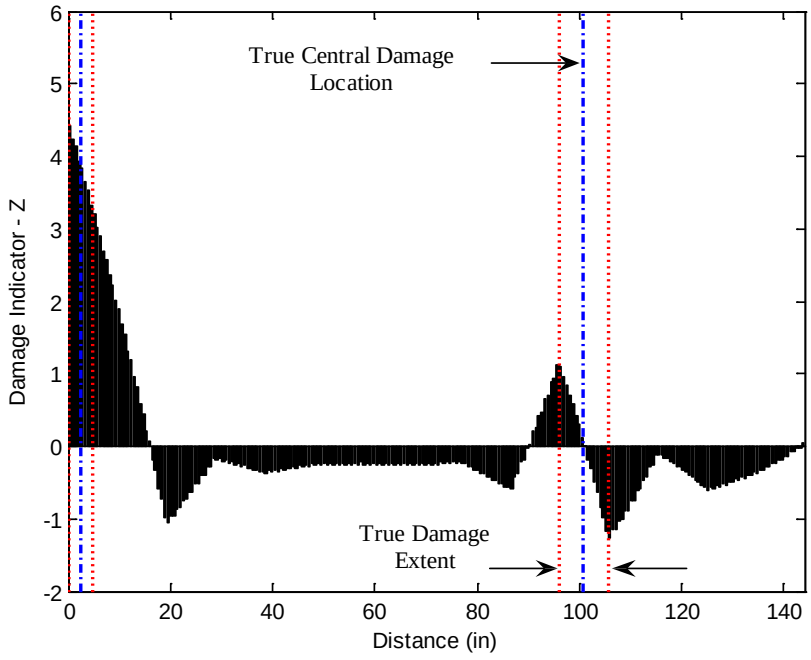

Figure 5.18 Damage Localization Result for Damage Case SB 5 Using EB Pseudo β_j

Table 5.17 Assessment of the Damage Localization Accuracy for Damage Case SB 5 Using EB Pseudo β_j

Damage Central Location (in)		Error (%)	$P(T \subset P)$
True	Predicted		
2.4	0.3	1.5	100%
100.8	96.3	3.1	50%

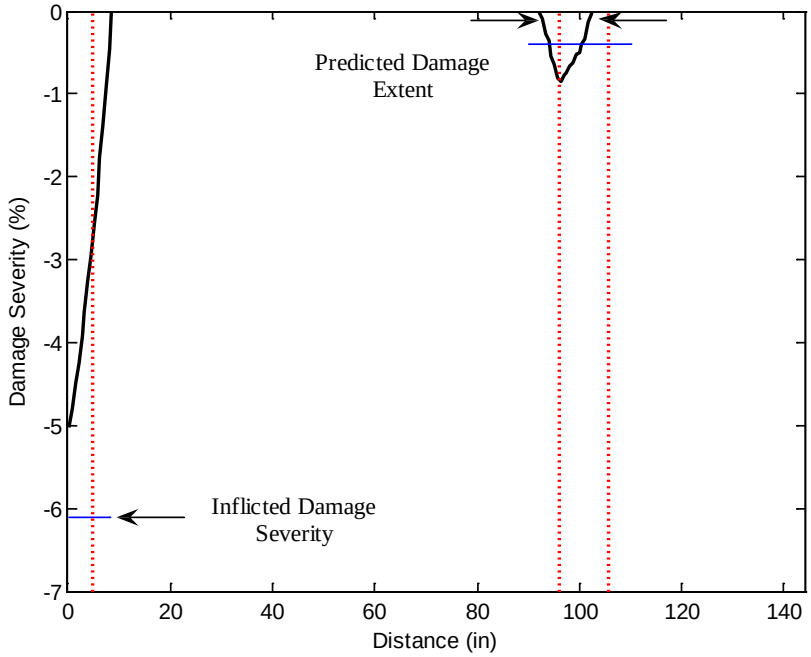

Figure 5.19 Damage Extent and Severity Estimate for Damage Case SB 5 Using EB Pseudo β_j

Table 5.18 Assessment of the Damage Extent and Severity Accuracy for Damage Case SB 5 Using EB Pseudo β_j

Damage Extent (in)		Error (%)	Damage Severity (%)		Error (%)
True	Predicted		True	Predicted Lower Bound/Upper Bound	
4.8	8.7	-2.7	-6.1	-2.8/-5.0	54.1/18.0
9.6	10.2	-0.4	-0.4	-0.5/-0.9	-25.0/-125.0

Figures 5.20 and 5.21 depict the damage prediction results for Damage Case SB 5 using the damage indicator EB Pseudo γ_j. Tables 5.19 and 5.20 tabulate the performance of the damage detection methodology that utilizes EB Pseudo γ_j for damage detection.

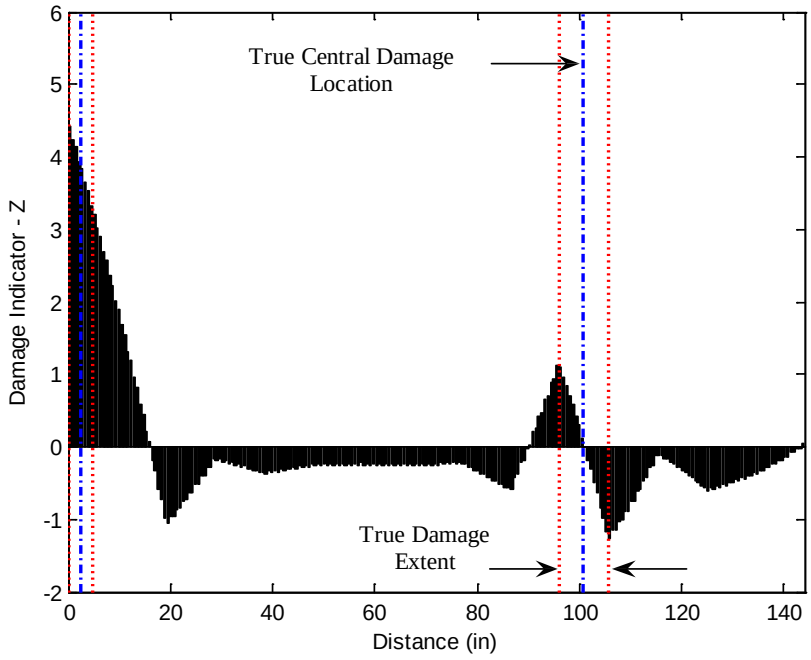

Figure 5.20 Damage Localization Result for Damage Case SB 5 Using EB Pseudo γ_j

Table 5.19 Assessment of the Damage Localization Accuracy for Damage Case SB 5 Using EB Pseudo γ_j

Damage Central Location (in)		Error (%)	$P(T \subset P)$
True	Predicted		
2.4	0.3	1.5	100%
100.8	96.3	3.1	50%

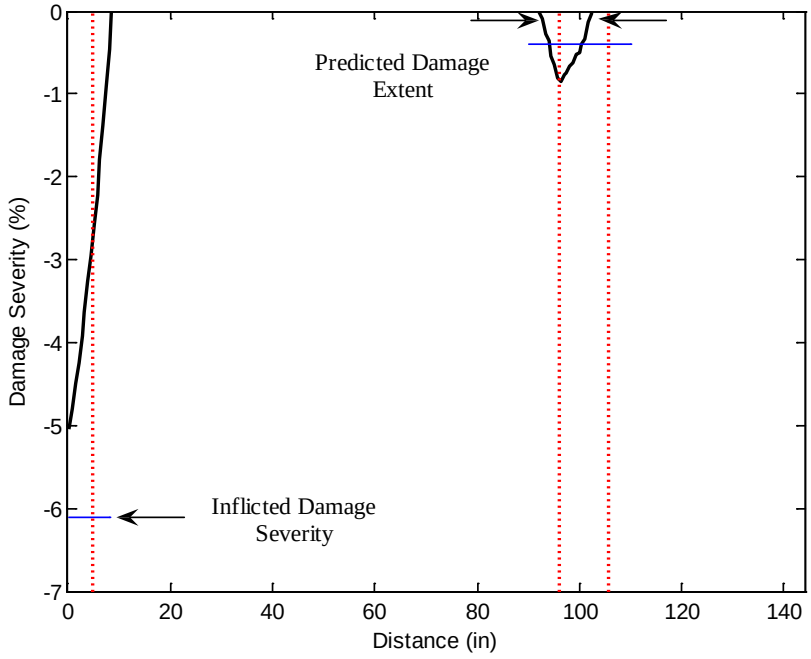

Figure 5.21 Damage Extent and Severity Estimate for Damage Case SB 5 Using EB Pseudo γ_j

Table 5.20 Assessment of the Damage Extent and Severity Accuracy for Damage Case SB 5 Using EB Pseudo γ_j

Damage Extent (in)		Error (%)	Damage Severity (%)		Error (%)
True	Predicted		True	Predicted Lower Bound/Upper Bound	
4.8	8.7	-2.7	-6.1	-2.8/-5.0	54.1/18.0
9.6	10.2	-0.4	-0.4	-0.5/-0.9	-25.0/-125.0

The Intermediate Beam

Damage detection results for the intermediate beam are presented in this subsection. The curvature profile of the 15th modal flexibility is utilized to compute the nodal curvatures of the undamaged and damaged beam. Cubic spline functions with 0.5 in. uniform intervals are used to generate a finer sensor layout along the length the beam. This procedure leads to 241 nodal points. Curvatures are estimated by the central difference approximation after interpolation.

Damage Case IB 1

Figures 5.22 and 5.23 depict the damage prediction results for Damage Case IB 1 using the damage indicator EB Pseudo β_j. Tables 5.21 and 5.22 tabulate the performance of the damage detection methodology for the damage case.

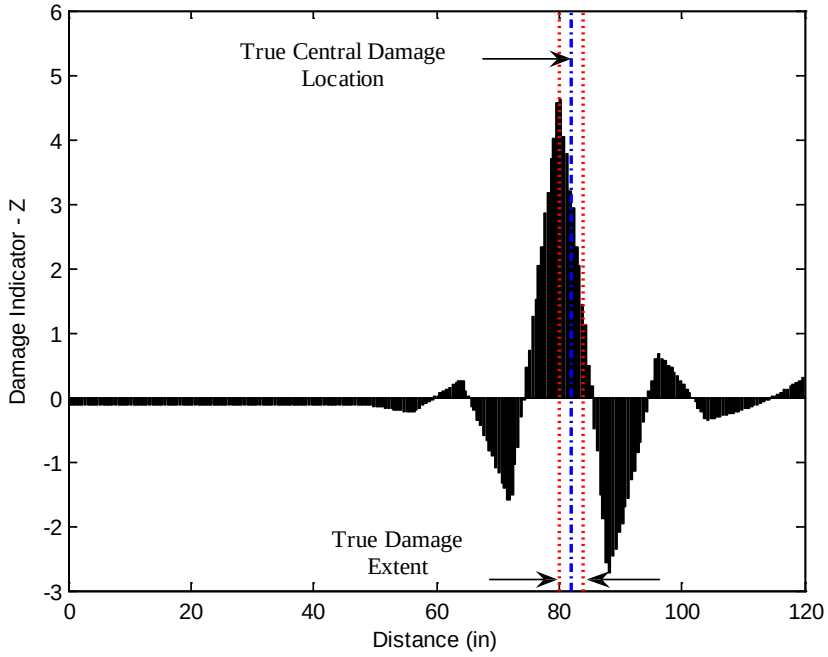

Figure 5.22 Damage Localization Result for Damage Case IB 1 Using EB Pseudo β_j

Table 5.21 Assessment of the Damage Localization Accuracy for Damage Case IB 1 Using EB Pseudo β_j

Damage Central Location (in)		Error (%)	$P(T \subset P)$
True	Predicted		
82.0	80.3	1.4	100%

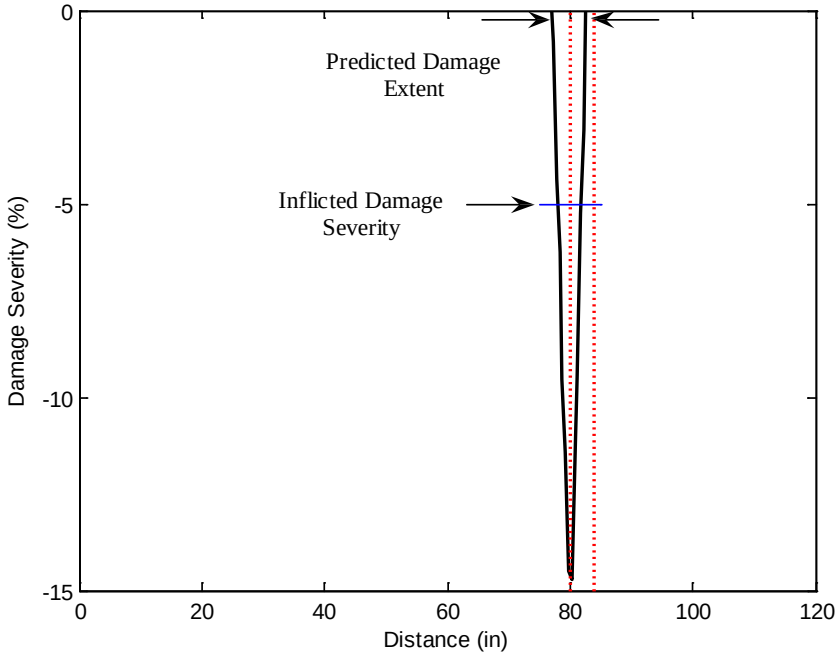

Figure 5.23 Damage Extent and Severity Estimate for Damage Case IB 1 Using EB Pseudo β_j

Table 5.22 Assessment of the Damage Extent and Severity Accuracy for Damage Case IB 1 Using EB Pseudo β_j

Damage Extent (in)		Error	Damage Severity (%)		Error (%)
True	Predicted	(%)	True	Predicted Lower Bound/Upper Bound	
4.0	5.5	-1.3	-5.0	-8.5/-14.5	-70.0/-190.0

Damage Case IB 2

Figures 5.24 and 5.25 depict the damage prediction results for Damage Case IB 2 using the damage indicator EB Pseudo β_j. Tables 5.23 and 5.24 tabulate the performance of the damage detection methodology for the damage case.

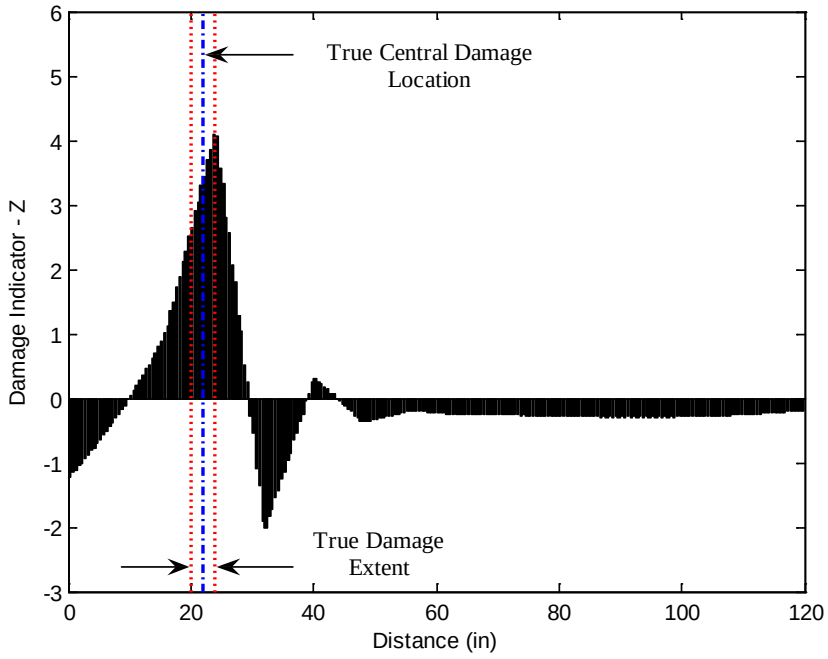

Figure 5.24 Damage Localization Result for Damage Case IB 2 Using EB Pseudo β_j

Table 5.23 Assessment of the Damage Localization Accuracy for Damage Case IB 2 Using EB Pseudo β_j

Damage Central Location (in)		Error (%)	$P(T \subset P)$
True	Predicted		
22.0	23.8	-1.5	100%

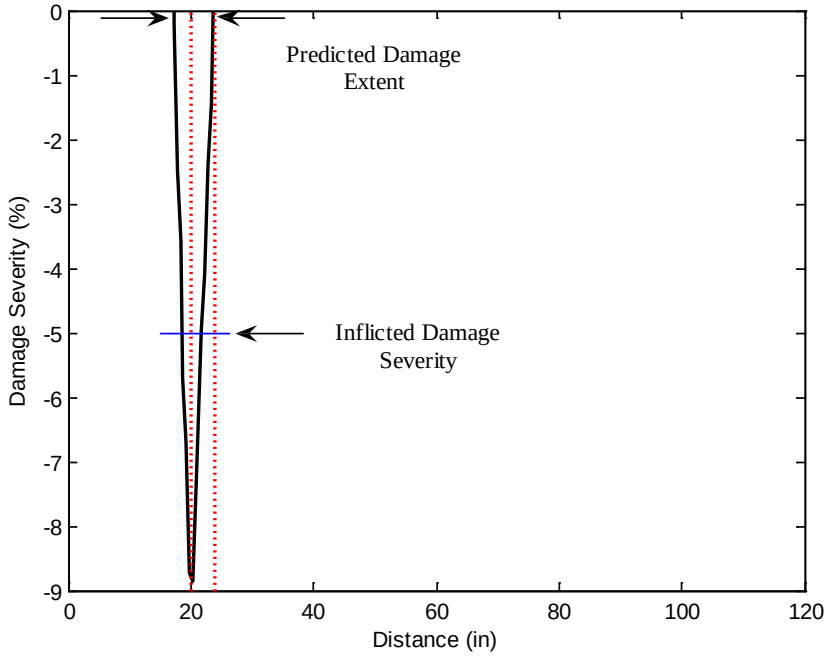

Figure 5.25 Damage Extent and Severity Estimate for Damage Case IB 2 Using EB Pseudo β_j

Table 5.24 Assessment of the Damage Extent and Severity Accuracy for Damage Case IB 2 Using EB Pseudo β_j

Damage Extent (in)		Error	Damage Severity (%)		Error (%)
True	Predicted	(%)	True	Predicted Lower Bound/Upper Bound	
4.0	6.5	-2.1	-5.0	-4.9/-8.8	2.0/-76.0

Damage Case IB 3

Figures 5.26 and 5.27 depict the damage prediction results for Damage Case IB 3 using the damage indicator EB Pseudo β_j. Tables 5.25 and 5.26 tabulate the performance of the damage detection methodology for the damage case.

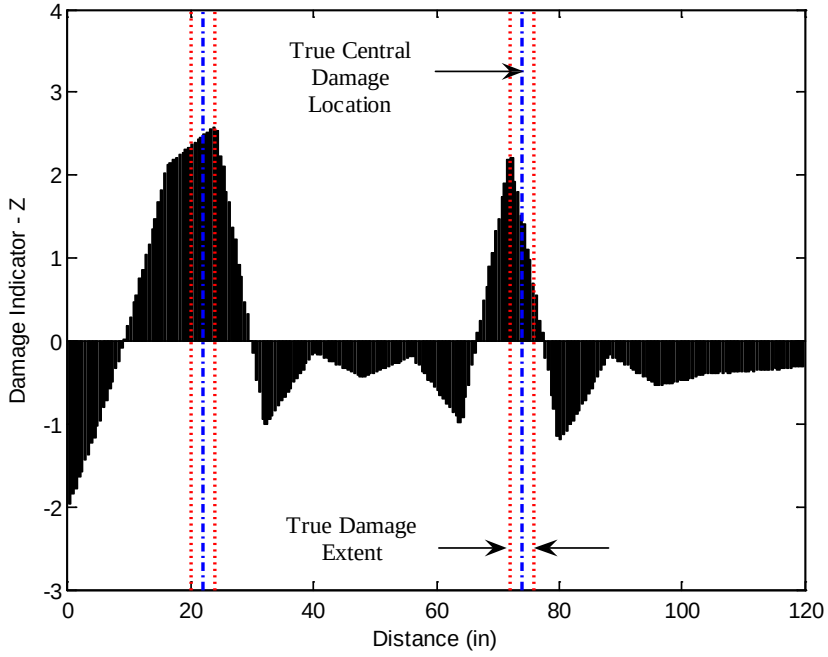

Figure 5.26 Damage Localization Result for Damage Case IB 3 Using EB Pseudo β_j

Table 5.25 Assessment of the Damage Localization Accuracy for Damage Case IB 3 Using EB Pseudo β_j

Damage Central Location (in)		Error (%)	$P(T \subset P)$
True	Predicted		
22.0	23.8	-1.5	100%
74	72.3	1.4	100%

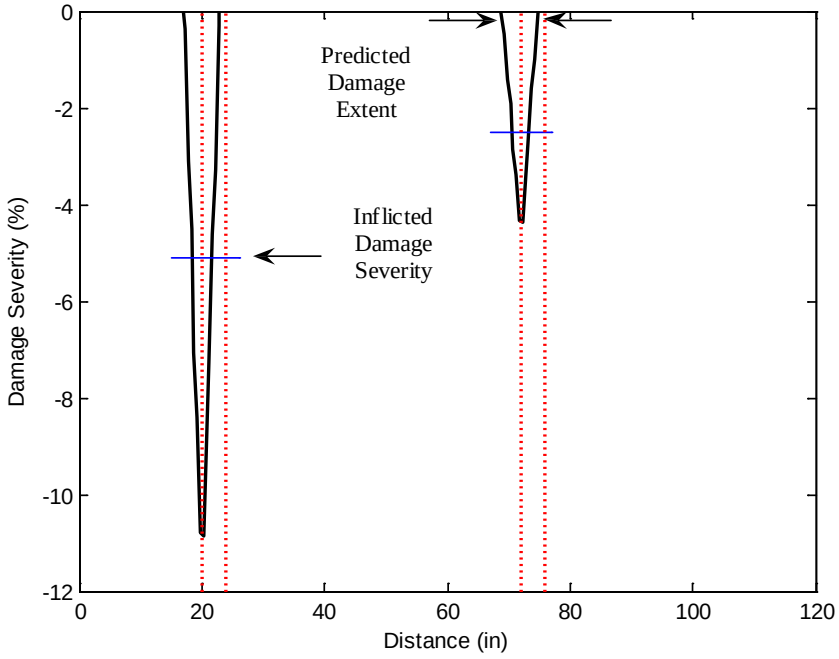

Figure 5.27 Damage Extent and Severity Estimate for Damage Case IB 3 Using EB Pseudo β_j

Table 5.26 Assessment of the Damage Extent and Severity Accuracy for Damage Case IB 3 Using EB Pseudo β_j

Damage Extent (in)		Error (%)	Damage Severity (%)		Error (%)
True	Predicted		True	Predicted Lower Bound/Upper Bound	
4.0	6.0	-1.7	-5.1	-5.9/-10.9	-15.7/-113.7
4.0	6.0	-1.7	-2.5	-2.5/-4.4	0.0/-76.0

Damage Case IB 4

Figures 5.28 and 5.29 depict the damage prediction results for Damage Case IB 4 using the damage indicator EB Pseudo β_j. Tables 5.27 and 5.28 tabulate the performance of the damage detection methodology for the damage case.

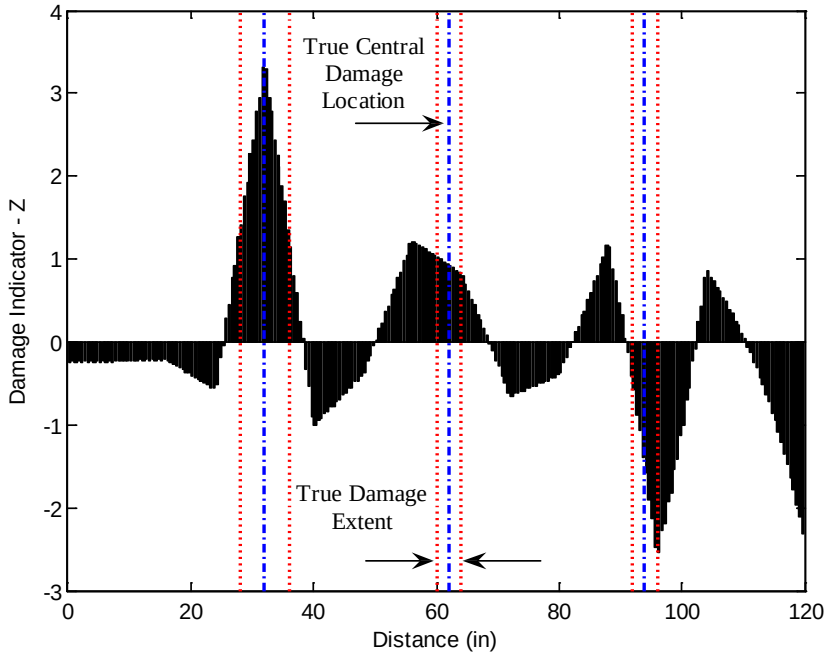

Figure 5.28 Damage Localization Result for Damage Case IB 4 Using EB Pseudo β_j

Table 5.27 Assessment of the Damage Localization Accuracy for Damage Case IB 4 Using EB Pseudo β_j

Damage Central Location (in)		Error (%)	$P(T \subset P)$
True	Predicted		
32.0	31.8	0.2	100%
62.0	56.3	4.8	100%
94.0	No	100.0	0%
FP	87.8	100.0	0%
FP	104.0	100.0	0%

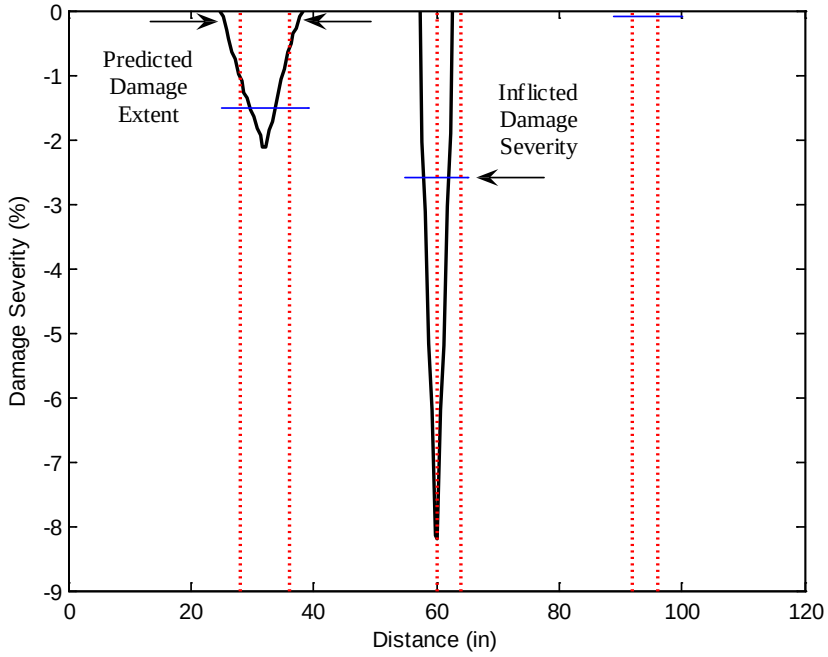

Figure 5.29 Damage Extent and Severity Estimate for Damage Case IB 4 Using EB Pseudo β_j

Table 5.28 Assessment of the Damage Extent and Severity Accuracy for Damage Case IB 4 Using EB Pseudo β_j

Damage Extent (in)		Error	Damage Severity (%)		Error (%)
True	Predicted	(%)	True	Predicted Lower Bound/Upper Bound	
8.0	13.5	-4.6	-1.5	-1.1/-2.1	26.7/-40.0
4.0	5.5	-1.3	-2.6	-5.0/-8.2	-92.3/-215.4
4.0	No	100.0	-0.1	No	100.0

Damage Case IB 5

Figures 5.30 and 5.31 depict the damage prediction results for Damage Case IB 5 using the damage indicator EB Pseudo β_j. Tables 5.29 and 5.30 tabulate the performance of the damage detection methodology for the damage case.

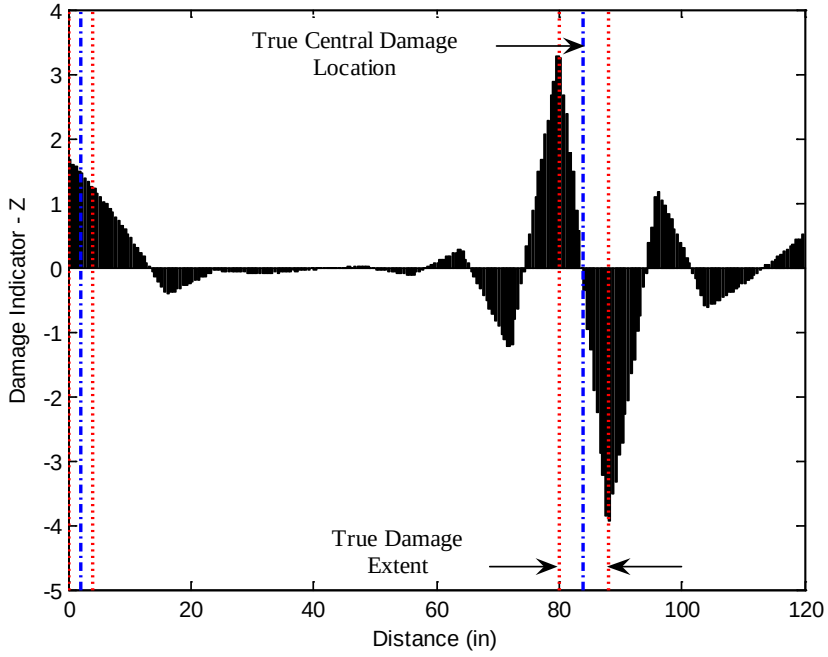

Figure 5.30 Damage Localization Result for Damage Case IB 5 Using EB Pseudo β_j

Table 5.29 Assessment of the Damage Localization Accuracy for Damage Case IB 5 Using EB Pseudo β_j

Damage Central Location (in)		Error (%)	$P(T \subset P)$
True	Predicted		
2.0	0.3	1.4	100%
84.0	79.8	3.5	50%
FP	96.3	100%	0%

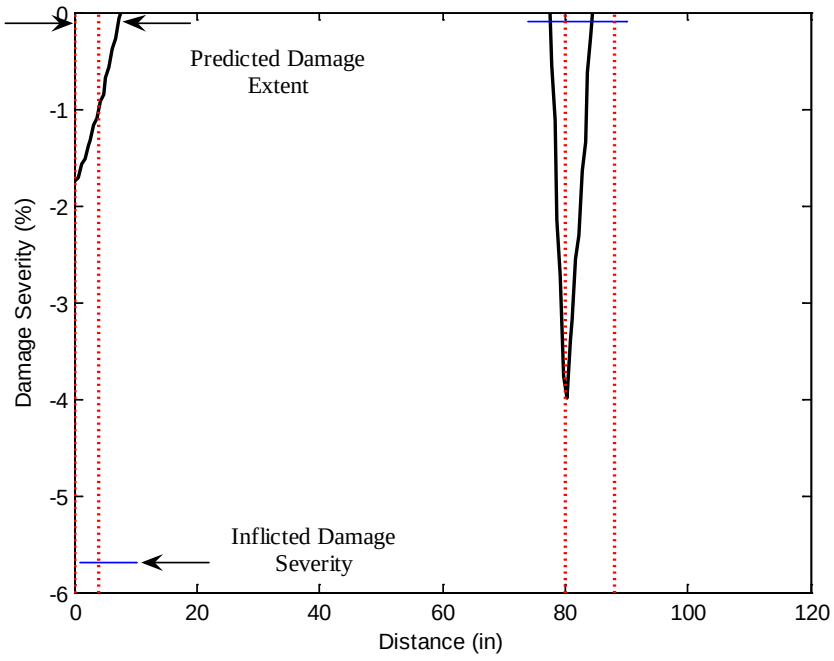

Figure 5.31 Damage Extent and Severity Estimate for Damage Case IB 5 Using EB Pseudo β_j

Table 5.30 Assessment of the Damage Extent and Severity Accuracy for Damage Case IB 5 Using EB Pseudo β_j

Damage Extent (in)		Error (%)	Damage Severity (%)		Error (%)
True	Predicted		True	Predicted Lower Bound/Upper Bound	
4.0	7.8	-3.2	-5.7	-1.0/-1.8	82.5/68.4
8.0	7.0	0.8	-0.1	-2.1/-4.0	-2000/-3900

The Deep Beam

Damage detection results for the deep beam are presented in this subsection. The deformed shapes of the undamaged and damaged beam are approximated using the 13th modal flexibility. Cubic spline functions with 0.3 in. uniform interval are used for interpolation in order to generate a finer sensor layout along the length the beam. This leads to 201 nodal points. Curvatures are estimated by the central difference approximation.

Damage Case DB 1

Figures 5.32 and 5.33 depict the damage prediction results for Damage Case DB 1 using the damage indicator EB Pseudo β_j. Tables 5.31 and 5.32 tabulate the performance of the damage detection methodology for the damage case.

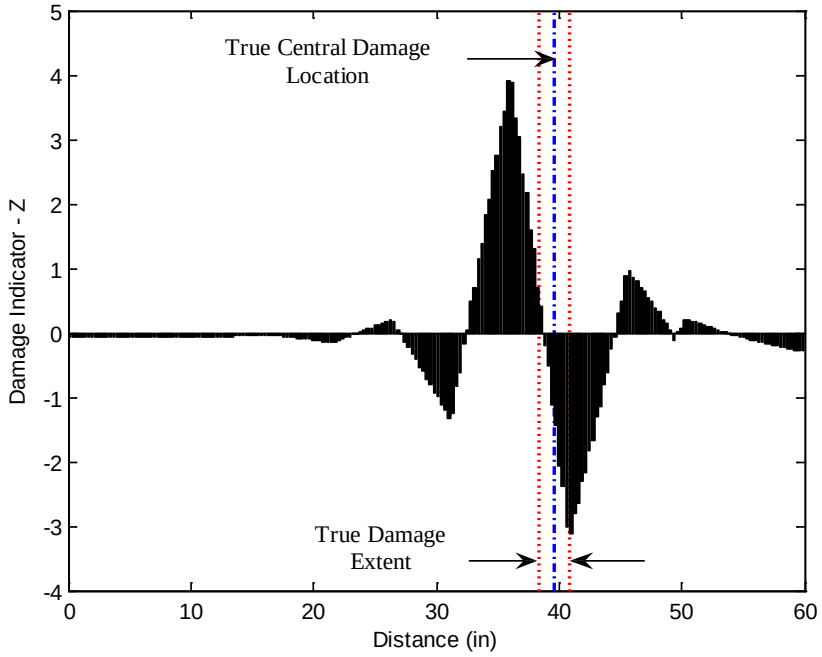

Figure 5.32 Damage Localization Result for Damage Case DB 1 Using EB Pseudo β_j

Table 5.31 Assessment of the Damage Localization Accuracy for Damage Case DB 1 Using EB Pseudo β_j

Damage Central Location (in)		Error (%)	$P(T \subset P)$
True	Predicted		
39.6	35.9	6.2	12.5%
FP	45.8	100.0	0%

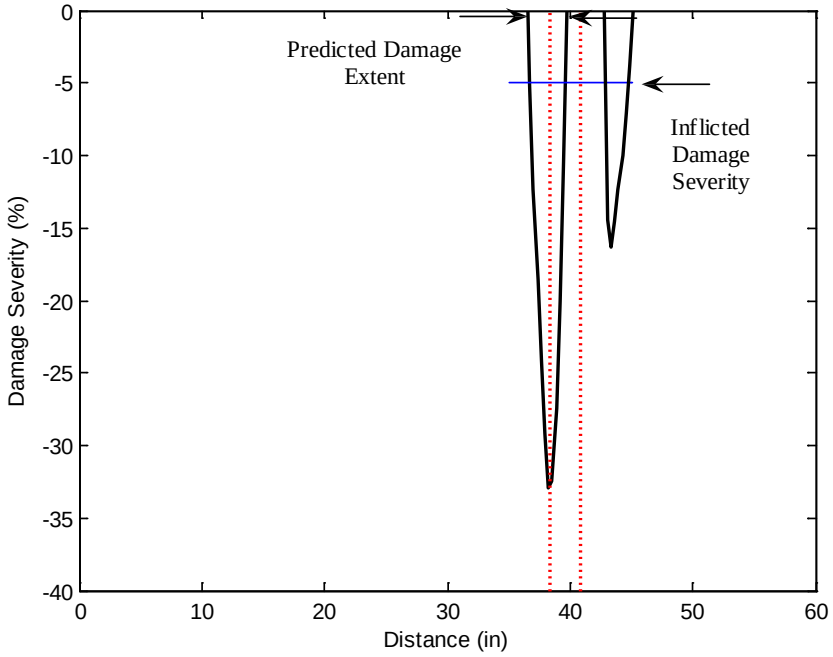

Figure 5.33 Damage Extent and Severity Estimate for Damage Case DB 1 Using EB Pseudo β_j

Table 5.32 Assessment of the Damage Extent and Severity Accuracy for Damage Case DB 1 Using EB Pseudo β_j

Damage Extent (in)		Error (%)	Damage Severity (%)		Error (%)
True	Predicted		True	Predicted Lower Bound/Upper Bound	
2.4	3.3	-1.5	-5.0	-20.9/-34.4	-318/-558
FP	2.4	100.0	FP	-10.1/-16.27	100/100

Damage Case DB 2

Figures 5.34 and 5.35 depict the damage prediction results for Damage Case DB 2 using the damage indicator EB Pseudo β_j. Tables 5.33 and 5.34 tabulate the performance of the damage detection methodology for the damage case.

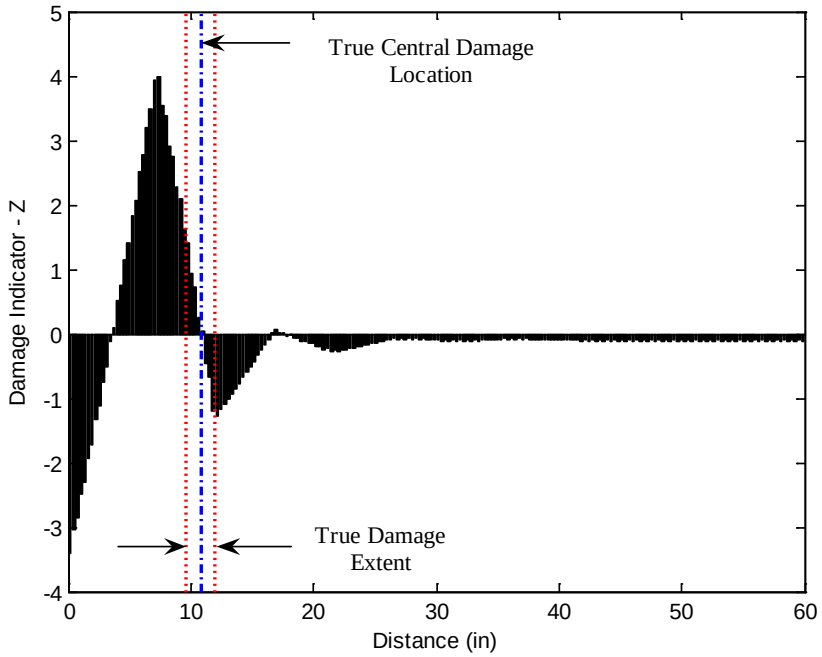

Figure 5.34 Damage Localization Result for Damage Case DB 2 Using EB Pseudo β_j

Table 5.33 Assessment of the Damage Localization Accuracy for Damage Case DB 2 Using EB Pseudo β_j

Damage Central Location (in)		Error (%)	$P(T \subset P)$
True	Predicted		
10.8	7.4	5.7	62.5%

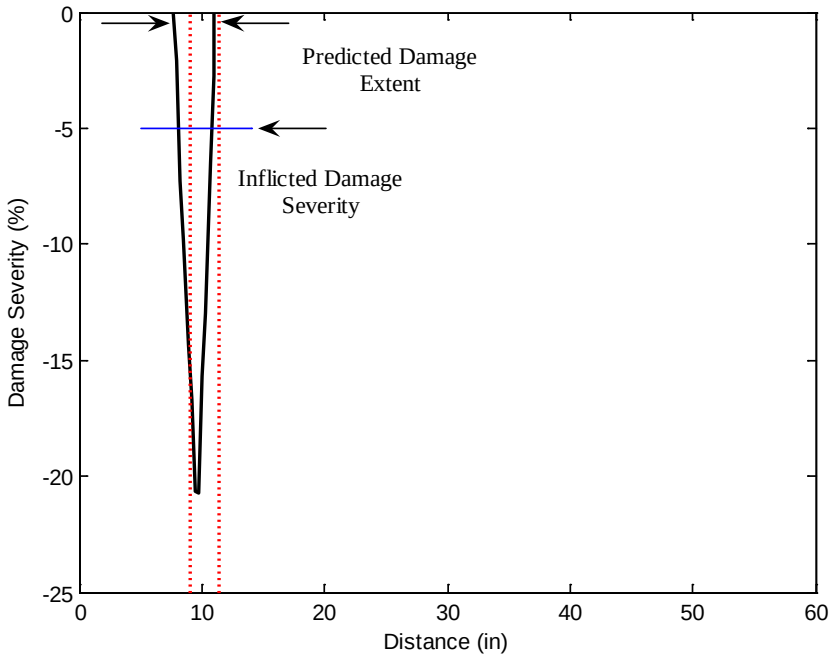

Figure 5.35 Damage Extent and Severity Estimate for Damage Case DB 2 Using EB Pseudo β_j

Table 5.34 Assessment of the Damage Extent and Severity Accuracy for Damage Case DB 2 Using EB Pseudo β_j

Damage Extent (in)		Error	Damage Severity (%)		Error (%)
True	Predicted	(%)	True	Predicted Lower Bound/Upper Bound	
2.4	3.3	-1.5	-5.0	-12.2/-20.7	-144/-314

Damage Case DB 3

Figures 5.36 and 5.37 depict the damage prediction results for Damage Case DB 3 using the damage indicator EB Pseudo β_j. Tables 5.35 and 5.36 tabulate the performance of the damage detection methodology for the damage case.

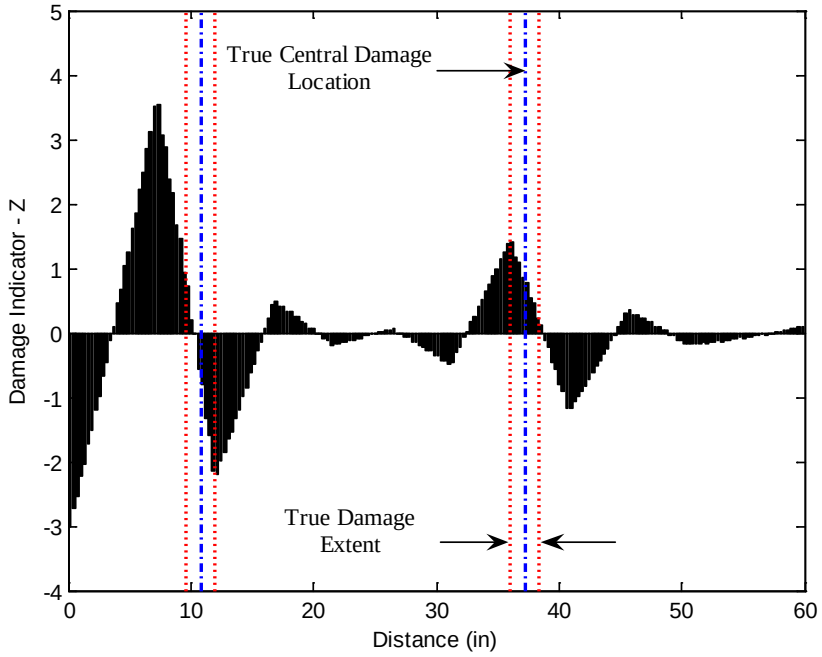

Figure 5.36 Damage Localization Result for Damage Case DB 3 Using EB Pseudo β_j

Table 5.35 Assessment of the Damage Localization Accuracy for Damage Case DB 3 Using EB Pseudo β_j

Damage Central Location (in)		Error (%)	$P(T \subset P)$
True	Predicted		
10.8	7.1	6.2	25%
37.2	35.9	2.2	100%

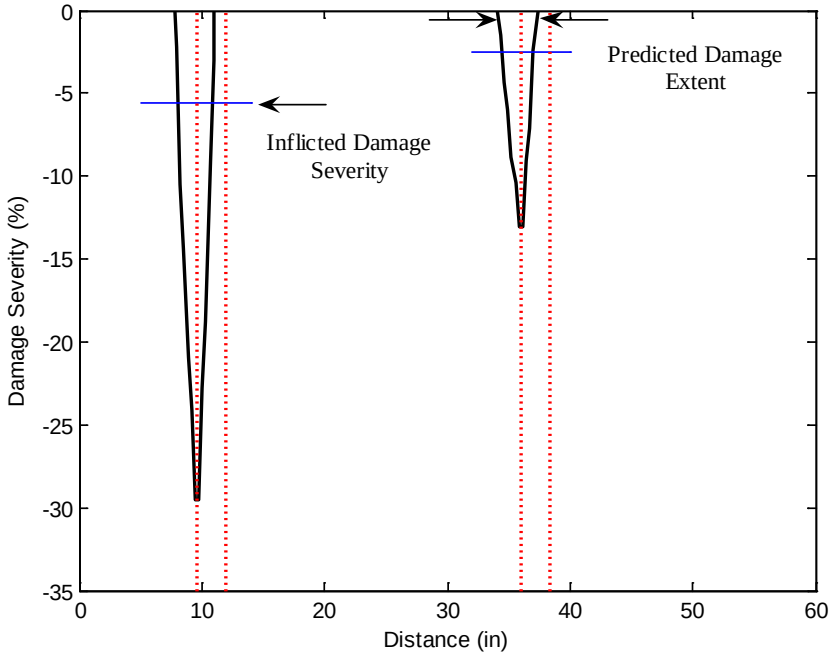

Figure 5.37 Damage Extent and Severity Estimate for Damage Case DB 3 Using EB Pseudo β_j

Table 5.36 Assessment of the Damage Extent and Severity Accuracy for Damage Case DB 3 Using EB Pseudo β_j

Damage Extent (in)		Error	Damage Severity (%)		Error (%)
True	Predicted	(%)	True	Predicted Lower Bound/Upper Bound	
2.4	3.3	-1.5	-5.6	-17.8/-29.6	-218/-429
2.4	3.3	-1.5	-2.5	-7.7/-13.0	-208/-420

Damage Case DB 4

Figures 5.38 and 5.39 depict the damage prediction results for Damage Case DB 4 using the damage indicator EB Pseudo β_j. Tables 5.37 and 5.38 tabulate the performance of the damage detection methodology for the damage case.

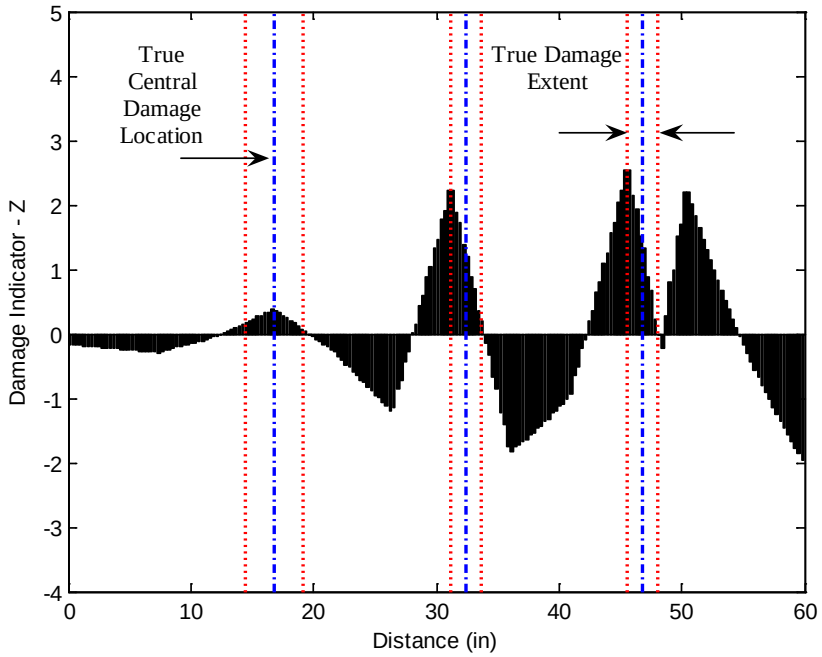

Figure 5.38 Damage Localization Result for Damage Case DB 4 Using EB Pseudo β_j

Table 5.37 Assessment of the Damage Localization Accuracy for Damage Case DB 4 Using EB Pseudo β_j

Damage Central Location (in)		Error (%)	$P(T \subset P)$
True	Predicted		
16.8	16.7	0.2	100%
32.4	31.1	2.2	100%
46.8	45.5	2.2	100%
FP	50.3	100.0	0%

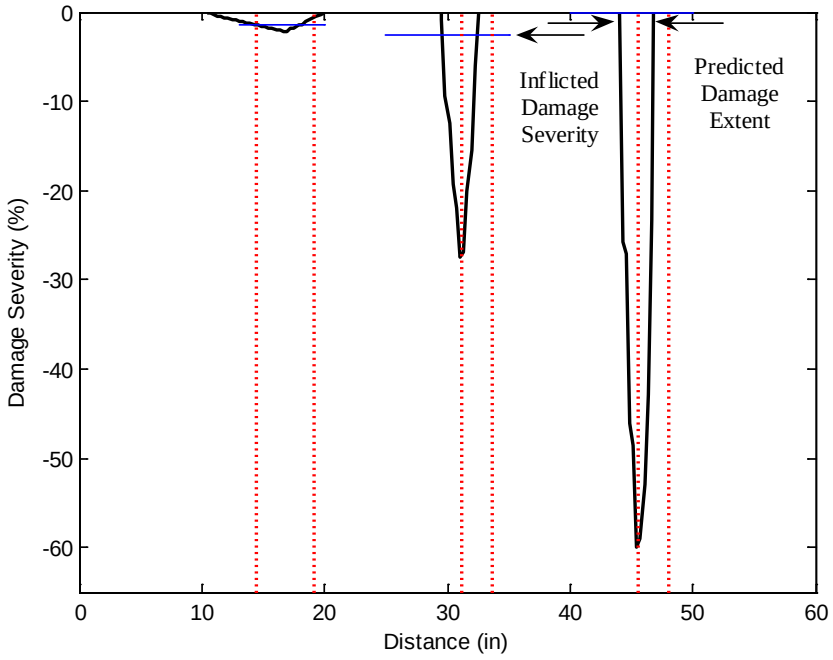

Figure 5.39 Damage Extent and Severity Estimate for Damage Case DB 4 Using EB Pseudo β_j

Table 5.38 Assessment of the Damage Extent and Severity Accuracy for Damage Case DB 4 Using EB Pseudo β_j

Damage Extent (in)		Error (%)	Damage Severity (%)		Error (%)
True	Predicted		True	Predicted Lower Bound/Upper Bound	
4.8	9.3	-7.5	-1.5	-1.2/-2.2	20.0/-46.7
2.4	3.0	-1.0	-2.5	-16.8/-27.5	-572/-1000
2.4	3.0	-1.0	-0.1	-45.9/-59.9	$(-46/-60)10^3$

Damage Case DB 5

Figures 5.40 and 5.41 depict the damage prediction results for Damage Case DB 5 using the damage indicator EB Pseudo β_j. Tables 5.39 and 5.40 tabulate the performance of the damage detection methodology for the damage case.

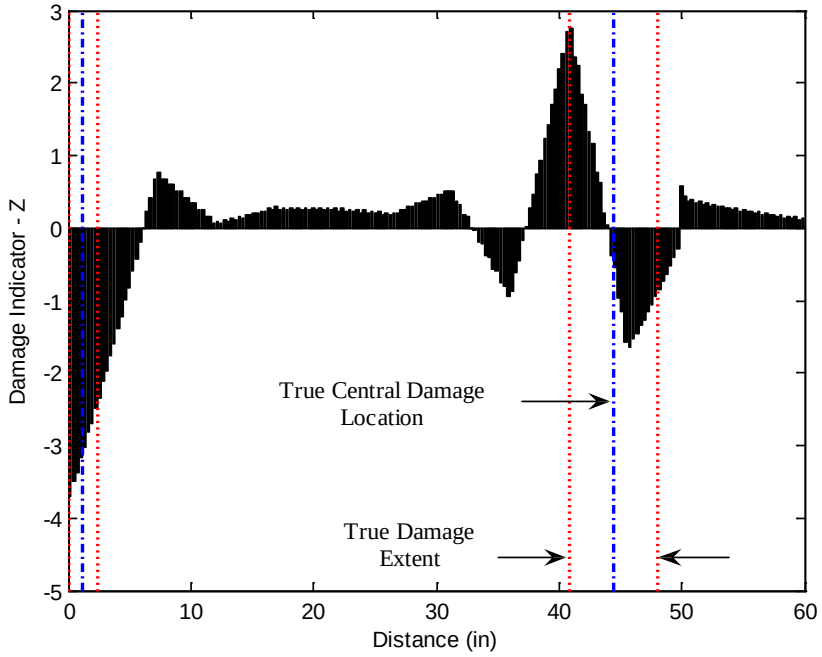

Figure 5.40 Damage Localization Result for Damage Case DB 5 Using EB Pseudo β_j

Table 5.39 Assessment of the Damage Localization Accuracy for Damage Case DB 5 Using EB Pseudo β_j

Damage Central Location (in)		Error (%)	$P(T \subset P)$
True	Predicted		
1.2	No	100.0	0%
44.4	41.0	5.7	45.8%

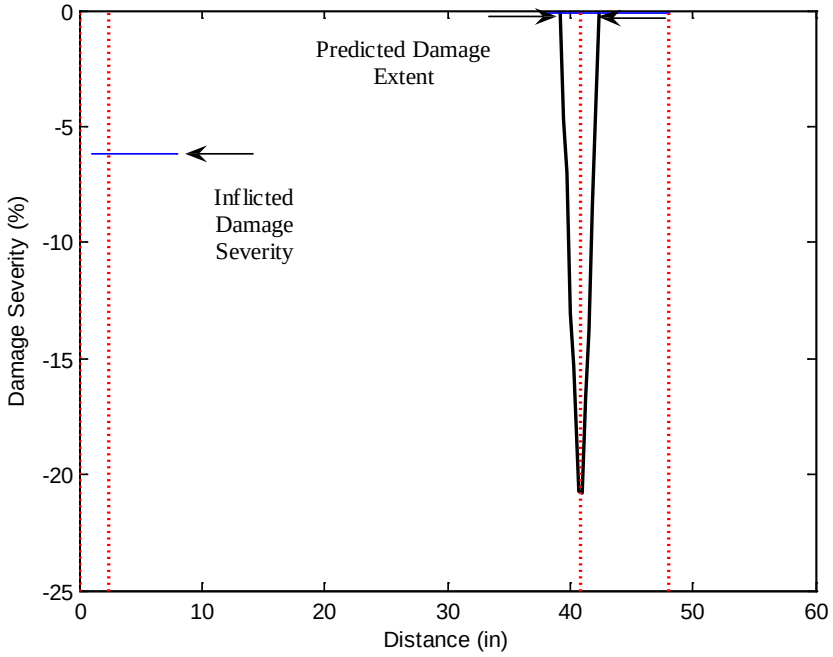

Figure 5.41 Damage Extent and Severity Estimate for Damage Case DB 5 Using EB Pseudo β_j

Table 5.40 Assessment of the Damage Extent and Severity Accuracy for Damage Case DB 5 Using EB Pseudo β_j

Damage Extent (in)		Error	Damage Severity (%)		Error (%)
True	Predicted	(%)	True	Predicted Lower Bound/Upper Bound	
2.4	No	100.0	-6.2	No/No	100/100
7.2	3.0	7.0	-0.1	-12.9/-20.8	$(-13/-21)10^3$

DISCUSSION OF RESULTS

Based on the damage prediction results, the following observations can be made regarding the performance of the EB Pseudo methods:

1. The proposed damage indicators, EB Pseudo β_j and EB Pseudo γ_j, provided almost identical damage prediction results as shown in the case of the slender beam. Due to this reason, only EB Pseudo β_j was utilized for damage detection in the intermediate and deep beams.

2. Damage prediction results presented above are very close to the damage prediction results presented in Chapter IV. This is an expected result since similar assumptions were utilized in formulating the damage indicators of the EB Pseudo and EB Direct methods. The EB Pseudo methods used the equality of the pre-damage and post-damage nodal moments, whereas the EB Direct Method exploited the equality of the moment distribution over an element before and after damage. It is still quite remarkable that the two methods offered such similar damage prediction results, since the final damage indices appear to be entirely independent from one another.

3. The results of the case studies indicated that local inspection is possible with the EB Pseudo Method through reducing the size of the system of linear equations given by either Eq. (5.13) or Eq. (5.26).

4. Utilizing the results of the case studies presented above, similar conclusions can be made to the ones given in Chapter IV regarding the accuracy of damage localization, damage extent prediction, and damage severity estimation. The EB Pseudo methods perform the best for slender beams. Damage localization accuracy is as a function of the beam type (slender, intermediate, or deep) and localization errors increase as the aspect ratio of the beam increases. Similarly, the probability of correctly locating the extent of the damage decreases as the beam becomes less slender. Finally, as expected, the range

and magnitude of the error in the prediction of the accuracy of the damage severity estimate increases as the depth to length ratio of the beam increases. These are direct results of using a damage detection theory that is based on the Euler-Bernoulli assumption.

SUMMARY AND CONCLUSIONS

An explicit damage index methodology based on the stress-displacement relations of the Euler-Bernoulli beam theory was developed. Damage was expressed in terms of local decreases in the flexural stiffness of structural members. Utilizing the concept of discontinuity, these local decreases were represented as singularities in the flexural stiffness distribution of the beam. The performance of the proposed damage detection methodology was evaluated by using the response data collected from the numerical experiments of Chapter III. The proposed methodology produced satisfactory damage localization results considering that it is based on the Euler-Bernoulli beam theory, however failed to provide accurate damage extent and damage severity estimations as the aspect ratio of the beams increased.

CHAPTER VI

DAMAGE INDEX USING THE PRINCIPLE OF INVARIANT STRESS RESULTANTS AND TIMOSHENKO BEAM THEORY

INTRODUCTION

The objective of this chapter is to develop an explicit damage index methodology that is based on the principle of invariant stress resultants and Timoshenko beam theory. Damage will be expressed in terms of local decreases in the bending and shear stiffnesses of structural members. It is shown that the proposed methodology may be used to predict local changes in Poisson's ratio as well. To meet the stated objective, this chapter is divided into four major sections: a section describing the proposed methodology; a section describing specific structural response parameters utilized in damage detection; a section evaluating the performance of the methodology using the numerical experiments introduced in Chapter III; and a section discussing the outcomes of the performed case studies.

PROPOSED METHODOLOGY

Assume that a local decrease in the stiffness of a beam-type structure may be expressed in terms of a decrease in the bending and shear stiffnesses of its sub-element(s). The problem here is to identify the location of the damaged sub-elements within the beam and quantify the amount of stiffness degradation inflicted at each damaged region. For a beam that is comprised of NE sub-elements and NN nodes (as depicted in Figure 6.1 & Figure 6.2), the pristine and damaged flexural stiffnesses of the j^{th} element may be represented by EI_j and EI_j^*, respectively. Similarly, the pristine and damaged shear stiffnesses of the j^{th} element may be represented by GA_j and GA_j^*, respectively. Using basic principles from solid mechanics, the following approach is taken to address the stated problem.

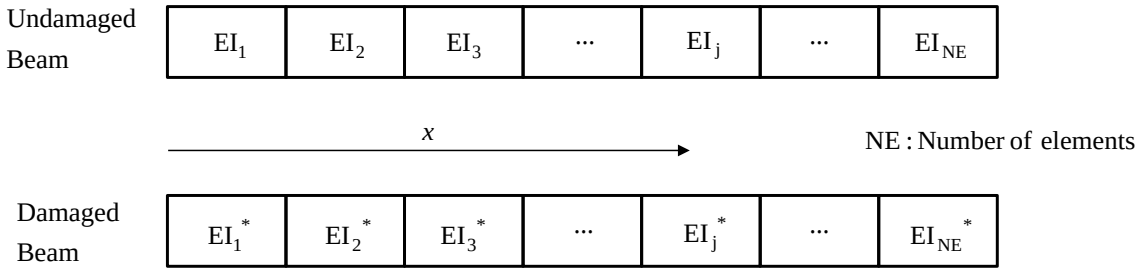

Figure 6.1 Damage Detection Model Utilized to Predict the Changes in Flexural Stiffness Distribution via the Principle of Invariant Stress Resultants and the Timoshenko Beam Theory

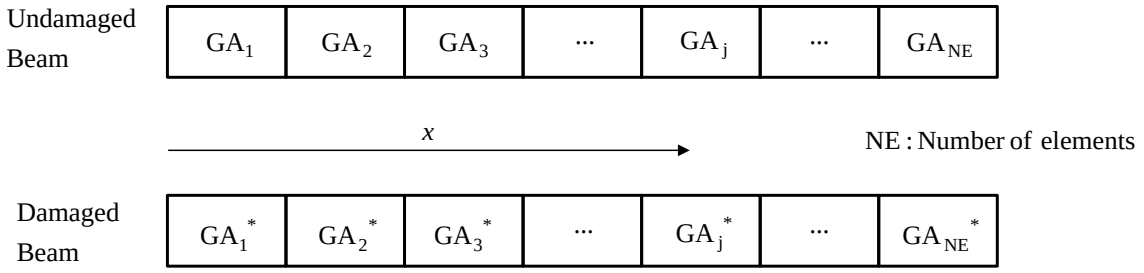

Figure 6.2 Damage Detection Model Utilized to Predict the Changes in Shear Stiffness Distribution via the Principle of Invariant Stress Resultants and the Timoshenko Beam Theory

Assuming that the internal force distribution in the beam is not affected by the inflicted damage, the following conditions hold for the bending moment and shear force along the length of the beam:

$$M(x) = M(x)^{*} \tag{6.1}$$

$$V(x) = V(x)^{*} \tag{6.2}$$

where the asterisks in Eq. (6.1) and Eq. (6.2) represent bending moment and shear force distribution in the damaged beam.

Integrating the moment distribution over the j^{th} element using Eq. (6.1) leads to

$$\int_{j} M(x)\, dx = \int_{j} M^{*}(x)\, dx \tag{6.3}$$

Utilizing the fundamental relationship between the first derivative of the rotation and bending moment as given by the Timoshenko beam theory (Eq. (2.20)), following result may be obtained from Eq. (6.3):

$$\int_{j} EI_{j} \frac{d\phi(x)}{dx}\, dx = \int_{j} EI_{j}^{*} \frac{d\phi^{*}(x)}{dx}\, dx \tag{6.4}$$

Eq. (6.4) yields the ratio of the flexural stiffnesses before and after damage assuming that the pristine and damaged flexural stiffnesses, EI_j and EI_j^{*}, attain constant values over the j^{th} element. This damage indicator is represented by β_j^{M}.

$$\beta_j^{M} = \frac{EI_j}{EI_j^{*}} = \frac{\int_{j} \frac{d\phi^{*}(x)}{dx}\, dx}{\int_{j} \frac{d\phi(x)}{dx}\, dx} \tag{6.5}$$

Note that the damage indicator, β_j^{M}, given above is greater than unity in regions where flexural stiffness degradation has occurred. This damage indicator is designated as "the TB Direct β_j^{M}" for identification purposes.

The severity of the inflicted damage for localized damaged regions may be expressed in terms of the pristine and damaged flexural stiffnesses:

$$\alpha_j = \frac{\Delta EI_j}{EI_j} = \frac{EI_j^{*} - EI_j}{EI_j} \tag{6.6}$$

which in turn can be written in terms of the damage indicator β_j^{M} given in Eq. (6.5):

$$\alpha_j^{M} = \frac{EI_j^{*}}{EI_j} - 1 = \frac{1}{\beta_j^{M}} - 1 \tag{6.7}$$

Integrating the shear force distribution over the j^{th} element using Eq. (6.2) leads to

$$\int_j V(x)\,dx = \int_j V^{*}(x)\,dx \tag{6.8}$$

According to Timoshenko beam theory, shear force may be written in terms of the shear stiffness, the shear correction factor, the rotation of the cross section, and the derivative of the transverse deflection. Utilizing this relationship, Eq. (6.8) may be written as:

$$\int_j GA_j K_s\left(\phi(x) + \frac{dw(x)}{dx}\right)dx = \int_j GA_j^{*} K_s\left(\phi^{*}(x) + \frac{dw^{*}(x)}{dx}\right)dx \tag{6.9}$$

Eq. (6.9) yields the ratio of the shear stiffnesses before and after damage assuming that the pristine and damaged shear stiffnesses, GA_j and GA_j^{*}, attain constant values over the j^{th} element. This damage indicator is designated as "the TB Direct β_j^{V}" for identification purposes.

$$\beta_j^{V} = \frac{GA_j}{GA_j^{*}} = \frac{\int_j \left(\phi^{*}(x) + \frac{dw^{*}(x)}{dx} \right) dx}{\int_j \left(\phi(x) + \frac{dw(x)}{dx} \right) dx} \tag{6.10}$$

The severity of the inflicted damage for localized damaged regions may be expressed in terms of the pristine and damaged shear stiffnesses:

$$\alpha_j = \frac{\Delta GA_j}{GA_j} = \frac{GA_j^{*} - GA_j}{GA_j} \tag{6.11}$$

Consecutively, this can be written in terms of the damage indicator β_j^{V} given in Eq. (6.10):

$$\alpha_j^{V} = \frac{GA_j^{*}}{GA_j} - 1 = \frac{1}{\beta_j^{V}} - 1 \tag{6.12}$$

Damage indices predicting the local changes in the bending and shear stiffnesses, will now be utilized to estimate local changes in Poisson's ratio. In order to accomplish this, the fundamental relationship between the modulus of elasticity and the shear modulus is used:

$$G = \frac{E}{2(1+\nu)} \tag{6.13}$$

where ν is the Poisson's ratio.

Multiplying both sides of Eq. (6.13) by the cross-sectional area A gives:

$$GA = \frac{EA}{2(1+\nu)} \tag{6.14}$$

For the damaged structure, Eq. (6.14) may be written as:

$$GA^* = \frac{EA^*}{2(1+\nu^*)} \tag{6.15}$$

where asterisks represents the damaged material properties.

Radius of gyration (represented by r) may be used to express the cross-sectional area A in terms of the moment of inertia I:

$$A = \frac{I}{r^2} \tag{6.16}$$

Utilizing Eq. (6.16), the right hand side of Eq. (6.14) may be written in terms of the moment of inertia and the radius of gyration:

$$GA = \frac{EI}{2(1+\nu)r^2} \tag{6.17}$$

Similarly, for the damaged structure, following must be true:

$$GA^* = \frac{EI^*}{2(1+\nu^*)r^{*2}} \tag{6.18}$$

Assuming that the radius of gyration is not affected by the inflicted damage (this assumption is true if damage is reflected only as effective changes in modulus, and not the structural geometry), dividing Eq. (6.17) by Eq. (6.18) gives:

$$\frac{GA}{GA^*} = \frac{EI}{EI^*}\frac{(1+\nu^*)}{(1+\nu)} \tag{6.19}$$

The left hand side of Eq. (6.19) is the ratio of shear stiffnesses before and after damage, whereas the right hand side contains the ratio of bending stiffnesses as well as Poisson's

ratio before and after damage. Utilizing damage indicators β^M and β^V given in Eq. (6.5) and Eq. (6.10) respectively, Eq. (6.19) may be written as the following:

$$\beta^V = \beta^M \frac{(1+\nu^*)}{(1+\nu)} \tag{6.20}$$

from which the Poisson's ratio of the damaged structure may be found if β^M, β^V, and ν are known.

$$\nu^* = \beta^V \frac{(1+\nu)}{\beta^M} - 1 \tag{6.21}$$

PROPOSED EXPERIMENTAL ARRANGEMENT AND BASIC MEASUREMENTS REQUIRED BY THEORY

The proposed damage detection methodology utilizes the rotations and vertical displacements of the pristine and damaged beams. The following sensor layouts are used in order to collect the data required for damage detection:

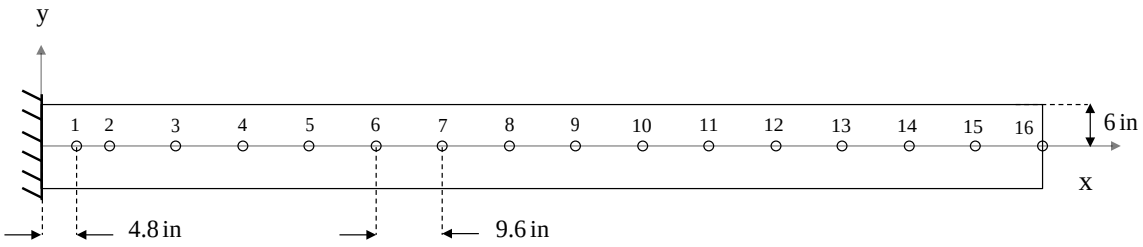

Figure 6.3 Sensor Layout for the Slender Beam

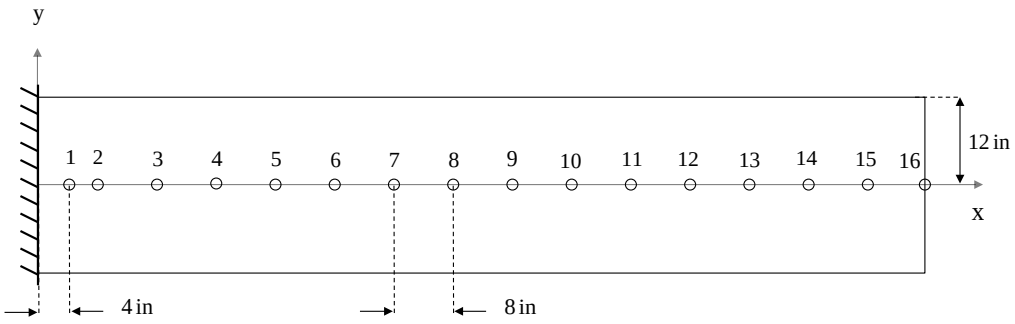

Figure 6.4 Sensor Layout for the Intermediate Beam

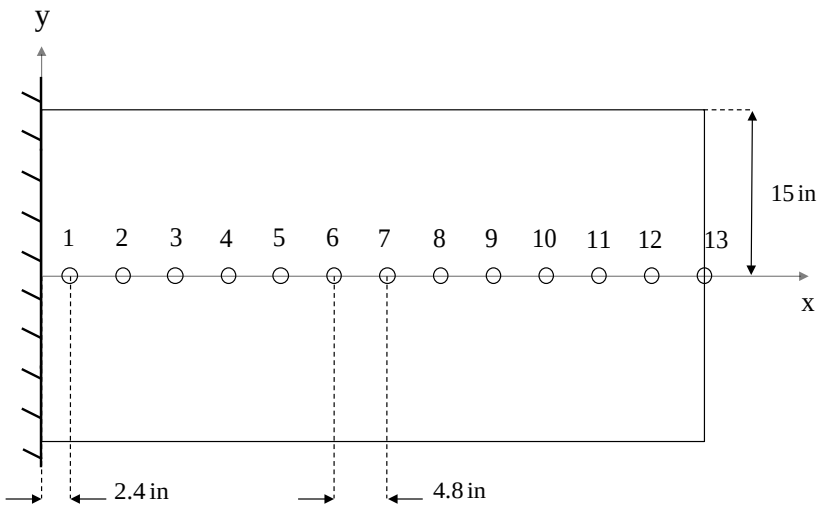

Figure 6.5 Sensor Layout for the Deep Beam

Figures 6.3, 6.4 and 6.5 depict the sensor locations for the slender, intermediate, and deep beam, respectively.

It is assumed that an output-only modal testing is performed for both the undamaged and damaged beams. The outcomes of these tests are the first three natural frequencies and transverse as well as rotational degrees of freedom of the mode shapes measured at the given sensor locations. The modal flexibility matrix may be constructed utilizing the collected modal information. A typical row of the flexibility matrix represents the

deformed shape of the beam under a unit load applied at the corresponding DOF. The deformed shape may include approximations of the vertical displacements as well as the cross-sectional rotations under an external unit load. The vertical displacement profile at the centerline of each test beam may be obtained by utilizing the transverse degree of freedoms of the mode shapes. Similarly, the rotation of the cross-section measured at the centerline of each test beam may be obtained by utilizing the rotational degree of freedoms of the mode shapes. A more concise description of the procedure is provided in Appendix A.

Utilizing the given sensor layout, response data are collected from the numerical experiments presented in Chapter III. It should be noted however; that the improved quadrilateral elements (Q6) utilized to build the finite element model of each test beam contains horizontal and vertical degree of freedoms only. Thus, while translational modal amplitudes are readily available as the vertical DOFs, rotations must be approximated by using the horizontal DOFs of the quadrilaterals. In the case of the slender beam for instance, the rotational modal amplitudes are obtained as follows: Consider the schematic given in Figure 6.6, which shows a fraction of the deflected shape corresponding to the first bending mode of the beam. The rotational modal amplitude at the centerline of the beam may be approximated by:

$$\phi = \frac{u_x^{top} - u_x^{bottom}}{h} \tag{6.22}$$

where u_x^{top} and u_x^{bottom} are the horizontal modal displacements that correspond to the outermost top and bottom points of the beam's cross-section respectively and h denotes the depth of the beam.

The same procedure is followed in order to obtain the rotational modal amplitudes of the intermediate and deep beam as well. Note that Figure 6.6 is not intended to represent an actual schematic of the deflected shape. It is only provided for visualization purposes.

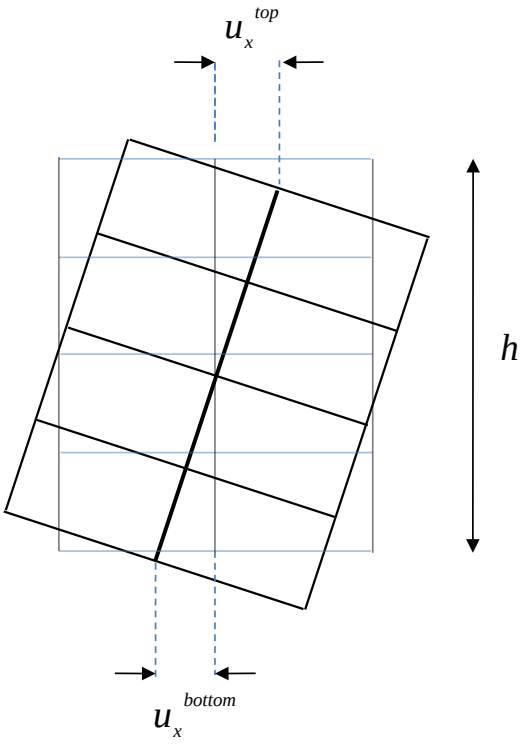

Figure 6.6 Fraction of the Deflected Shape at the First Bending Mode

ASSESSMENT OF THE PROPOSED METHODOLOGIES VIA NUMERICAL EXPERIMENTS

The performance of the proposed damage detection methodology is evaluated in this section. The numerical experiments previously defined in Chapter III are utilized to evaluate the performance of the NDE methodologies. The performance of the methods is based on accurately identifying the location, the extent, and the severity of the damage as before. These items are described in Chapter III. Note that the proposed methodology is limited to one-dimensional Timoshenko Beam Theory. Therefore, possible damage locations may only be identified along the length of the beam and the distribution of

damage through the beam depth is not addressed. The location, the extent, and the severity of damage are predicted according to the procedures described in Chapter IV.

The Slender Beam

The number of degrees of freedom for the modal flexibility is 32 (16 translations and 16 rotations) excluding the support, since the displacement due to a unit load at the support is zero. The vertical displacements and cross-sectional rotations are estimated by the 31st and 32nd modal flexibilities, respectively. Note that these correspond to the deformed shape of the beam due to the unit load applied at the location of sensor 16. Unit load applied prior to a damaged region will not provide any useful information regarding damage since the bending moment and shear force are zero to the right of the point of excitation. For this reason, it is deemed appropriate to utilize the deformed shape of the beam under the unit load applied at the tip.

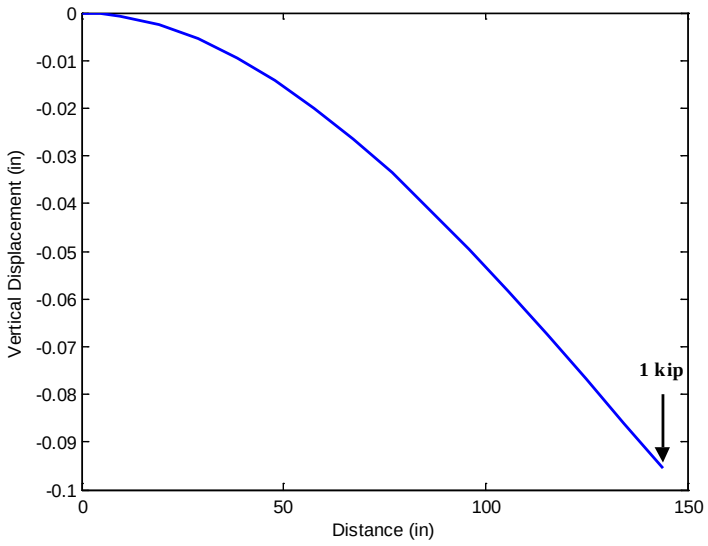

Figure 6.7 Vertical Displacement of the Beam Axis of the Slender Beam Approximated by the 31st Modal Flexibility

The 31st modal flexibility presents an approximation for the vertical displacement of the beam axis by utilizing the transverse degree of freedoms of the mode shapes. Similarly, the 32nd modal flexibility provides an estimate for the rotation of the beam axis by utilizing the rotational degree of freedoms of the mode shapes. Figure 6.7 and Figure 6.8 depict the vertical displacements and rotations of the undamaged slender beam approximated in this manner.

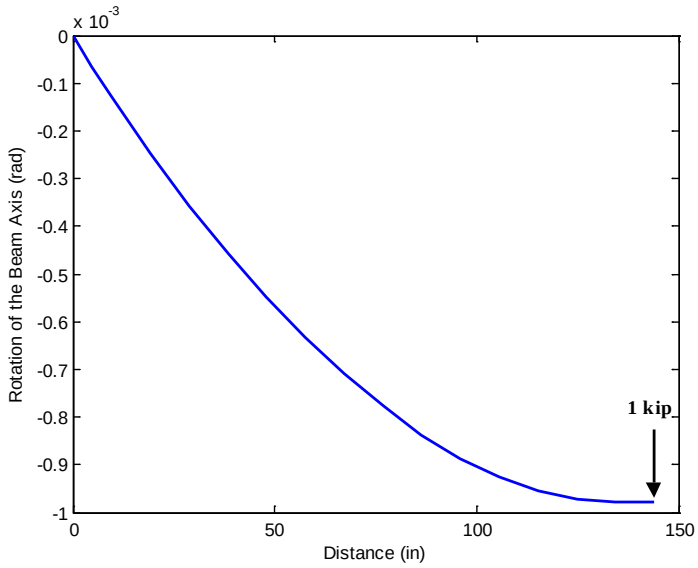

Figure 6.8 Rotation of the Beam Axis of the Slender Beam Approximated by the 32nd Modal Flexibility

Cubic spline interpolation with 0.6 in. uniform intervals is used to generate a finer sensor layout along the length the beam. This process leads to 241 nodal points including the node that corresponds to the clamped support. Central difference approximation of the first derivative is used to compute the first derivative of the rotation required by Eq. (6.5). The trapezoidal rule is applied to compute the integration schemes in these equations.

Damage Case SB 1

Figures 6.9 and 6.10 depict the damage prediction results for Damage Case SB 1 using the damage indicator TB Direct β_j^M. Tables 6.1 and 6.2 tabulate the performance of the damage detection methodology for the damage case. The error between the central location of the true and the predicted damages is computed by Eq. (3.1). Note that $P(T \subset P)$ indicates the probability that the true damaged region is a subset of the predicted damaged regions. Also, note that the damage severity and extent estimates are computed by utilizing an improved sensor resolution, which corresponds to the nodes of the finite element mesh at the centerline of the beam. It is assumed that the extent of damage corresponds to the length of the region where predicted damage severity is less than zero. Detailed descriptions of the tabulated items are provided in Chapter IV.

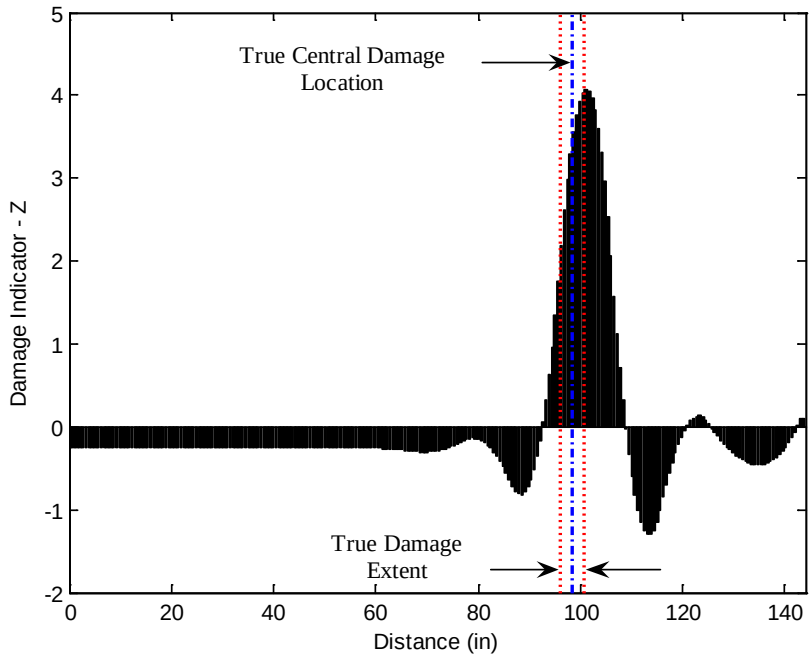

Figure 6.9 Damage Localization Result for Damage Case SB 1 Using TB Direct β_j^M

Table 6.1 Assessment of the Damage Localization Accuracy for Damage Case SB 1 Using TB Direct β_j^M

Damage Central Location (in)		Error (%)	$P(T \subset P)$
True	Predicted		
98.4	101.1	-1.9	100%

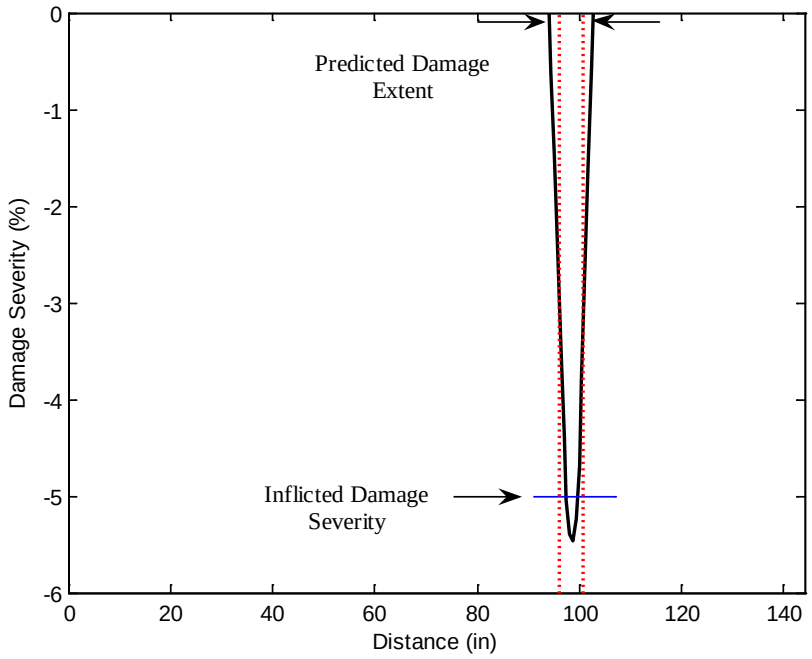

Figure 6.10 Damage Extent and Severity Estimate for Damage Case SB 1 Using TB Direct β_j^M

Table 6.2 Assessment of the Damage Extent and Severity Accuracy for Damage Case SB 1 Using TB Direct β_j^M

Damage Extent (in)		Error (%)	Damage Severity (%)		Error (%)
True	Predicted		True	Predicted Lower Bound/Upper Bound	
4.8	9.0	-2.9	-5.0	-3.4/-5.5	32.0/-10.0

Damage Case SB 2

Figures 6.11 and 6.12 depict the damage prediction results for Damage Case SB 2 using the damage indicator TB Direct β_j^M. Tables 6.3 and 6.4 tabulate the performance of the damage detection methodology for the damage case.

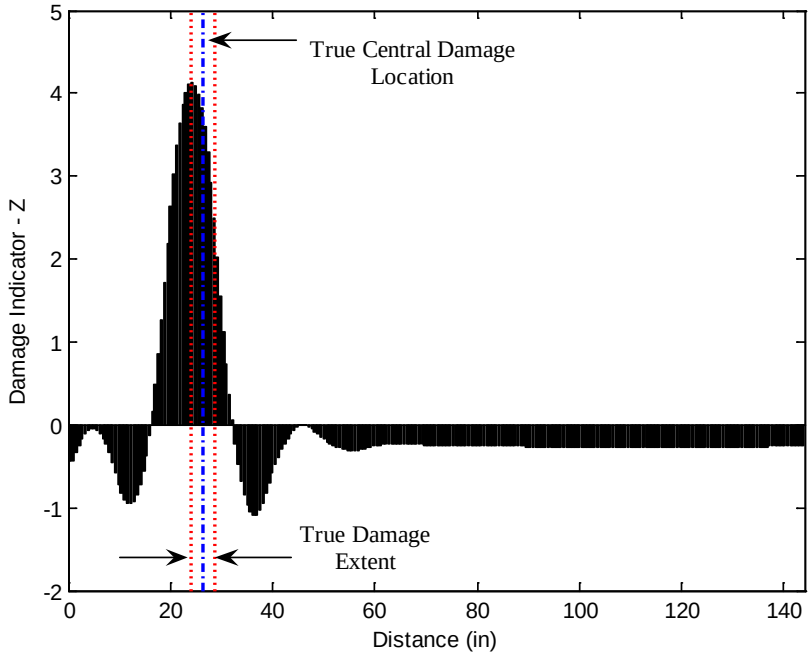

Figure 6.11 Damage Localization Result for Damage Case SB 2 Using TB Direct $\beta_j{}^M$

Table 6.3 Assessment of the Damage Localization Accuracy for Damage Case SB 2 Using TB Direct $\beta_j{}^M$

Damage Central Location (in)		Error (%)	$P(T \subset P)$
True	Predicted		
26.4	24.3	1.5	100%

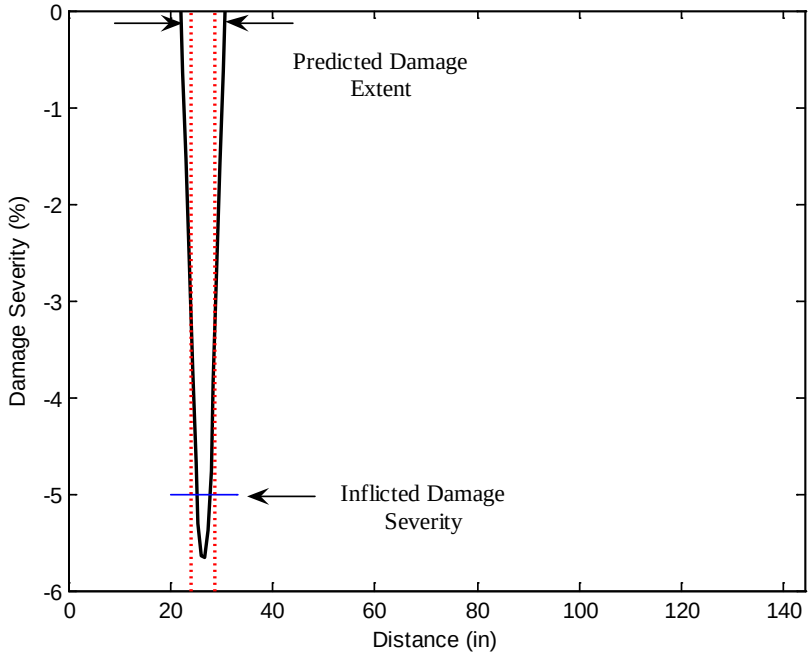

Figure 6.12 Damage Extent and Severity Estimate for Damage Case SB 2 Using TB Direct β_j^M

Table 6.4 Assessment of the Damage Extent and Severity Accuracy for Damage Case SB 2 Using TB Direct β_j^M

Damage Extent (in)		Error	Damage Severity (%)		Error (%)
True	Predicted	(%)	True	Predicted Lower Bound/Upper Bound	
4.8	9.0	-2.9	-5.0	-3.5/-5.7	30.0/-14.0

Damage Case SB 3

Figures 6.13 and 6.14 depict the damage prediction results for Damage Case SB 3 using the damage indicator TB Direct β_j^M. Tables 6.5 and 6.6 tabulate the performance of the damage detection methodology for the damage case.

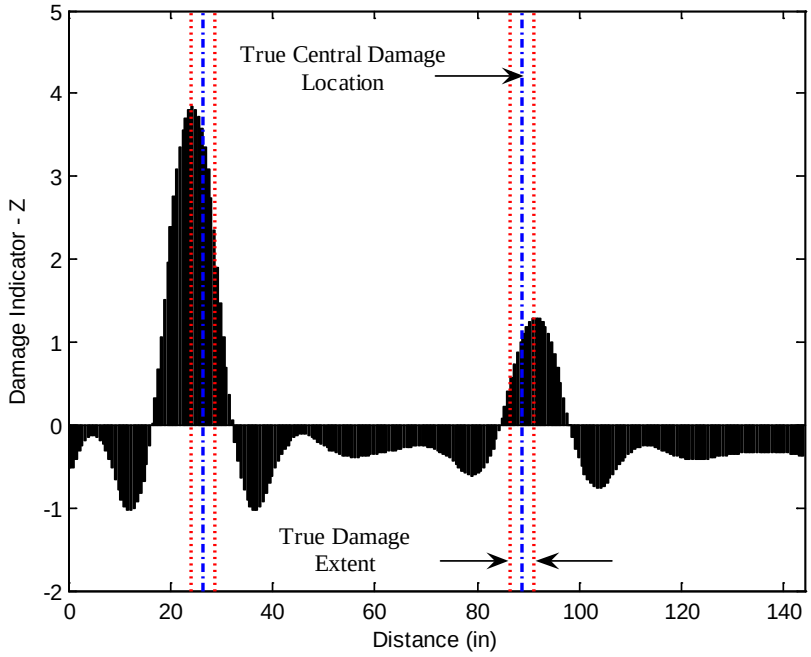

Figure 6.13 Damage Localization Result for Damage Case SB 3 Using TB Direct β_j^M

Table 6.5 Assessment of the Damage Localization Accuracy for Damage Case SB 3 Using TB Direct β_j^M

Damage Central Location (in)		Error (%)	$P(T \subset P)$
True	Predicted		
26.4	24.3	1.5	100%
88.8	91.5	-1.9	100%

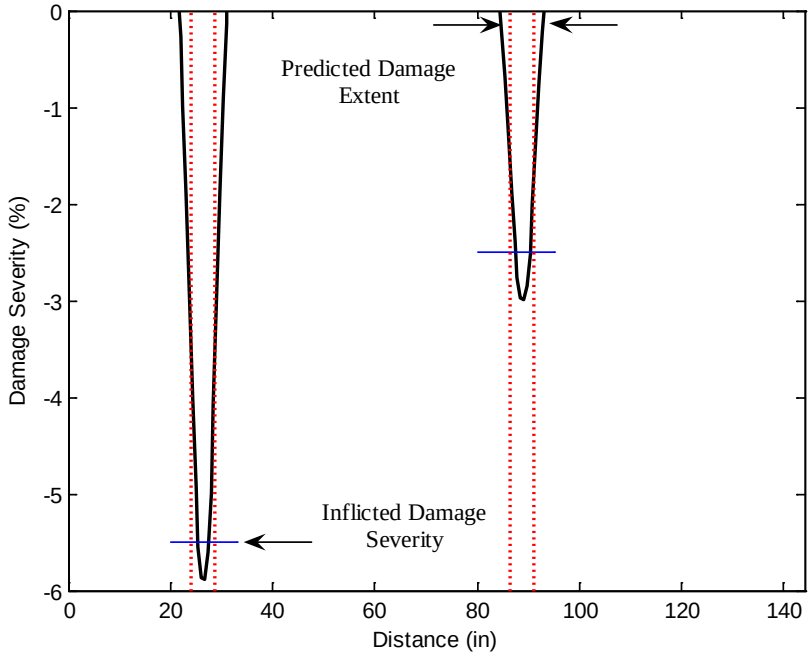

Figure 6.14 Damage Extent and Severity Estimate for Damage Case SB 3 Using TB Direct β_j^M

Table 6.6 Assessment of the Damage Extent and Severity Accuracy for Damage Case SB 3 Using TB Direct β_j^M

Damage Extent (in)		Error (%)	Damage Severity (%)		Error (%)
True	Predicted		True	Predicted Lower Bound/Upper Bound	
4.8	9.6	-3.3	-5.5	-3.3/-5.9	40.0/-7.3
4.8	8.4	-2.5	-2.5	-1.8/-3.0	28.0/-20.0

Damage Case SB 4

Figures 6.15 and 6.16 depict the damage prediction results for Damage Case SB 4 using the damage indicator TB Direct β_j^M. Tables 6.7 and 6.8 tabulate the performance of the damage detection methodology for the damage case.

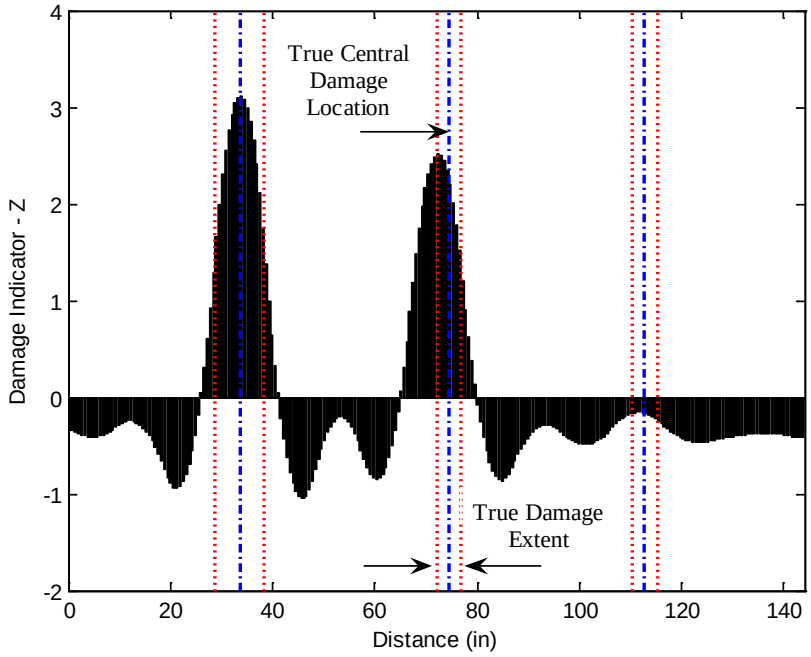

Figure 6.15 Damage Localization Result for Damage Case SB 4 Using TB Direct β_j^M

Table 6.7 Assessment of the Damage Localization Accuracy for Damage Case SB 4 Using TB Direct β_j^M

Damage Central Location (in)		Error (%)	$P(T \subset P)$
True	Predicted		
33.6	33.9	-0.2	100%
74.4	72.3	1.5	100%
112.8	No	100.0	0%

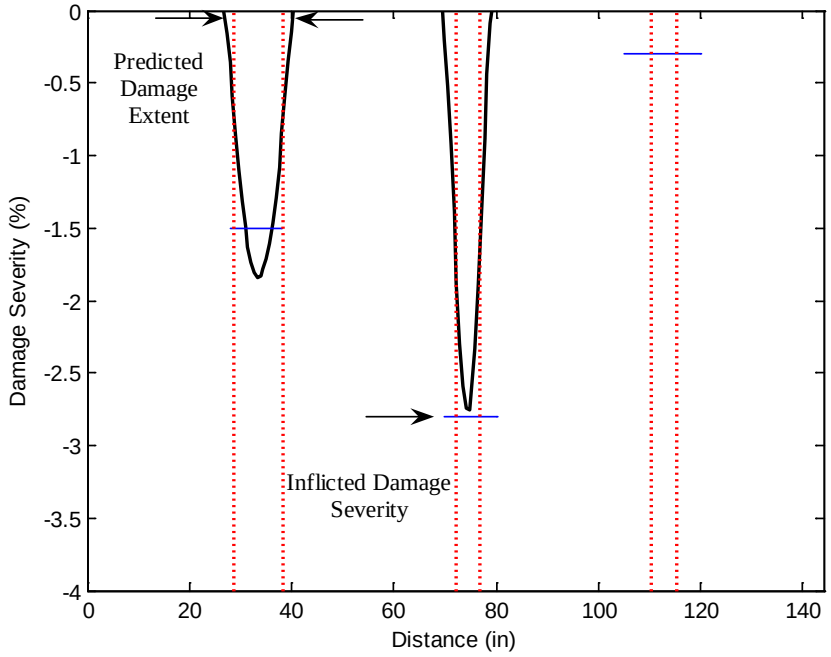

Figure 6.16 Damage Extent and Severity Estimate for Damage Case SB 4 Using TB Direct β_j^M

Table 6.8 Assessment of the Damage Extent and Severity Accuracy for Damage Case SB 4 Using TB Direct β_j^M

Damage Extent (in)		Error	Damage Severity (%)		Error (%)
True	Predicted	(%)	True	Predicted Lower Bound/Upper Bound	
9.6	13.8	-2.9	-1.5	-1.1/-1.8	26.7/-20.0
4.8	9.6	-3.3	-2.8	-1.6/-2.8	42.9/0.0
4.8	No	100.0	-0.3	No/No	100.0/100.0

Damage Case SB 5

Figures 6.17 and 6.18 depict the damage prediction results for Damage Case SB 5 using the damage indicator TB Direct β_j^M. Tables 6.9 and 6.10 tabulate the performance of the damage detection methodology for the damage case.

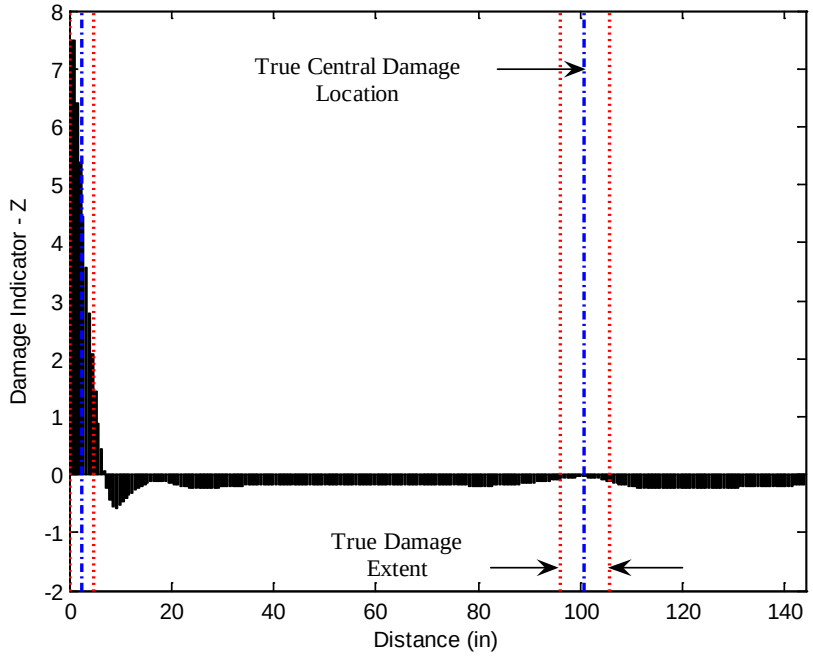

Figure 6.17 Damage Localization Result for Damage Case SB 5 Using TB Direct β_j^M

Table 6.9 Assessment of the Damage Localization Accuracy for Damage Case SB 5 Using TB Direct β_j^M

Damage Central Location (in)		Error (%)	$P(T \subset P)$
True	Predicted		
2.4	0.9	1.0	100%
100.8	No	100.0	0%

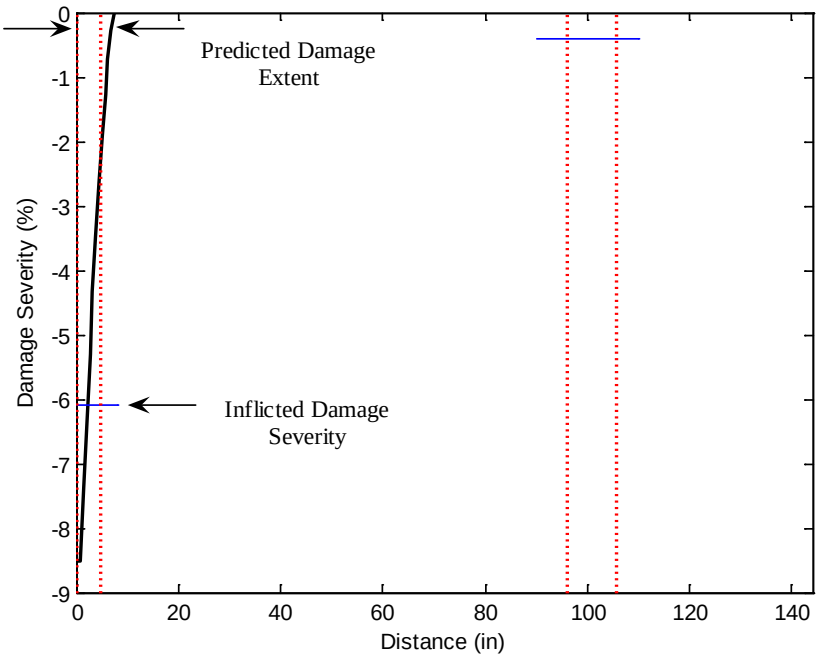

Figure 6.18 Damage Extent and Severity Estimate for Damage Case SB 5 Using TB Direct β_j^M

Table 6.10 Assessment of the Damage Extent and Severity Accuracy for Damage Case SB 5 Using TB Direct $\beta_j{}^M$

Damage Extent (in)		Error (%)	Damage Severity (%)		Error (%)
True	Predicted		True	Predicted Lower Bound/Upper Bound	
4.8	7.5	-1.9	-6.1	-4.3/-8.5	29.5/-39.3
9.6	No	100.0	-0.4	No/No	100/100

The Intermediate Beam

Damage detection results for the intermediate beam are presented in this subsection. As was done in the slender beam, the vertical displacements and cross-sectional rotations are estimated by the modal flexibility. Figure 6.19 and Figure 6.20 depict the vertical displacements and rotations of the undamaged intermediate beam approximated using the modal flexibility.

Cubic spline interpolation with 0.5 in. uniform intervals is used to generate a finer sensor layout along the length the beam. This leads to 241 nodal points including the node that corresponds to the clamped support. Central difference approximation of the first derivative is used to compute the first derivative of the rotation and the vertical displacement required by Eq. (6.5) and Eq. (6.10). The trapezoidal rule is applied to compute the integration schemes in these equations.

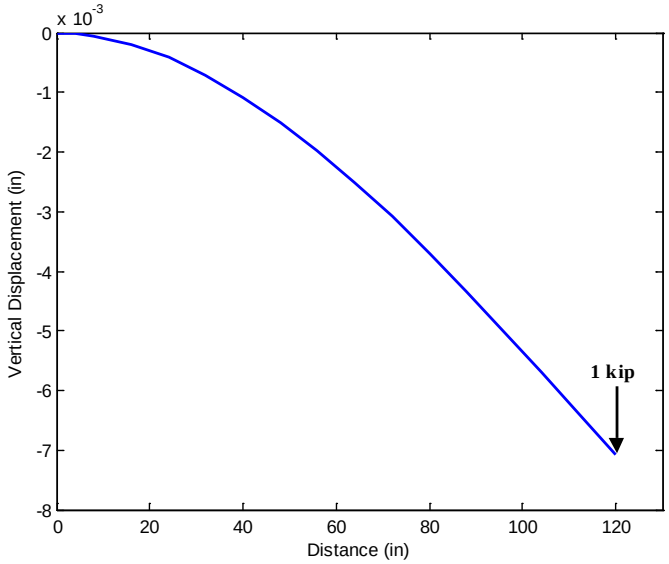

Figure 6.19 Vertical Displacement of the Beam Axis of the Intermediate Beam Approximated by the 31st Modal Flexibility

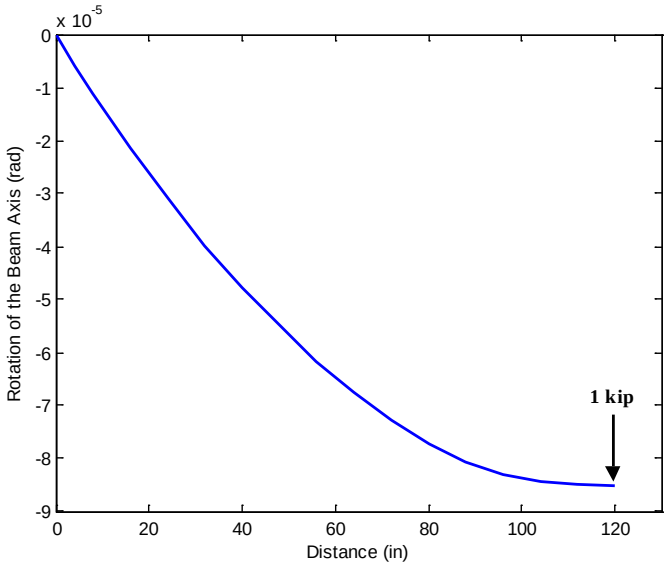

Figure 6.20 Rotation of the Beam Axis of the Intermediate Beam Approximated by the 32nd Modal Flexibility

Damage Case IB 1

Figures 6.21 and 6.22 depict the damage prediction results for Damage Case IB 1 using the damage indicator TB Direct β_j^M. Tables 6.11 and 6.12 tabulate the performance of the damage detection methodology for the damage case.

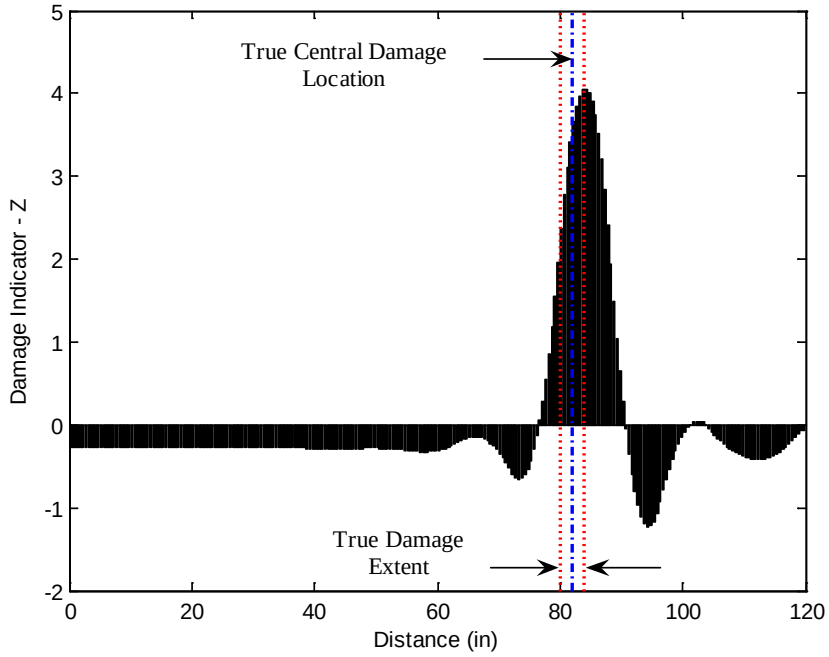

Figure 6.21 Damage Localization Result for Damage Case IB 1 Using TB Direct β_j^M

Table 6.11 Assessment of the Damage Localization Accuracy for Damage Case IB 1 Using TB Direct $\beta_j{}^M$

Damage Central Location (in)		Error (%)	$P(T \subset P)$
True	Predicted		
82.0	84.3	-1.9	100%

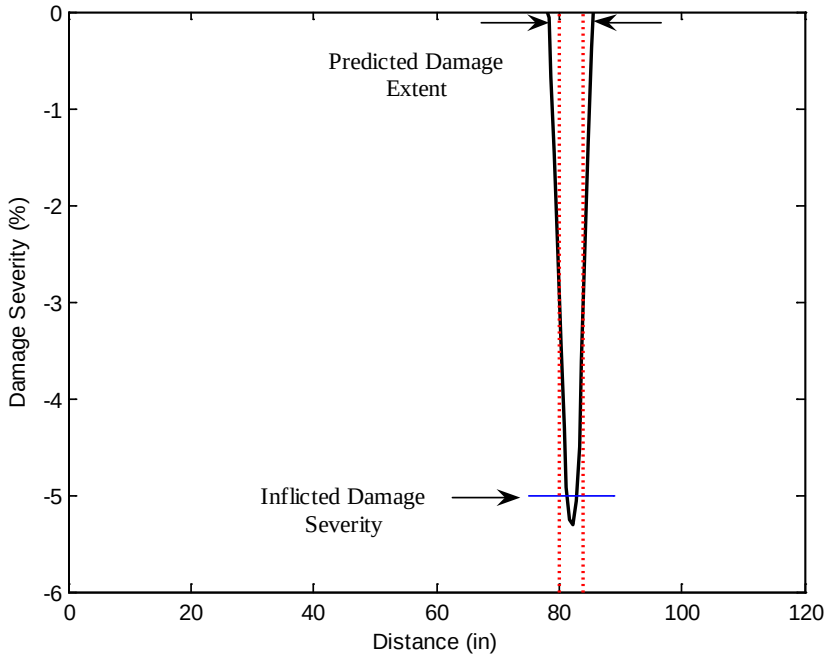

Figure 6.22 Damage Extent and Severity Estimate for Damage Case IB 1 Using TB Direct $\beta_j{}^M$

Table 6.12 Assessment of the Damage Extent and Severity Accuracy for Damage Case IB 1 Using TB Direct β_j^M

Damage Extent (in)		Error (%)	Damage Severity (%)		Error (%)
True	Predicted		True	Predicted Lower Bound/Upper Bound	
4.0	7.5	-2.9	-5.0	-3.1/-5.3	38.0/-6.0

Damage Case IB 2

Figures 6.23 and 6.24 depict the damage prediction results for Damage Case IB 2 using the damage indicator TB Direct β_j^M. Tables 6.13 and 6.14 tabulate the performance of the damage detection methodology for the damage case.

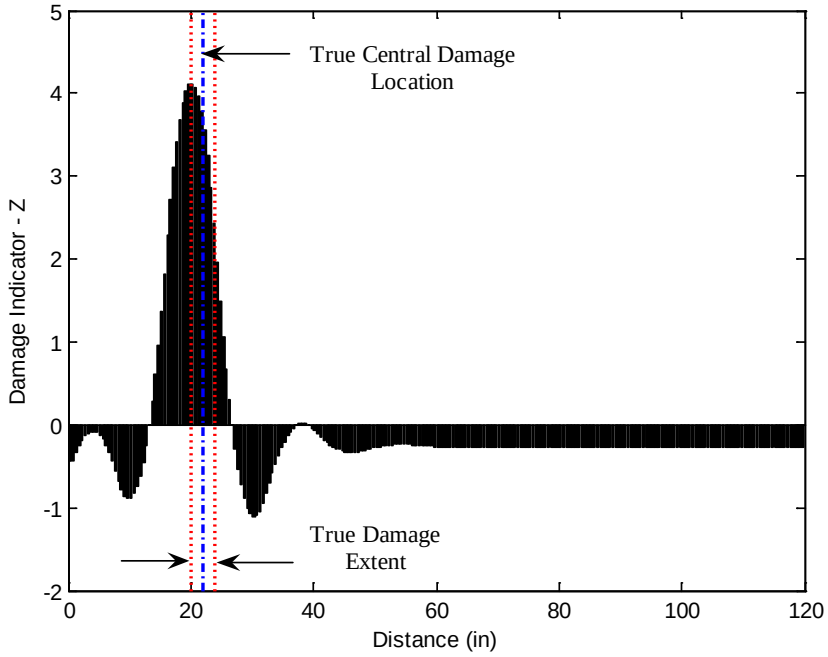

Figure 6.23 Damage Localization Result for Damage Case IB 2 Using TB Direct $\beta_j{}^M$

Table 6.13 Assessment of the Damage Localization Accuracy for Damage Case IB 2 Using TB Direct $\beta_j{}^M$

Damage Central Location (in)		Error (%)	$P(T \subset P)$
True	Predicted		
22.0	20.3	1.4	100%

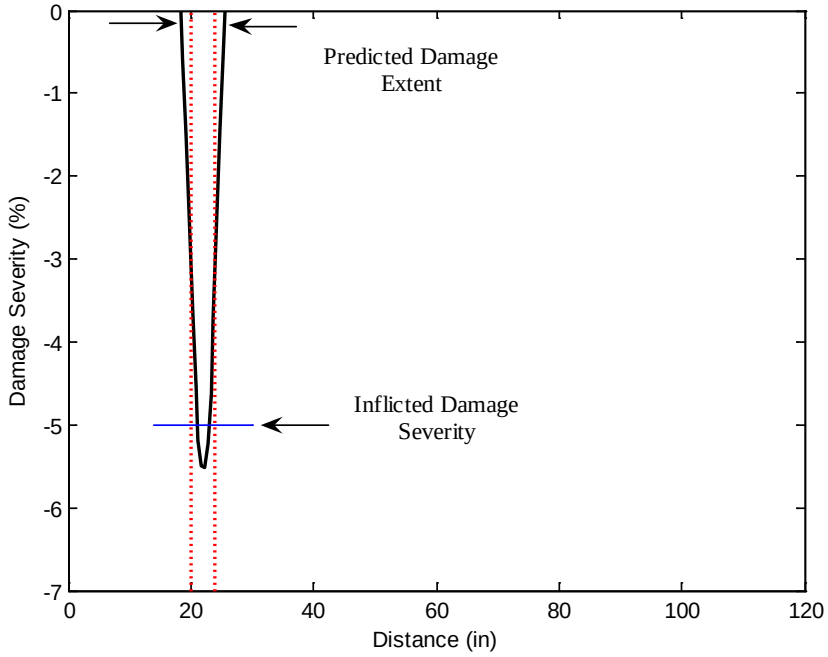

Figure 6.24 Damage Extent and Severity Estimate for Damage Case IB 2 Using TB Direct β_j^M

Table 6.14 Assessment of the Damage Extent and Severity Accuracy for Damage Case IB 2 Using TB Direct β_j^M

Damage Extent (in)		Error	Damage Severity (%)		Error (%)
True	Predicted	(%)	True	Predicted Lower Bound/Upper Bound	
4.0	7.5	-2.9	-5.0	-3.4/-5.5	32.0/-10.0

Damage Case IB 3

Figures 6.25 and 6.26 depict the damage prediction results for Damage Case IB 3 using the damage indicator TB Direct β_j^M. Tables 6.15 and 6.16 tabulate the performance of the damage detection methodology for the damage case.

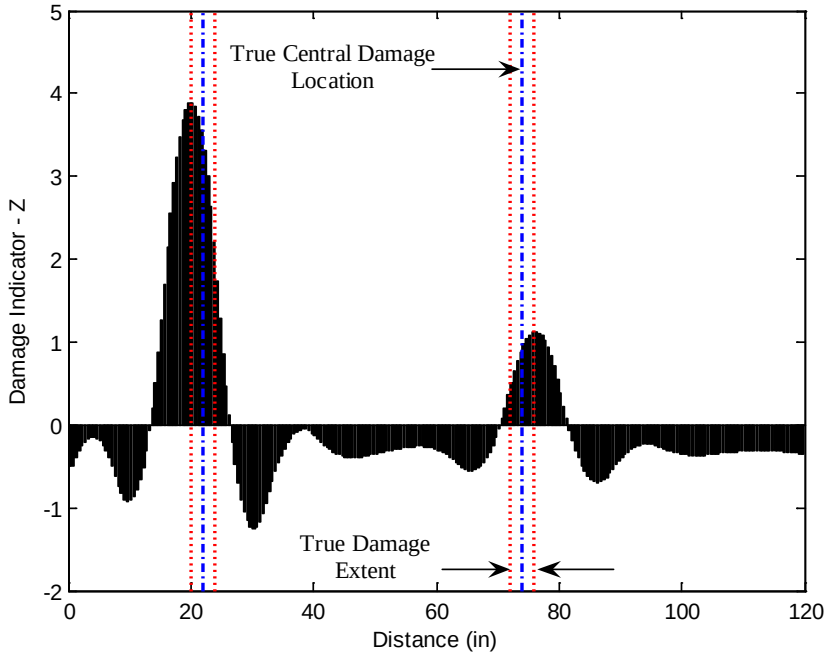

Figure 6.25 Damage Localization Result for Damage Case IB 3 Using TB Direct β_j^M

Table 6.15 Assessment of the Damage Localization Accuracy for Damage Case IB 3 Using TB Direct β_j^M

Damage Central Location (in)		Error (%)	$P(T \subset P)$
True	Predicted		
22.0	20.3	1.4	100%
74.0	76.3	-1.9	100%

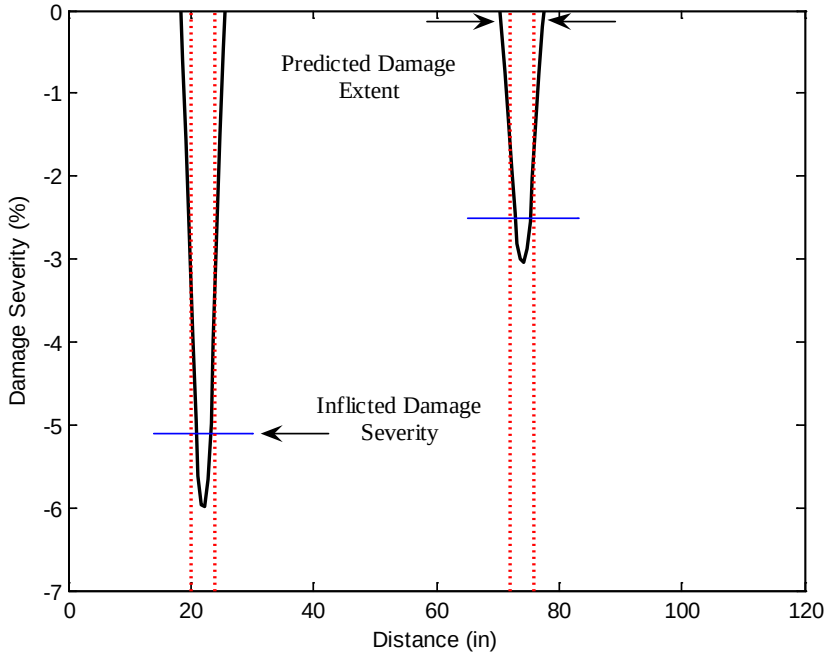

Figure 6.26 Damage Extent and Severity Estimate for Damage Case IB 3 Using TB Direct β_j^M

Table 6.16 Assessment of the Damage Extent and Severity Accuracy for Damage Case IB 3 Using TB Direct β_j^M

Damage Extent (in)		Error (%)	Damage Severity (%)		Error (%)
True	Predicted		True	Predicted Lower Bound/Upper Bound	
4.0	7.5	-2.9	-5.1	-3.7/-6.0	27.5/-17.6
4.0	7.5	-2.9	-2.5	-1.8/-3.0	28.0/-20.0

Figures 6.27 and 6.28 depict the damage prediction results for Damage Case IB 3 using the damage indicator TB Direct β_j^V. Tables 6.17 and 6.18 tabulate the performance of the damage detection methodology for the damage case.

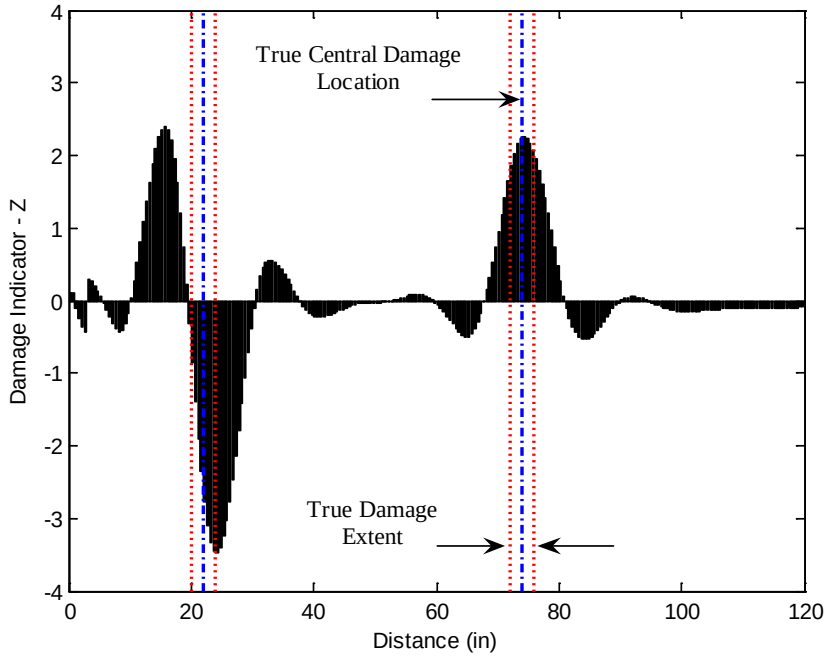

Figure 6.27 Damage Localization Result for Damage Case IB 3 Using TB Direct β_j^V

Table 6.17 Assessment of the Damage Localization Accuracy for Damage Case IB 3 Using TB Direct β_j^V

Damage Central Location (in)		Error (%)	$P(T \subset P)$
True	Predicted		
22.0	15.8	5.2	0%
FP	32.8	100.0	0%
74.0	74.3	-0.2	100%

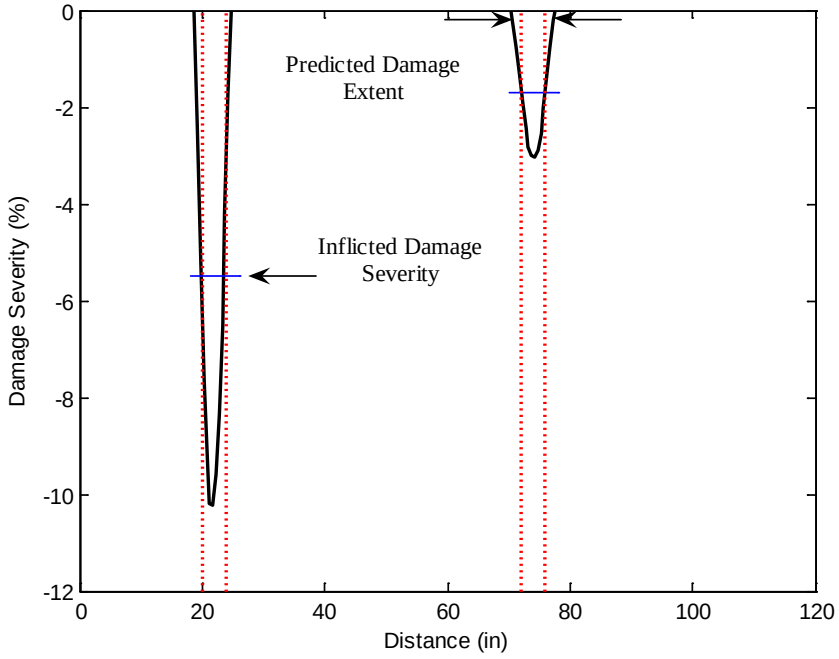

Figure 6.28 Damage Extent and Severity Estimate for Damage Case IB 3 Using TB Direct β_j^V

Table 6.18 Assessment of the Damage Extent and Severity Accuracy for Damage Case IB 3 Using TB Direct β_j^V

Damage Extent (in)		Error	Damage Severity (%)		Error (%)
True	Predicted	(%)	True	Predicted Lower Bound/Upper Bound	
2.0	6.0	-3.3	-5.5	-7.0/-10.2	-27.3/-85.5
2.0	7.5	-4.6	-1.7	-1.6/-3.0	5.9/-76.5

Damage Case IB 4

Figures 6.29 and 6.30 depict the damage prediction results for Damage Case IB 4 using the damage indicator TB Direct β_j^M. Tables 6.19 and 6.20 tabulate the performance of the damage detection methodology for the damage case.

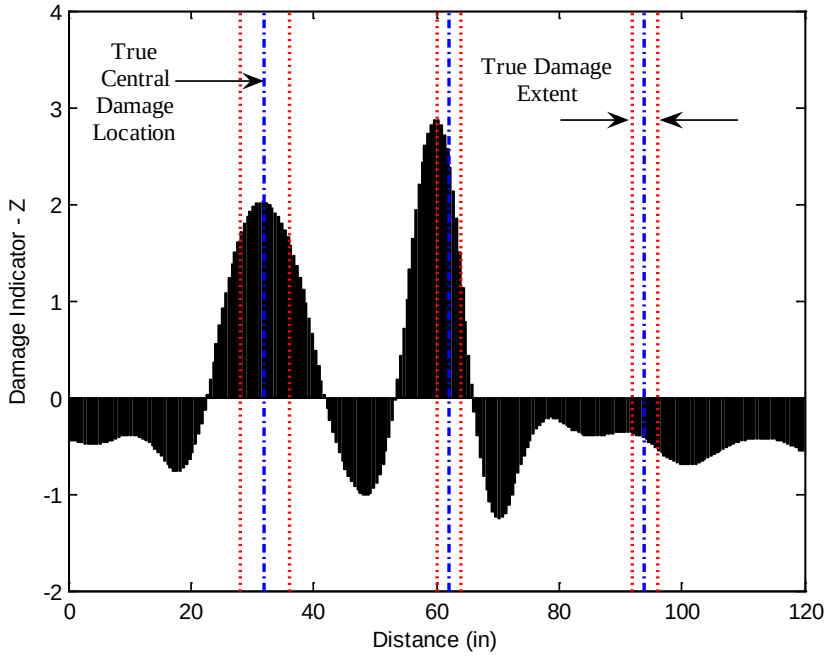

Figure 6.29 Damage Localization Result for Damage Case IB 4 Using TB Direct β_j^M

Table 6.19 Assessment of the Damage Localization Accuracy for Damage Case IB 4 Using TB Direct β_j^M

Damage Central Location (in)		Error (%)	$P(T \subset P)$
True	Predicted		
32.0	31.8	0.2	100%
62.0	59.8	1.8	100%
94.0	No	100.0	0%

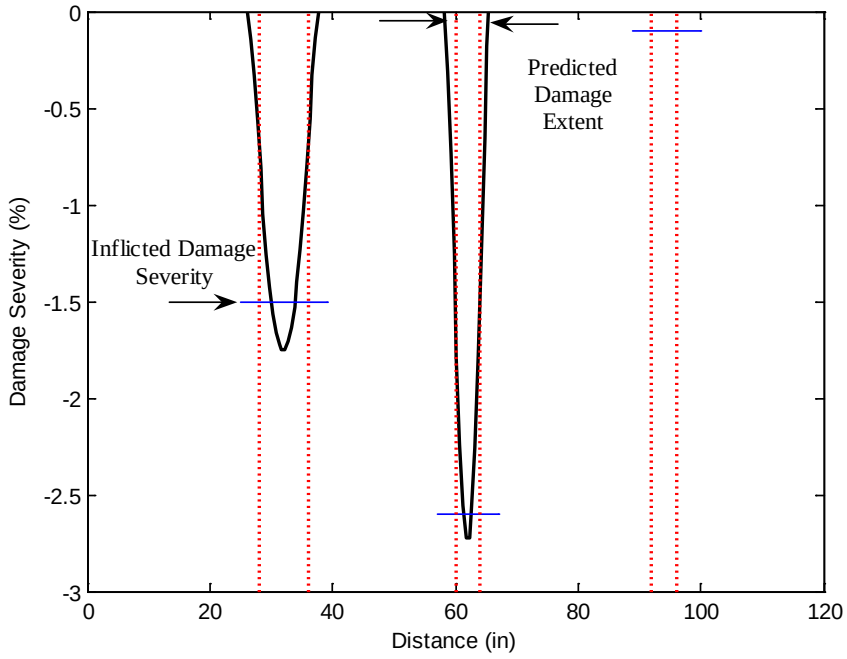

Figure 6.30 Damage Extent and Severity Estimate for Damage Case IB 4 Using TB Direct β_j^M

Table 6.20 Assessment of the Damage Extent and Severity Accuracy for Damage Case IB 4 Using TB Direct β_j^M

Damage Extent (in)		Error (%)	Damage Severity (%)		Error (%)
True	Predicted		True	Predicted Lower Bound/Upper Bound	
8.0	11.5	-2.9	-1.5	-1.1/-1.8	26.7/-20.0
4.0	7.0	-2.5	-2.6	-1.7/-2.7	34.6/-3.8
4.0	No	100.0	-0.1	No	100.0

Damage Case IB 5

Figures 6.31 and 6.32 depict the damage prediction results for Damage Case IB 5 using the damage indicator TB Direct β_j^M. Tables 6.21 and 6.22 tabulate the performance of the damage detection methodology for the damage case.

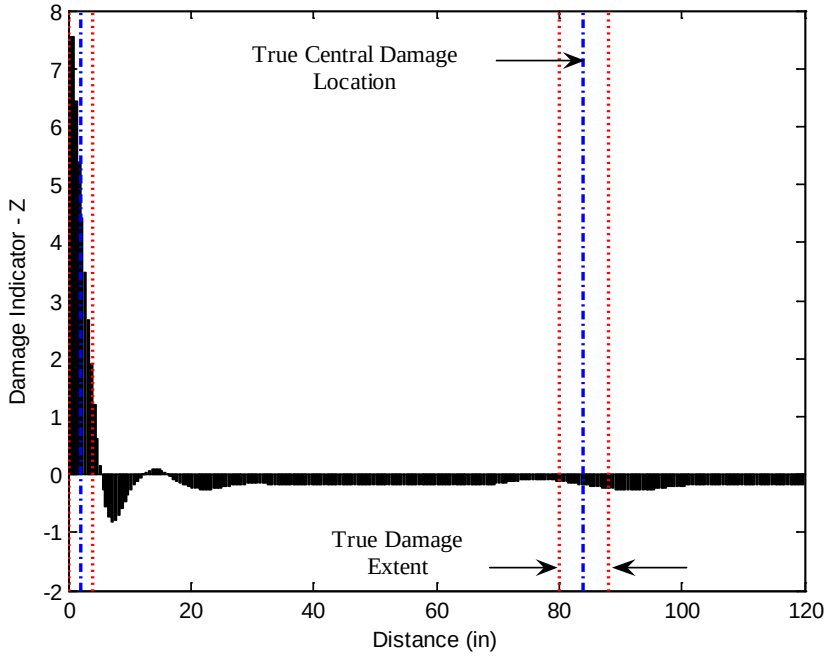

Figure 6.31 Damage Localization Result for Damage Case IB 5 Using TB Direct $\beta_j{}^M$

Table 6.21 Assessment of the Damage Localization Accuracy for Damage Case IB 5 Using TB Direct $\beta_j{}^M$

Damage Central Location (in)		Error (%)	$P(T \subset P)$
True	Predicted		
2.0	0.8	1.0	100%
84.0	No	100.0	0%

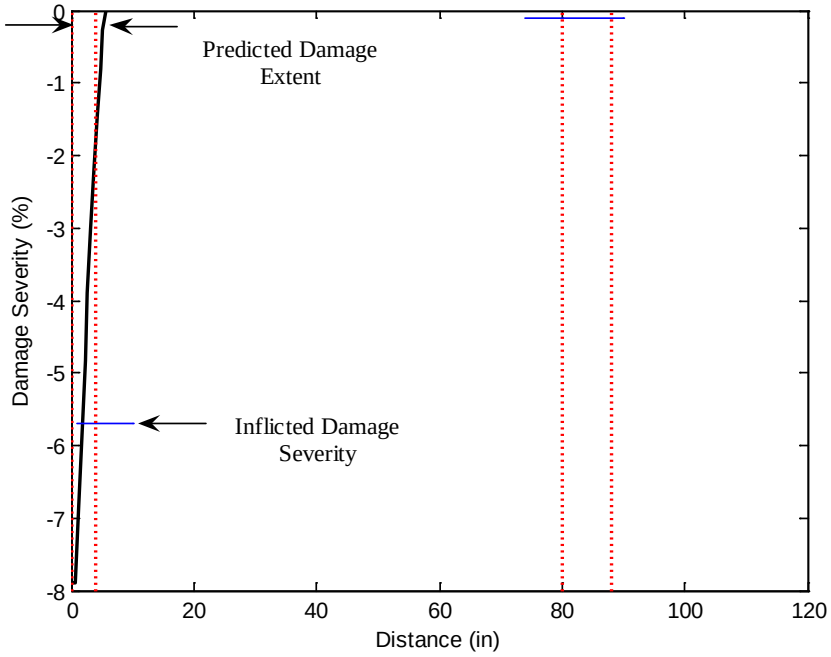

Figure 6.32 Damage Extent and Severity Estimate for Damage Case IB 5 Using TB Direct β_j^M

Table 6.22 Assessment of the Damage Extent and Severity Accuracy for Damage Case IB 5 Using TB Direct β_j^M

Damage Extent (in)		Error (%)	Damage Severity (%)		Error (%)
True	Predicted		True	Predicted Lower Bound/Upper Bound	
4.0	5.8	-1.5	-5.7	-4.2/-7.9	26.3/-38.6
8.0	No	100.0	-0.1	No/No	100/100

Figures 6.33 and 6.34 depict the damage prediction results for Damage Case IB 5 using the damage indicator TB Direct β_j^V. Tables 6.23 and 6.24 tabulate the performance of the damage detection methodology for the damage case.

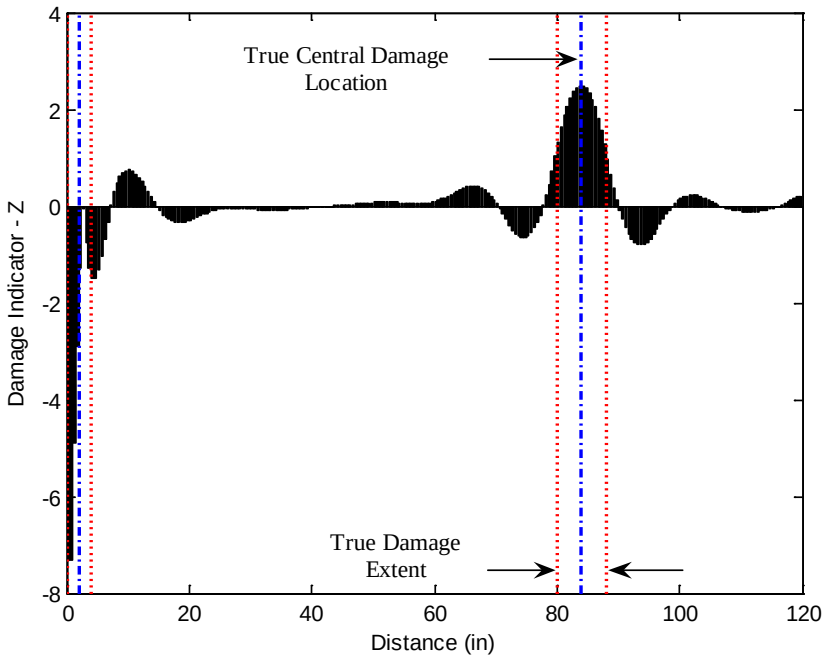

Figure 6.33 Damage Localization Result for Damage Case IB 5 Using TB Direct β_j^V

Table 6.23 Assessment of the Damage Localization Accuracy for Damage Case IB 5 Using TB Direct β_j^V

Damage Central Location (in)		Error (%)	$P(T \subset P)$
True	Predicted		
2.0	No	100.0	0%
FP	10.3	100.0	0%
84.0	83.8	0.2	100%

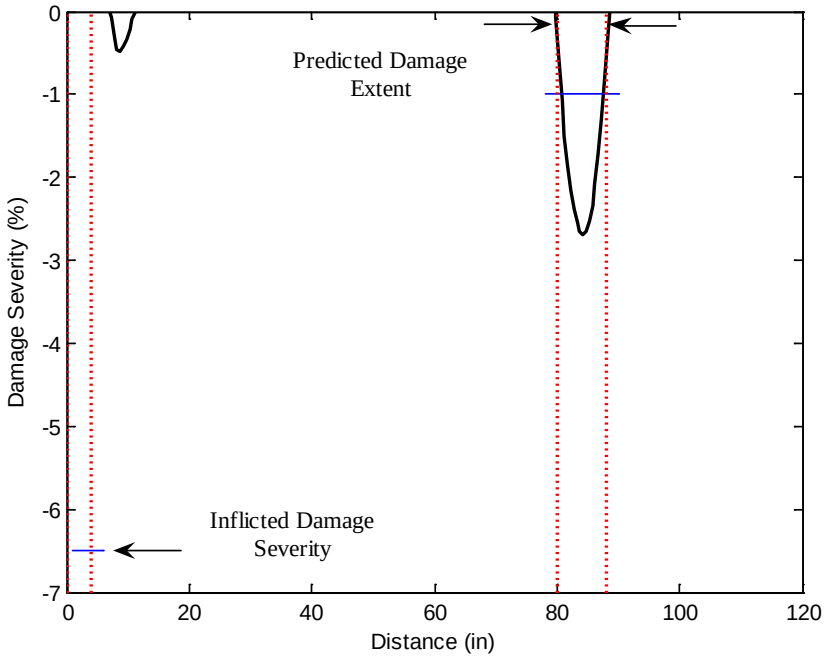

Figure 6.34 Damage Extent and Severity Estimate for Damage Case IB 5 Using TB Direct β_j^V

Table 6.24 Assessment of the Damage Extent and Severity Accuracy for Damage Case IB 5 Using TB Direct β_j^V

Damage Extent (in)		Error (%)	Damage Severity (%)		Error (%)
True	Predicted		True	Predicted Lower Bound/Upper Bound	
4.0	No	100.0	-6.5	No/No	100/100
FP	4.0	100.0	FP	-0.3/-0.5	100/100
8.0	9.0	-0.8	-1.0	-1.7/-2.7	-70.0/-170

The Deep Beam

Damage detection results for the deep beam are presented in this subsection. The number of degrees of freedom for the modal flexibility is 26 (13 translations and 13 rotations) excluding the support, since the displacement due to a unit load at the support is zero. The vertical displacements and cross-sectional rotations are estimated by the 25^{th} and 26^{th} modal flexibilities, respectively. Figure 6.35 and Figure 6.36 depict the vertical displacements and rotations of the undamaged deep beam approximated in this manner. Cubic spline functions with 0.3 in. uniform interval are used for interpolation in order to generate a finer sensor layout along the length the beam. This leads to 201 nodal points including an ideally assumed zero displacement at the support. Curvature profiles are estimated from the deflected shapes of the undamaged and damaged beams using the central difference approximation.

Central difference approximation of the first derivative is used to compute the first derivative of the rotation and the vertical displacement required by Eq. (6.5) and Eq. (6.10). The trapezoidal rule is applied to compute the integration schemes in these equations.

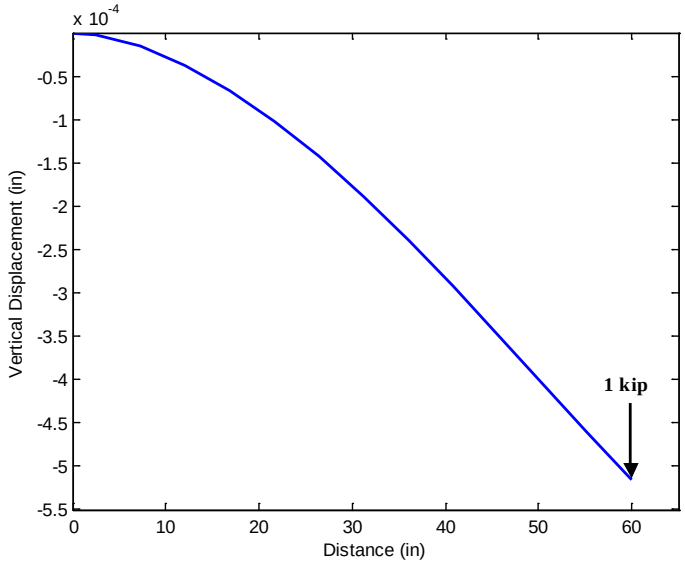

Figure 6.35 Vertical Displacement of the Beam Axis of the Deep Beam Approximated by the 25th Modal Flexibility

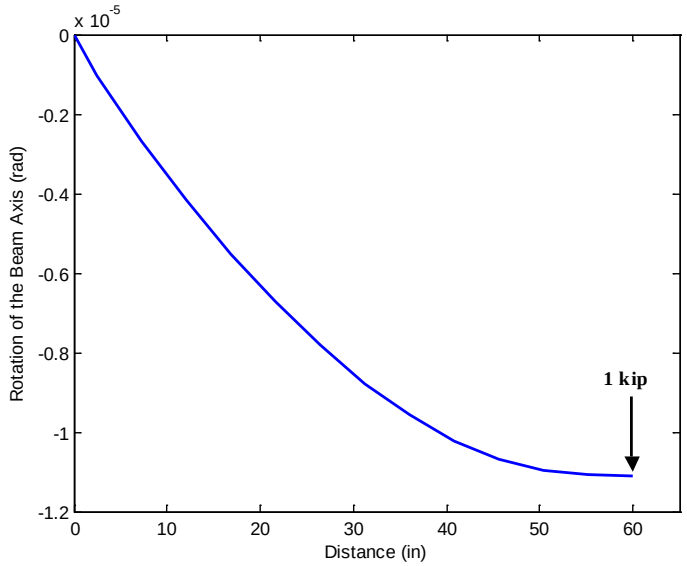

Figure 6.36 Rotation of the Beam Axis of the Deep Beam Approximated by the 26th Modal Flexibility

Damage Case DB 1

Figures 6.37 and 6.38 depict the damage prediction results for Damage Case DB 1 using the damage indicator TB Direct β_j^M. Tables 6.25 and 6.26 tabulate the performance of the damage detection methodology for the damage case.

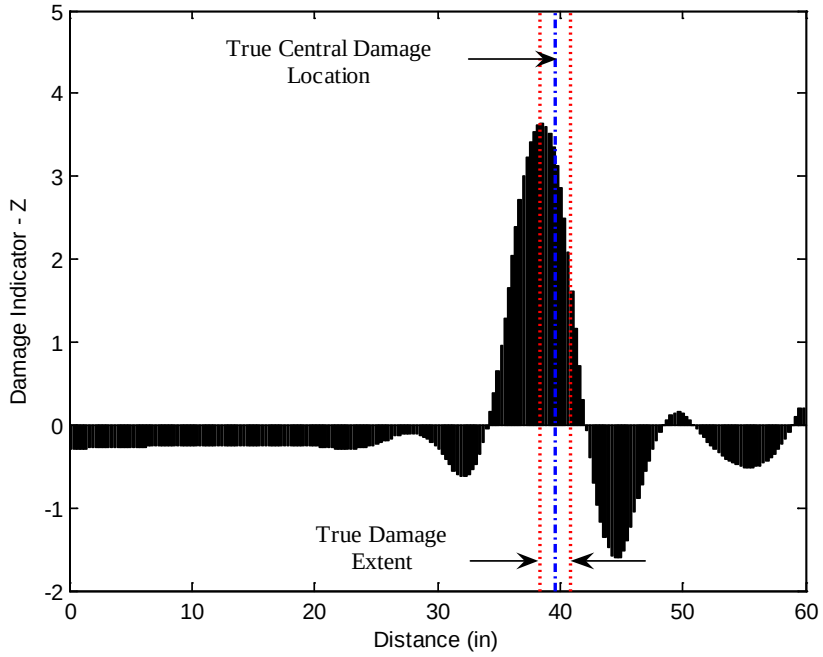

Figure 6.37 Damage Localization Result for Damage Case DB 1 Using TB Direct β_j^M

Table 6.25 Assessment of the Damage Localization Accuracy for Damage Case DB 1 Using TB Direct β_j^M

Damage Central Location (in)		Error (%)	$P(T \subset P)$
True	Predicted		
39.6	38.6	1.7	100%

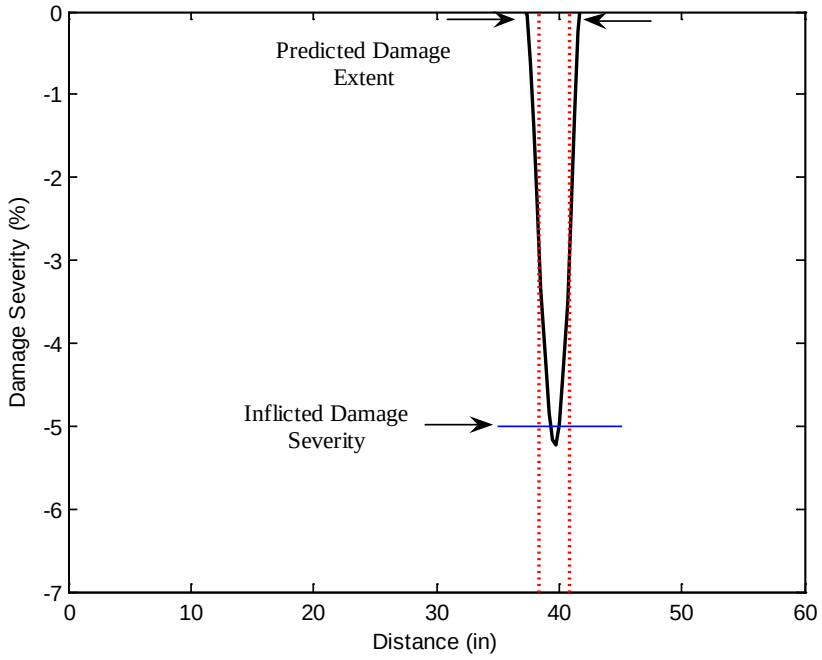

Figure 6.38 Damage Extent and Severity Estimate for Damage Case DB 1 Using TB Direct β_j^M

Table 6.26 Assessment of the Damage Extent and Severity Accuracy for Damage Case DB 1 Using TB Direct β_j^M

Damage Extent (in)		Error (%)	Damage Severity (%)		Error (%)
True	Predicted		True	Predicted Lower Bound/Upper Bound	
2.4	4.5	-3.5	-5.0	-3.0/-5.2	40.0/-4.0

Damage Case DB 2

Figures 6.39 and 6.40 depict the damage prediction results for Damage Case DB 2 using the damage indicator TB Direct β_j^M. Tables 6.27 and 6.28 tabulate the performance of the damage detection methodology for the damage case.

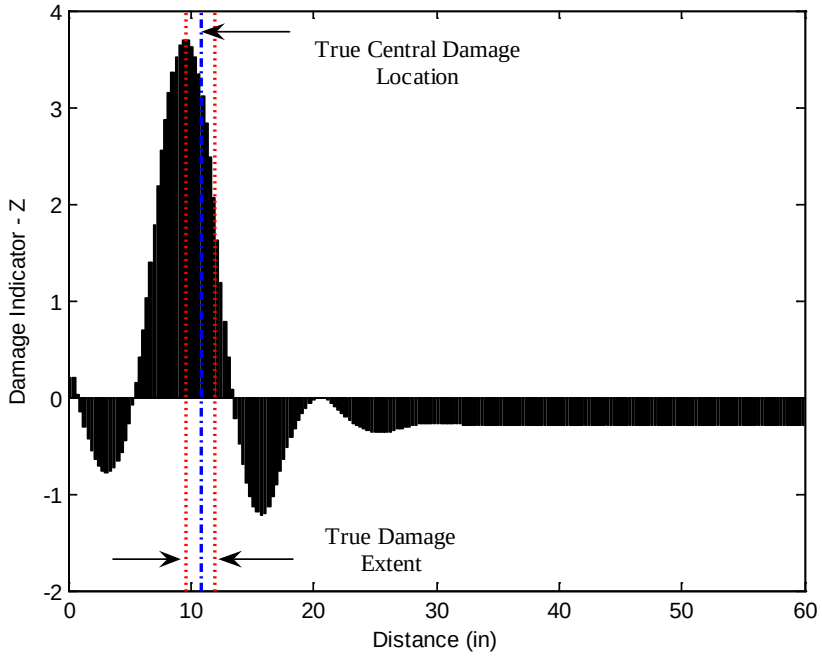

Figure 6.39 Damage Localization Result for Damage Case DB 2 Using TB Direct β_j^M

Table 6.27 Assessment of the Damage Localization Accuracy for Damage Case DB 2 Using TB Direct β_j^M

Damage Central Location (in)		Error (%)	$P(T \subset P)$
True	Predicted		
10.8	9.8	1.7	100%

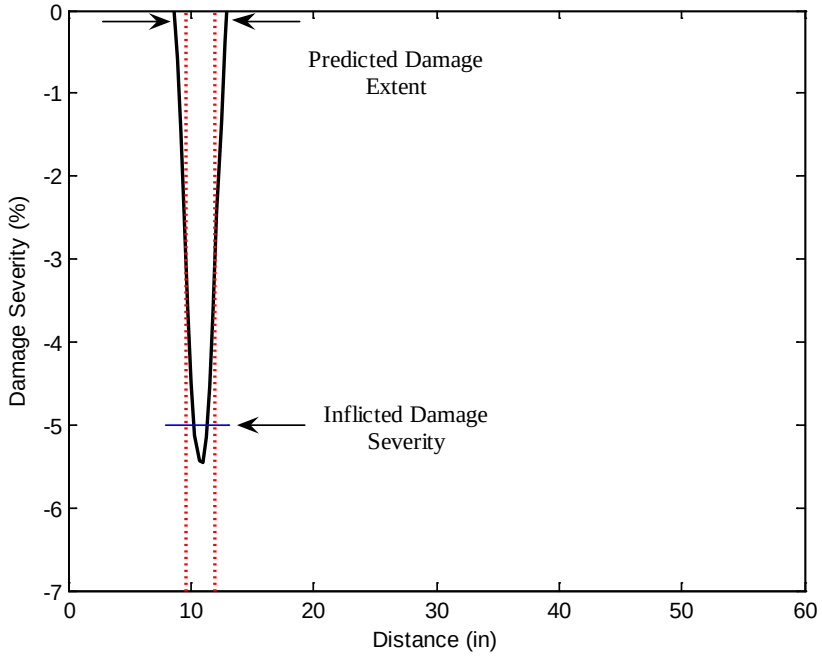

Figure 6.40 Damage Extent and Severity Estimate for Damage Case DB 2 Using TB Direct β_j^M

Table 6.28 Assessment of the Damage Extent and Severity Accuracy for Damage Case DB 2 Using TB Direct β_j^M

Damage Extent (in)		Error	Damage Severity (%)		Error (%)
True	Predicted	(%)	True	Predicted Lower Bound/Upper Bound	
2.4	4.5	-3.5	-5.0	-3.3/-5.5	34.0/-10.0

Damage Case DB 3

Figures 6.41 and 6.42 depict the damage prediction results for Damage Case DB 3 using the damage indicator TB Direct β_j^M. Tables 6.29 and 6.30 tabulate the performance of the damage detection methodology for the damage case.

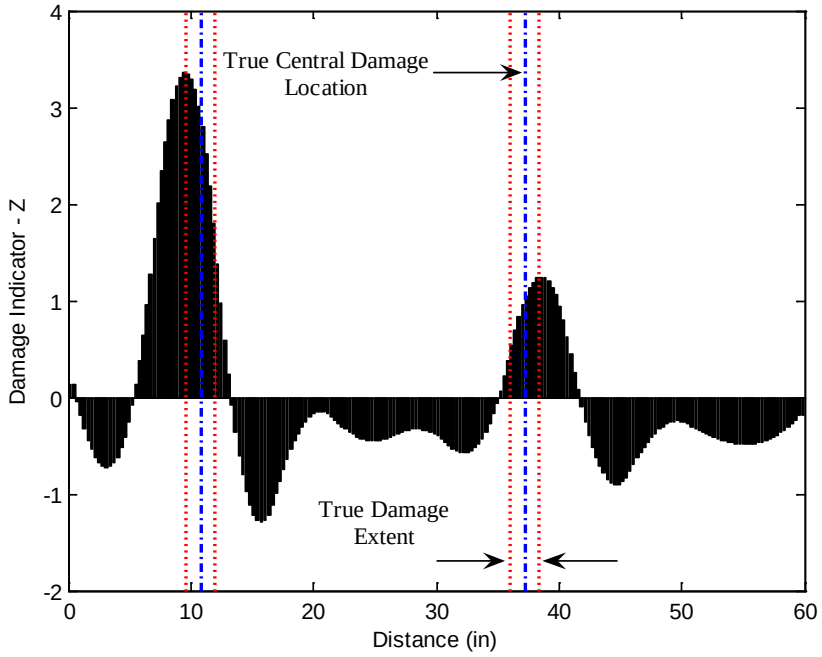

Figure 6.41 Damage Localization Result for Damage Case DB 3 Using TB Direct β_j^M

Table 6.29 Assessment of the Damage Localization Accuracy for Damage Case DB 3 Using TB Direct β_j^M

Damage Central Location (in)		Error (%)	$P(T \subset P)$
True	Predicted		
10.8	9.8	1.7	100%
37.2	38.6	-2.3	100%

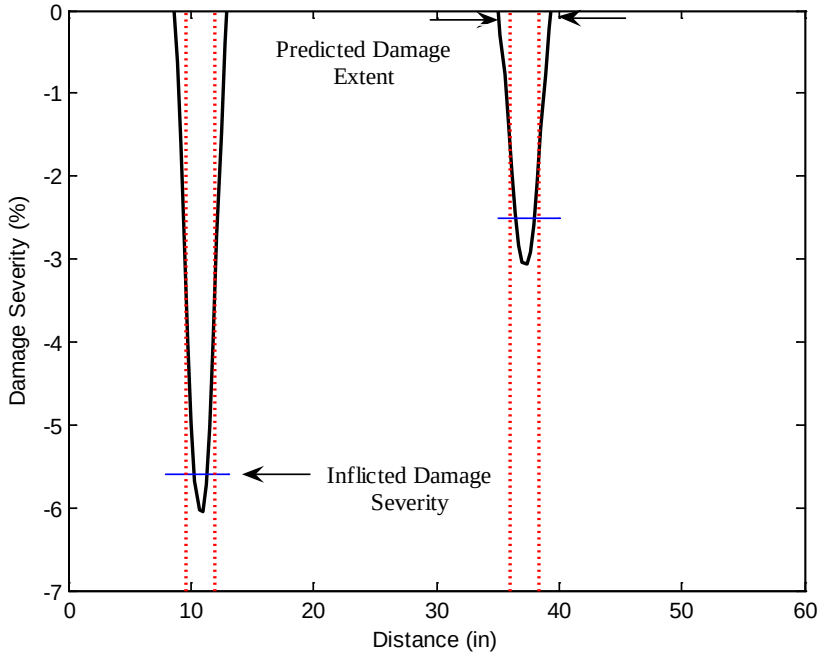

Figure 6.42 Damage Extent and Severity Estimate for Damage Case DB 3 Using TB Direct β_j^M

Table 6.30 Assessment of the Damage Extent and Severity Accuracy for Damage Case DB 3 Using TB Direct β_j^M

Damage Extent (in)		Error (%)	Damage Severity (%)		Error (%)
True	Predicted		True	Predicted Lower Bound/Upper Bound	
2.4	4.5	-3.5	-5.6	-3.7/-6.0	33.9/-7.1
2.4	4.2	-3.0	-2.5	-1.8/-3.1	28.0/-24.0

Figures 6.43 and 6.44 depict the damage prediction results for Damage Case DB 3 using the damage indicator TB Direct β_j^V. Tables 6.31 and 6.32 tabulate the performance of the damage detection methodology for the damage case.

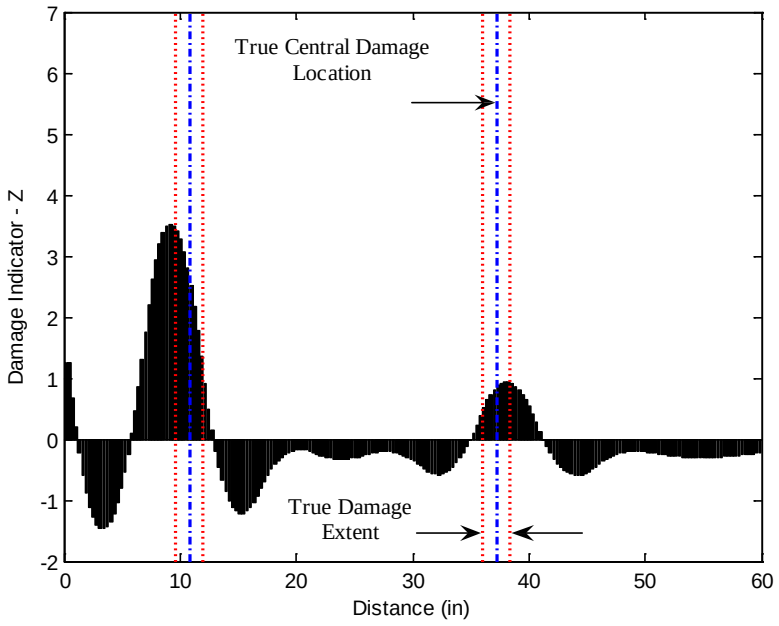

Figure 6.43 Damage Localization Result for Damage Case DB 3 Using TB Direct β_j^V

Table 6.31 Assessment of the Damage Localization Accuracy for Damage Case DB 3 Using TB Direct β_j^V

Damage Central Location (in)		Error (%)	$P(T \subset P)$
True	Predicted		
FP	0.5	100.0	0%
10.8	9.2	2.7	100%
37.2	38.0	-1.3	100%

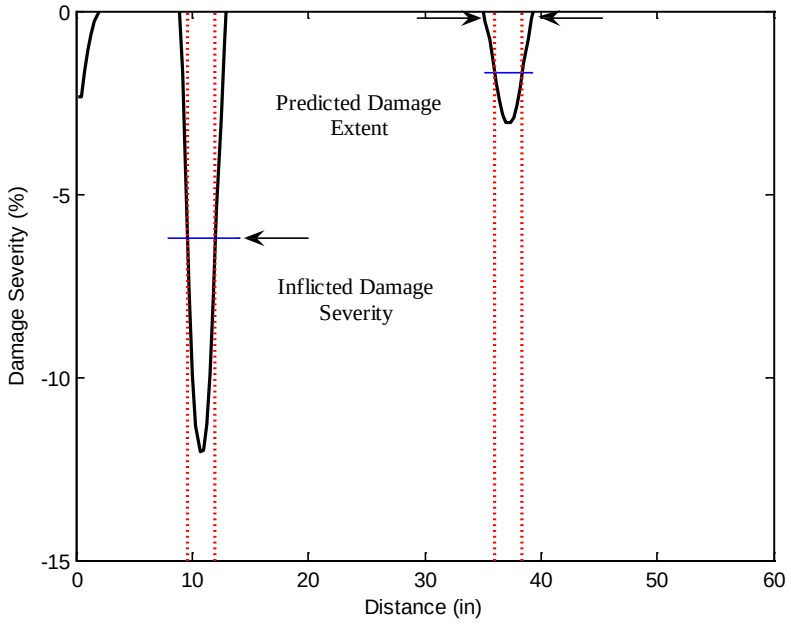

Figure 6.44 Damage Extent and Severity Estimate for Damage Case DB 3 Using TB Direct β_j^V

Table 6.32 Assessment of the Damage Extent and Severity Accuracy for Damage Case DB 3 Using TB Direct β_j^V

Damage Extent (in)		Error (%)	Damage Severity (%)		Error (%)
True	Predicted		True	Predicted Lower Bound/Upper Bound	
FP	2.0	100.0	FP	-1.2/-2.3	100.0
2.4	3.9	-2.5	-6.2	-7.7/-12.0	-24.2/-93.5
2.4	4.2	-3.0	-1.7	-1.6/-3.1	5.9/-82.4

Damage Case DB 4

Figures 6.45 and 6.46 depict the damage prediction results for Damage Case DB 4 using the damage indicator TB Direct β_j^M. Tables 6.33 and 6.34 tabulate the performance of the damage detection methodology for the damage case.

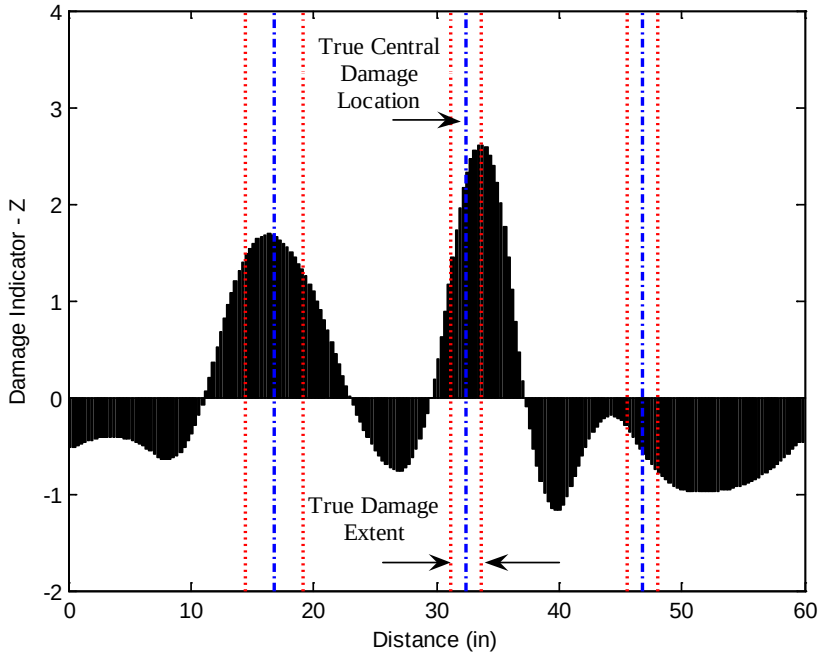

Figure 6.45 Damage Localization Result for Damage Case DB 4 Using TB Direct β_j^M

Table 6.33 Assessment of the Damage Localization Accuracy for Damage Case DB 4 Using TB Direct β_j^M

Damage Central Location (in)		Error (%)	$P(T \subset P)$
True	Predicted		
16.8	16.4	0.7	100%
32.4	33.8	-2.3	100%
46.8	No	100.0	0%

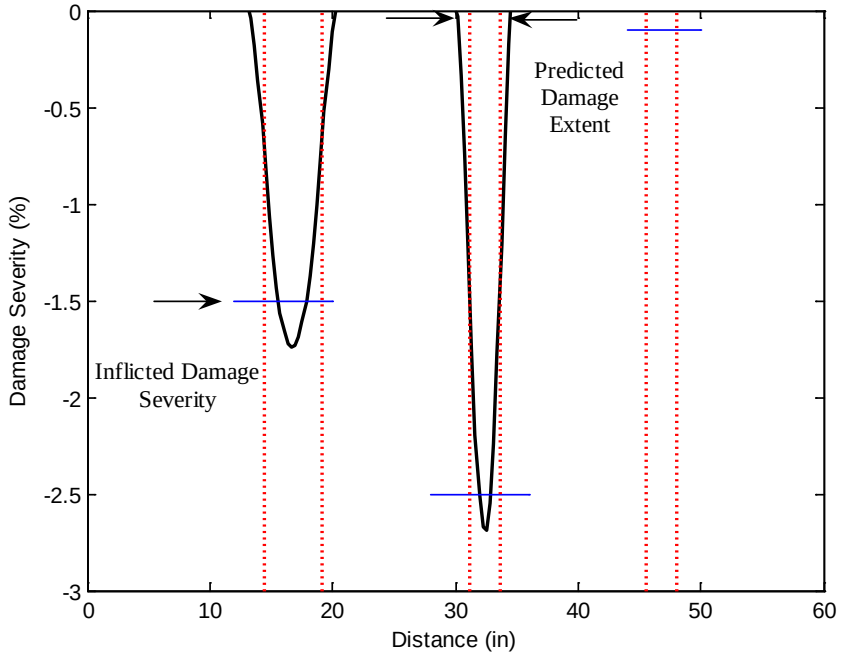

Figure 6.46 Damage Extent and Severity Estimate for Damage Case DB 4 Using TB Direct β_j^M

Table 6.34 Assessment of the Damage Extent and Severity Accuracy for Damage Case DB 4 Using TB Direct β_j^M

Damage Extent (in)		Error	Damage Severity (%)		Error (%)
True	Predicted	(%)	True	Predicted Lower Bound/Upper Bound	
4.8	7.2	-4.0	-1.5	-1.1/-1.7	26.7/-13.3
2.4	4.5	-3.5	-2.5	-1.5/-2.7	40.0/-8.0
2.4	No	100.0	-0.1	No/No	100/100

Damage Case DB 5

Figures 6.47 and 6.48 depict the damage prediction results for Damage Case DB 5 using the damage indicator TB Direct β_j^M. Tables 6.35 and 6.36 tabulate the performance of the damage detection methodology for the damage case.

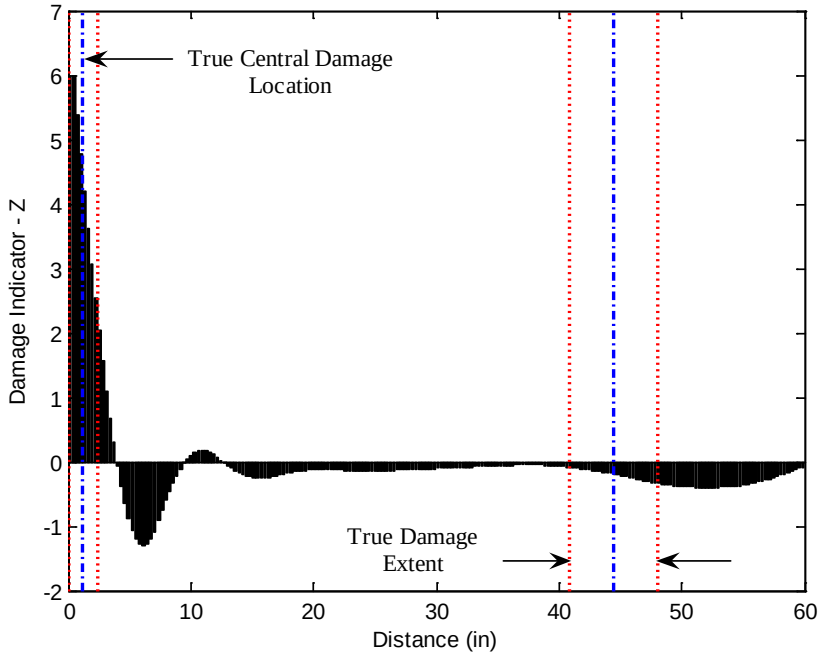

Figure 6.47 Damage Localization Result for Damage Case DB 5 Using TB Direct β_j^M

Table 6.35 Assessment of the Damage Localization Accuracy for Damage Case DB 5 Using TB Direct β_j^M

Damage Central Location (in)		Error (%)	$P(T \subset P)$
True	Predicted		
1.2	0.5	1.2	100%
44.4	No	100.0	0%

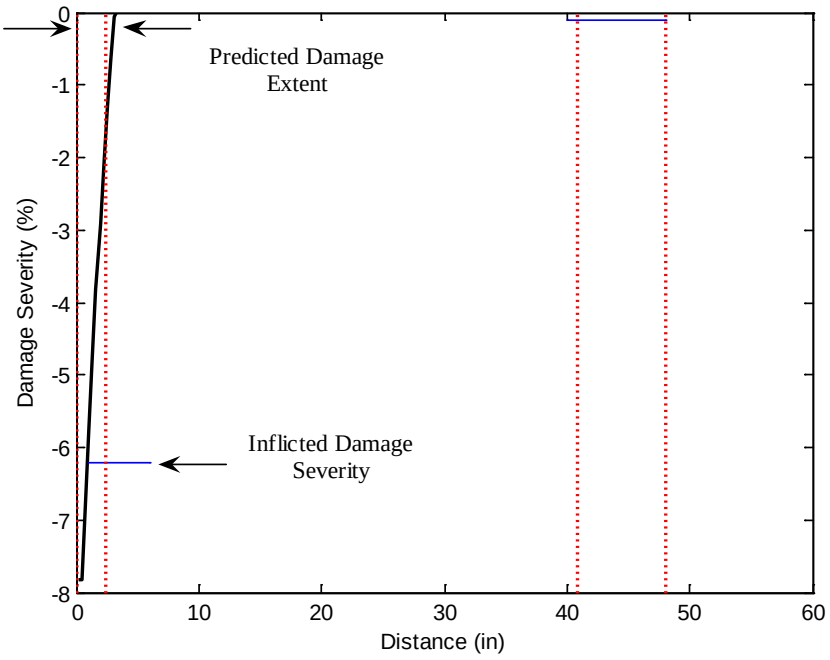

Figure 6.48 Damage Extent and Severity Estimate for Damage Case DB 5 Using TB Direct β_j^M

Table 6.36 Assessment of the Damage Extent and Severity Accuracy for Damage Case DB 5 Using TB Direct β_j^M

Damage Extent (in)		Error (%)	Damage Severity (%)		Error (%)
True	Predicted		True	Predicted Lower Bound/Upper Bound	
2.4	3.2	-0.7	-6.2	-4.1/-7.8	33.9/-25.8
7.2	No	6.0	-0.1	No/No	100/100

Figures 6.49 and 6.50 depict the damage prediction results for Damage Case DB 5 using the damage indicator TB Direct β_j^V. Tables 6.37 and 6.38 tabulate the performance of the damage detection methodology for the damage case.

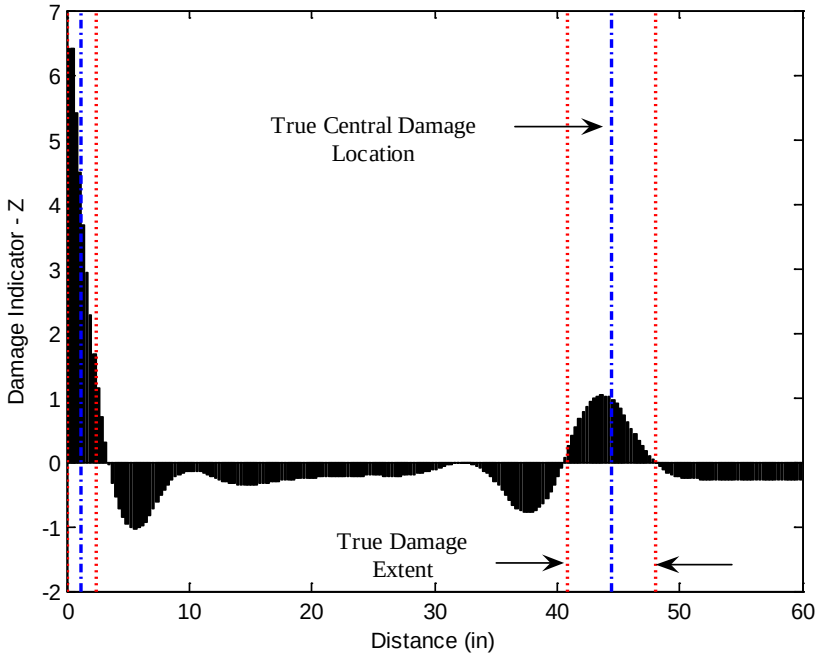

Figure 6.49 Damage Localization Result for Damage Case DB 5 Using TB Direct β_j^V

Table 6.37 Assessment of the Damage Localization Accuracy for Damage Case DB 5 Using TB Direct β_j^V

Damage Central Location (in)		Error (%)	$P(T \subset P)$
True	Predicted		
1.2	0.5	1.2	100%
44.4	43.7	1.2	100%

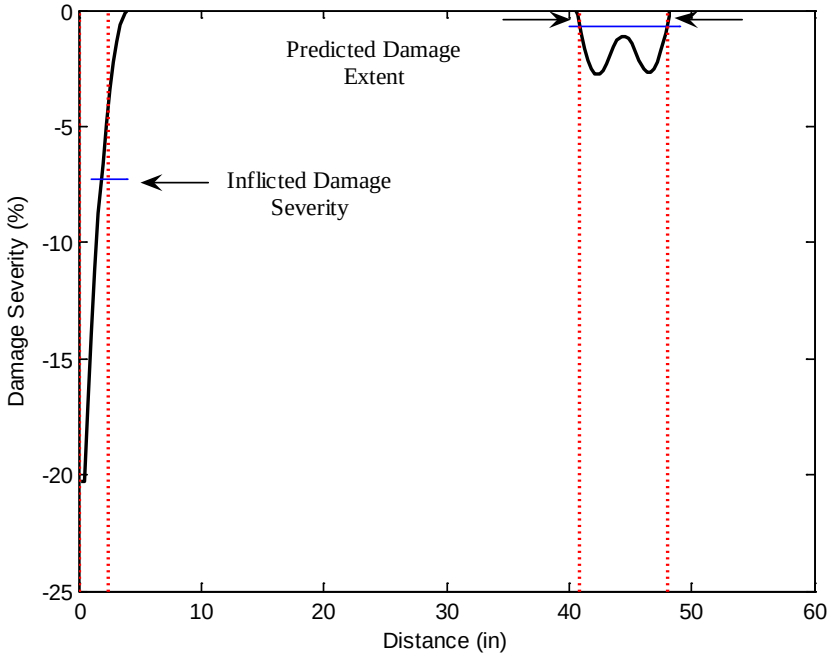

Figure 6.50 Damage Extent and Severity Estimate for Damage Case DB 5 Using TB Direct β_j^V

Table 6.38 Assessment of the Damage Extent and Severity Accuracy for Damage Case DB 5 Using TB Direct β_j^V

Damage Extent (in)		Error	Damage Severity (%)		Error (%)
True	Predicted	(%)	True	Predicted Lower Bound/Upper Bound	
2.4	3.8	-2.3	-7.3	-9.1/-20.3	-24.7/-178.1
7.2	7.5	-0.5	-0.7	-1.8/-2.8	-157.1/-300

DISCUSSION OF RESULTS

On reviewing the damage prediction results obtained through using TB Direct β_j^M, the following observations can be made regarding the accuracy of damage localization.

For damage scenarios SB 1 through SB 5, the error between the central location of the true and the predicted damages, e_L, ranged from a minimum of 0.2% in Damage Case SB 4 to a maximum of 1.9% in Damage Case SB 1 and Damage Case SB 3. This indicates a slight improvement in damage localization although there were two false negative (FN) predictions (one in Damage Case SB 4 and another in Damage Case SB 5). Note that these false predictions would have been identified, had the improved sensor layout utilized for damage extent and severity prediction, was utilized for damage localization as well. Also note that damage localization results given for Damage Case SB 5 indicated a small peak centered at around 100 in., which is the true central damage location. It appears that the magnitude of damage inflicted at the clamped support dominated the damage detection results and made the second damage location visually obsolete.

For damage scenarios IB 1 through IB 4, the maximum error between the central location of the true and predicted damages was 1.9% in Damage Cases IB 1 and IB 3. The minimum localization error was as low as 0.2% (Damage Case IB 4) among all damage scenarios excluding the two FN predictions in Damage Cases IB 4 and IB 5. Note that these correspond to the damage locations, which were not identified at the slender beam either. There were no false positive (FP) predictions.

For damage scenarios DB 1 through DB 5, the error between the true central damage and the predicted central damage ranged from a minimum of 0.7% in Damage Case DB 4 to a maximum of 2.3% in Damage Case DB 3. Locations of the two FN predictions were consistent with the previous case studies.

From the above observations, it may confidently be stated that the accuracy of damage localization is not function of the aspect ratio and remains fairly the same for any type of beam (slender, intermediate, or deep). Damage localization accuracy may further be improved by utilizing a finer set of sensor layout, which would have reduced the number of FN predictions to zero. TB Direct Method provided no FP damage predictions in any of the case studies. This is quite important, as it shows the method's reliability for damage detection.

On reviewing the results, the following observations can be made regarding the method's capability of monitoring the extent of the damage. As before, the capability to monitor the extent of the damage was measured by the probability that the true damaged region was a subset of the predicted damaged regions (i.e. $P(T \subset P)$) . Note that once damage was localized and, the damage severity and extent estimates were quantified by utilizing a refined sensor resolution (which corresponds to the nodes of the finite element mesh at the centerline of the beam). It was assumed that the length of the region where predicted damage severity is less than zero indicated the total extent of damage.

Excluding the two FN predictions in Damage Cases 4 and 5, for any type of beam (slender, intermediate, deep), the probability of zooming in on the damage was 100%.

As far as the error between the true and the predicted damage extent is concerned, the TB Direct Method provides predictions that are more reliable. For the case of the slender beam for instance, e_L ranged from a minimum 1.9% in Damage Case SB 5 to a maximum of 3.3% in Damage Case SB 3. This is a slight improvement considering the largest error of 5.0% in Damage Case SB 3 using the EB Direct method. More significant than the numerical error estimates however, it can be seen that the center of the true and predicted damage extends coincided precisely for all damage scenarios independent of the beam type. Note that, this is undoubtedly an improvement over the EB Direct method. The small disparity between the inflicted and predicted damage

extents are due to the stress concentrations, which lead to inevitable spillovers in extent calculations.

From the observations, we conclude that the probability of correctly locating the extent of the damage is independent of the aspect ratio when using a damage detection theory that is developed on the basis of the Timoshenko beam theory.

On reviewing the results for the damage predictions using the TB Direct Method, the following observations can be made regarding the accuracy of the damage severity:

Using the upper bound measurement as the damage error indicator, for damage scenarios SB 1 to SB 5, the error between the true bending damage severity and the predicted bending damage severity ranged from a minimum of 0% for Damage Case SB 4 to a maximum of 39.3% for Damage Case SB 5 excluding the two FN predictions.

Again, using the upper bound measurement as the estimate of the severity for damage scenarios IB 1 to IB 5, the error between the true damage severity and the damage severity predicted using the TB Direct Method, ranged from a minimum of 3.8% for Damage Case IB 4 to a maximum of 38.6% in Damage Case IB 5. Note that these correspond to the same damage cases identified for the slender beam.

Finally, using the upper bound measurement as the damage indicator, for damage scenarios DB 1 to DB 5, the error between the true damage severity and the predicted damage severity, using the TB Direct Method, ranged from a minimum of 4.0% in Damage Case DB 1 to a maximum of 25.8% in Damage Case DB 5. These are significant improvements compared to their counterparts computed using the EB Direct Method. It can be inferred from these results that the upper bound measurement generally provides slightly larger estimates for damage severity, which may be used as conservative predictions.

The most significant improvement of the TB Direct Method over the EB Direct Method is that the inflicted damage severity always remains in between the lower and upper bound severity estimates, and is likely to be closer to the upper bound estimate than the lower bound estimate. The range and magnitude of the error in the prediction of the accuracy of the damage severity estimate does not depend on the aspect ratio of the beam.

On reviewing the damage prediction results obtained through using TB Direct β_j^V, the following observations can be made regarding the performance of the damage indicator:

The proposed damage indicator provides better damage prediction results for deeper beams (as the aspect ratio of the beam increases). This is an expected result since shear force dominates the behavior of deep beams. Due to this reason, TB Direct β_j^V was not utilized for the case studies of the slender beam. Excluding the FP prediction located within the vicinity of the clamped support in Damage Case DB 3, TB Direct β_j^V successfully localized damage in damage scenarios DB 3 and DB 5. In fact, this damage indicator outperformed TB Direct β_j^M in Damage Case DB 5 by correctly identifying the previous FN prediction. However, damage severity estimates were not as accurate as damage localization results since damage severity predictions ranged from a minimum of 5.9% in Damage Case DB 3 to a maximum of 300.0% in Damage Case DB 5. Consequently, predicting local changes in Poisson's ratio via Eq. (6.21) will not provide reliable estimates since TB Direct β_j^V yields unstable damage prediction results.

SUMMARY AND CONCLUSIONS

Explicit damage index methodologies based on the principle of invariant stress resultants of the Timoshenko beam theory were developed. The performance of the proposed damage detection methodologies were evaluated by using the response data

collected from the numerical experiments of Chapter III. It was concluded that the accuracy of damage localization is not function of the aspect ratio and remains fairly the same for any type of beam (slender, intermediate, or deep). It was also observed that the center of the true and predicted damage extends coincided precisely for all damage scenarios independent of the beam type. Finally, stable damage severity estimates were obtained through using the damage indicator TB Direct β_j^M and it was examined that the inflicted damage severity always remains in between the lower and upper bound damage severity estimates.

CHAPTER VII

DAMAGE INDICES BASED ON NODAL ROTATIONS

INTRODUCTION

The objective of this chapter is to develop explicit damage index methodologies utilizing the stress-displacement relations of the Timoshenko beam theory. Damage is expressed in terms of local decreases in the flexural stiffness of structural members in beam-type structures. These local decreases are represented as singularities in the flexural stiffness distribution of the beam. Utilizing the concept of discontinuity developed in Chapter II in conjunction with the derivatives of cross sectional rotation, the location and magnitude of local stiffness degradations may be identified.

To accomplish the stated objective, this chapter is divided into four major sections: a section articulating the proposed methodology; a section describing specific structural response parameters utilized in the proposed damage detection methodology; a section evaluating the performance of the method using the numerical experiments introduced in Chapter III; and a section discussing the outcomes of the performed case studies.

PROPOSED METHODOLOGY

Assume that a local decrease in the stiffness of a beam-type structure may be expressed in terms of a decrease in the bending stiffness of its sub-element(s). In order to model this, assume that the beam that is comprised of NE sub-elements and NN nodes as depicted in Figure 7.1. The problem here is to identify the location of the damaged sub-elements within the beam and quantify the amount of stiffness degradation inflicted at each damaged region. Following methodologies are proposed in order to address the stated problem. Note that the proposed methodologies are based on the stress-displacement relations of the Timoshenko beam theory.

Nodal Flexural Stiffness Based on the Average of the First Derivative of Rotation at the Point of Flexural Discontinuity

Let the pristine and damaged flexural stiffnesses of the j^{th} element located between the coordinates $x = l_i$ and $x = l_{i+1}$ be represented by EI_j and EI_j^*, respectively. Utilizing the principle of invariant stress resultants, following condition holds at the i^{th} node of the beam:

$$M_i = M_i^* \tag{7.1}$$

where the asterisk represents the moment at $x = l_i$ in the damaged beam.

Utilizing the fundamental relationship between the first derivative of the rotation and bending moment as given by the Timoshenko beam theory (Eq. (2.20)), the bending moment at the i^{th} node may be expressed in terms of the flexural stiffness and the derivative of cross sectional rotation computed at the i^{th} node. Thus in terms of the deformation, Eq. (7.1) may be written as:

$$EI_i \frac{d\phi_i}{dx} = EI_i^* \frac{d\phi_i^*}{dx} \tag{7.2}$$

where ϕ_i, and ϕ_i^* denote the nodal rotations measured before and after damage, respectively.

At the i^{th} node, discrete values of the flexural stiffnesses EI_{j-1}^* and EI_j^*, leads to a discontinuity in the stiffness distribution of the damaged structure. Utilizing Eq. (2.35), nodal flexural stiffness at the i^{th} node of the damaged beam may be represented by an equivalent flexural stiffness term written in terms of the stiffnesses of the adjacent elements.

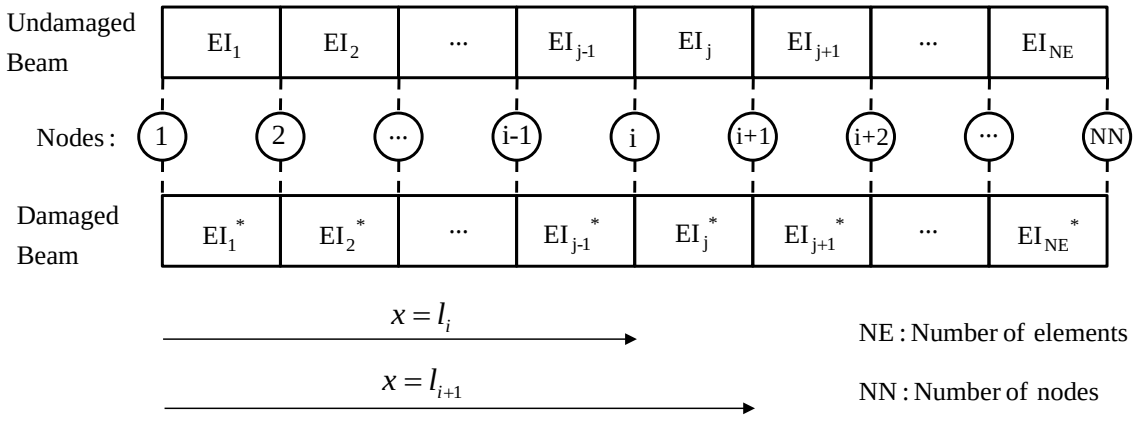

Figure 7.1 Damage Detection Model Utilized to Predict Local Changes in the Flexural Stiffness Distribution via Nodal Rotations

$$EI_i^* = 2\left(\frac{EI_{j-1}^* \, EI_j^*}{EI_{j-1}^* + EI_j^*}\right) \tag{7.3}$$

Substituting Eq. (7.3) into Eq. (7.2) yields:

$$EI_i \frac{d\phi_i}{dx} = 2\left(\frac{EI_{j-1}^* \, EI_j^*}{EI_{j-1}^* + EI_j^*}\right)\frac{d\phi_i^*}{dx} \tag{7.4}$$

Assuming constant flexural stiffness distribution for the pristine structure (i.e. for $i = 1...NN, EI_i = EI$), Eq. (7.4) may be written as:

$$EI \frac{d\phi_i}{dx} = 2\left(\frac{EI_{j-1}^* \, EI_j^*}{EI_{j-1}^* + EI_j^*}\right)\frac{d\phi_i^*}{dx} \tag{7.5}$$

Collecting the bending stiffnesses of the sub-elements at the right hand side of Eq. (7.5) leads to:

$$EI\left(\frac{EI_{j-1}^{*}+EI_{j}^{*}}{EI_{j-1}^{*}\,EI_{j}^{*}}\right)\frac{d\phi_i}{dx}=2\frac{d\phi_i}{dx}^{*} \tag{7.6}$$

Factoring out the denominator of the left hand side of Eq. (7.6) yields:

$$EI\left(\frac{EI_{j-1}^{*}}{EI_{j-1}^{*}\,EI_{j}^{*}}+\frac{EI_{j}^{*}}{EI_{j-1}^{*}\,EI_{j}^{*}}\right)\frac{d\phi_i}{dx}=2\frac{d\phi_i}{dx}^{*} \tag{7.7}$$

Cancelling out the like terms within parenthesis leads to a more compact form given as:

$$\left(\frac{EI}{EI_{j}^{*}}+\frac{EI}{EI_{j-1}^{*}}\right)\frac{d\phi_i}{dx}=2\frac{d\phi_i}{dx}^{*} \tag{7.8}$$

Eq. (7.8) further simplifies into Eq. (7.10) upon introducing the damage indicator β_j:

$$\beta_j=\frac{EI}{EI_{j}^{*}} \tag{7.9}$$

$$\left(\beta_j+\beta_{j-1}\right)\frac{d\phi_i}{dx}=2\frac{d\phi_i}{dx}^{*} \tag{7.10}$$

Using the recursive scheme established in Eq. (7.10), the relation between the damage indices for the j^{th} and $j+1^{th}$ beam elements at the $(i+1)^{th}$ node become:

$$\left(\beta_{j+1}+\beta_j\right)\frac{d\phi_{i+1}}{dx}=2\frac{d\phi_{i+1}}{dx}^{*} \tag{7.11}$$

For a beam with NN nodes and NE sub-elements, where $NE = NN-1$, $NN-2$ number of linear equations may be written using the procedure described by Eq. (7.10) and Eq. (7.11). This process results in a system of underdetermined linear equations. Singular value decomposition based (SVD) *pseudo-inverse* techniques may then be used

to obtain an optimal solution for the values of the element damage indices. The system of equations may be written in the form:

$$A_{(NN-2)x(NE)}\ \beta_{(NEx1)} = B_{(NN-2)x1} \tag{7.12}$$

where the $NEx1$ vector, β, denotes the damage index vector to be evaluated.

$$\beta_{(NEx1)} = \begin{bmatrix} \cdots \\ \beta_j \\ \beta_{j+1} \\ \cdots \end{bmatrix} \tag{7.13}$$

The $(NN-2)x(NE)$ matrix A and $(NN-2)x1$ matrix B contain the derivatives of the nodal cross sectional rotations of the undamaged and damaged beams, respectively.

$$A_{(NN-2)x(NE)} = \begin{bmatrix} \cdots & \cdots & \cdots & \cdots & \cdots & \cdots & \cdots \\ \cdots & 0 & \dfrac{d\phi_i}{dx} & \dfrac{d\phi_i}{dx} & 0 & \cdots & \cdots \\ \cdots & \cdots & 0 & \dfrac{d\phi_{i+1}}{dx} & \dfrac{d\phi_{i+1}}{dx} & 0 & \cdots \\ \cdots & \cdots & \cdots & \cdots & \cdots & \cdots & \cdots \end{bmatrix} \tag{7.14}$$

$$B_{(NN-2)x1} = \begin{bmatrix} \cdots \\ 2\dfrac{d\phi_i}{dx}^{*} \\ 2\dfrac{d\phi_{i+1}}{dx}^{*} \\ \cdots \end{bmatrix} \tag{7.15}$$

The solution to Eq. (7.12) is given by:

$$\beta = A^{-1}B \tag{7.16}$$

where A^{-1} is the *pseudo-inverse* of A.

Note that the damage indicator, β_j, computed above is greater than unity in regions where stiffness degradation has occurred. This damage indicator is designated as "the TB Pseudo β_j" for identification purposes.

The severity of the inflicted damage for localized damaged regions may be expressed in terms of the pristine and damaged flexural stiffnesses as before.

$$\alpha_j = \frac{\Delta EI_j}{EI_j} = \frac{EI_j^* - EI_j}{EI_j} \tag{7.17}$$

which in turn can be written in terms of the damage indicator β_j given in Eq. (7.16):

$$\alpha_j = \frac{EI_j^*}{EI_j} - 1 = \frac{1}{\beta_j} - 1 \tag{7.18}$$

Nodal Flexural Stiffness Based on the Average of Flexural Stiffnesses at the Point of Flexural Discontinuity

An analogous formulation to the one given in Eq. (7.12) can be obtained by using Eq. (2.37) in lieu of Eq. (2.35) to express the nodal flexural stiffness. Flexural stiffness at the i^{th} node is now represented by the mean value of the flexural stiffnesses of its adjacent elements, namely $j-1$ and j as was shown in Figure 7.1. Thus, at the i^{th} node:

$$EI_i^* = \frac{1}{2}\left(EI_{j-1}^* + EI_j^*\right) \tag{7.19}$$

Substituting Eq. (7.19) for EI_i^* into Eq. (7.2) gives:

$$EI_i \frac{d\phi_i}{dx} = \frac{1}{2}\left(EI_{j-1}^* + EI_j^*\right)\frac{d\phi_i^*}{dx} \tag{7.20}$$

As before, assuming constant flexural stiffness distribution for the pristine structure (i.e. for $i = 1...NN, EI_i = EI$), Eq. (7.20) can be written as:

$$EI\,\frac{d\phi_i}{dx} = \frac{1}{2}\left(EI_{j-1}^{\ *} + EI_j^{\ *}\right)\frac{d\phi_i^{\ *}}{dx} \tag{7.21}$$

Dividing the right hand side of Eq. (7.21) by the flexural stiffness of the undamaged beam, EI , results in:

$$2\frac{d\phi_i}{dx} = \left(\gamma_{j-1} + \gamma_j\right)\frac{d\phi_i^{\ *}}{dx} \tag{7.22}$$

where the equivalent damage indicator γ_j is given by:

$$\gamma_j = \frac{EI_j^{\ *}}{EI} \tag{7.23}$$

Using the recursive scheme established in Eq. (7.22), the relation between the damage indices for the j^{th} and $j+1^{th}$ beam elements at the $(i+1)^{th}$ node become:

$$2\frac{d\phi_{i+1}}{dx} = \left(\gamma_j + \gamma_{j+1}\right)\frac{d\phi_{i+1}^{\ *}}{dx} \tag{7.24}$$

As before, for a beam with NN nodes and NE sub-elements, where $NE = NN - 1$, $NN - 2$ number of linear equations may be written using the procedure described by Eq. (7.22) and Eq. (7.24). This procedure results in a system of underdetermined linear equations. Singular value decomposition based (SVD) *pseudo-inverse* techniques may then be used to obtain an optimal solution for the values of the element damage indices given in Eq. (7.23). The system of equations can be written in the form:

$$C_{(NN-2)x(NE)}\,\gamma_{(NEx1)} = D_{(NN-2)x1} \tag{7.25}$$

where the $NEx1$ vector, γ, denotes the damage index vector to be evaluated.

$$\gamma_{(NEx1)} = \begin{bmatrix} \dots \\ \gamma_j \\ \gamma_{j+1} \\ \dots \end{bmatrix} \tag{7.26}$$

The $(NN-2)x(NE)$ matrix C and $(NN-2)x1$ matrix D contain the derivatives of cross sectional rotations of the damaged and undamaged beams, respectively.

$$C_{(NN-2)x(NE)} = \begin{bmatrix} \dots & \dots & \dots & \dots & \dots & \dots & \dots \\ \dots & 0 & \frac{d\phi_i^*}{dx} & \frac{d\phi_i^*}{dx} & 0 & \dots & \dots \\ \dots & \dots & 0 & \frac{d\phi_{i+1}^*}{dx} & \frac{d\phi_{i+1}^*}{dx} & 0 & \dots \\ \dots & \dots & \dots & \dots & \dots & \dots & \dots \end{bmatrix} \tag{7.27}$$

$$D_{(NN-2)x1} = \begin{bmatrix} \dots \\ 2\frac{d\phi_i}{dx} \\ 2\frac{d\phi_{i+1}}{dx} \\ \dots \end{bmatrix} \tag{7.28}$$

The solution to Eq. (7.25) is given by:

$$\gamma = A^{-1}B \tag{7.29}$$

where A^{-1} is the *pseudo-inverse* of A.

The damage indicator, γ_j, computed above is less than unity in regions where stiffness degradation has occurred. This damage indicator is designated as "the TB Pseudo γ_j" for identification purposes.

As usual, the severity of the inflicted damage for localized damaged regions may be expressed in terms of the pristine and damaged flexural stiffnesses as:

$$\alpha_j = \frac{\Delta EI_j}{EI_j} = \frac{EI_j^* - EI_j}{EI_j} \tag{7.30}$$

This in turn can be written in terms of the damage indicator γ given in Eq. (7.29):

$$\alpha_j = \frac{EI_j^*}{EI_j} - 1 = \gamma_j - 1 \tag{7.31}$$

PROPOSED EXPERIMENTAL ARRANGEMENT AND BASIC MEASUREMENTS REQUIRED BY THEORY

The proposed NDE methodology utilizes the pre- and post-damaged nodal rotations for damage detection. The proposed experimental arrangement is identical to the one given in Chapter VI. The derivatives of cross sectional rotations computed previously in Chapter VI are employed in the proposed damage detection methodologies.

ASSESSMENT OF THE PROPOSED METHODOLOGIES VIA NUMERICAL EXPERIMENTS

The performance of the proposed damage detection methodology is evaluated in this section. The numerical experiments previously defined in Chapter III are utilized to evaluate the performance of the NDE methodologies. The performance of the methods is based on accurately identifying the location, the extent, and the severity of the damage as before. These items are described in Chapter IV.

The Slender Beam

Damage detection results for the slender beam are presented in this subsection. The modal flexibility is utilized to approximate the pre- and post-damaged nodal rotations of

the beam axis. Cubic spline functions with 0.6 in. uniform intervals are used to generate a finer sensor layout along the length the beam. This procedure leads to 241 nodal points. Central difference approximation of the first derivative is used to compute the first derivative of the rotation after interpolation.

Damage Case SB 1

Figures 7.2 and 7.3 depict the damage prediction results for Damage Case SB 1 using the damage indicator TB Pseudo β_j. Tables 7.1 and 7.2 tabulate the performance of the damage detection methodology that utilizes TB Pseudo β_j for damage detection. The error between the central location of the true and the predicted damages is computed by Eq. (3.1). Note that $P(T \subset P)$ indicates the probability that the true damaged region is a subset of the predicted damaged regions. The damage severity and extent estimates are computed by utilizing an improved sensor resolution, which corresponds to the nodes of the finite element mesh at the centerline of the beam. It is assumed that only the regions previously identified by the damage localization results are instrumented for predicting the severity and the extent of damage. This process reduces the size of the system of linear equations given by Eq. (7.12).

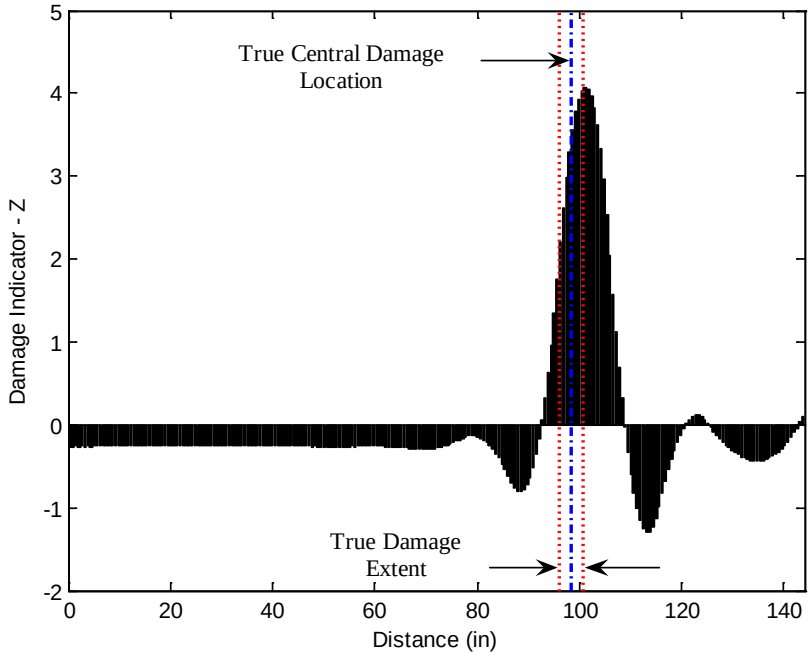

Figure 7.2 Damage Localization Result for Damage Case SB 1 Using TB Pseudo β_j

Table 7.1 Assessment of the Damage Localization Accuracy for Damage Case SB 1 Using TB Pseudo β_j

Damage Central Location (in)		Error (%)	$P(T \subset P)$
True	Predicted		
98.4	101.1	-1.9	100%

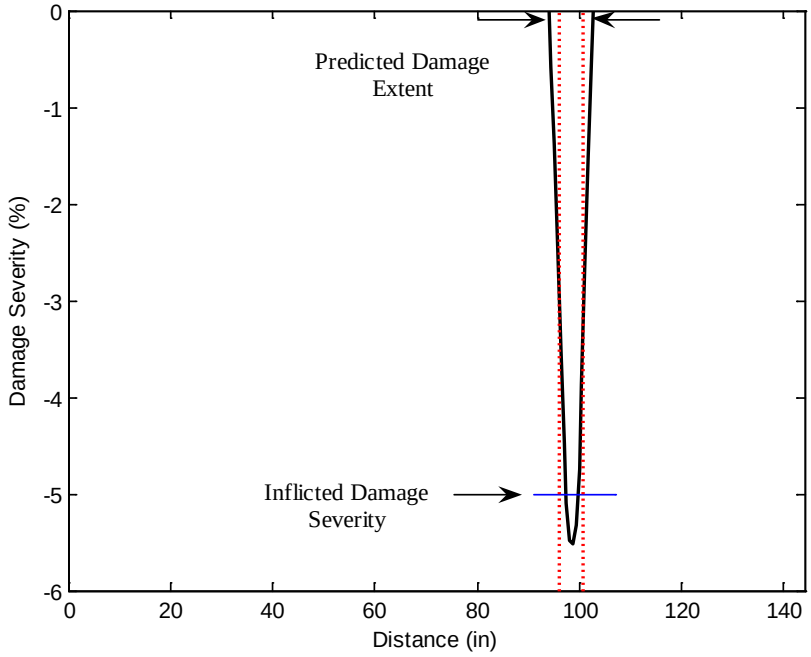

Figure 7.3 Damage Extent and Severity Estimate for Damage Case SB 1 Using TB Pseudo β_j

Table 7.2 Assessment of the Damage Extent and Severity Accuracy for Damage Case SB 1 Using TB Pseudo β_j

Damage Extent (in)		Error (%)	Damage Severity (%)		Error (%)
True	Predicted		True	Predicted Lower Bound/Upper Bound	
4.8	9.0	-2.9	-5.0	-3.4/-5.5	32.0/-10.0

Damage Case SB 2

Figures 7.4 and 7.5 depict the damage prediction results for Damage Case SB 2 using the damage indicator TB Pseudo β_j. Tables 7.3 and 7.4 tabulate the performance of the damage detection methodology for the damage case.

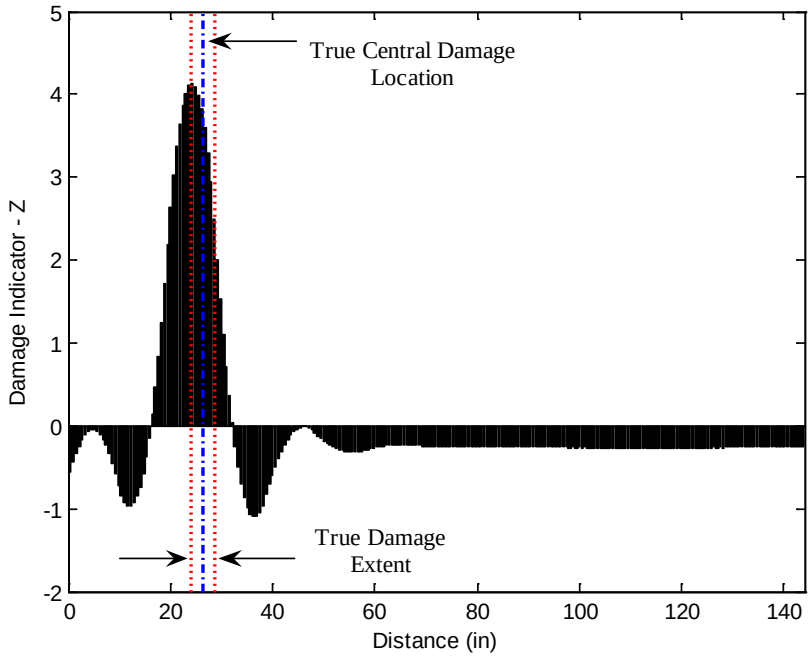

Figure 7.4 Damage Localization Result for Damage Case SB 2 Using TB Pseudo β_j

Table 7.3 Assessment of the Damage Localization Accuracy for Damage Case SB 2 Using TB Pseudo β_j

Damage Central Location (in)		Error (%)	$P(T \subset P)$
True	Predicted		
26.4	24.3	1.5	100%

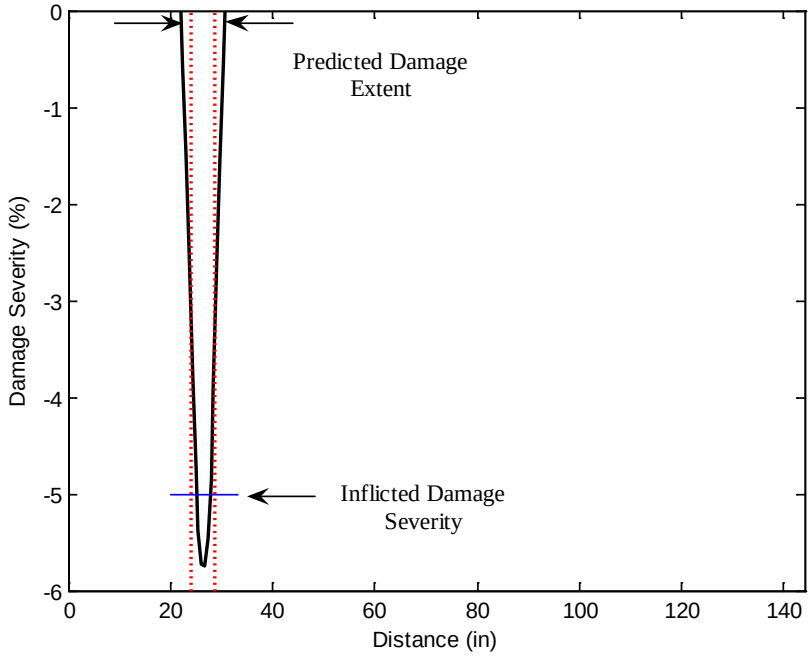

Figure 7.5 Damage Extent and Severity Estimate for Damage Case SB 2 Using TB Pseudo β_j

Table 7.4 Assessment of the Damage Extent and Severity Accuracy for Damage Case SB 2 Using TB Pseudo β_j

Damage Extent (in)		Error	Damage Severity (%)		Error (%)
True	Predicted	(%)	True	Predicted Lower Bound/Upper Bound	
4.8	9.0	-2.9	-5.0	-3.5/-5.7	30.0/-14.0

Damage Case SB 3

Figures 7.6 and 7.7 depict the damage prediction results for Damage Case SB 3 using the damage indicator TB Pseudo β_j. Tables 7.5 and 7.6 tabulate the performance of the damage detection methodology for the damage case.

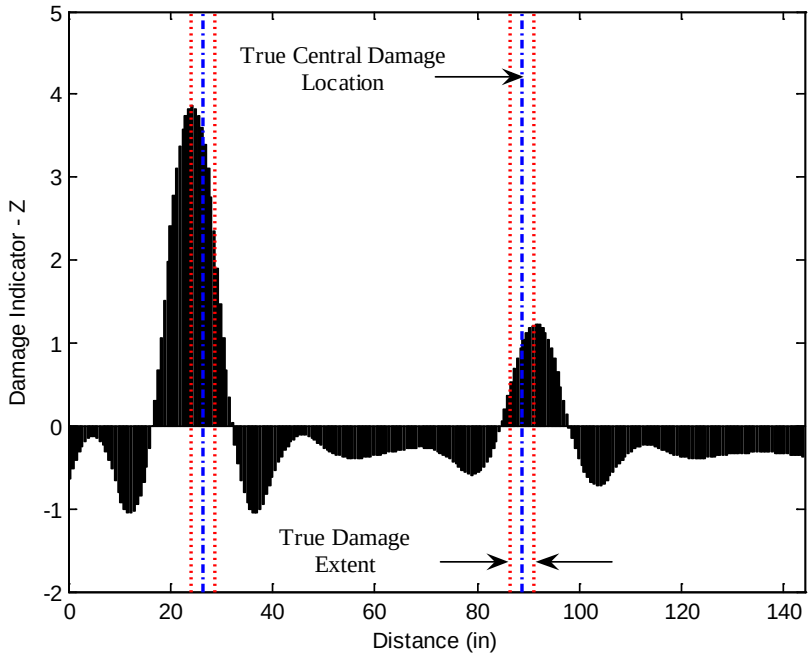

Figure 7.6 Damage Localization Result for Damage Case SB 3 Using TB Pseudo β_j

Table 7.5 Assessment of the Damage Localization Accuracy for Damage Case SB 3 Using TB Pseudo β_j

Damage Central Location (in)		Error (%)	$P(T \subset P)$
True	Predicted		
26.4	24.3	1.5	100%
88.8	91.5	-1.9	100%

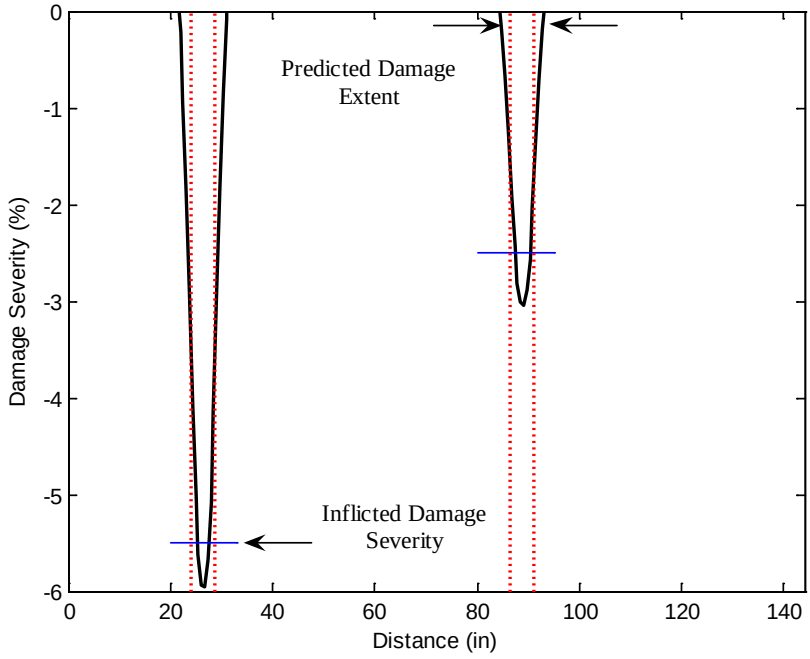

Figure 7.7 Damage Extent and Severity Estimate for Damage Case SB 3 Using TB Pseudo β_j

Table 7.6 Assessment of the Damage Extent and Severity Accuracy for Damage Case SB 3 Using TB Pseudo β_j

Damage Extent (in)		Error (%)	Damage Severity (%)		Error (%)
True	Predicted		True	Predicted Lower Bound/Upper Bound	
4.8	9.6	-3.3	-5.5	-3.4/-6.0	38.2/-9.1
4.8	8.4	-2.5	-2.5	-1.8/-3.0	28.0/-20.0

Damage Case SB 4

Figures 7.8 and 7.9 depict the damage prediction results for Damage Case SB 4 using the damage indicator TB Pseudo β_j. Tables 7.7 and 7.8 tabulate the performance of the damage detection methodology for the damage case.

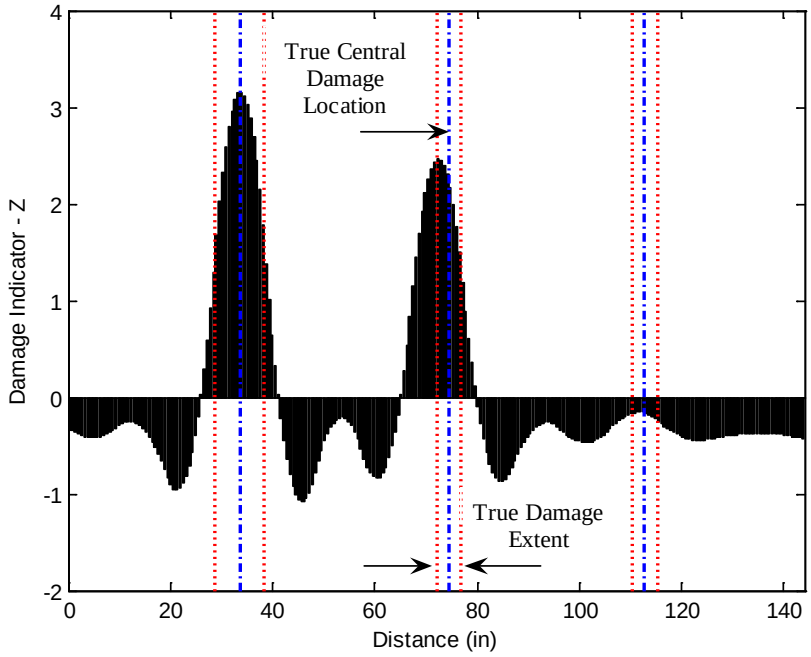

Figure 7.8 Damage Localization Result for Damage Case SB 4 Using TB Pseudo β_j

Table 7.7 Assessment of the Damage Localization Accuracy for Damage Case SB 4 Using TB Pseudo β_j

Damage Central Location (in)		Error (%)	$P(T \subset P)$
True	Predicted		
33.6	33.9	-0.2	100%
74.4	72.3	1.5	100%
112.8	No	100.0	0%

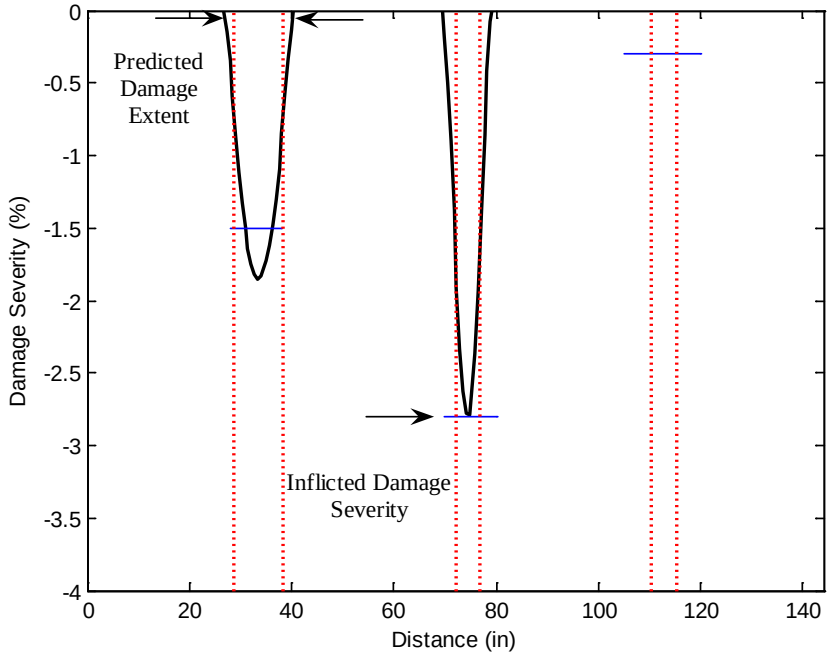

Figure 7.9 Damage Extent and Severity Estimate for Damage Case SB 4 Using TB Pseudo β_j

Table 7.8 Assessment of the Damage Extent and Severity Accuracy for Damage Case SB 4 Using TB Pseudo β_j

Damage Extent (in)		Error	Damage Severity (%)		Error (%)
True	Predicted	(%)	True	Predicted Lower Bound/Upper Bound	
9.6	13.8	-2.9	-1.5	-1.1/-1.8	26.7/-20.0
4.8	9.6	-3.3	-2.8	-1.6/-2.8	42.9/0.0
4.8	No	100.0	-0.3	No/No	100.0/100.0

Damage Case SB 5

Figures 7.10 and 7.11 depict the damage prediction results for Damage Case SB 5 using the damage indicator TB Pseudo β_j. Tables 7.9 and 7.10 tabulate the performance of the damage detection methodology for the damage case.

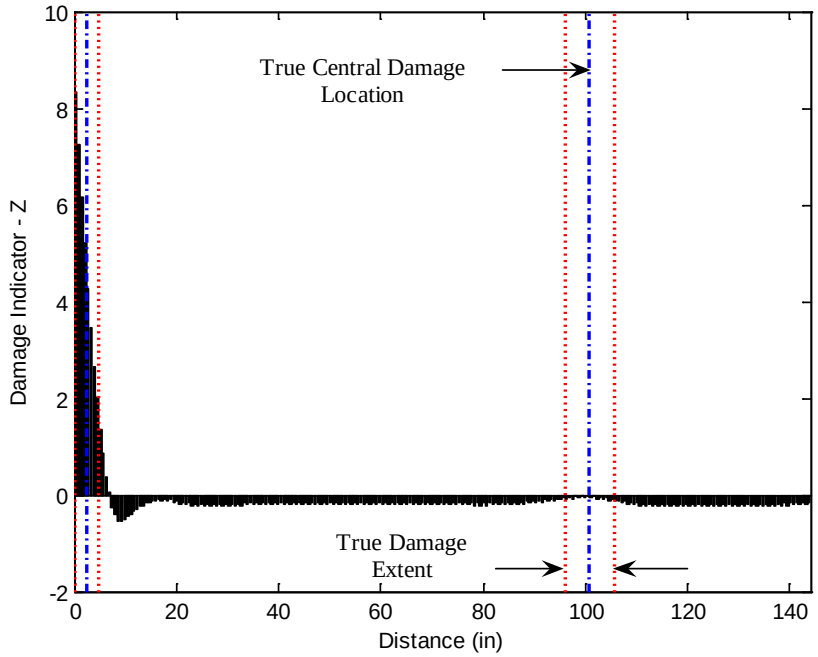

Figure 7.10 Damage Localization Result for Damage Case SB 5 Using TB Pseudo β_j

Table 7.9 Assessment of the Damage Localization Accuracy for Damage Case SB 5 Using TB Pseudo β_j

Damage Central Location (in)		Error (%)	$P(T \subset P)$
True	Predicted		
2.4	0.3	1.5	100%
100.8	No	100.0	0%

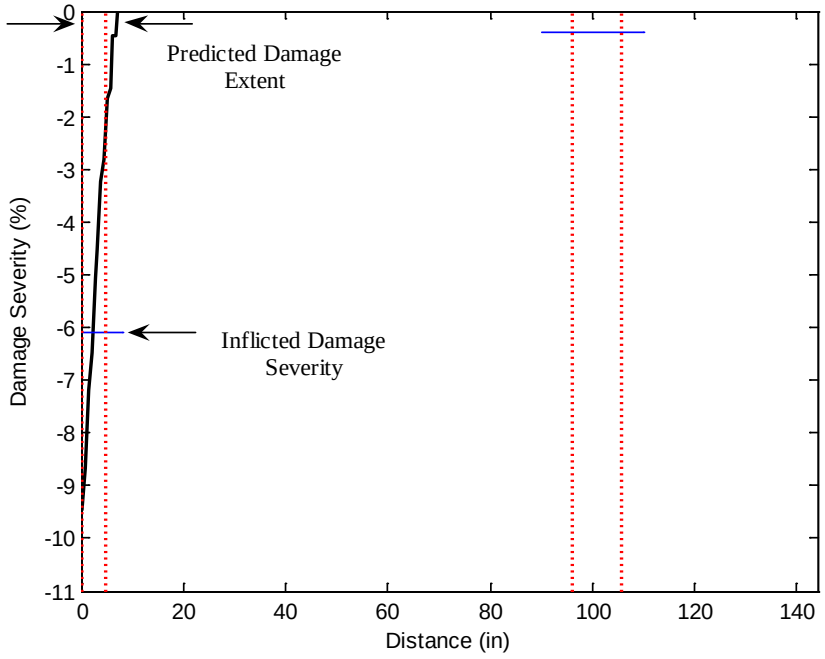

Figure 7.11 Damage Extent and Severity Estimate for Damage Case SB 5 Using TB Pseudo β_j

Table 7.10 Assessment of the Damage Extent and Severity Accuracy for Damage Case SB 5 Using TB Pseudo β_j

Damage Extent (in)		Error (%)	Damage Severity (%)		Error (%)
True	Predicted		True	Predicted Lower Bound/Upper Bound	
4.8	7.5	-1.9	-6.1	-4.4/-9.5	27.9/-55.7
9.6	No	100.0	-0.4	No/No	100/100

The Intermediate Beam

Damage detection results for the intermediate beam are presented in this subsection. The modal flexibility is utilized to approximate the pre- and post-damaged nodal rotations of the beam axis. Cubic spline functions with 0.5 in. uniform intervals are used to generate a finer sensor layout along the length the beam. This procedure leads to 241 nodal points. Central difference approximation of the first derivative is used to compute the first derivative of the rotation after interpolation.

Damage Case IB 1

Figures 7.12 and 7.13 depict the damage prediction results for Damage Case IB 1 using the damage indicator TB Pseudo β_j. Tables 7.11 and 7.12 tabulate the performance of the damage detection methodology for the damage case.

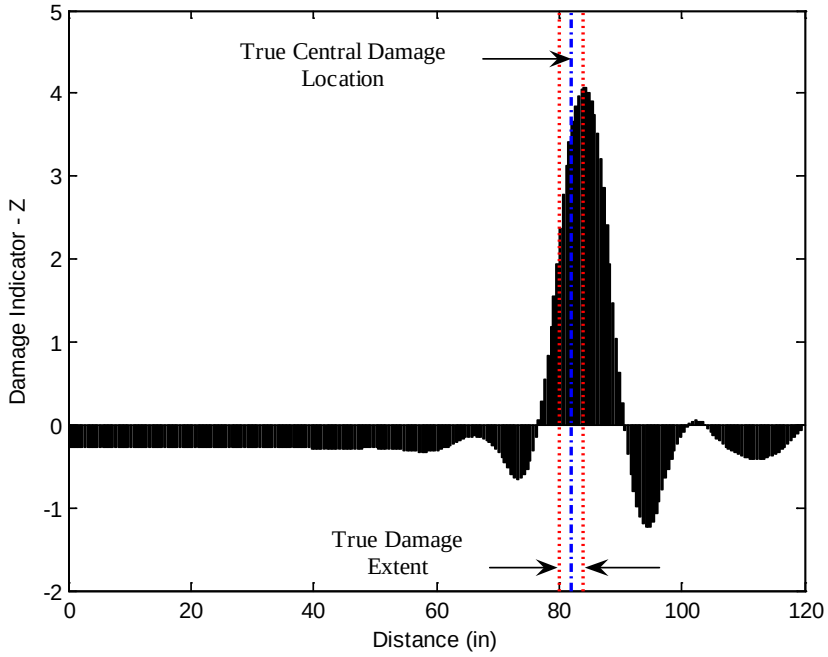

Figure 7.12 Damage Localization Result for Damage Case IB 1 Using TB Pseudo β_j

Table 7.11 Assessment of the Damage Localization Accuracy for Damage Case IB 1 Using TB Pseudo β_j

Damage Central Location (in)		Error (%)	$P(T \subset P)$
True	Predicted		
82.0	84.3	-1.9	100%

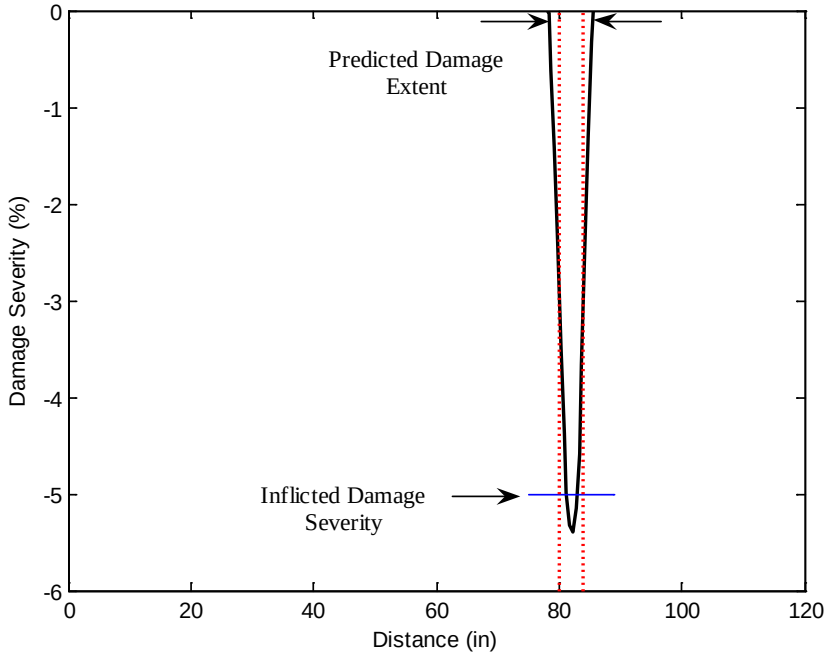

Figure 7.13 Damage Extent and Severity Estimate for Damage Case IB 1 Using TB Pseudo β_j

Table 7.12 Assessment of the Damage Extent and Severity Accuracy for Damage Case IB 1 Using TB Pseudo β_j

Damage Extent (in)		Error (%)	Damage Severity (%)		Error (%)
True	Predicted		True	Predicted Lower Bound/Upper Bound	
4.0	7.5	-2.9	-5.0	-3.1/-5.4	38.0/-8.0

Damage Case IB 2

Figures 7.14 and 7.15 depict the damage prediction results for Damage Case IB 2 using the damage indicator TB Pseudo β_j. Tables 7.13 and 7.14 tabulate the performance of the damage detection methodology for the damage case.

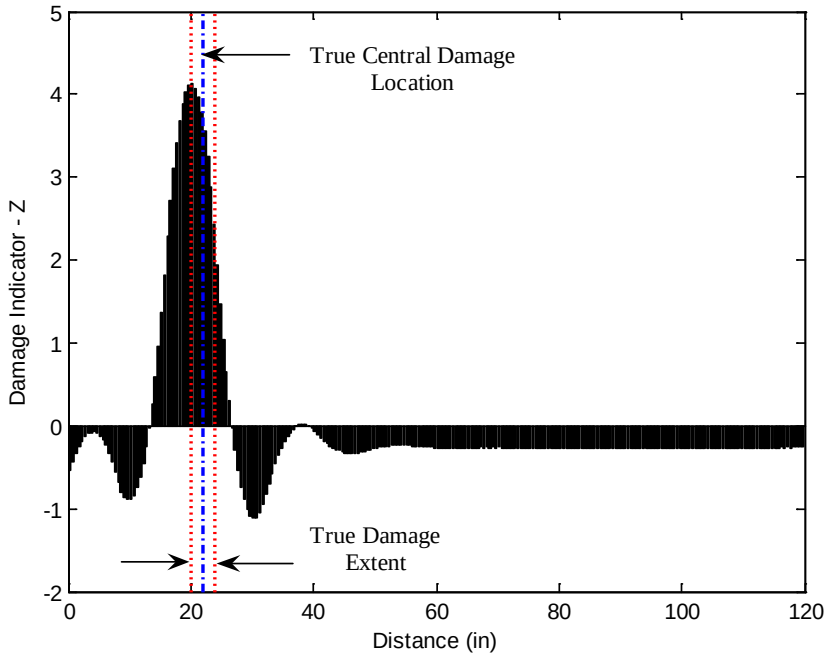

Figure 7.14 Damage Localization Result for Damage Case IB 2 Using TB Pseudo β_j

Table 7.13 Assessment of the Damage Localization Accuracy for Damage Case IB 2 Using TB Pseudo β_j

Damage Central Location (in)		Error (%)	$P(T \subset P)$
True	Predicted		
22.0	20.3	1.4	100%

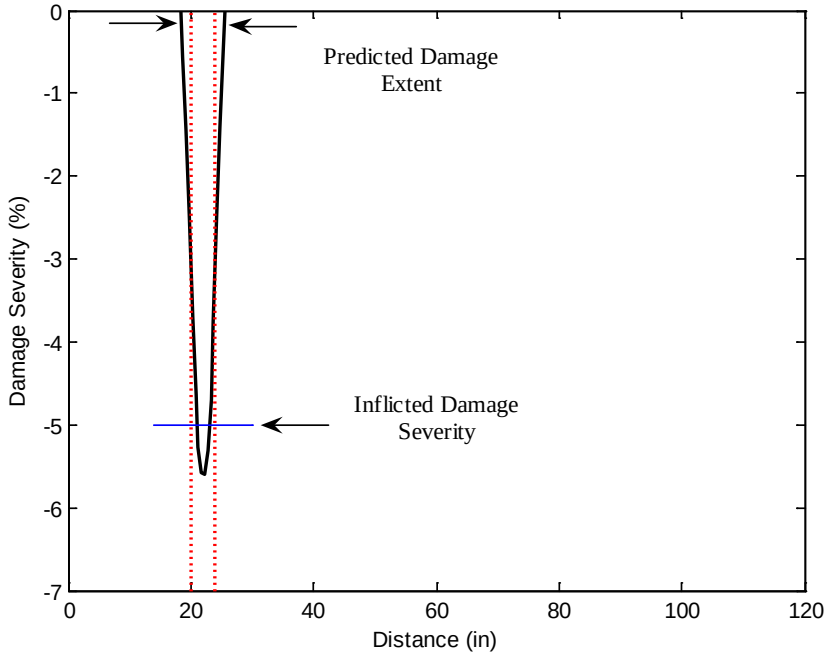

Figure 7.15 Damage Extent and Severity Estimate for Damage Case IB 2 Using TB Pseudo β_j

Table 7.14 Assessment of the Damage Extent and Severity Accuracy for Damage Case IB 2 Using TB Pseudo β_j

Damage Extent (in)		Error (%)	Damage Severity (%)		Error (%)
True	Predicted		True	Predicted Lower Bound/Upper Bound	
4.0	7.5	-2.9	-5.0	-3.4/-5.6	32.0/-12.0

Damage Case IB 3

Figures 7.16 and 7.17 depict the damage prediction results for Damage Case IB 3 using the damage indicator TB Pseudo β_j. Tables 7.15 and 7.16 tabulate the performance of the damage detection methodology for the damage case.

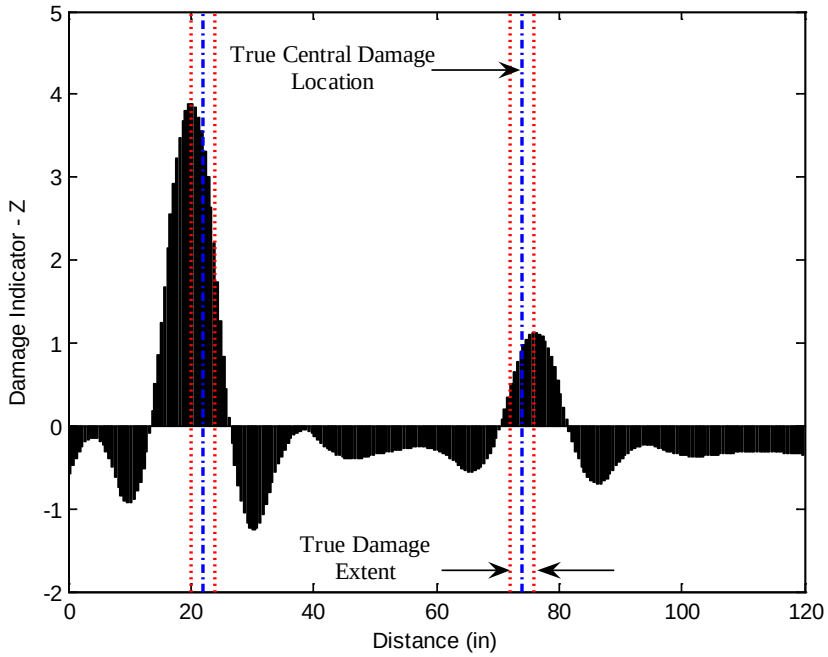

Figure 7.16 Damage Localization Result for Damage Case IB 3 Using TB Pseudo β_j

Table 7.15 Assessment of the Damage Localization Accuracy for Damage Case IB 3 Using TB Pseudo β_j

Damage Central Location (in)		Error (%)	$P(T \subset P)$
True	Predicted		
22.0	20.3	1.4	100%
74.0	76.3	-1.9	100%

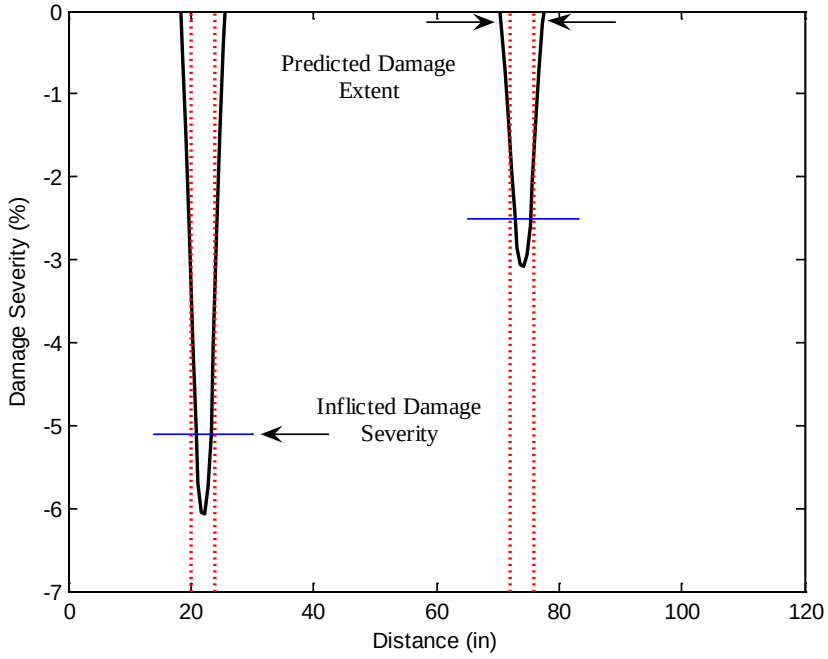

Figure 7.17 Damage Extent and Severity Estimate for Damage Case IB 3 Using TB Pseudo β_j

Table 7.16 Assessment of the Damage Extent and Severity Accuracy for Damage Case IB 3 Using TB Pseudo β_j

Damage Extent (in)		Error (%)	Damage Severity (%)		Error (%)
True	Predicted		True	Predicted Lower Bound/Upper Bound	
4.0	7.5	-2.9	-5.1	-3.7/-6.1	27.5/-19.6
4.0	7.5	-2.9	-2.5	-1.8/-3.1	28.0/-24.0

Damage Case IB 4

Figures 7.18 and 7.19 depict the damage prediction results for Damage Case IB 4 using the damage indicator TB Pseudo β_j. Tables 7.17 and 7.18 tabulate the performance of the damage detection methodology for the damage case.

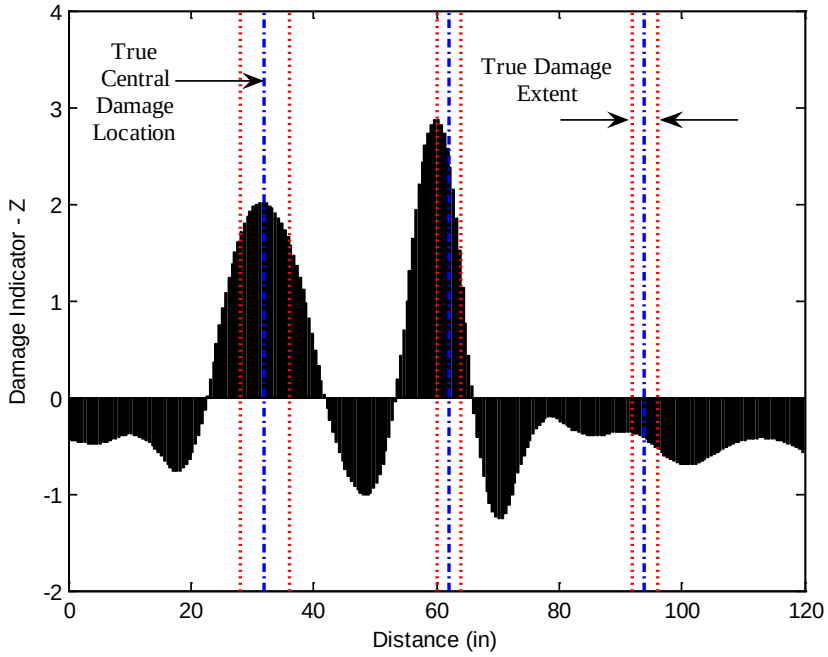

Figure 7.18 Damage Localization Result for Damage Case IB 4 Using TB Pseudo β_j

Table 7.17 Assessment of the Damage Localization Accuracy for Damage Case IB 4 Using TB Pseudo β_j

Damage Central Location (in)		Error (%)	$P(T \subset P)$
True	Predicted		
32.0	31.8	0.2	100%
62.0	59.8	1.8	100%
94.0	No	100.0	0%

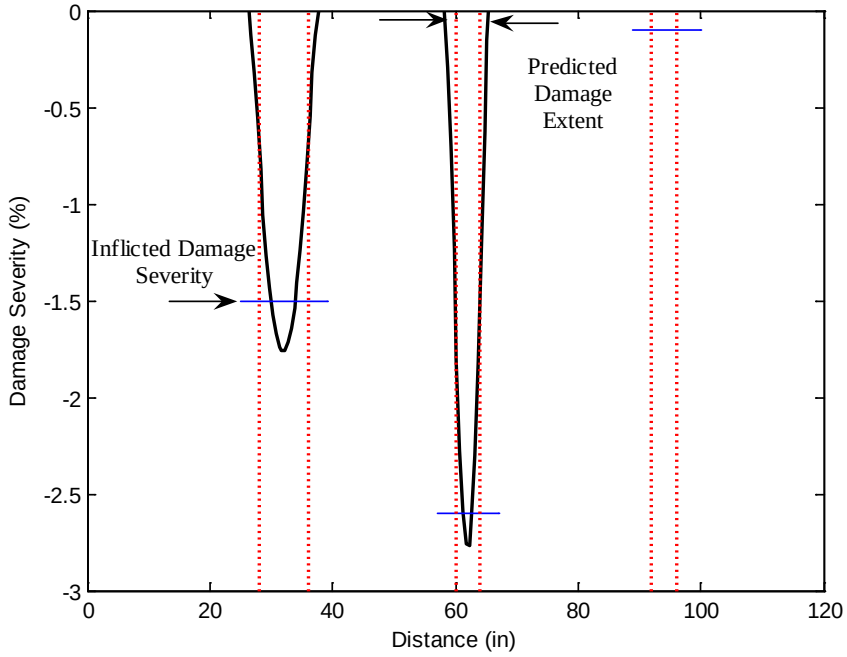

Figure 7.19 Damage Extent and Severity Estimate for Damage Case IB 4 Using TB Pseudo β_j

Table 7.18 Assessment of the Damage Extent and Severity Accuracy for Damage Case IB 4 Using TB Pseudo β_j

Damage Extent (in)		Error (%)	Damage Severity (%)		Error (%)
True	Predicted		True	Predicted Lower Bound/Upper Bound	
8.0	11.5	-2.9	-1.5	-1.1/-1.8	26.7/-20.0
4.0	7.0	-2.5	-2.6	-1.7/-2.8	34.6/-7.7
4.0	No	100.0	-0.1	No	100.0

Damage Case IB 5

Figures 7.20 and 7.21 depict the damage prediction results for Damage Case IB 5 using the damage indicator TB Pseudo β_j. Tables 7.19 and 7.20 tabulate the performance of the damage detection methodology for the damage case.

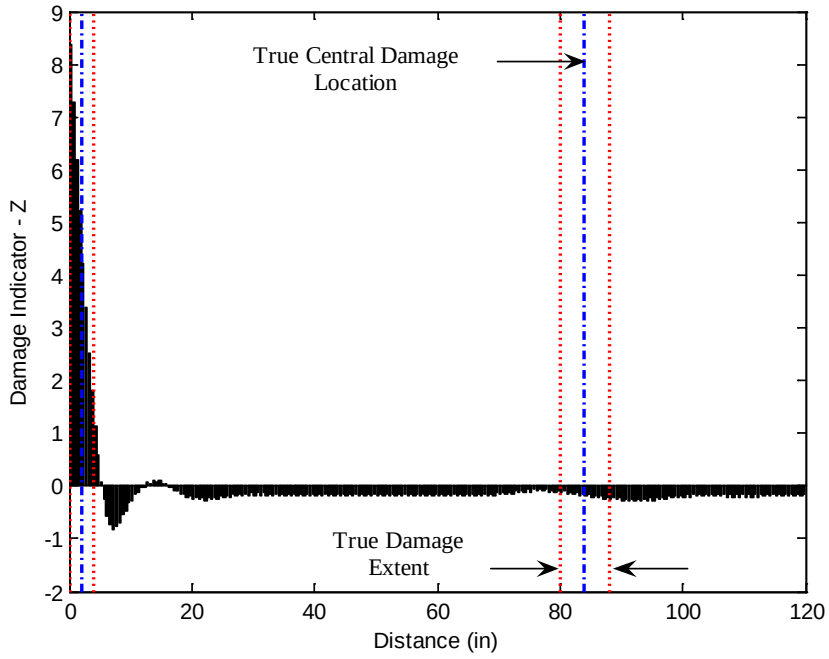

Figure 7.20 Damage Localization Result for Damage Case IB 5 Using TB Pseudo β_j

Table 7.19 Assessment of the Damage Localization Accuracy for Damage Case IB 5 Using TB Pseudo β_j

Damage Central Location (in)		Error (%)	$P(T \subset P)$
True	Predicted		
2.0	0.3	1.4	100%
84.0	No	100.0	0%

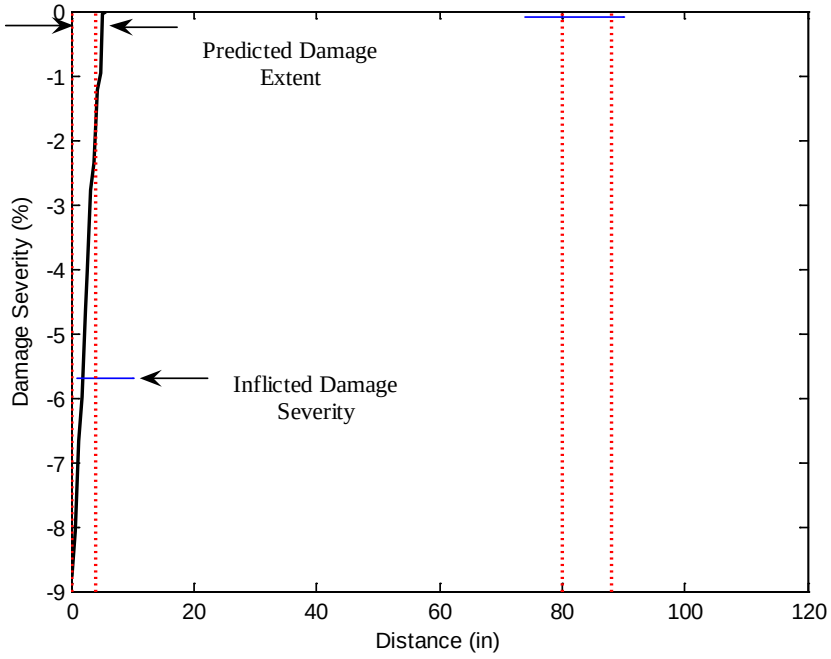

Figure 7.21 Damage Extent and Severity Estimate for Damage Case IB 5 Using TB Pseudo β_j

Table 7.20 Assessment of the Damage Extent and Severity Accuracy for Damage Case IB 5 Using TB Pseudo β_j

Damage Extent (in)		Error (%)	Damage Severity (%)		Error (%)
True	Predicted		True	Predicted Lower Bound/Upper Bound	
4.0	5.8	-1.5	-5.7	-3.9/-8.8	31.6/-54.4
8.0	No	100.0	-0.1	No/No	100/100

The Deep Beam

Damage detection results for the deep beam are presented in this subsection. The modal flexibility is utilized to approximate the pre- and post-damaged nodal rotations of the beam axis. Cubic spline functions with 0.3 in. uniform interval are used for interpolation in order to generate a finer sensor layout along the length the beam. This leads to 201 nodal points. Central difference approximation of the first derivative is used to compute the first derivative of the rotation after interpolation.

Damage Case DB 1

Figures 7.22 and 7.23 depict the damage prediction results for Damage Case DB 1 using the damage indicator TB Pseudo β_j. Tables 7.21 and 7.22 tabulate the performance of the damage detection methodology for the damage case.

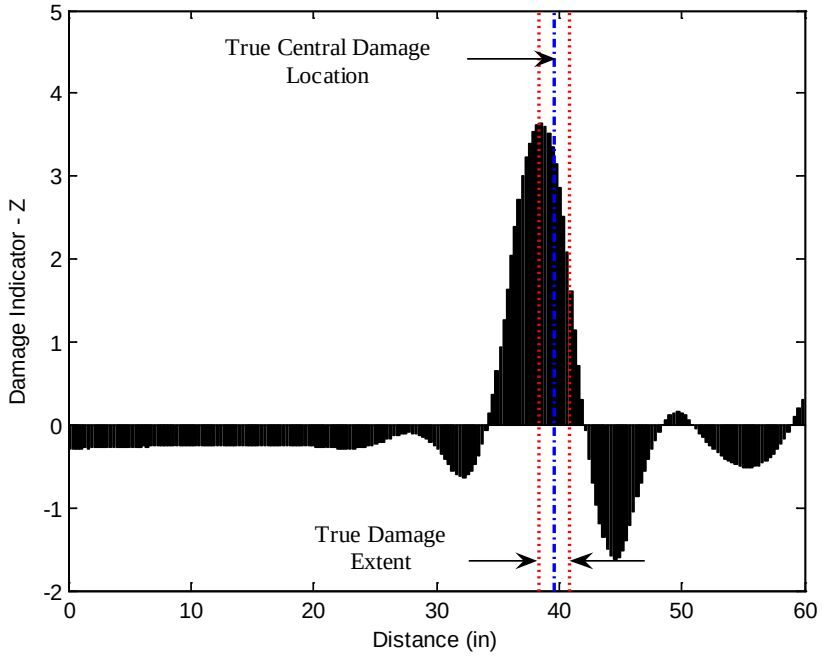

Figure 7.22 Damage Localization Result for Damage Case DB 1 Using TB Pseudo β_j

Table 7.21 Assessment of the Damage Localization Accuracy for Damage Case DB 1 Using TB Pseudo β_j

Damage Central Location (in)		Error (%)	$P(T \subset P)$
True	Predicted		
39.6	38.6	1.7	100%

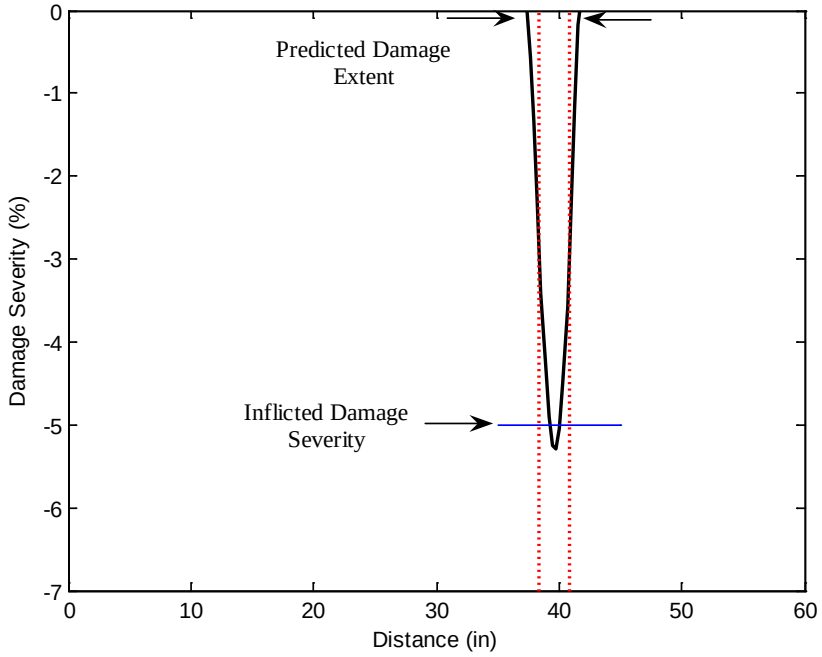

Figure 7.23 Damage Extent and Severity Estimate for Damage Case DB 1 Using TB Pseudo β_j

Table 7.22 Assessment of the Damage Extent and Severity Accuracy for Damage Case DB 1 Using TB Pseudo β_j

Damage Extent (in)		Error (%)	Damage Severity (%)		Error (%)
True	Predicted		True	Predicted Lower Bound/Upper Bound	
2.4	4.5	-3.5	-5.0	-3.2/-5.3	36.0/-6.0

Damage Case DB 2

Figures 7.24 and 7.25 depict the damage prediction results for Damage Case DB 2 using the damage indicator TB Pseudo β_j. Tables 7.23 and 7.24 tabulate the performance of the damage detection methodology for the damage case.

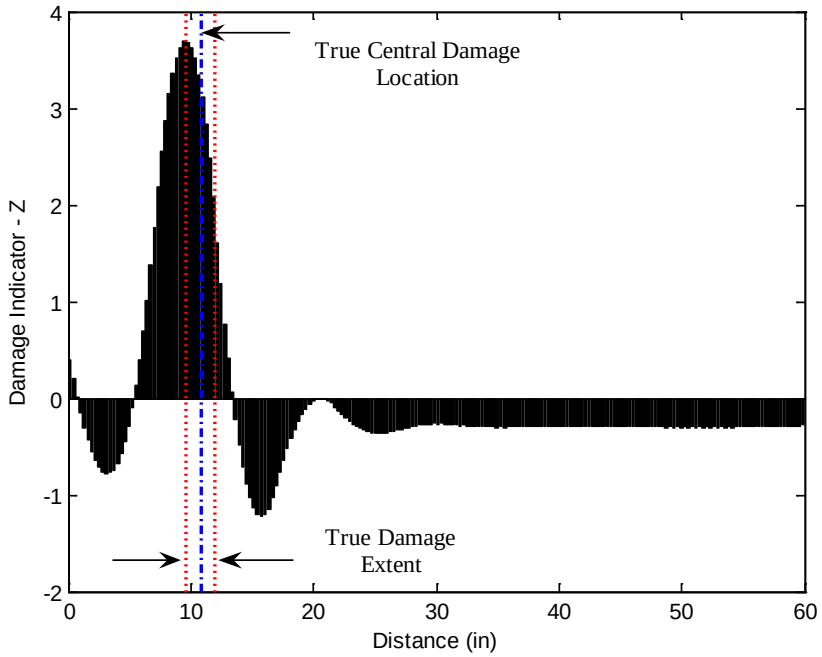

Figure 7.24 Damage Localization Result for Damage Case DB 2 Using TB Pseudo β_j

Table 7.23 Assessment of the Damage Localization Accuracy for Damage Case DB 2 Using TB Pseudo β_j

Damage Central Location (in)		Error (%)	$P(T \subset P)$
True	Predicted		
10.8	9.8	1.7	100%

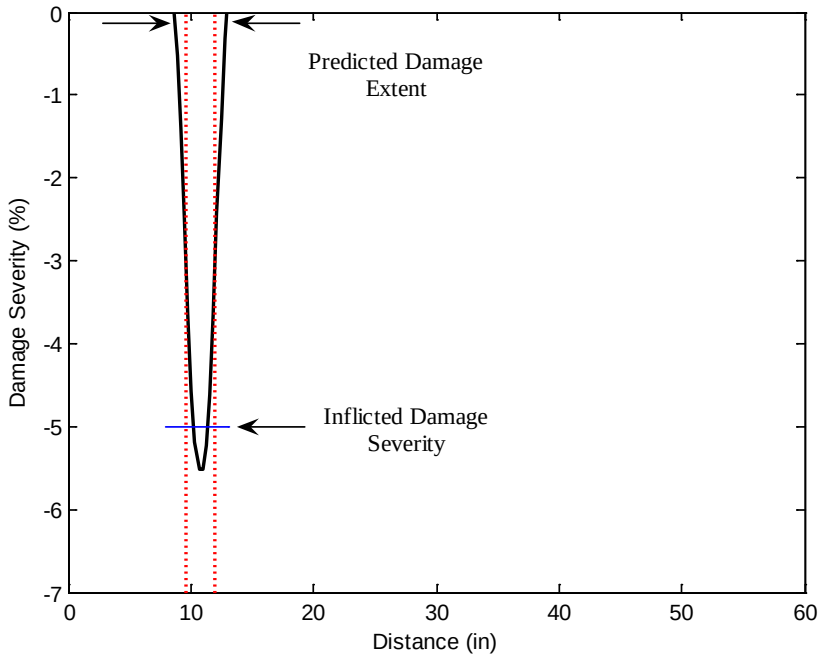

Figure 7.25 Damage Extent and Severity Estimate for Damage Case DB 2 Using TB Pseudo β_j

Table 7.24 Assessment of the Damage Extent and Severity Accuracy for Damage Case DB 2 Using TB Pseudo β_j

Damage Extent (in)		Error	Damage Severity (%)		Error (%)
True	Predicted	(%)	True	Predicted Lower Bound/Upper Bound	
2.4	4.5	-3.5	-5.0	-3.3/-5.5	34.0/-10.0

Damage Case DB 3

Figures 7.26 and 7.27 depict the damage prediction results for Damage Case DB 3 using the damage indicator TB Pseudo β_j. Tables 7.25 and 7.26 tabulate the performance of the damage detection methodology for the damage case.

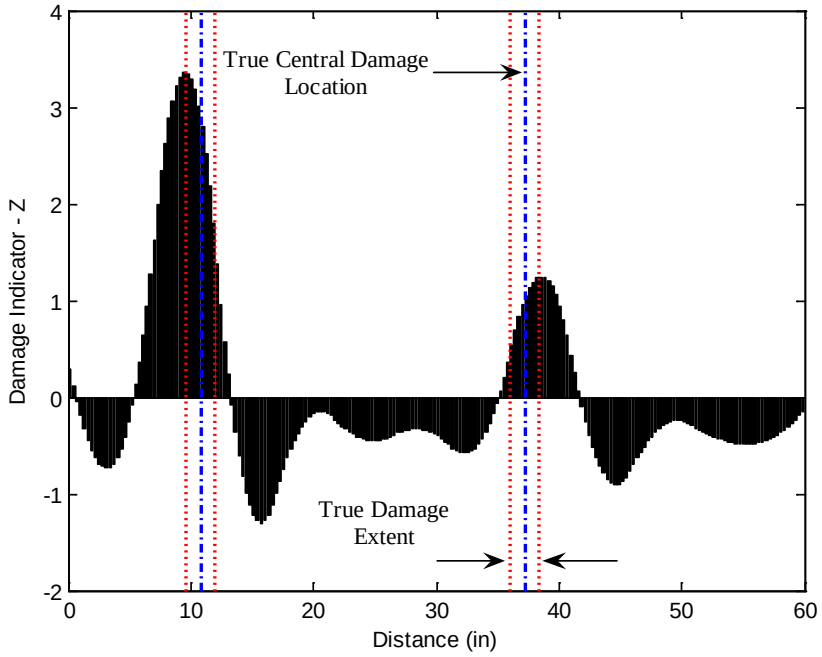

Figure 7.26 Damage Localization Result for Damage Case DB 3 Using TB Pseudo β_j

Table 7.25 Assessment of the Damage Localization Accuracy for Damage Case DB 3 Using TB Pseudo β_j

Damage Central Location (in)		Error (%)	$P(T \subset P)$
True	Predicted		
10.8	9.8	1.7	100%
37.2	38.6	-2.3	100%

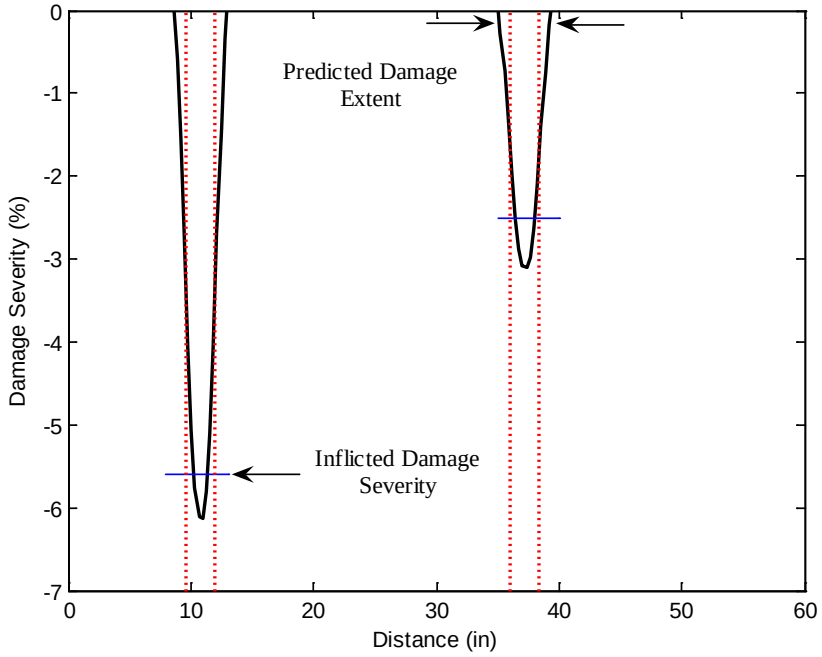

Figure 7.27 Damage Extent and Severity Estimate for Damage Case DB 3 Using TB Pseudo β_j

Table 7.26 Assessment of the Damage Extent and Severity Accuracy for Damage Case DB 3 Using TB Pseudo β_j

Damage Extent (in)		Error (%)	Damage Severity (%)		Error (%)
True	Predicted		True	Predicted Lower Bound/Upper Bound	
2.4	4.5	-3.5	-5.6	-3.7/-6.1	33.9/-8.9
2.4	4.2	-3.0	-2.5	-1.8/-3.1	28.0/-24.0

Damage Case DB 4

Figures 7.28 and 7.29 depict the damage prediction results for Damage Case DB 4 using the damage indicator TB Pseudo β_j. Tables 7.27 and 7.28 tabulate the performance of the damage detection methodology for the damage case.

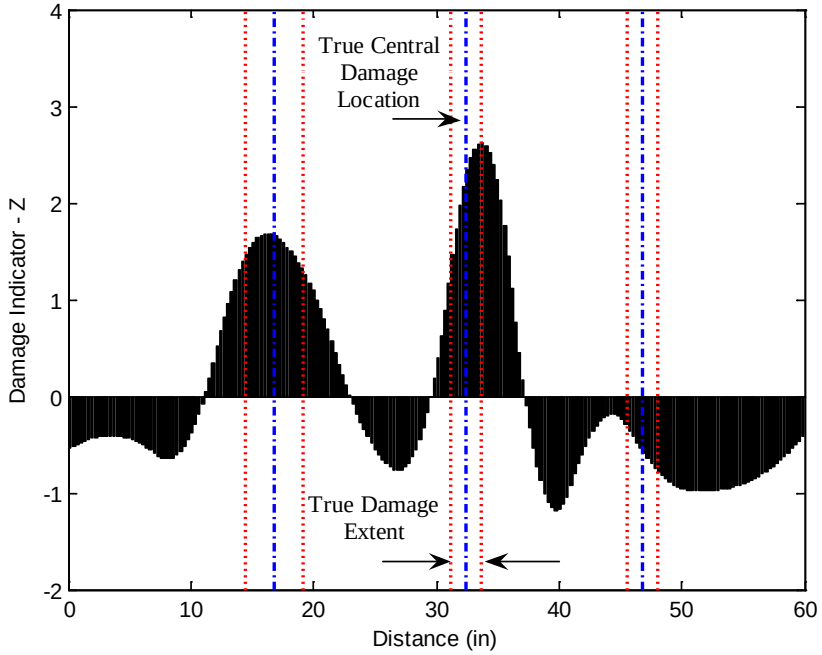

Figure 7.28 Damage Localization Result for Damage Case DB 4 Using TB Pseudo β_j

Table 7.27 Assessment of the Damage Localization Accuracy for Damage Case DB 4 Using TB Pseudo β_j

Damage Central Location (in)		Error (%)	$P(T \subset P)$
True	Predicted		
16.8	16.4	0.7	100%
32.4	33.8	-2.3	100%
46.8	No	100.0	0%

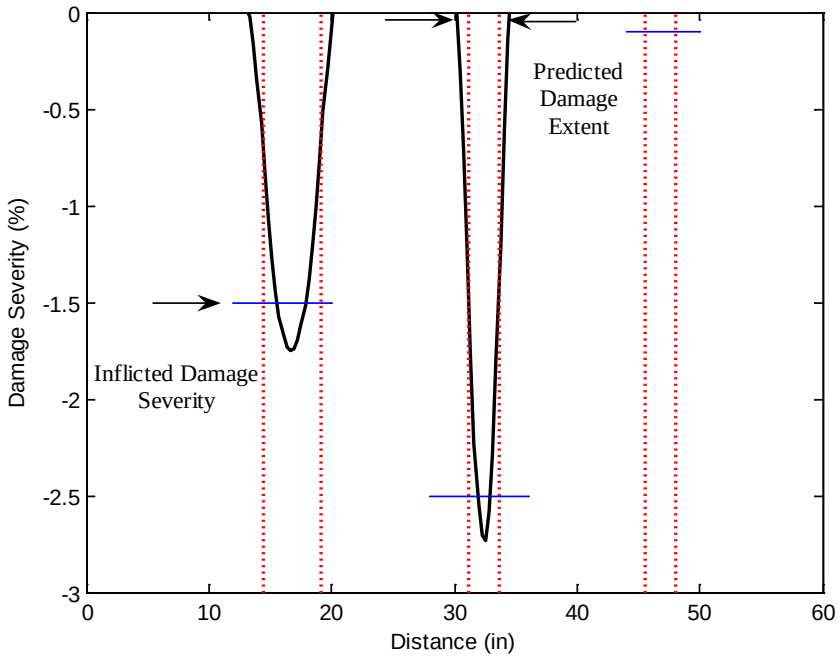

Figure 7.29 Damage Extent and Severity Estimate for Damage Case DB 4 Using TB Pseudo β_j

Table 7.28 Assessment of the Damage Extent and Severity Accuracy for Damage Case DB 4 Using TB Pseudo β_j

Damage Extent (in)		Error (%)	Damage Severity (%)		Error (%)
True	Predicted		True	Predicted Lower Bound/Upper Bound	
4.8	7.2	-4.0	-1.5	-1.1/-1.8	26.7/-20.0
2.4	4.5	-3.5	-2.5	-1.5/-2.7	40.0/-8.0
2.4	No	100.0	-0.1	No/No	100/100

Damage Case DB 5

Figures 7.30 and 7.31 depict the damage prediction results for Damage Case DB 5 using the damage indicator TB Pseudo β_j. Tables 7.29 and 7.30 tabulate the performance of the damage detection methodology for the damage case.

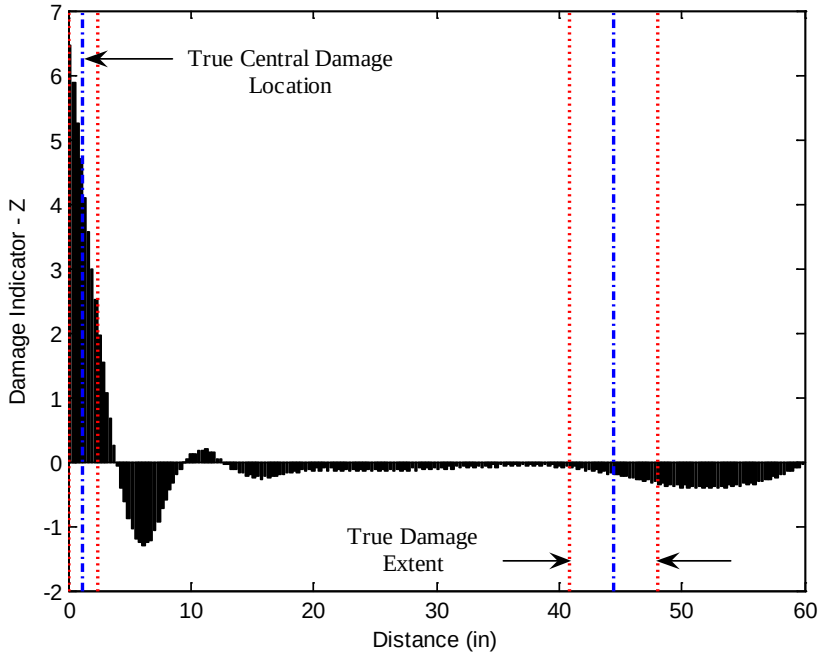

Figure 7.30 Damage Localization Result for Damage Case DB 5 Using TB Pseudo β_j

Table 7.29 Assessment of the Damage Localization Accuracy for Damage Case DB 5 Using TB Pseudo β_j

Damage Central Location (in)		Error (%)	$P(T \subset P)$
True	Predicted		
1.2	0.2	1.7	100%
44.4	No	100.0	0%

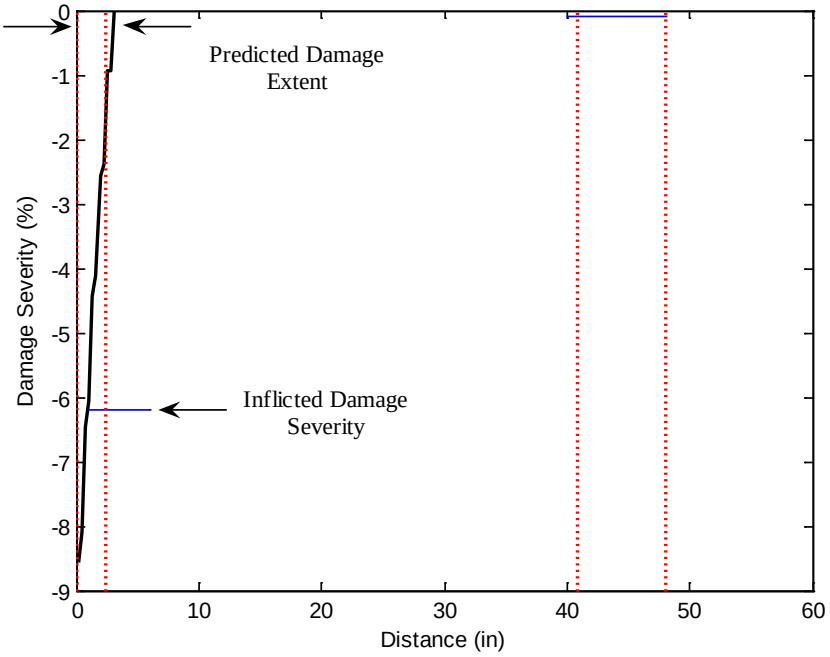

Figure 7.31 Damage Extent and Severity Estimate for Damage Case DB 5 Using TB Pseudo β_j

Table 7.30 Assessment of the Damage Extent and Severity Accuracy for Damage Case DB 5 Using TB Pseudo β_j

Damage Extent (in)		Error (%)	Damage Severity (%)		Error (%)
True	Predicted		True	Predicted Lower Bound/Upper Bound	
2.4	3.2	-0.7	-6.2	-4.5/-8.6	27.4/-38.7
7.2	No	6.0	-0.1	No/No	100/100

DISCUSSION OF RESULTS

Based on the damage prediction results, the following observations can be made regarding the performance of the TB Pseudo Method:

1. Damage prediction results presented in this chapter are very close to the damage prediction results presented in Chapter VI. This is an expected result since similar assumptions were utilized in formulating the damage indicators of the TB Pseudo and TB Direct methods. It is remarkable that the two methods offered such similar damage prediction results, since the final damage indices appear to be entirely independent from one another.

2. The results of the case studies indicated that local inspection is possible with the TB Pseudo Method through reducing the size of the system of linear equations given in Eq. (7.12).

3. Utilizing the results of the case studies presented above, similar conclusions can be made to the ones given in Chapter VI (through using TB Direct $\beta_j{}^M$) regarding the accuracy of damage localization, damage extent prediction, and damage severity estimation. The accuracy of damage localization is not function of the aspect ratio and remains practically the same for any type of beam (slender, intermediate, or deep). Excluding the two FN predictions in Damage Cases 4 and 5, independent of the beam type, the probability of zooming in on the damage was 100%. The center of the true and predicted damage extends coincided precisely for all damage scenarios. As far as damage severity estimation is concerned, the inflicted damage severity always remains in between the lower and upper bound severity estimates, and is likely to be closer to the upper bound estimate than the lower bound estimate. The range and magnitude of the error in the prediction of the accuracy of the damage severity estimate does not depend on the aspect ratio of the beam.

4. The results of the case studies, which utilize TB Pseudo γ_j for damage detection, were not included to the set of outcomes presented in this chapter. This is mainly to avoid repetition. Since the Timoshenko Beam Theory is an extension of the Euler-Bernoulli Beam Theory (it was shown in Chapter II that the latter may conveniently be obtained from the former upon neglecting the transverse shear deformations), and EB Pseudo β_j and EB Pseudo γ_j provided almost identical damage prediction results, similar outcomes are expected when TB methods are used for damage prediction. Due to this reason, TB Pseudo β_j was solely utilized for damage detection in this chapter.

SUMMARY AND CONCLUSIONS

An explicit damage index methodology based on the stress-displacement relations of the Timoshenko beam theory was developed. Damage was expressed in terms of local decreases in the flexural stiffness of structural members. Utilizing the concept of discontinuity, these local decreases were represented as singularities in the flexural stiffness distribution of the beam. Utilizing the concept of discontinuity developed in Chapter II in conjunction with the derivatives of cross sectional rotation, the location and magnitude of local stiffness degradations were identified. The performance of the proposed damage detection methodology was evaluated by using the response data collected from the numerical experiments of Chapter III. It was concluded that the accuracy of damage prediction is not function of the aspect ratio and remains fairly the same for any type of beam (slender, intermediate, or deep) when using a damage detection theory that is developed on the basis of the Timoshenko beam theory.

CHAPTER VIII

DAMAGE INDICES DERIVED FROM LINEAR ELASTICITY THEORY

INTRODUCTION

The objective of this chapter is to develop explicit damage index methodologies based on linear elasticity solutions. It will be shown that if the beam is subjected to the same external loads before and after damage, utilizing Saint-Venant's principle, local changes in the structural and material properties of beam-type structural elements can be expressed in terms of pre-damage and post-damage strain distributions.

To accomplish the stated objective, this chapter is divided into four sections: a section articulating the proposed methodology; a section describing specific structural response parameters utilized in the proposed damage detection algorithm; a section evaluating the performance of the methodology using the numerical experiments introduced in Chapter III; and a section discussing the outcomes of the performed case studies.

PROPOSED METHODOLOGY

Linear elasticity solutions of two-dimensional problems (such as the bending of a beam subject to external loading) involve integration of differential equations of equilibrium under any external force system along with the use of appropriate boundary conditions and the compatibility equation. Three-dimensional elasticity problems may be reduced to two-dimensional problems in such cases as plane stress or plane strain, upon utilizing certain simplifications regarding the state of stress or strain in a body (Ugural and Fenster 2003).

Explicit damage indices based on linear elasticity solutions for bending of a cantilever loaded at the free end, and bending of a beam under uniform loading will be developed in this section utilizing the state of plane stress. It will be shown that if the

beam is subjected to the same external loads before and after damage, utilizing Saint-Venant's principle, local changes in the structural and material properties of beam-type structural elements can be expressed in terms of pre-damage and post-damage strain distributions.

Damage Indices for a Cantilever Beam Loaded at its Free End

Consider, as shown in Figure 8.1, a rectangular cantilever beam with unit thickness subjected to a concentrated load P at its free end. The cantilever is assumed to be in a state of plane stress.

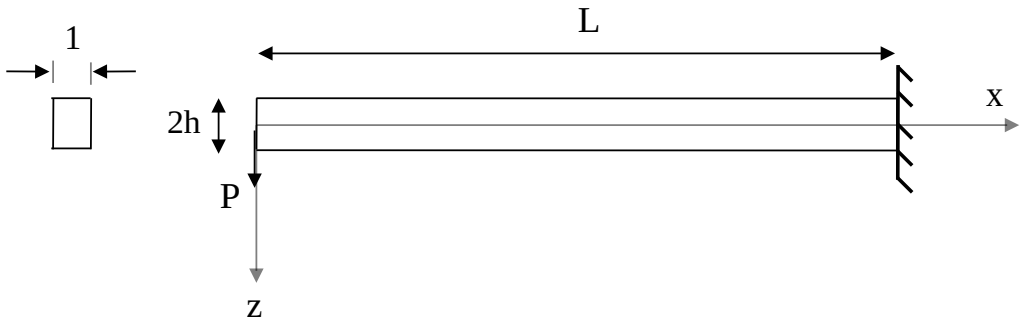

Figure 8.1 Cantilever Beam Loaded at Its Free End

The stress distribution in the cantilever beam depicted above may be given as:

$$\sigma_{xx} = -\frac{Pxz}{I}, \tag{8.1}$$

$$\sigma_{zz} = 0, \text{ and} \tag{8.2}$$

$$\tau_{xz} = -\frac{P}{2I}\left(h^2 - z^2\right) \tag{8.3}$$

where I $\left(\frac{2}{3}h^3\right)$ denotes the moment of inertia of the cross section.

Assuming that the beam's thickness is small compared to its depth $2h$ and linear elastic behavior prevails, the stress-strain relationships for plane stress may be written as:

$$\varepsilon_{xx} = \frac{1}{E}\left(\sigma_{xx} - \nu\sigma_{zz}\right), \tag{8.4}$$

$$\varepsilon_{zz} = \frac{1}{E}\left(\sigma_{zz} - \nu\sigma_{xx}\right), \text{ and} \tag{8.5}$$

$$\gamma_{xz} = \frac{\tau_{xz}}{G} \tag{8.6}$$

The substitution of Eq. (8.4) to (8.6) back into Eq. (8.1) to (8.3) leads to the following expressions (where the strains are written in terms of the applied loads as well as material and cross sectional properties of the cantilever beam):

$$\varepsilon_{xx} = -\frac{Pxz}{EI}, \tag{8.7}$$

$$\varepsilon_{zz} = \frac{\nu Pxz}{EI}, \text{ and} \tag{8.8}$$

$$\gamma_{xz} = -\frac{P}{2GI}\left(h^2 - z^2\right) \tag{8.9}$$

where E, G and ν are the modulus of elasticity, shear modulus and Poisson's ratio of the material, respectively.

By replacing GI in Eq. (8.9) with GA by utilizing $I = \frac{1}{3}Ah^2$, the shear stiffness may be expressed in the more familiar fashion as:

$$\gamma_{xz} = -\frac{3P}{2GA}\left(1-\frac{z^2}{h^2}\right) \tag{8.10}$$

where A denotes the cross sectional area ($2h$) of the beam.

In order to obtain the displacement components at a point, the following stress-displacement relationships must be used:

$$\varepsilon_{xx} = \frac{\partial u}{\partial x}, \tag{8.11}$$

$$\varepsilon_{zz} = \frac{\partial v}{\partial z}, \text{ and} \tag{8.12}$$

$$\gamma_{xz} = \frac{\partial u}{\partial z} + \frac{\partial v}{\partial x} \tag{8.13}$$

Utilizing the strains derived in Eq. (8.7) through (8.10) in conjunction with the boundary conditions:

$$\begin{aligned} &u = v = 0 \\ &\frac{du}{dz} = 0 \end{aligned} \qquad \text{For } x = L \text{ and } z = 0, \tag{8.14}$$

the following equations for elastic displacements may be obtained for the cantilever beam depicted in Figure 8.1:

$$u = \frac{P(L^2 - x^2)z}{2EI} - \frac{\nu\, Pz^3}{6EI} + \frac{Pz^3}{2GAh^2}, \text{ and} \tag{8.15}$$

$$v = \frac{P}{EI}\left[\frac{x^3}{6} + \frac{L^3}{3} + \frac{x}{2}(\nu z^2 - L^2)\right] + \frac{3P}{2GA}(L - x) \tag{8.16}$$

Equations (8.15) and (8.16) are the displacement components in the horizontal and vertical directions respectively. This concludes the elastic solution of the problem and

details of the procedure may be found in any textbook on the theory of elasticity (Timoshenko and Goodier (1951), Ugural and Fenster (2003)).

Now assume that a localized damage is inflicted on the beam which alters the bending and shear stiffnesses as well as Poisson's ratio along the coordinates x and z. Under the same loading conditions as for the undamaged beam, utilizing the expressions given in Eq. (8.7) through (8.10), the strain distribution of the damaged structure may be written as:

$$\varepsilon_{xx}^{*} = -\frac{Pxz}{EI^{*}}, \tag{8.17}$$

$$\varepsilon_{zz}^{*} = \frac{\nu^{*} Pxz}{EI^{*}}, \text{ and} \tag{8.18}$$

$$\gamma_{xz}^{*} = -\frac{3P}{2GA^{*}}\left(1-\frac{z^2}{h^2}\right) \tag{8.19}$$

where the asterisk denotes damage.

Utilizing Saint-Venant's principle as paraphrased by Southwell (1936): "…forces applied at one part of an elastic body will involve stresses which, except in a region close to that part, will depend almost entirely upon their resultant action, and very little upon their distribution.". Here, it is reasonable to assume that measured strains will only reflect the change in material properties at the localized damaged region. Therefore, pre- and post-damage strain distributions may be related to local damage occurred within a structure and a proper mathematical formulation may reveal its extent and severity.

Solving Equations (8.17) through (8.19) for a common external concentrated load P, and substituting these results back into the strain equations given for the undamaged beam (Eq. (8.7) through Eq. (8.10)) leads to:

$$\varepsilon_{xx} = -\frac{-\frac{\varepsilon_{xx}^{*} EI^{*}}{xz} xz}{EI}, \tag{8.20}$$

$$\varepsilon_{zz} = \frac{\nu \frac{\varepsilon_{zz}^{*} EI^{*}}{\nu^{*} xz} xz}{EI}, \text{ and} \tag{8.21}$$

$$\gamma_{xz} = -3 \frac{-\frac{2}{3} \frac{\gamma_{xz}^{*} GA^{*}}{\left(1 - \frac{y^2}{h^2}\right)}}{2GA} \left(1 - \frac{y^2}{h^2}\right) \tag{8.22}$$

Upon simplification, Eq. (8.20) gives the ratio of the pre-damage and post-damage flexural stiffnesses as a ratio of the normal strains measured before and after damage. That is, stiffness damage can be inferred from the pre-damage and post-damage strain measurements:

$$\frac{EI}{EI^{*}} = \frac{\varepsilon_{xx}^{*}}{\varepsilon_{xx}} \tag{8.23}$$

Similarly, simplifying Eq. (8.21) leads to the ratio of flexural stiffness and Poisson's ratio before and after damage in terms of strains measured before and after the inflicted damage. Namely:

$$\frac{\nu^{*}}{\nu} \frac{EI}{EI^{*}} = \frac{\varepsilon_{zz}^{*}}{\varepsilon_{zz}} \tag{8.24}$$

Using the results of Eq. (8.23), Eq. (8.24) reduces into:

$$\frac{\nu^{*}}{\nu} \frac{\varepsilon_{xx}^{*}}{\varepsilon_{xx}} = \frac{\varepsilon_{zz}^{*}}{\varepsilon_{zz}} \tag{8.25}$$

or simply:

$$\frac{\nu}{\nu^*} = \frac{\varepsilon_{zz}}{\varepsilon_{zz}^*}\frac{\varepsilon_{xx}^*}{\varepsilon_{xx}} \tag{8.26}$$

That is the change in Poisson's ratio due to damage may also be expressed in terms of the pre-damage and post-damage strain distributions.

Finally, simplifying Eq. (8.22) gives the ratio of the shear strains measured before and after damage, which are a function of the changes in shear stiffness within the cantilever beam.

$$\frac{GA}{GA^*} = \frac{\gamma_{xz}^*}{\gamma_{xz}} \tag{8.27}$$

In this section, damage indices for bending stiffness, shear stiffness, and Poisson's ratio for the cantilever beam loaded at its free end using the solution from the theory of elasticity have been derived. It will be shown in the subsequent section that the pre-mentioned expressions for damage indices hold for other loading conditions under certain assumptions.

Damage Indices for a Simply Supported Beam Subjected to Uniform Loading

Consider now a simply supported narrow rectangular beam with unit width subjected to a uniformly distributed load of intensity q as shown in Figure 8.2. The stress distribution in the beam may be given as (Timoshenko and Goodier (1951)):

$$\sigma_{xx} = \frac{q}{2I}\left(L^2 - x^2\right)z + \frac{q}{2I}\left(\frac{2}{3}z^2 - \frac{2}{5}h^2\right)z\,, \tag{8.28}$$

$$\sigma_{zz} = -\frac{q}{2I}\left(\frac{1}{3}z^3 - h^2 z + \frac{2}{3}h^3\right), \text{ and} \tag{8.29}$$

$$\tau_{xz} = -\frac{q}{2I}\left(h^2 - z^2\right)x \tag{8.30}$$

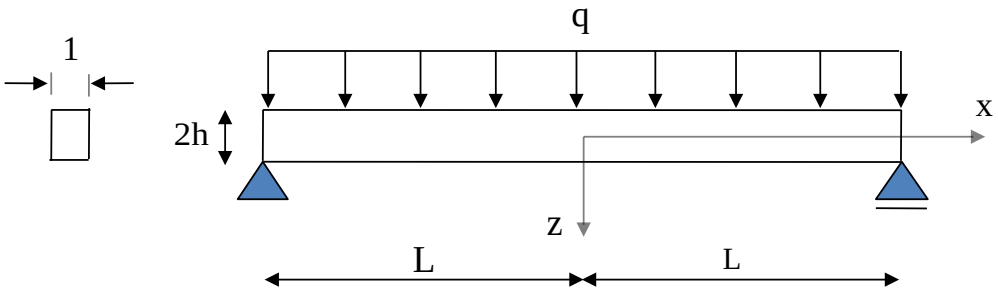

Figure 8.2 Simply Supported Beam with a Uniformly Distributed Load

Assuming this loading condition to be a case of plane stress, and utilizing linear elastic behavior, the strain distribution in the beam may be written as (Timoshenko and Goodier (1951)):

$$\varepsilon_{xx} = \frac{q}{30EI}\left(15zL^2 - 15zx^2 + 10z^3 - 6h^2z + 5\nu z^3 - 15\nu h^2 z + 10\nu h^3\right), \tag{8.31}$$

$$\varepsilon_{zz} = -\frac{q}{30EI}\left(5z^3 - 15h^2z + 10h^3 + 15\nu zL^2 - 15\nu zx^2 + 10\nu z^3 - 6\nu h^2 z\right), \text{ and} \tag{8.32}$$

$$\gamma_{xz} = -\frac{q}{2GA}\left(3h^2 - 3z^2\right)h^2 x \tag{8.33}$$

where I and A denote the moment of inertia $\left(\frac{2}{3}h^3\right)$ and cross sectional area ($2h$) of the beam, respectively.

The displacements in the simply supported beam may be obtained in a similar fashion to manner they were obtained in the cantilever beam described previously. Note that such solutions are available in literature (Timoshenko and Goodier (1951)).

As before, assume that a localized damage is inflicted, which alters the bending, and shear stiffnesses as well as Poisson's ratio along the beam. Under the same uniformly distributed load, strain distribution of the damaged structure may be written as:

$$\varepsilon_{xx}^{\ *} = \frac{q}{30EI^*}\left(15zL^2 - 15zx^2 + 10z^3 - 6h^2z + 5\nu^* z^3 - 15\nu^* h^2 z + 10\nu^* h^3\right), \tag{8.34}$$

$$\varepsilon_{zz}^{\ *} = -\frac{q}{30EI^*}\left(5z^3 - 15h^2z + 10h^3 + 15\nu^* zL^2 - 15\nu^* zx^2 + 10\nu^* z^3 - 6\nu^* h^2 z\right), \tag{8.35}$$

$$\gamma_{xz}^{\ *} = -\frac{q}{2GA^*}\left(3h^2 - 3z^2\right)h^2 x \tag{8.36}$$

where the asterisk denotes damage.

As was done in the cantilever beam problem, solving Equations (8.34) through (8.36) for the distributed load q, and substituting these back into the strain equations given for the undamaged beam (Eq. (8.31) through Eq. (8.33)) leads to the following results after some algebraic manipulation:

$$\varepsilon_{xx} = \frac{\dfrac{30\,EI^*\varepsilon_{xx}^{\ *}}{(a+b\nu^*)}}{30EI}(a+b\nu), \tag{8.37}$$

$$\varepsilon_{zz} = -\frac{-\dfrac{30\,EI^*\varepsilon_{zz}^{\ *}}{(b+a\nu^*)}}{30EI}(b+a\nu), \text{ and} \tag{8.38}$$

$$\gamma_{xz} = -\frac{-\dfrac{2\,GA^*\gamma_{xz}^{\ *}}{(3h^2-3z^2)h^2x}}{2GA}(3h^2-3z^2)h^2x \tag{8.39}$$

where, for simplification the known parameters a and b are given by:

$$a = 15zL^2 - 15zx^2 + 10z^3 - 6h^2 z \text{, and} \tag{8.40}$$

$$b = 5z^3 - 15h^2 z + 10h^3 \tag{8.41}$$

As before, simplifying Eq. (8.39) gives the ratio of the shear strains measured before and after damage, which reflects the changes in shear stiffness within the simply supported beam:

$$\frac{GA}{GA^*} = \frac{\gamma_{xz}^*}{\gamma_{xz}} \tag{8.42}$$

Rearranging Eq. (8.37) and Eq. (8.38) gives two equations containing two unknowns, namely the change in the flexural stiffness and the Poisson's ratio of the damaged beam.

$$\begin{aligned} \frac{EI}{EI^*}\frac{\varepsilon_{xx}}{\varepsilon_{xx}^*}(a + b\nu^*) &= (a + b\nu) \\ \frac{EI}{EI^*}\frac{\varepsilon_{zz}}{\varepsilon_{zz}^*}(b + a\nu^*) &= (b + a\nu) \end{aligned} \tag{8.43}$$

Solving the above system of linear equations leads to:

$$\frac{EI}{EI^*} = \frac{\dfrac{\varepsilon_{zz}}{\varepsilon_{zz}^*}a^2 - \dfrac{\varepsilon_{xx}}{\varepsilon_{xx}^*}b^2 + ab\nu\left(\dfrac{\varepsilon_{zz}}{\varepsilon_{zz}^*} - \dfrac{\varepsilon_{xx}}{\varepsilon_{xx}^*}\right)}{\dfrac{\varepsilon_{zz}}{\varepsilon_{zz}^*}\dfrac{\varepsilon_{xx}}{\varepsilon_{xx}^*}\left(a^2 - b^2\right)} \text{, and} \tag{8.44}$$

$$\nu^* = \frac{ab\left(\dfrac{\varepsilon_{xx}}{\varepsilon_{xx}^*} - \dfrac{\varepsilon_{zz}}{\varepsilon_{zz}^*}\right) + \nu\left(\dfrac{\varepsilon_{xx}}{\varepsilon_{xx}^*}a^2 - \dfrac{\varepsilon_{zz}}{\varepsilon_{zz}^*}b^2\right)}{\dfrac{\varepsilon_{zz}}{\varepsilon_{zz}^*}a^2 - \dfrac{\varepsilon_{xx}}{\varepsilon_{xx}^*}b^2 + ab\nu\left(\dfrac{\varepsilon_{zz}}{\varepsilon_{zz}^*} - \dfrac{\varepsilon_{xx}}{\varepsilon_{xx}^*}\right)} \tag{8.45}$$

where the left hand side of Eq. (8.44) and (8.45) contains the unknown damaged parameters, namely the change in the flexural stiffness and Poisson's ratio of the damaged structure respectively, while the right hand side contains the measured pre-damage and post-damage strains as well as the assumed known value of the Poisson's ratio of the undamaged structure. The terms a and b are given in Eq. (8.40) and (8.41).

Note that the damage indices obtained above are much more complex compared to the indices developed for the case of the cantilever beam presented in the previous section. This result is simply due to the fact that a stress distribution in z direction exists in the simply supported beam whereas it was zero in the cantilever problem. Note that the stress σ_{zz} given in Eq. (8.29) is equal to the intensity of the distributed load at the top of the beam ($z = -h$) and vanishes at the bottom ($z = h$), since the bottom surface is free of any applied load. Except for the case of deep beams (where the depth to length ratio may be as high as 1 to 5), the stress distribution in the z direction is negligible compared to the one along the longitudinal x axis. Thus, for practical purposes, σ_{zz} may assumed to be zero (which is the case in the elementary strength of materials solution). Utilizing the assumption of plane stress and linear elastic behavior, the normal strain distribution (since the distribution of shear strain will not be affected from this modification) given previously in Eq. (8.31) and (8.32) simplify to:

$$\varepsilon_{xx} = \frac{qz}{30EI}\left(15L^2 - 15x^2 + 10z^2 - 6h^2\right), \text{ and} \tag{8.46}$$

$$\varepsilon_{zz} = -\frac{\nu qz}{30EI}\left(15L^2 - 15x^2 + 10z^2 - 6h^2\right) \tag{8.47}$$

The analogous post-damage strain distributions are:

$$\varepsilon_{xx}^{*} = \frac{qz}{30EI^{*}}\left(15L^2 - 15x^2 + 10z^2 - 6h^2\right), \text{ and} \tag{8.48}$$

$$\varepsilon_{zz}^{\ *} = -\frac{\nu^{*} qz}{30EI^{*}}\left(15L^{2} - 15x^{2} + 10z^{2} - 6h^{2}\right) \tag{8.49}$$

Solving Eq. (8.48) for the distributed load q, and substituting these results back into the strain expression given for the undamaged beam, yields the ratio of the normal strains measured before and after damage as a function of the change in the flexural stiffness within the structure.

$$\frac{EI}{EI^{*}} = \frac{\varepsilon_{xx}^{\ *}}{\varepsilon_{xx}} \tag{8.50}$$

Similarly, change in Poisson's ratio due to damage may be expressed in terms of the pre-damage and post-damage strain distributions by utilizing Eq. (8.48), Eq. (8.49) and Eq. (8.50):

$$\frac{\nu}{\nu^{*}} = \frac{\varepsilon_{zz}}{\varepsilon_{zz}^{\ *}} \frac{\varepsilon_{xx}^{\ *}}{\varepsilon_{xx}} \tag{8.51}$$

These equations are identical to the ones given in the cantilever beam problem and it should be noted that the damage indicators for shear stiffness are the same for both loading scenarios. It can be concluded that the damage indices derived from tip loaded cantilever beam hold for the simply supported beam subjected to uniform loading under certain assumptions.

PROPOSED EXPERIMENTAL ARRANGEMENT AND BASIC MEASUREMENTS REQUIRED BY THEORY

The damage detection methodology proposed here utilizes the pre-damage and post-damage strain measurements for damage detection. Figures 8.3, 8.4 and 8.5 depict the sensor locations for the slender, intermediate, and deep beam, respectively. Point strains are measured at the given locations.

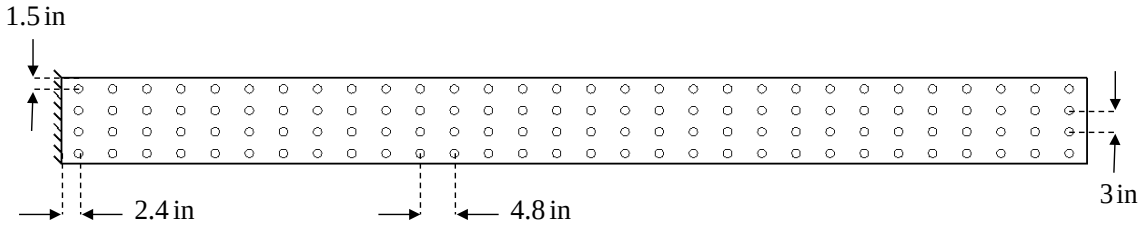

Figure 8.3 Ideal Sensor Layout for the Slender Beam

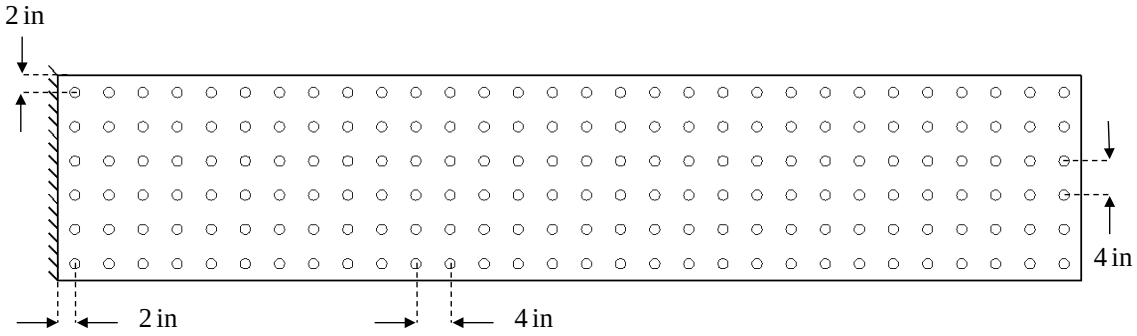

Figure 8.4 Ideal Sensor Layout for the Intermediate Beam

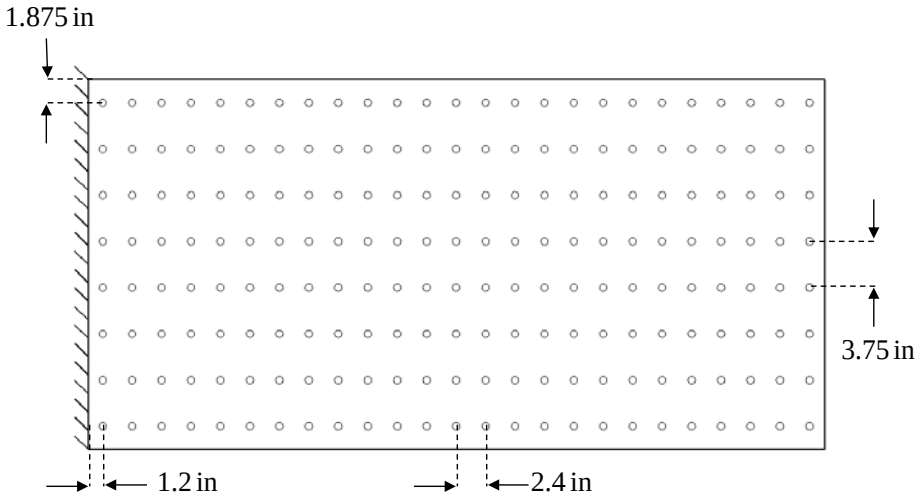

Figure 8.5 Ideal Sensor Layout for the Deep Beam

Certainly, in practical applications of this methodology a smaller number of sensors should be utilized in the analysis. It should be noted however, that, such a dense sensor grid is currently feasible with contemporary fiber optics technology.

ASSESSMENT OF THE PROPOSED METHODOLOGIES VIA NUMERICAL EXPERIMENTS

The performance of the proposed damage detection methodology is evaluated in this section. The numerical experiments previously defined in Chapter III are utilized to evaluate the performance of the NDE methodologies. The pre-damage and post-damage point strains are computed at the center of each Q6 element (note that this corresponds to the ideal sensor layouts given in Figure 8.3 through Figure 8.5) by interpolating the strains measured at the nodes of the element.

Eq. (8.23) is utilized in order to predict damage in the flexural stiffness distribution. This damage indicator, given in Eq. (8.52), is designated as "the Elasticity $\beta_j^{\,M}$" for identification purposes.

$$\beta_j^{\,M} = \frac{EI_j}{EI_j^{\,*}} = \frac{\varepsilon_{xx}^{\,*}}{\varepsilon_{xx}} \tag{8.52}$$

Eq. (8.27) is used in order to predict damage in the shear stiffness distribution. This damage indicator, given in Eq. (8.53), is designated as "the Elasticity $\beta_j^{\,V}$" for identification purposes.

$$\beta_j^{\,V} = \frac{GA_j}{GA_j^{\,*}} = \frac{\gamma_{xz}^{\,*}}{\gamma_{xz}} \tag{8.53}$$

Finally, Eq. (8.26) is utilized in order to predict damage in the Poisson's ratio. This damage indicator, given in Eq. (8.54), is designated as "the Elasticity $\beta_j^{\,\nu}$" for identification purposes.

$$\beta_j^{\nu} = \frac{\nu_j}{\nu_j^*} = \frac{\varepsilon_{zz}}{\varepsilon_{zz}^*}\frac{\varepsilon_{xx}^*}{\varepsilon_{xx}} \tag{8.54}$$

The Slender Beam

Damage detection results for the slender beam are presented in this subsection. Damage localization results are presented in terms of the normalized damage indicator Z_j given in Eq. (4.8). The percent error in severity estimates are computed by Eq. (3.3).

Damage Case SB 1

Figure 8.6 shows the schematic representation of Damage Case SB 1 on the FE mesh of the slender beam. Figure 8.7 depicts the damage localization results and Figure 8.8 shows the damage severity estimates for Damage Case SB 1 using the damage indicator Elasticity β_j^M. Table 8.1 tabulates the percent error in severity estimation.

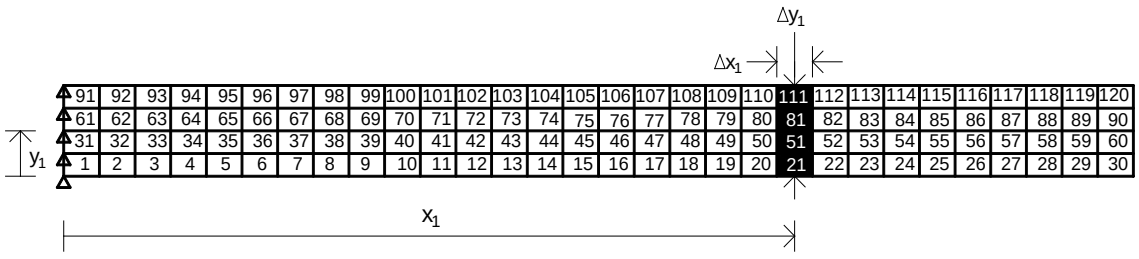

Figure 8.6 Schematic Representation of Damage Case SB 1

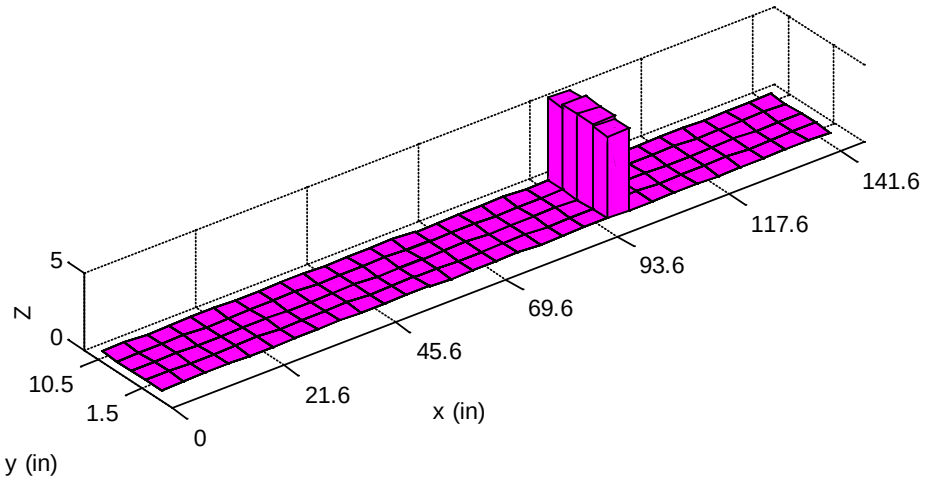

Figure 8.7 Damage Localization Result for Damage Case SB 1 Using Elasticity β_j^M

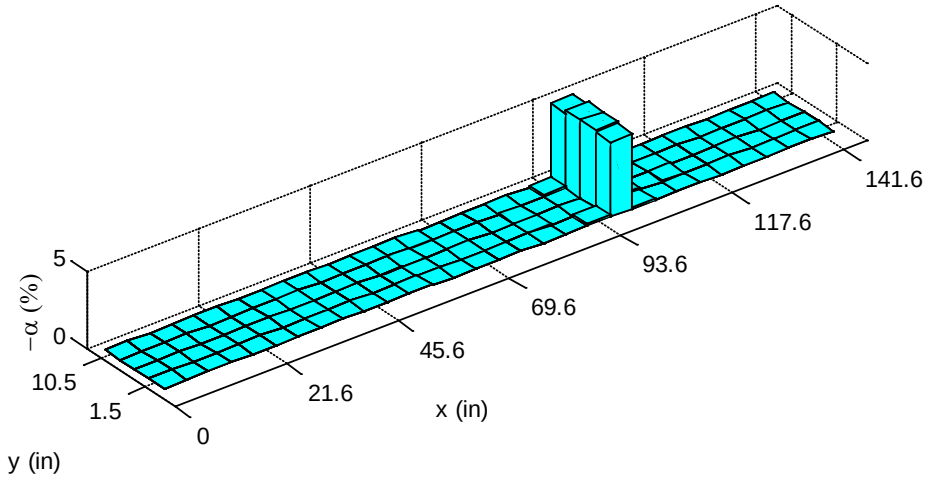

Figure 8.8 Damage Severity Estimates for Damage Case SB 1 Using Elasticity β_j^M

Table 8.1 Percent Error in Severity Estimates for Damage Case SB 1 Using Elasticity β_j^M

Damage Location		Damaged Element	Damage Severity (%)		Error (%)
x (in)	y (in)		Inflicted	Predicted	
98.4	1.5	21	-5.0	-4.8	4.0
98.4	4.5	51	-5.0	-5.0	0.0
98.4	7.5	81	-5.0	-5.0	0.0
98.4	10.5	111	-5.0	-4.8	4.0

Damage Case SB 2

Figure 8.9 shows the schematic representation of Damage Case SB 2 on the FE mesh of the slender beam. Figure 8.10 depicts the damage localization results and Figure 8.11 shows the damage severity estimates for Damage Case SB 2 using the damage indicator Elasticity β_j^M. Table 8.2 tabulates the percent error in severity estimation.

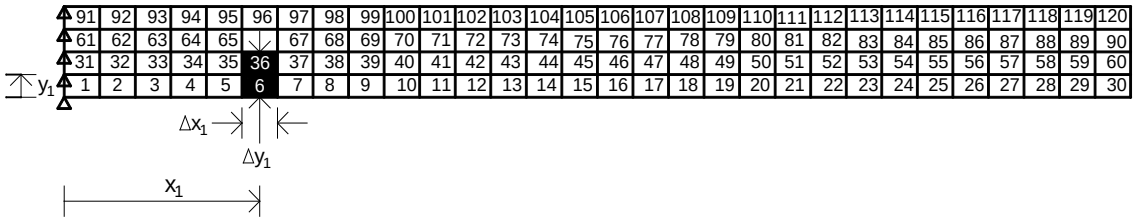

Figure 8.9 Schematic Representation of Damage Case SB 2

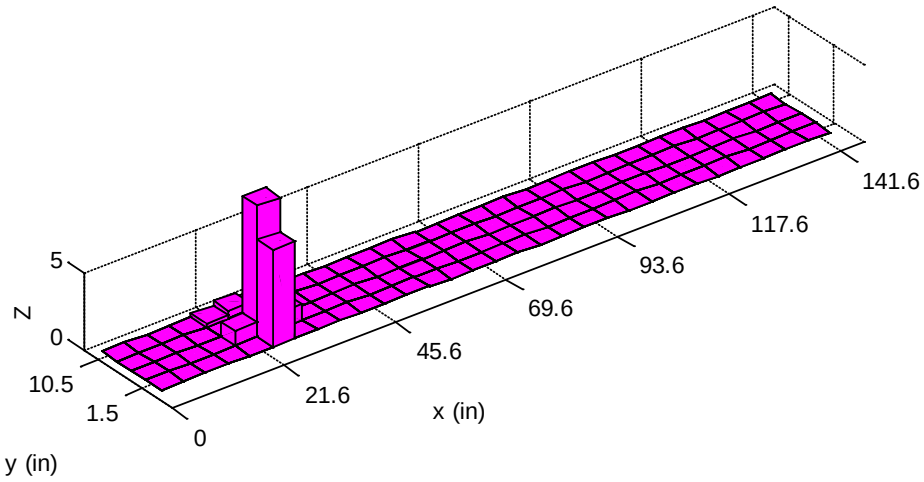

Figure 8.10 Damage Localization Result for Damage Case SB 2 Using Elasticity β_j^M

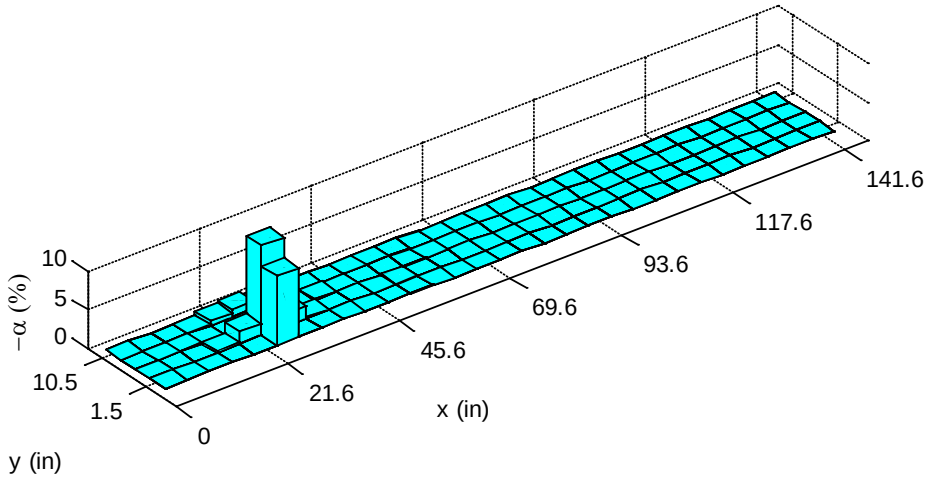

Figure 8.11 Damage Severity Estimates for Damage Case SB 2 Using Elasticity β_j^M

Table 8.2 Percent Error in Severity Estimates for Damage Case SB 2 Using Elasticity β_j^M

Damage Location		Damaged Element	Damage Severity (%)		Error (%)
x (in)	y (in)		Inflicted	Predicted	
26.4	1.5	6	-10.0	-8.9	11.0
26.4	4.5	36	-10.0	-11.6	-16.0

Damage Case SB 3

Figure 8.12 shows the schematic representation of Damage Case SB 3 on the FE mesh of the slender beam. Figure 8.13 depicts the damage localization results and Figure 8.14 shows the damage severity estimates for Damage Case SB 3 using the damage indicator Elasticity β_j^M . Table 8.3 tabulates the percent error in severity estimation.

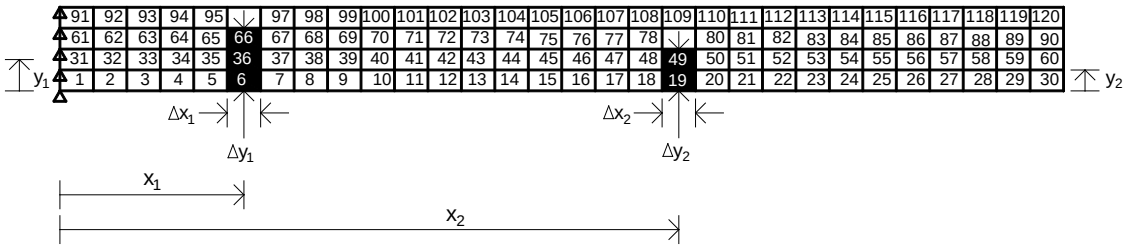

Figure 8.12 Schematic Representation of Damage Case SB 3

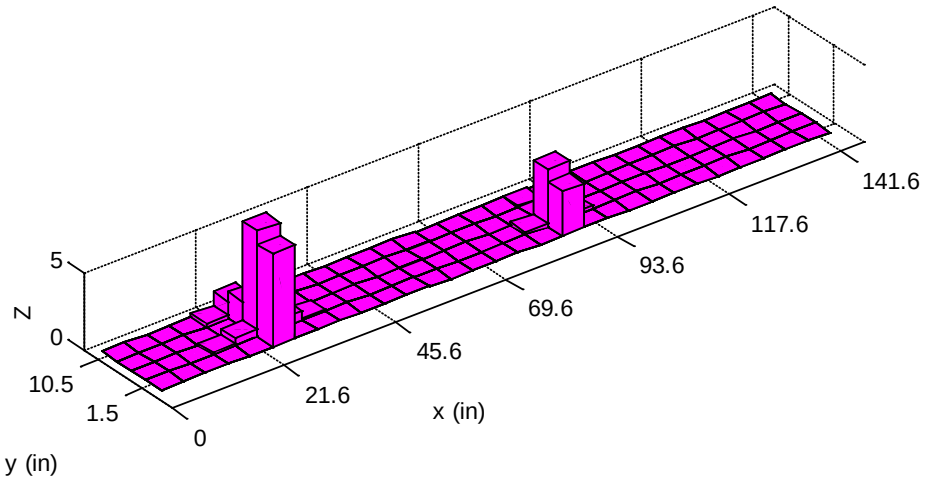

Figure 8.13 Damage Localization Result for Damage Case SB 3 Using Elasticity β_j^M

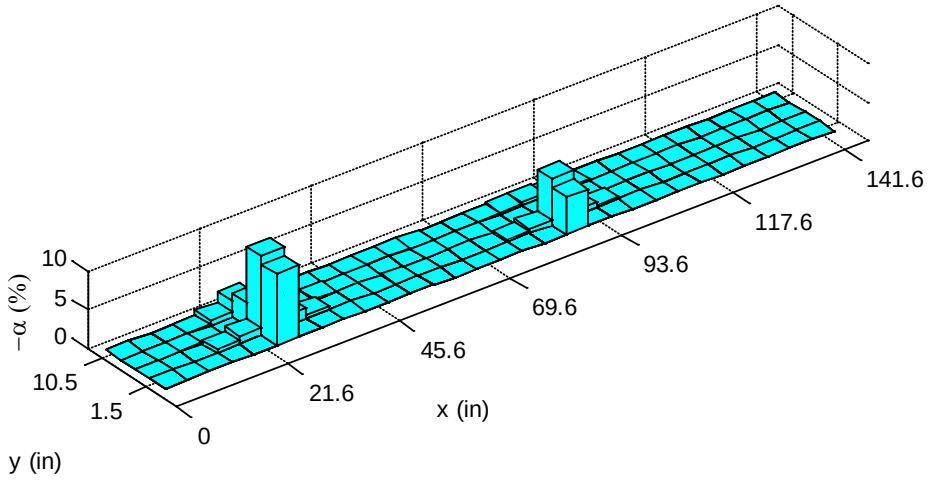

Figure 8.14 Damage Severity Estimates for Damage Case SB 3 Using Elasticity β_j^M

Table 8.3 Percent Error in Severity Estimates for Damage Case SB 3 Using Elasticity β_j^M

Damage Location		Damaged Element	Damage Severity (%)		Error (%)
x (in)	y (in)		Inflicted	Predicted	
26.4	1.5	6	-10.0	-9.2	8.0
26.4	4.5	36	-10.0	-10.3	-3.0
26.4	7.5	66	-10.0	-2.9	71.0
88.8	1.5	19	-5.0	-4.7	6.0
88.8	4.5	49	-5.0	-5.9	-18.0

Figure 8.15 depicts the damage localization results and Figure 8.16 shows the damage severity estimates for Damage Case SB 3 using the damage indicator Elasticity β_j^V (Eq. (8.53)). Table 8.4 tabulates the percent error in severity estimation.

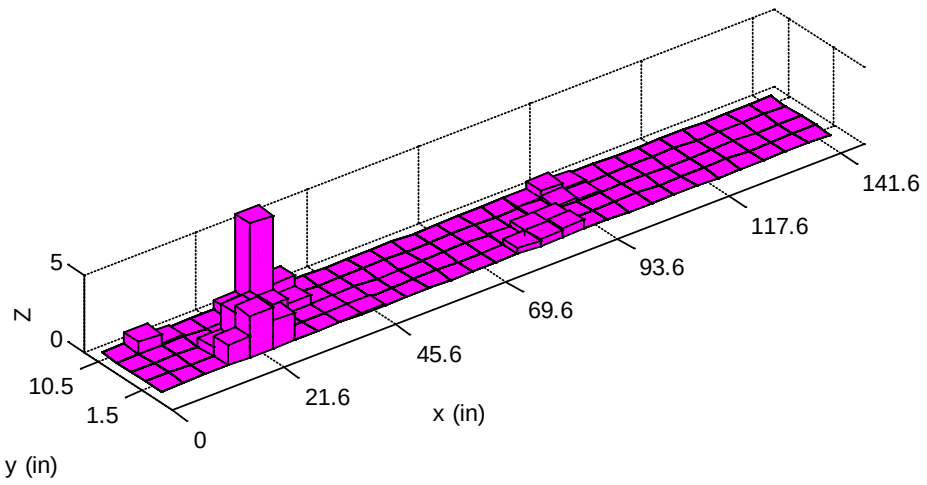

Figure 8.15 Damage Localization Result for Damage Case SB 3 Using Elasticity β_j^V

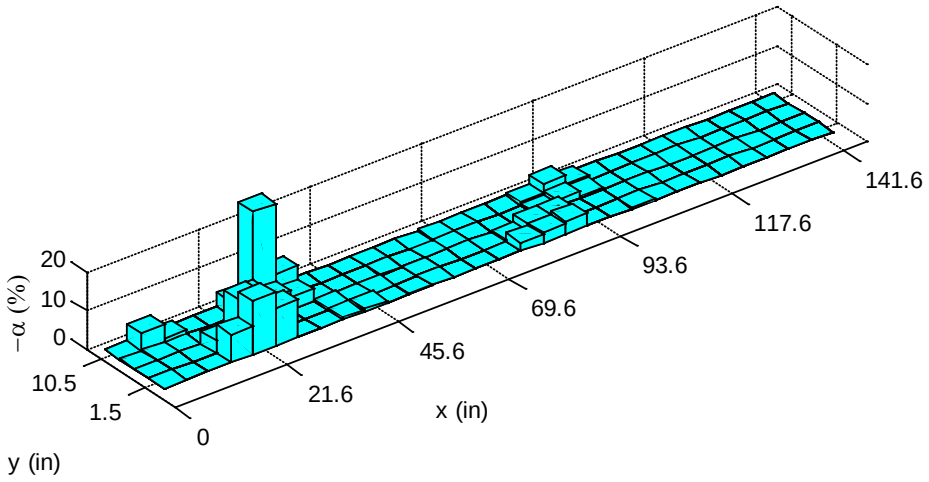

Figure 8.16 Damage Severity Estimates for Damage Case SB 3 Using Elasticity β_j^V

Table 8.4 Percent Error in Severity Estimates for Damage Case SB 3 Using Elasticity β_j^V

Damage Location		Damaged Element	Damage Severity (%)		Error (%)
x (in)	y (in)		Inflicted	Predicted	
26.4	1.5	6	-8.3	-9.6	-15.7
26.4	4.5	36	-8.3	-7.2	13.3
26.4	7.5	66	-8.3	-7.2	13.3
88.8	1.5	19	-3.4	-3.3	2.9
88.8	4.5	49	-3.4	-2.6	23.5

Figure 8.17 depicts the damage localization results and Figure 8.18 shows the damage severity estimates for Damage Case SB 3 using the damage indicator Elasticity β_j^{ν} (Eq. (8.54)). Table 8.5 tabulates the percent error in severity estimation.

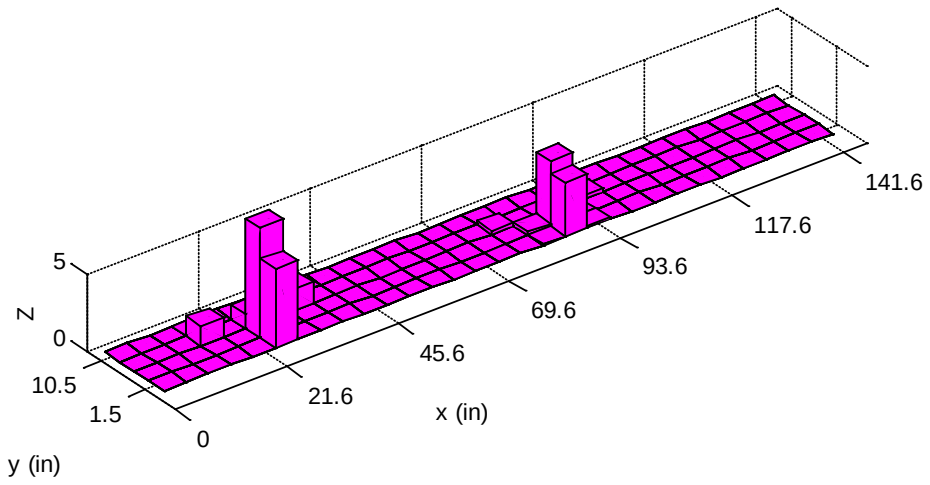

Figure 8.17 Damage Localization Result for Damage Case SB 3 Using Elasticity β_j^{ν}

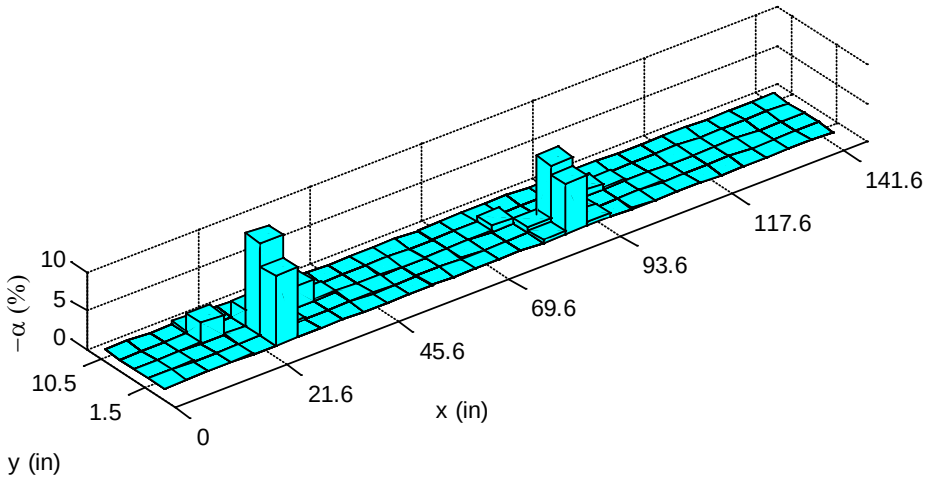

Figure 8.18 Damage Severity Estimates for Damage Case SB 3 Using Elasticity β_j^{ν}

Table 8.5 Percent Error in Severity Estimates for Damage Case SB 3 Using Elasticity β_j^{ν}

Damage Location		Damaged Element	Damage Severity (%)		Error (%)
x (in)	y (in)		Inflicted	Predicted	
26.4	1.5	6	-8.0	-9.0	-12.5
26.4	4.5	36	-8.0	-12.0	-50.0
26.4	7.5	66	-8.0	-2.0	75.0
88.8	1.5	19	-7.0	-6.4	8.6
88.8	4.5	49	-7.0	-7.6	-8.6

Damage Case SB 4

Figure 8.19 shows the schematic representation of Damage Case SB 4 on the FE mesh of the slender beam. Figure 8.20 depicts the damage localization results and Figure 8.21 shows the damage severity estimates for Damage Case SB 4 using the damage indicator Elasticity $\beta_j^{\,M}$. Table 8.6 tabulates the percent error in severity estimation.

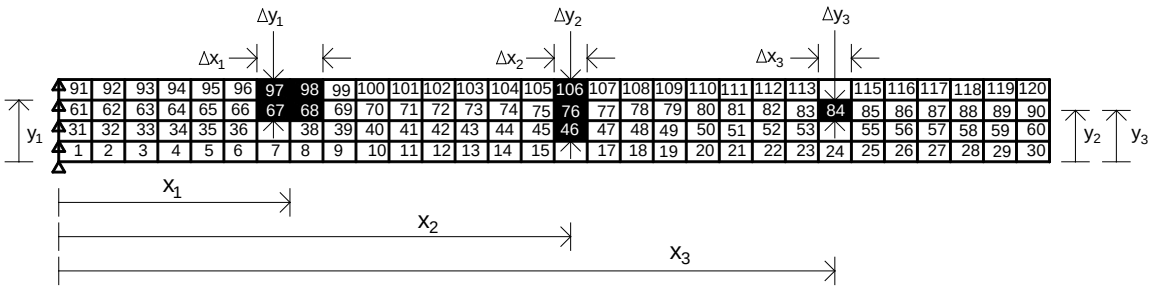

Figure 8.19 Schematic Representation of Damage Case SB 4

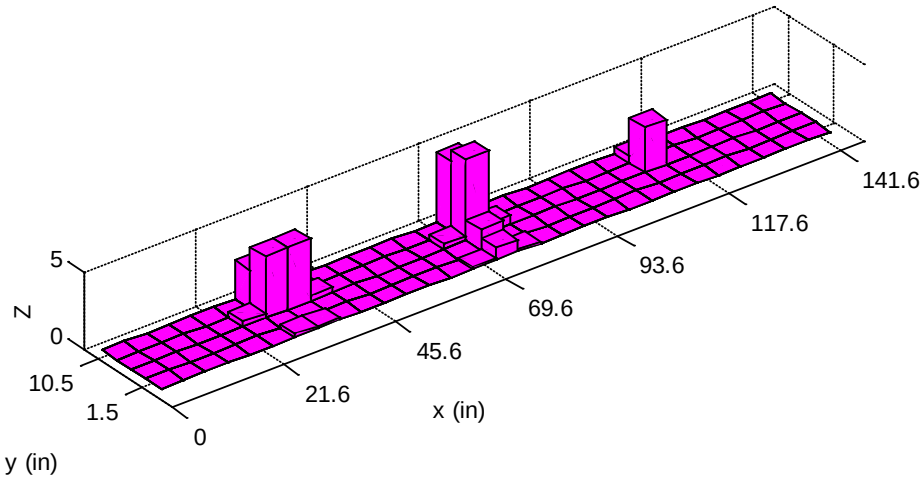

Figure 8.20 Damage Localization Result for Damage Case SB 4 Using Elasticity β_j^M

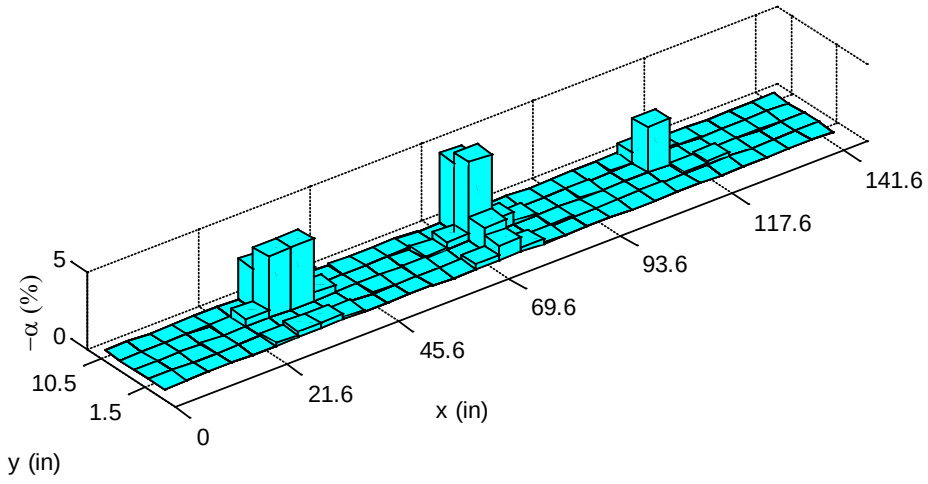

Figure 8.21 Damage Severity Estimates for Damage Case SB 4 Using Elasticity β_j^M

Table 8.6 Percent Error in Severity Estimates for Damage Case SB 4 Using Elasticity β_j^M

Damage Location		Damaged Element	Damage Severity (%)		Error (%)
x (in)	y (in)		Inflicted	Predicted	
31.2	7.5	67	-3.0	-4.0	-33.3
31.2	10.5	97	-3.0	-2.6	13.3
36.0	7.5	68	-3.0	-4.0	-33.3
36.0	10.5	98	-3.0	-2.6	13.3
74.4	4.5	46	-5.0	-1.5	70.0
74.4	7.5	76	-5.0	-5.1	-2.0
74.4	10.5	106	-5.0	-4.4	12.0
112.8	7.5	84	-6.0	-3.0	50.0

Damage Case SB 5

Figure 8.22 shows the schematic representation of Damage Case SB 5 on the FE mesh of the slender beam. Figure 8.23 depicts the damage localization results and Figure 8.24 shows the damage severity estimates for Damage Case SB 5 using the damage indicator Elasticity β_j^M . Table 8.7 tabulates the percent error in severity estimation.

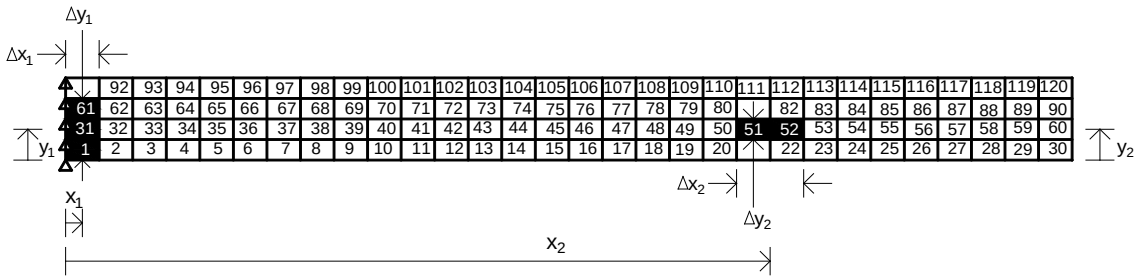

Figure 8.22 Schematic Representation of Damage Case SB 5

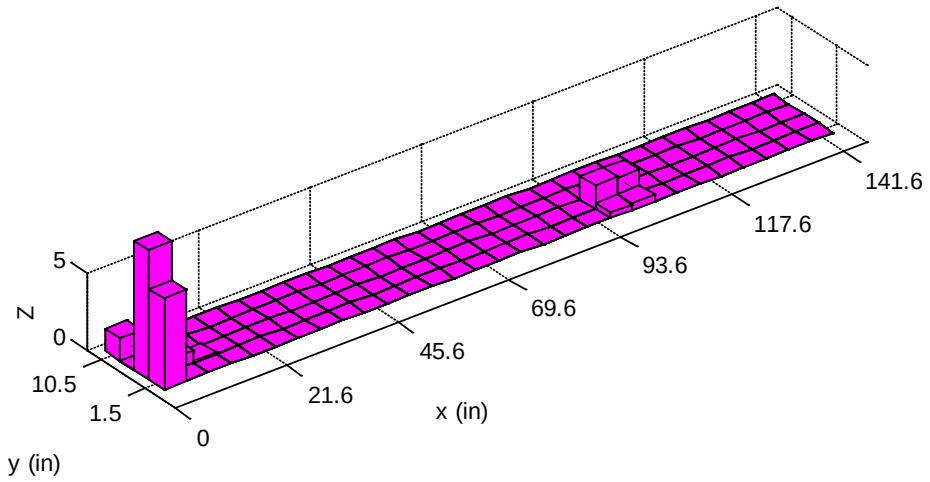

Figure 8.23 Damage Localization Result for Damage Case SB 5 Using Elasticity β_j^M

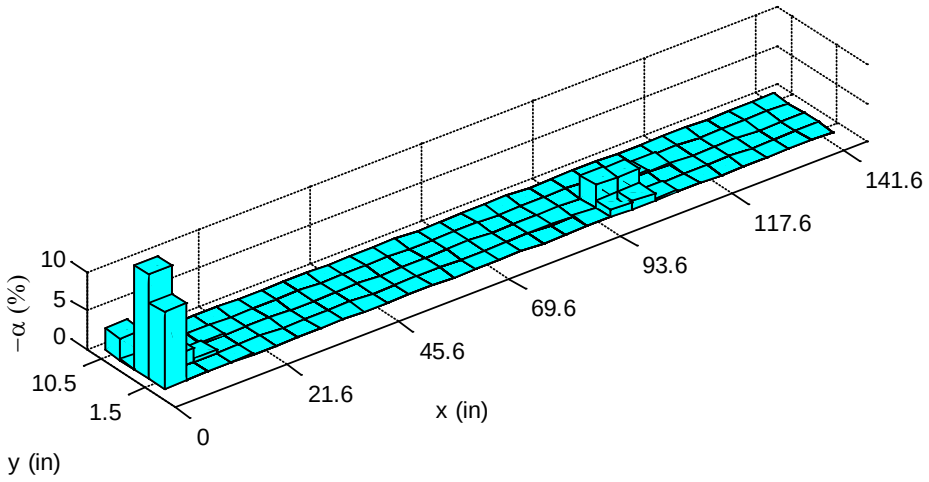

Figure 8.24 Damage Severity Estimates for Damage Case SB 5 Using Elasticity β_j^M

Table 8.7 Percent Error in Severity Estimates for Damage Case SB 5 Using Elasticity β_j^M

Damage Location		Damaged Element	Damage Severity (%)		Error (%)
x (in)	y (in)		Inflicted	Predicted	
2.4	1.5	1	-11.0	-9.8	10.9
2.4	4.5	31	-11.0	-13.4	-21.8
2.4	7.5	61	-11.0	0.0	100.0
98.4	4.5	51	-7.0	-2.9	58.6
103.2	4.5	52	-7.0	-2.8	60.0

Figure 8.25 depicts the damage localization results and Figure 8.26 shows the damage severity estimates for Damage Case SB 5 using the damage indicator Elasticity β_j^V (Eq. (8.53)). Table 8.8 tabulates the percent error in severity estimation.

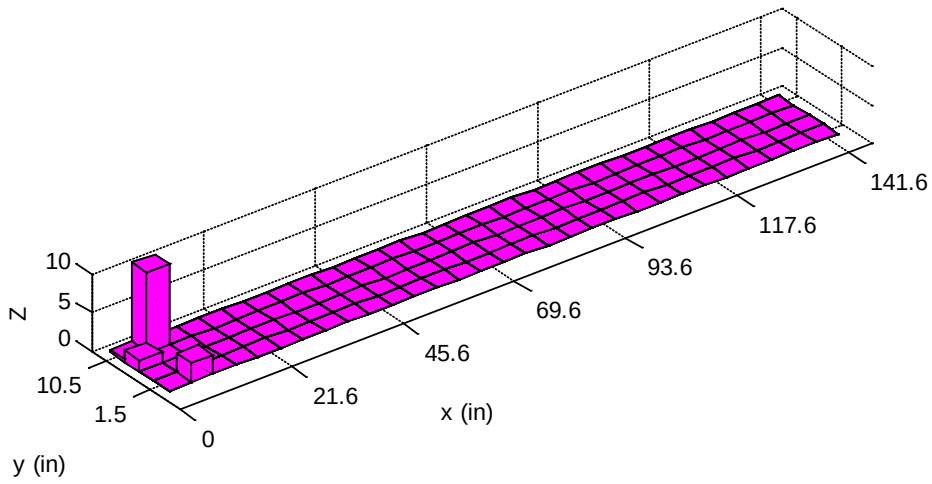

Figure 8.25 Damage Localization Result for Damage Case SB 5 Using Elasticity β_j^V

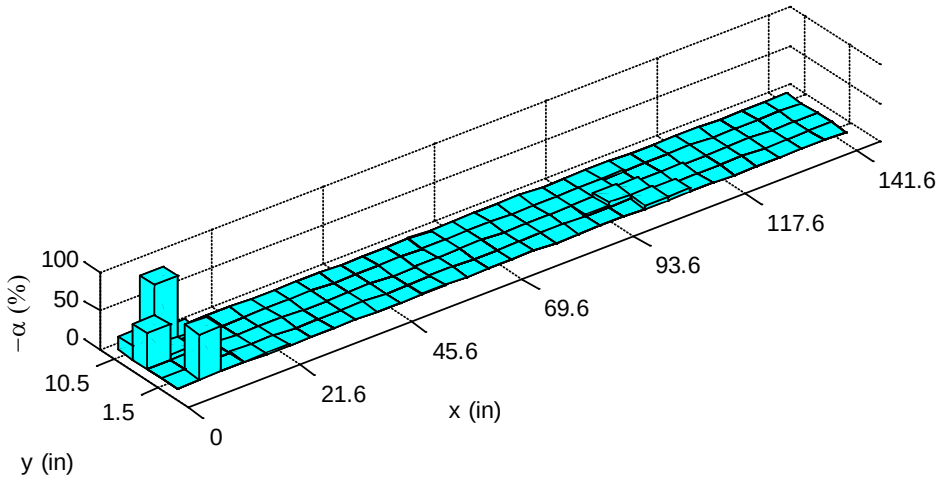

Figure 8.26 Damage Severity Estimates for Damage Case SB 5 Using Elasticity β_j^V

Table 8.8 Percent Error in Severity Estimates for Damage Case SB 5 Using Elasticity β_j^V

Damage Location		Damaged Element	Damage Severity (%)		Error (%)
x (in)	y (in)		Inflicted	Predicted	
2.4	1.5	1	-9.8	0.0	100.0
2.4	4.5	31	-9.8	0.0	100.0
2.4	7.5	61	-9.8	-45.7	-366.3
98.4	4.5	51	-5.9	-6.1	-3.4
103.2	4.5	52	-5.9	-3.9	33.9

Figure 8.27 depicts the damage localization results and Figure 8.28 shows the damage severity estimates for Damage Case SB 5 using the damage indicator Elasticity β_j^{ν} (Eq. (8.54)). Table 8.9 tabulates the percent error in severity estimation.

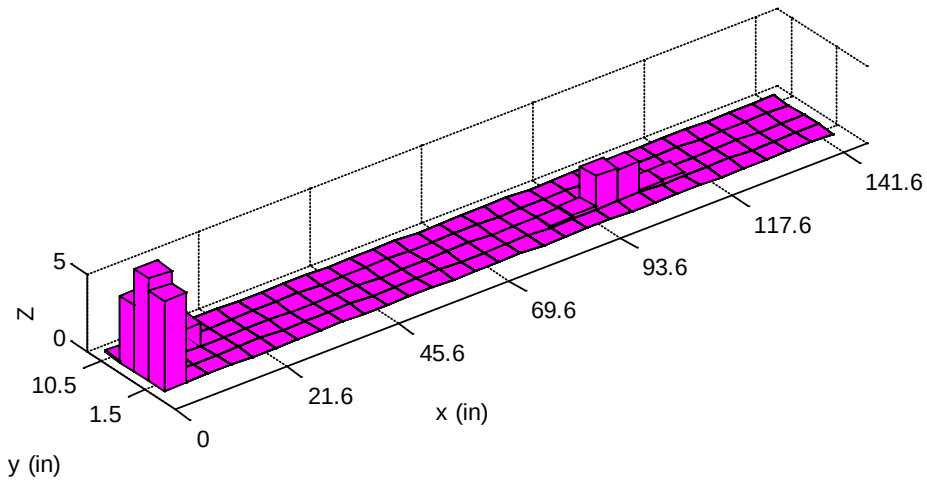

Figure 8.27 Damage Localization Result for Damage Case SB 5 Using Elasticity β_j^{ν}

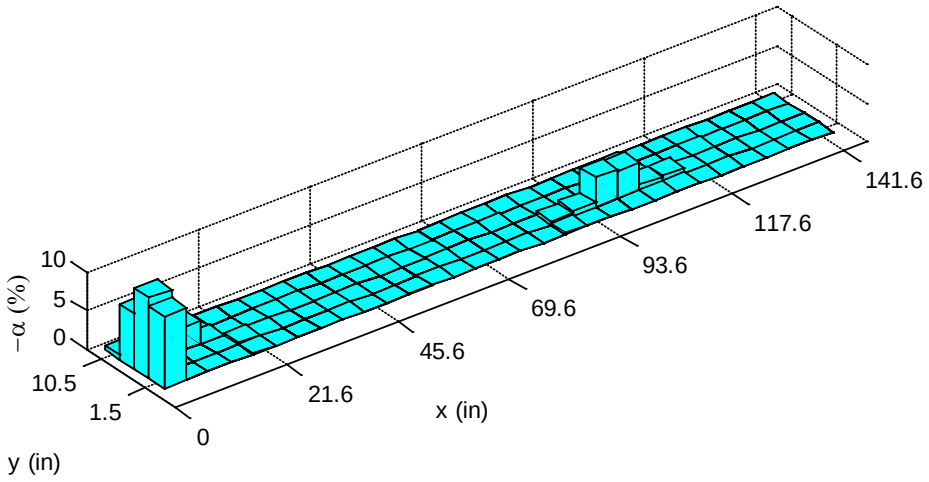

Figure 8.28 Damage Severity Estimates for Damage Case SB 5 Using Elasticity β_j^{ν}

Table 8.9 Percent Error in Severity Estimates for Damage Case SB 5 Using Elasticity β_j^{ν}

Damage Location		Damaged Element	Damage Severity (%)		Error (%)
x (in)	y (in)		Inflicted	Predicted	
2.4	1.5	1	-6.0	-9.3	-55.0
2.4	4.5	31	-6.0	-10.4	-73.3
2.4	7.5	61	-6.0	-7.1	-18.3
98.4	4.5	51	-5.0	-3.9	22.0
103.2	4.5	52	-5.0	-3.6	28.0

The Intermediate Beam

Damage detection results for the intermediate beam are presented in this subsection. Damage localization results are presented in terms of the normalized damage indicator Z_j given in Eq. (4.8). The percent error in severity estimates are computed by Eq. (3.3).

Damage Case IB 1

Figure 8.29 shows the schematic representation of Damage Case IB 1 on the FE mesh of the intermediate beam. Figure 8.30 depicts the damage localization results and Figure 8.31 shows the damage severity estimates for Damage Case IB 1 using the damage indicator Elasticity β_j^M. Table 8.10 tabulates the percent error in severity estimation.

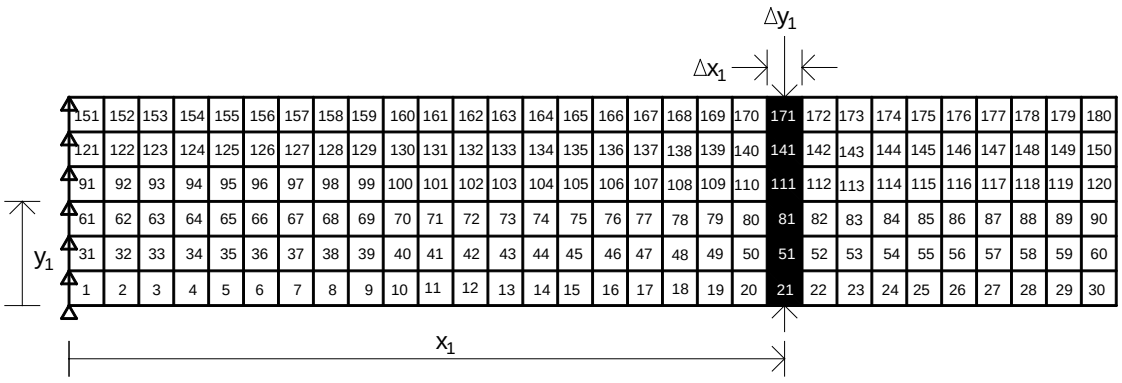

Figure 8.29 Schematic Representation of Damage Case IB 1

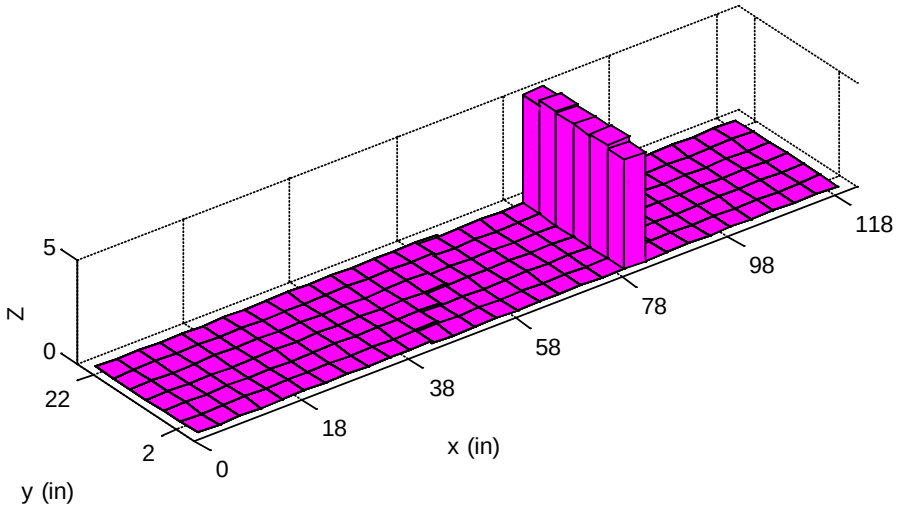

Figure 8.30 Damage Localization Result for Damage Case IB 1 Using Elasticity β_j^M

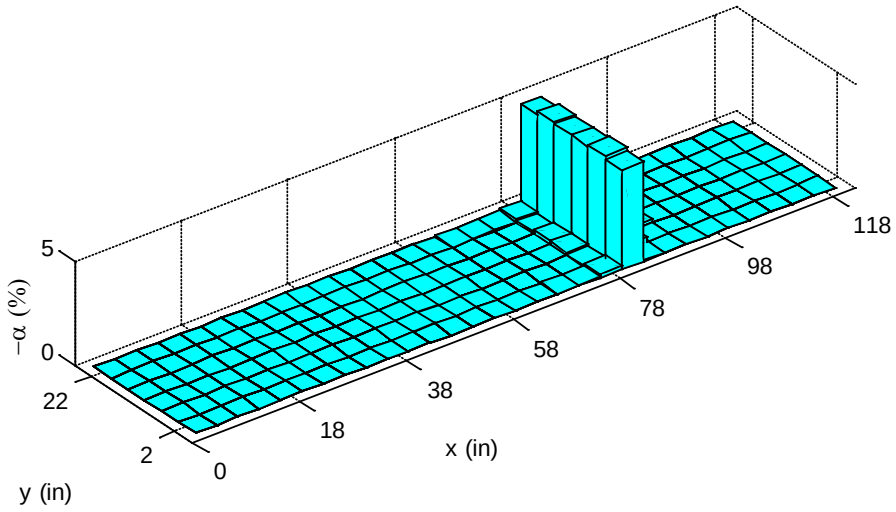

Figure 8.31 Damage Severity Estimates for Damage Case IB 1 Using Elasticity β_j^M

Table 8.10 Percent Error in Severity Estimates for Damage Case IB 1 Using Elasticity β_j^M

Damage Location		Damaged Element	Damage Severity (%)		Error (%)
x (in)	y (in)		Inflicted	Predicted	
82.0	2.0	21	-5.0	-4.8	4.0
82.0	6.0	51	-5.0	-4.9	2.0
82.0	10.0	81	-5.0	-4.9	2.0
82.0	14.0	111	-5.0	-4.9	2.0
82.0	18.0	141	-5.0	-4.9	2.0
82.0	22.0	171	-5.0	-4.8	4.0

Damage Case IB 2

Figure 8.32 shows the schematic representation of Damage Case IB 2 on the FE mesh of the intermediate beam. Figure 8.33 depicts the damage localization results and Figure 8.34 shows the damage severity estimates for Damage Case IB 2 using the damage indicator Elasticity β_j^M. Table 8.11 tabulates the percent error in severity estimation.

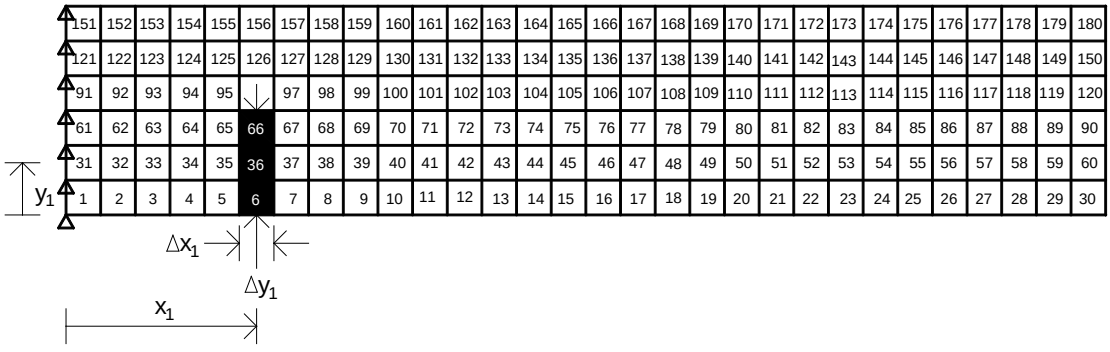

Figure 8.32 Schematic Representation of Damage Case IB 2

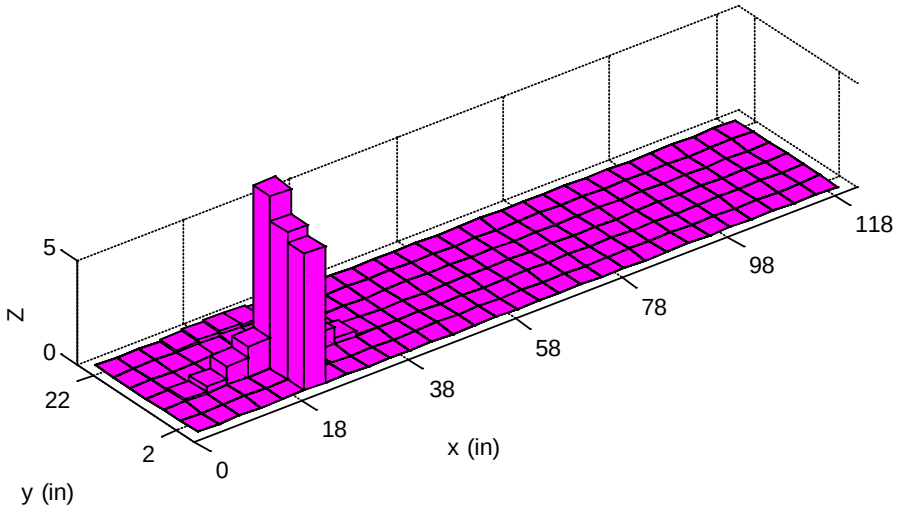

Figure 8.33 Damage Localization Result for Damage Case IB 2 Using Elasticity β_j^M

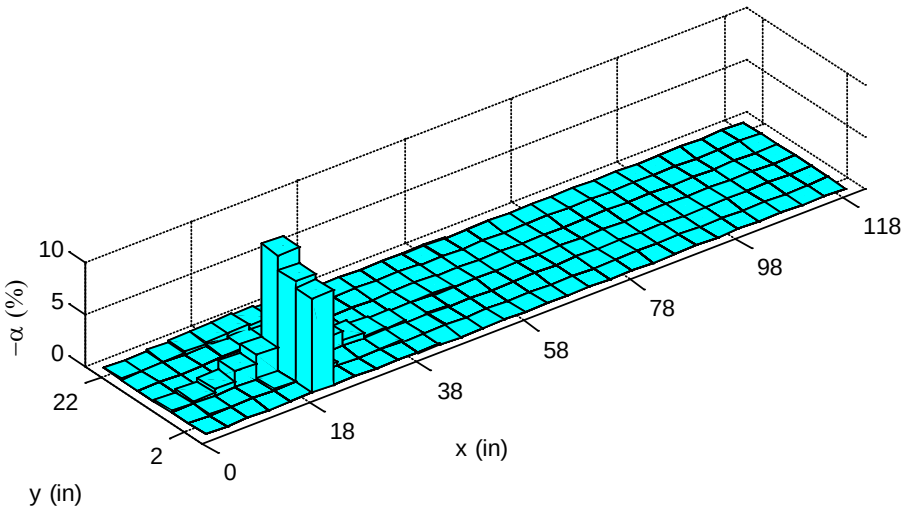

Figure 8.34 Damage Severity Estimates for Damage Case IB 2 Using Elasticity β_j^M

Table 8.11 Percent Error in Severity Estimates for Damage Case IB 2 Using Elasticity β_j^M

Damage Location		Damaged Element	Damage Severity (%)		Error (%)
x (in)	y (in)		Inflicted	Predicted	
22.0	2.0	6	-10.0	-9.1	9.0
22.0	6.0	36	-10.0	-9.7	3.0
22.0	10.0	66	-10.0	-11.1	-11.0

Damage Case IB 3

Figure 8.35 shows the schematic representation of Damage Case IB 3 on the FE mesh of the intermediate beam. Figure 8.36 depicts the damage localization results and Figure 8.37 shows the damage severity estimates for Damage Case IB 3 using the damage indicator Elasticity β_j^M. Table 8.12 tabulates the percent error in severity estimation.

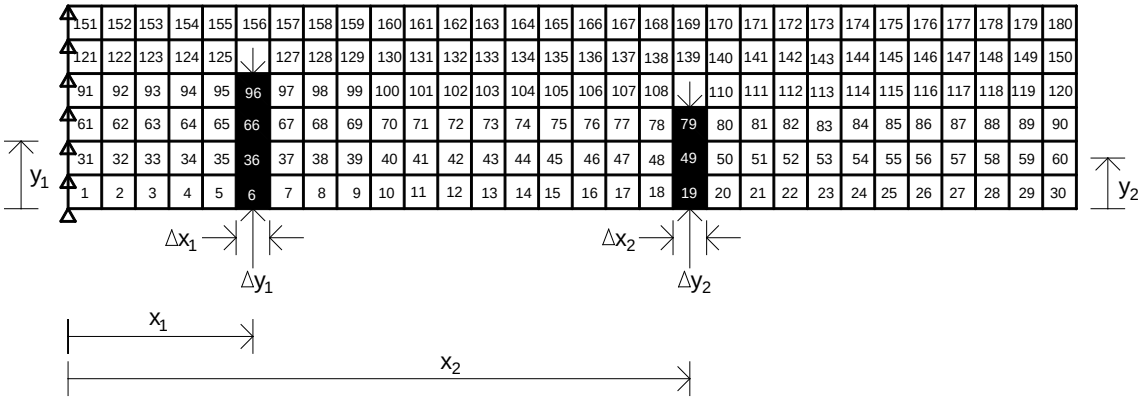

Figure 8.35 Schematic Representation of Damage Case IB 3

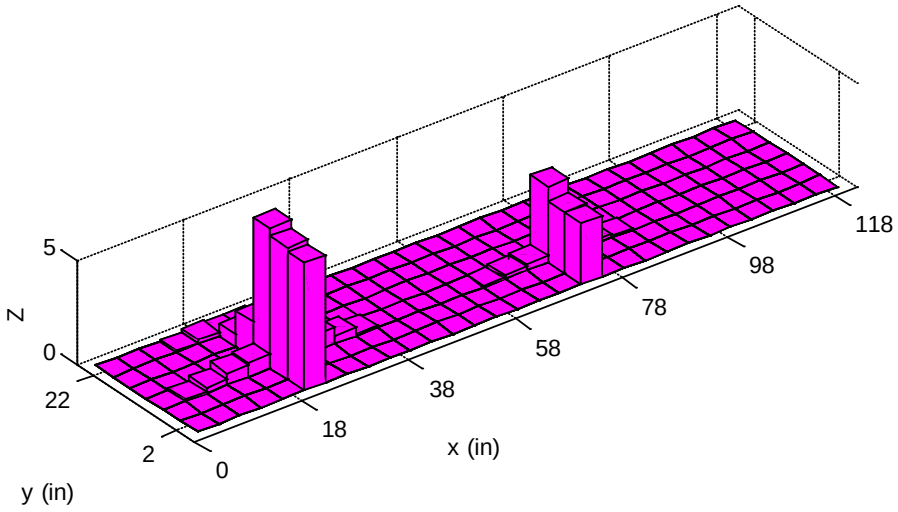

Figure 8.36 Damage Localization Result for Damage Case IB 3 Using Elasticity β_j^M

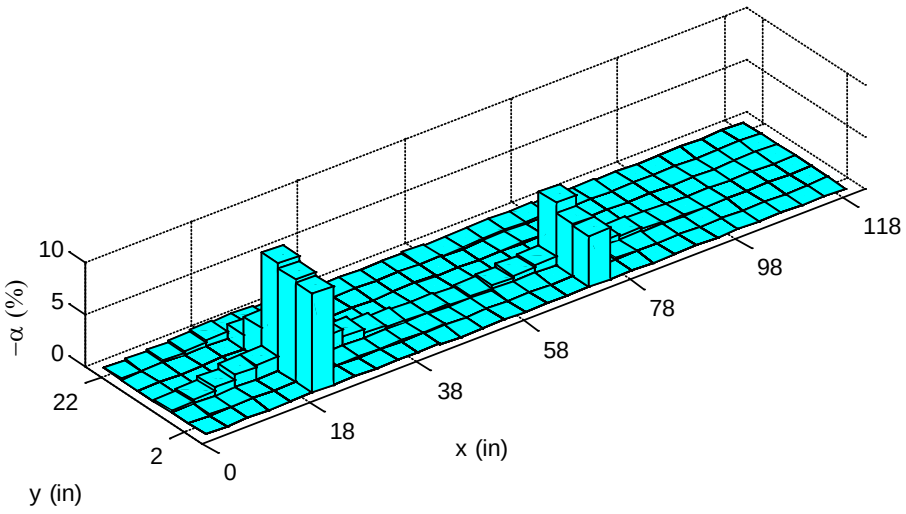

Figure 8.37 Damage Severity Estimates for Damage Case IB 3 Using Elasticity β_j^M

Table 8.12 Percent Error in Severity Estimates for Damage Case IB 3 Using Elasticity β_j^M

Damage Location		Damaged Element	Damage Severity (%)		Error (%)
x (in)	y (in)		Inflicted	Predicted	
22.0	2.0	6	-10.0	-9.5	5.0
22.0	6.0	36	-10.0	-9.8	2.0
22.0	10.0	66	-10.0	-10.3	-3.0
22.0	14.0	96	-10.0	-3.1	69.0
74.0	2.0	19	-5.0	-4.9	2.0
74.0	6.0	49	-5.0	-5.0	0.0
74.0	10.0	79	-5.0	-6.0	-20.0

Figure 8.38 depicts the damage localization results and Figure 8.39 shows the damage severity estimates for Damage Case IB 3 using the damage indicator Elasticity β_j^V (Eq. (8.53)). Table 8.13 tabulates the percent error in severity estimation.

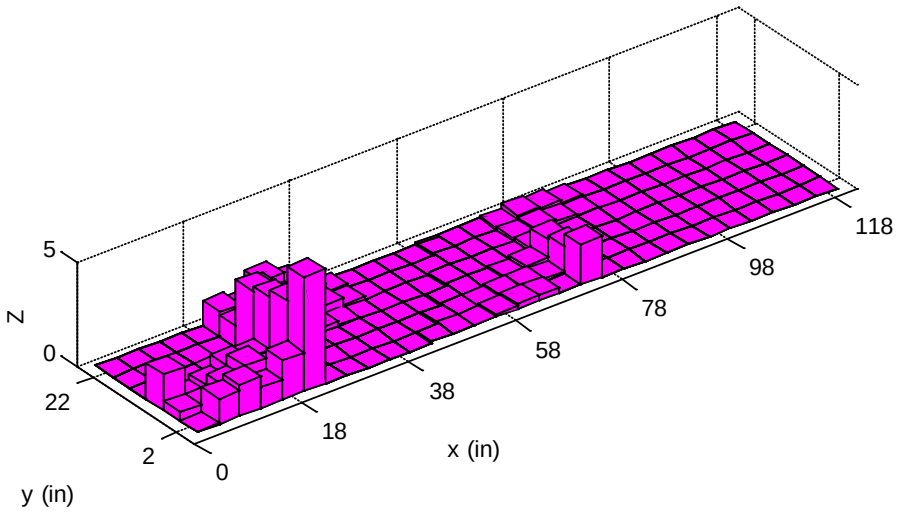

Figure 8.38 Damage Localization Result for Damage Case IB 3 Using Elasticity β_j^V

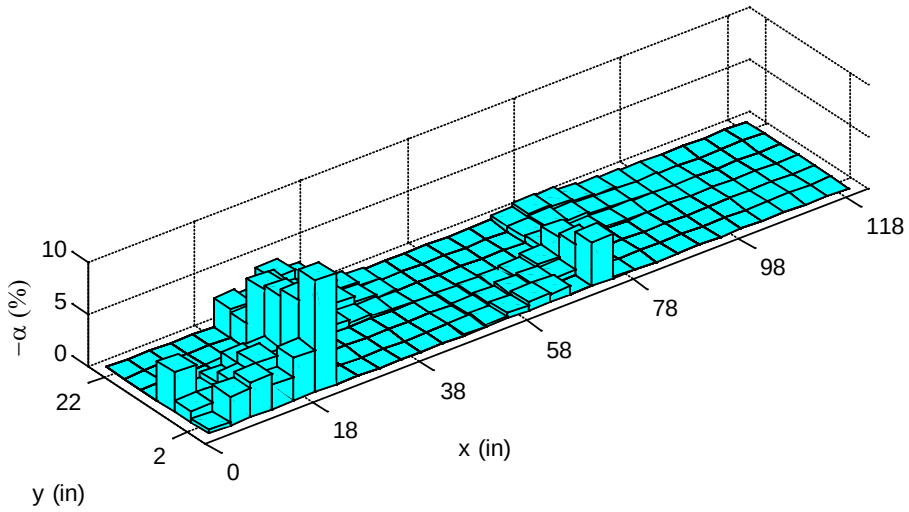

Figure 8.39 Damage Severity Estimates for Damage Case IB 3 Using Elasticity β_j^V

Table 8.13 Percent Error in Severity Estimates for Damage Case IB 3 Using Elasticity β_j^{V}

Damage Location		Damaged Element	Damage Severity (%)		Error (%)
x (in)	y (in)		Inflicted	Predicted	
22.0	2.0	6	-8.3	-10.7	-28.9
22.0	6.0	36	-8.3	-7.8	6.0
22.0	10.0	66	-8.3	-7.0	15.7
22.0	14.0	96	-8.3	-6.7	19.3
74.0	2.0	19	-3.4	-4.2	-23.5
74.0	6.0	49	-3.4	-2.9	14.7
74.0	10.0	79	-3.4	-2.5	26.5

Figure 8.40 depicts the damage localization results and Figure 8.41 shows the damage severity estimates for Damage Case IB 3 using the damage indicator Elasticity β_j^{ν} (Eq. (8.54)). Table 8.14 tabulates the percent error in severity estimation.

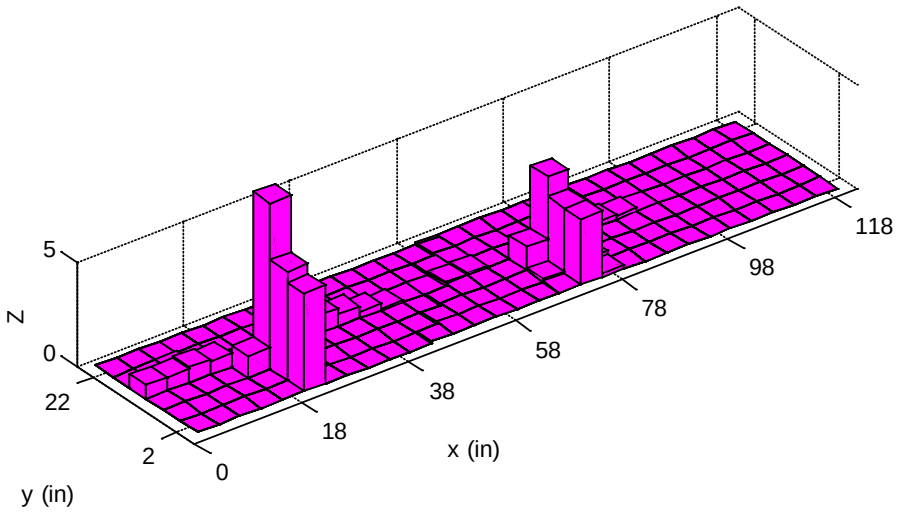

Figure 8.40 Damage Localization Result for Damage Case IB 3 Using Elasticity β_j^{ν}

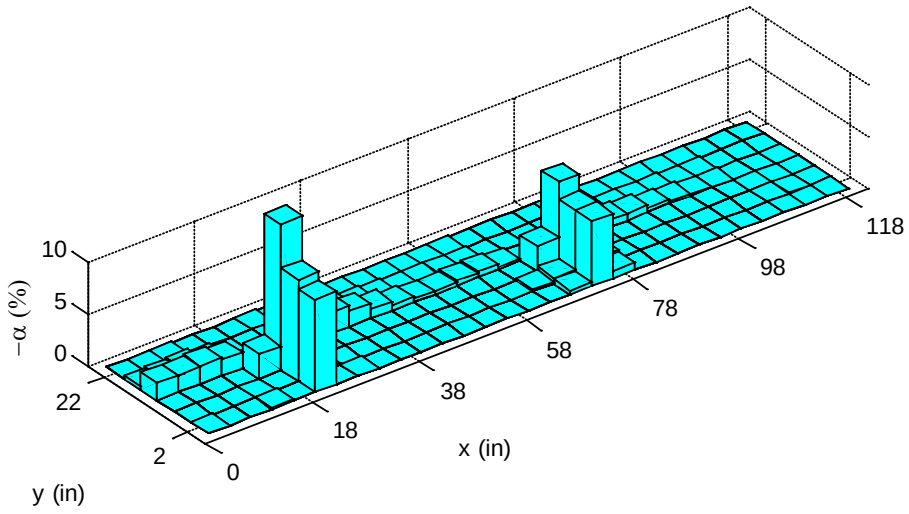

Figure 8.41 Damage Severity Estimates for Damage Case IB 3 Using Elasticity β_j^{ν}

Table 8.14 Percent Error in Severity Estimates for Damage Case IB 3 Using Elasticity β_j^{ν}

Damage Location		Damaged Element	Damage Severity (%)		Error (%)
x (in)	y (in)		Inflicted	Predicted	
22.0	2.0	6	-8.0	-8.9	-11.3
22.0	6.0	36	-8.0	-9.8	-22.5
22.0	10.0	66	-8.0	-14.1	-76.3
22.0	14.0	96	-8.0	0.0	100.0
74.0	2.0	19	-7.0	-6.2	11.4
74.0	6.0	49	-7.0	-6.2	11.4
74.0	10.0	79	-7.0	-7.9	-12.9

Damage Case IB 4

Figure 8.42 shows the schematic representation of Damage Case IB 4 on the FE mesh of the intermediate beam. Figure 8.43 depicts the damage localization results and Figure 8.44 shows the damage severity estimates for Damage Case IB 4 using the damage indicator Elasticity β_j^{M}. Table 8.15 tabulates the percent error in severity estimation.

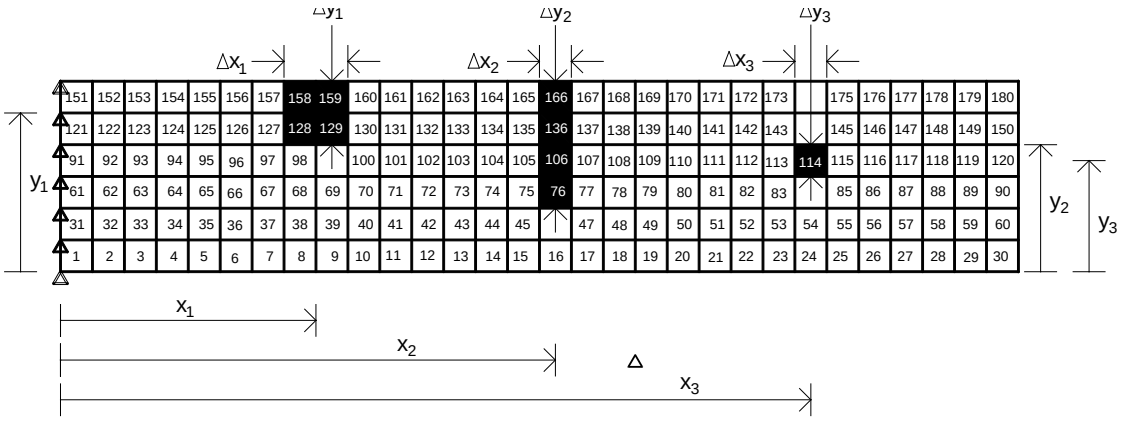

Figure 8.42 Schematic Representation of Damage Case IB 4
Δ

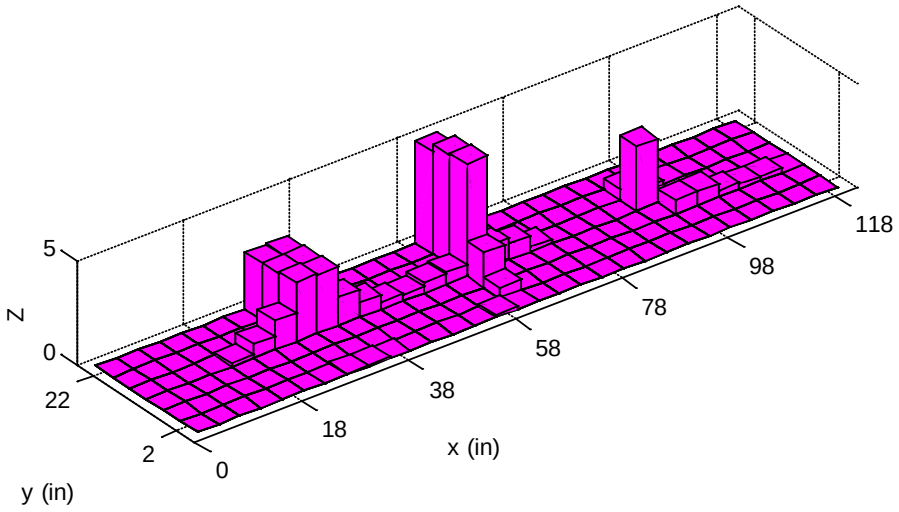

Figure 8.43 Damage Localization Result for Damage Case IB 4 Using Elasticity β_j^M

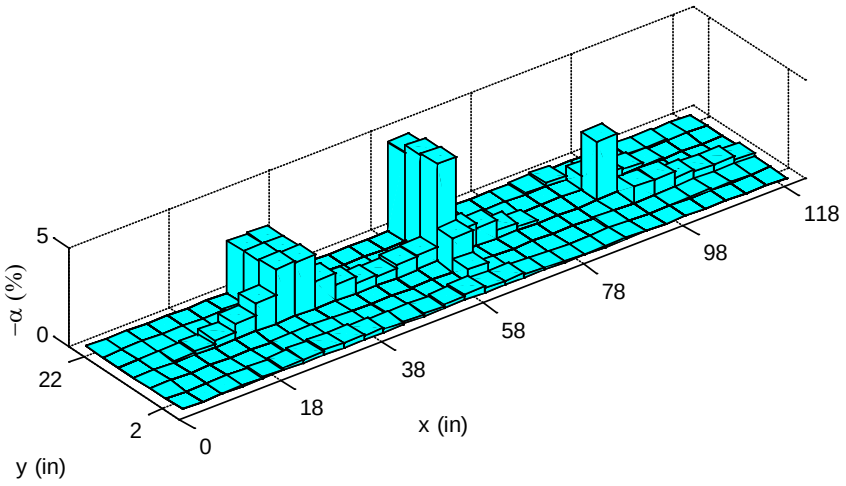

Figure 8.44 Damage Severity Estimates for Damage Case IB 4 Using Elasticity β_j^M

Table 8.15 Percent Error in Severity Estimates for Damage Case IB 4 Using Elasticity β_j^M

Damage Location		Damaged Element	Damage Severity (%)		Error (%)
x (in)	y (in)		Inflicted	Predicted	
30	18	128	-3.0	-2.7	10.0
30	22	158	-3.0	-2.6	13.3
34	18	129	-3.0	-2.7	10.0
34	22	159	-3.0	-2.6	13.3
62	10	76	-5.0	-1.7	66.0
62	14	106	-5.0	-4.9	2.0
62	18	136	-5.0	-4.8	4.0
62	22	166	-5.0	-4.5	10.0
94	14	114	-6.0	-3.0	50.0

Damage Case IB 5

Figure 8.45 shows the schematic representation of Damage Case IB 5 on the FE mesh of the intermediate beam. Figure 8.46 depicts the damage localization results and Figure 8.47 shows the damage severity estimates for Damage Case IB 5 using the damage indicator Elasticity β_j^M. Table 8.16 tabulates the percent error in severity estimation.

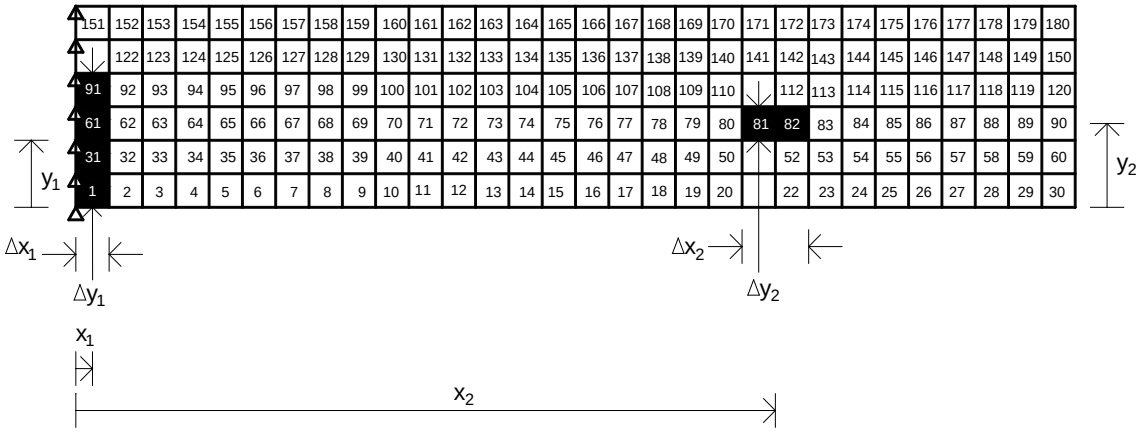

Figure 8.45 Schematic Representation of Damage Case IB 5

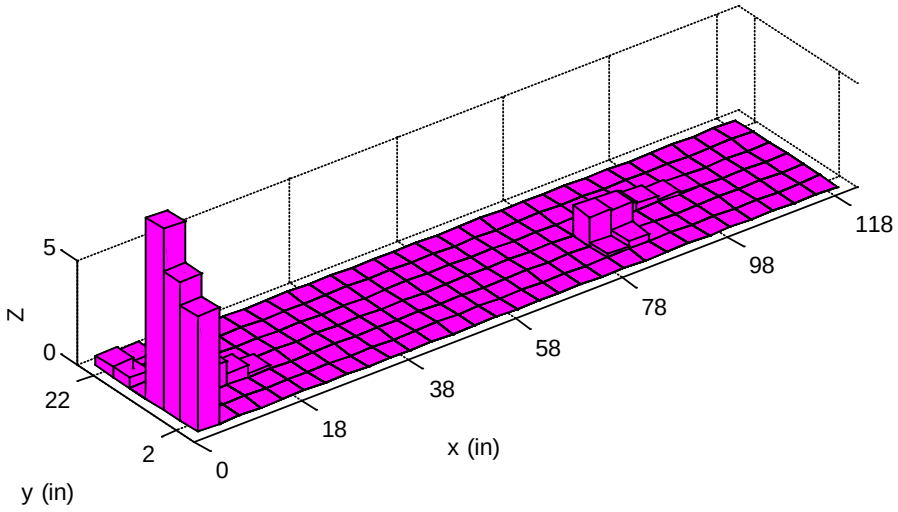

Figure 8.46 Damage Localization Result for Damage Case IB 5 Using Elasticity β_j^M

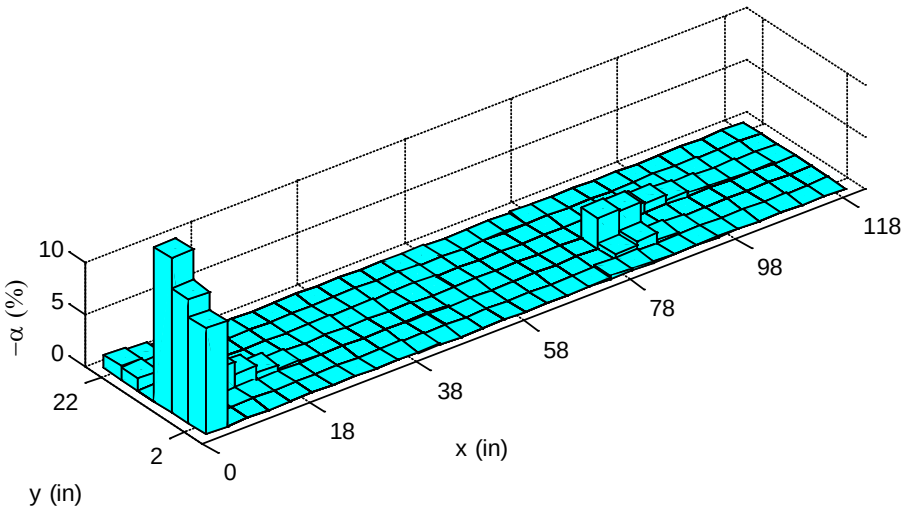

Figure 8.47 Damage Severity Estimates for Damage Case IB 5 Using Elasticity β_j^M

Table 8.16 Percent Error in Severity Estimates for Damage Case IB 5 Using Elasticity β_j^M

Damage Location		Damaged Element	Damage Severity (%)		Error (%)
x (in)	y (in)		Inflicted	Predicted	
2	2	1	-11.0	-10.2	7.3
2	6	31	-11.0	-11.9	-8.2
2	10	61	-11.0	-14.9	-35.5
2	14	91	-11.0	0.0	100.0
82	10	81	-7.0	-3.0	57.1
86	10	82	-7.0	-2.9	58.6

Figure 8.48 depicts the damage localization results and Figure 8.49 shows the damage severity estimates for Damage Case IB 5 using the damage indicator Elasticity β_j^V (Eq. (8.53)). Table 8.17 tabulates the percent error in severity estimation.

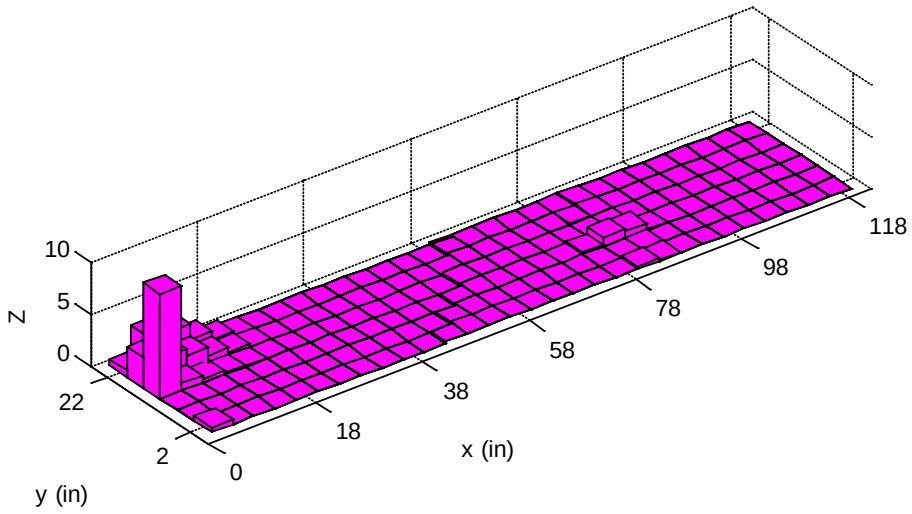

Figure 8.48 Damage Localization Result for Damage Case IB 5 Using Elasticity β_j^V

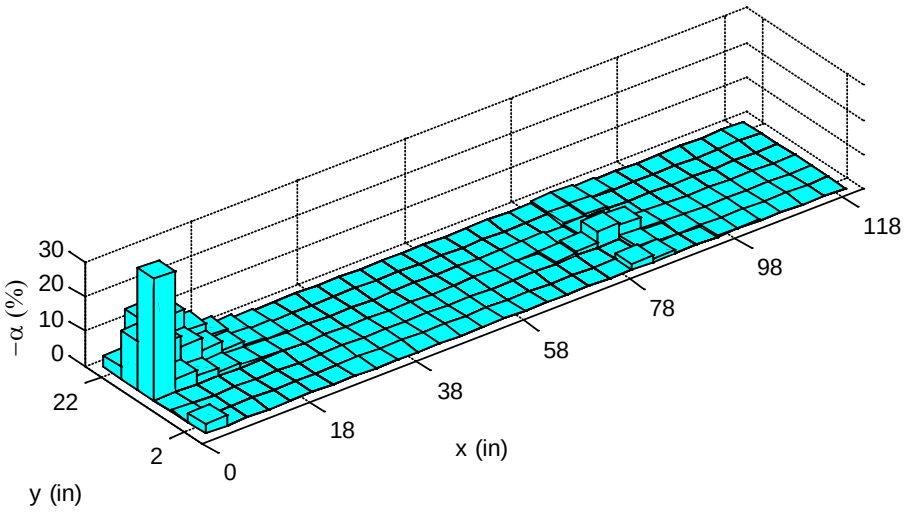

Figure 8.49 Damage Severity Estimates for Damage Case IB 5 Using Elasticity β_j^V

Table 8.17 Percent Error in Severity Estimates for Damage Case IB 5 Using Elasticity β_j^{V}

Damage Location		Damaged Element	Damage Severity (%)		Error (%)
x (in)	y (in)		Inflicted	Predicted	
2	2	1	-9.8	-2.8	71.4
2	6	31	-9.8	-0.3	96.9
2	10	61	-9.8	0.0	100.0
2	14	91	-9.8	-35.0	-257.1
82	10	81	-5.9	-4.6	22.0
86	10	82	-5.9	-4.1	30.5

Figure 8.50 depicts the damage localization results and Figure 8.51 shows the damage severity estimates for Damage Case IB 5 using the damage indicator Elasticity β_j^{ν} (Eq. (8.54)). Table 8.18 tabulates the percent error in severity estimation.

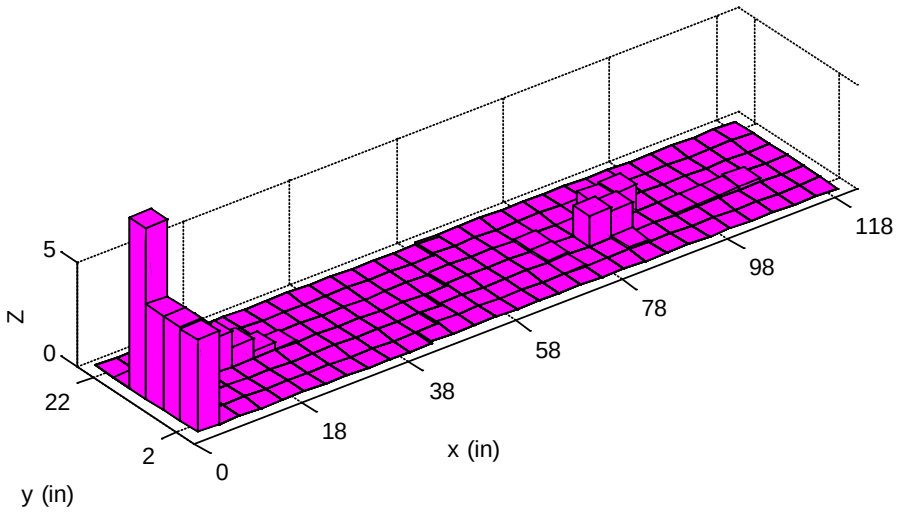

Figure 8.50 Damage Localization Result for Damage Case IB 5 Using Elasticity β_j^{ν}

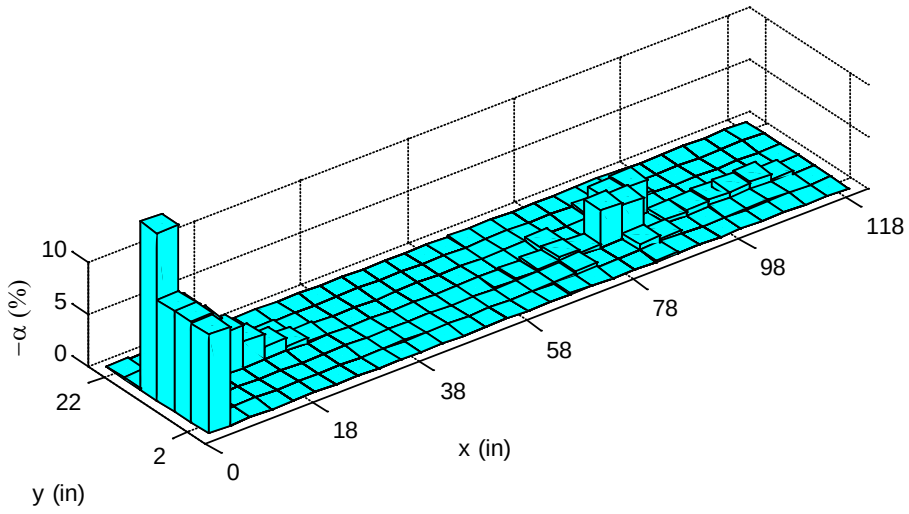

Figure 8.51 Damage Severity Estimates for Damage Case IB 5 Using Elasticity β_j^{ν}

Table 8.18 Percent Error in Severity Estimates for Damage Case IB 5 Using Elasticity β_j^{ν}

Damage Location		Damaged Element	Damage Severity (%)		Error (%)
x (in)	y (in)		Inflicted	Predicted	
2	2	1	-6.0	-9.5	-58.3
2	6	31	-6.0	-9.7	-61.7
2	10	61	-6.0	-9.7	-61.7
2	14	91	-6.0	-16.0	-166.7
82	10	81	-5.0	-3.6	28.0
86	10	82	-5.0	-3.3	34.0

The Deep Beam

Damage detection results for the deep beam are presented in this subsection. Damage localization results are presented in terms of the normalized damage indicator Z_j given in Eq. (4.8). The percent error in severity estimates are computed by Eq. (3.3).

Damage Case DB 1

Figure 8.52 shows the schematic representation of Damage Case DB 1 on the FE mesh of the deep beam. Figure 8.53 depicts the damage localization results and Figure 8.54 shows the damage severity estimates for Damage Case DB 1 using the damage indicator Elasticity β_j^{M}. Table 8.19 tabulates the percent error in severity estimation.

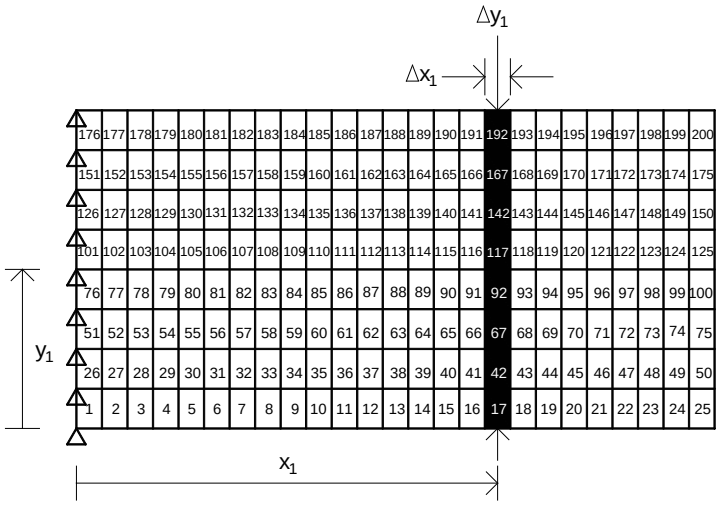

Figure 8.52 Schematic Representation of Damage Case DB 1

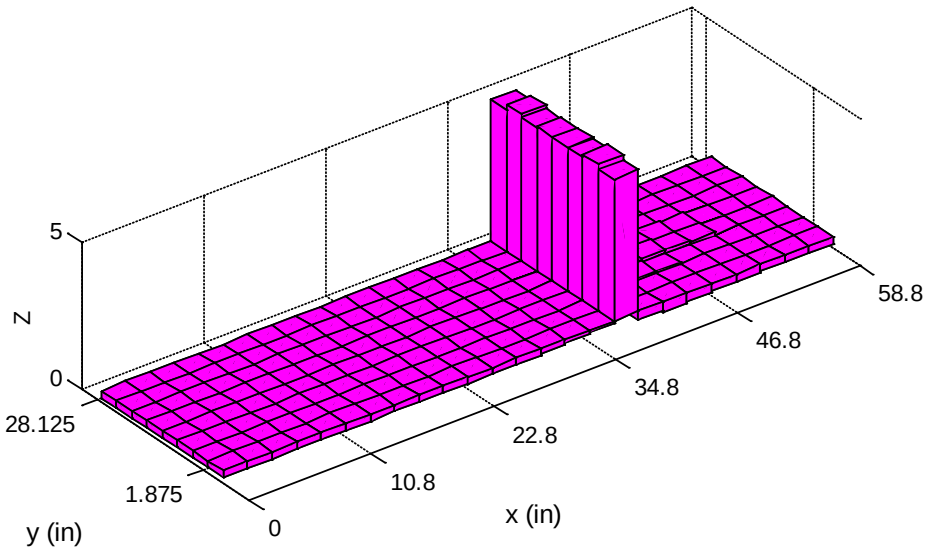

Figure 8.53 Damage Localization Result for Damage Case DB 1 Using Elasticity β_j^M

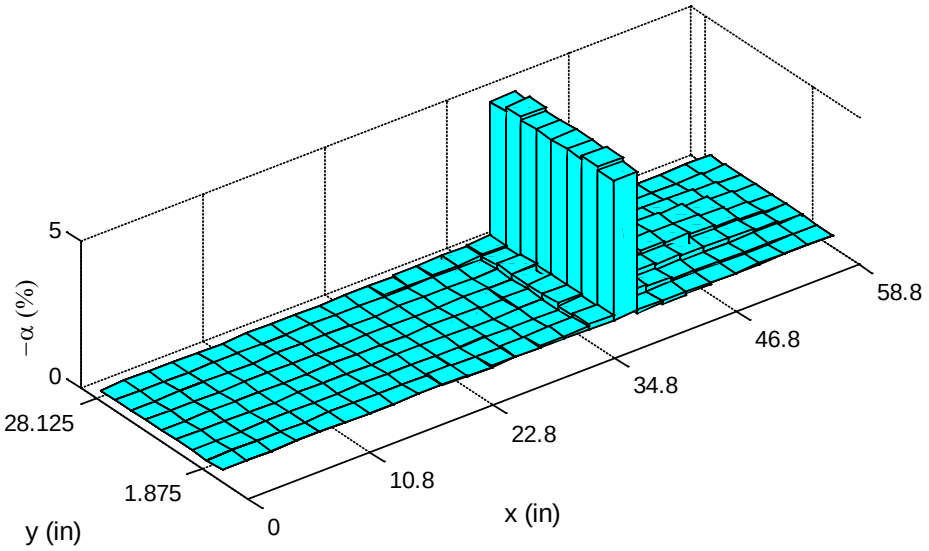

Figure 8.54 Damage Severity Estimates for Damage Case DB 1 Using Elasticity β_j^M

Table 8.19 Percent Error in Severity Estimates for Damage Case DB 1 Using Elasticity β_j^M

Damage Location		Damaged Element	Damage Severity (%)		Error (%)
x (in)	y (in)		Inflicted	Predicted	
39.6	1.875	17	-5.0	-4.7	6.0
39.6	5.625	42	-5.0	-4.9	2.0
39.6	9.375	67	-5.0	-4.8	4.0
39.6	13.125	92	-5.0	-4.8	4.0
39.6	16.875	117	-5.0	-4.8	4.0
39.6	20.625	142	-5.0	-4.8	4.0
39.6	24.375	167	-5.0	-4.9	2.0
39.6	28.125	192	-5.0	-4.7	6.0

Damage Case DB 2

Figure 8.55 shows the schematic representation of Damage Case DB 2 on the FE mesh of the deep beam. Figure 8.56 depicts the damage localization results and Figure 8.57 shows the damage severity estimates for Damage Case DB 2 using the damage indicator Elasticity $\beta_j^{\ M}$. Table 8.20 tabulates the percent error in severity estimation.

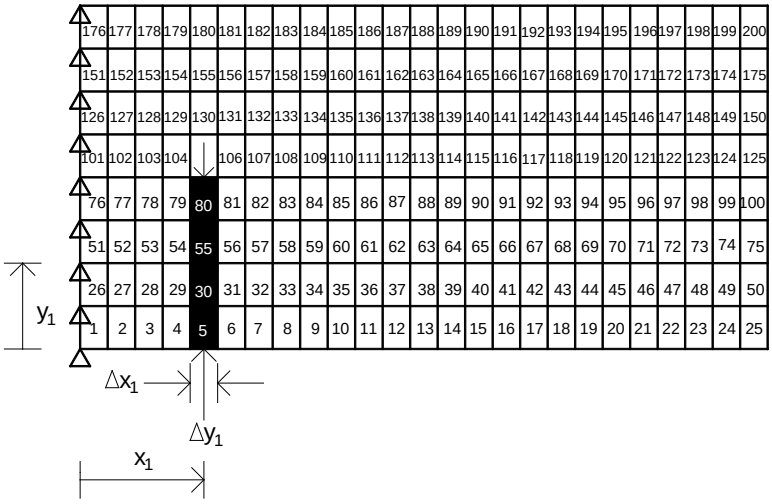

Figure 8.55 Schematic Representation of Damage Case DB 2

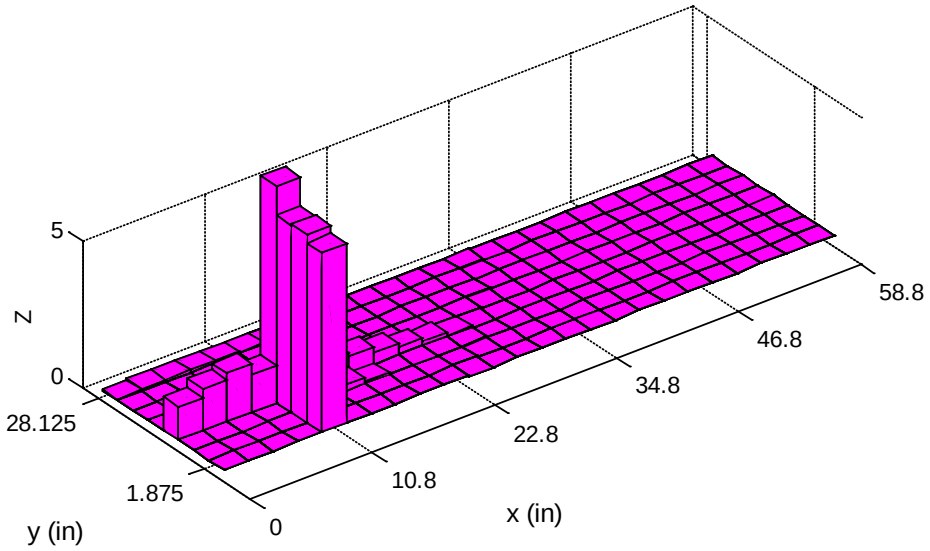

Figure 8.56 Damage Localization Result for Damage Case DB 2 Using Elasticity β_j^M

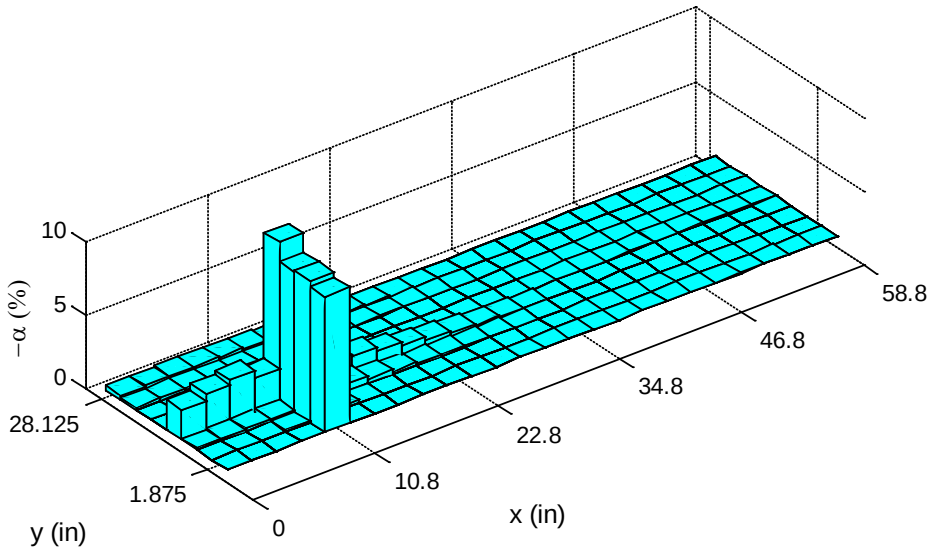

Figure 8.57 Damage Severity Estimates for Damage Case DB 2 Using Elasticity β_j^M

Table 8.20 Percent Error in Severity Estimates for Damage Case DB 2 Using Elasticity β_j^M

Damage Location		Damaged Element	Damage Severity (%)		Error (%)
x (in)	y (in)		Inflicted	Predicted	
10.8	1.875	5	-10.0	-9.1	9.0
10.8	5.625	30	-10.0	-9.5	5.0
10.8	9.375	55	-10.0	-9.5	5.0
10.8	13.125	80	-10.0	-10.8	-8.0

Damage Case DB 3

Figure 8.58 shows the schematic representation of Damage Case DB 3 on the FE mesh of the deep beam. Figure 8.59 depicts the damage localization results and Figure 8.60 shows the damage severity estimates for Damage Case DB 3 using the damage indicator Elasticity β_j^M. Table 8.21 tabulates the percent error in severity estimation.

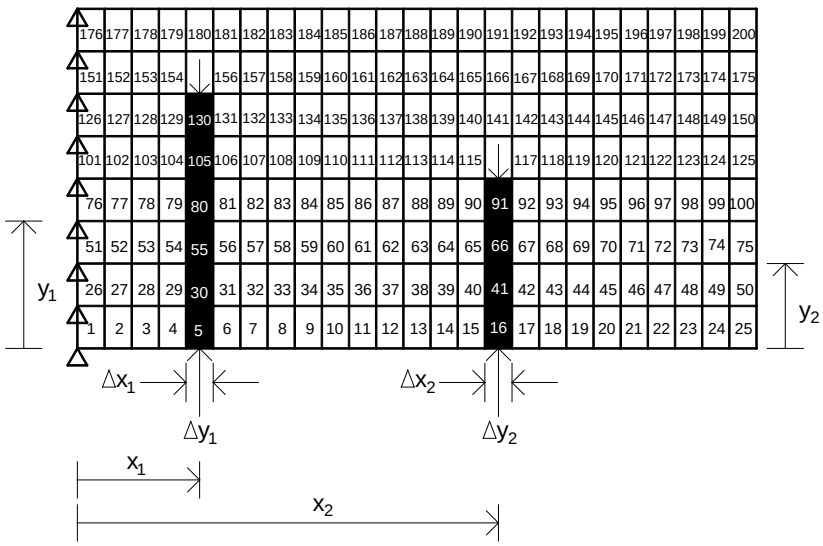

Figure 8.58 Schematic Representation of Damage Case DB 3

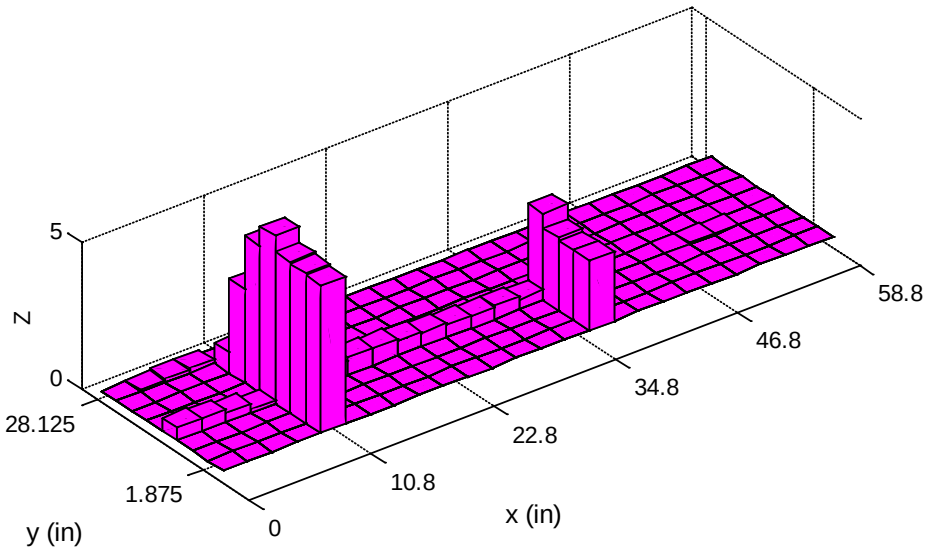

Figure 8.59 Damage Localization Result for Damage Case DB 3 Using Elasticity β_j^M

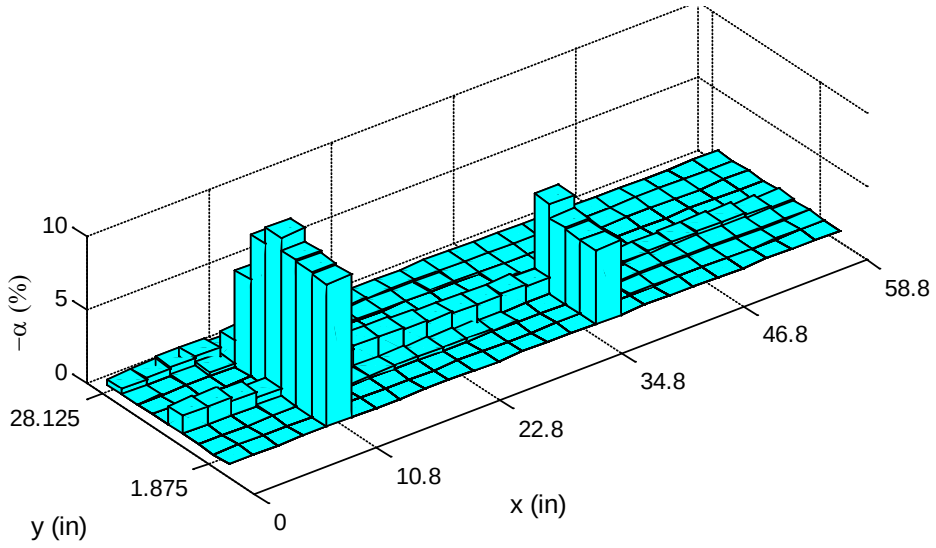

Figure 8.60 Damage Severity Estimates for Damage Case DB 3 Using Elasticity β_j^M

Table 8.21 Percent Error in Severity Estimates for Damage Case DB 3 Using Elasticity β_j^M

Damage Location		Damaged Element	Damage Severity (%)		Error (%)
x (in)	y (in)		Inflicted	Predicted	
10.8	1.875	5	-10.0	-9.7	3.0
10.8	5.625	30	-10.0	-9.8	2.0
10.8	9.375	55	-10.0	-9.9	1.0
10.8	13.125	80	-10.0	-10.8	-8.0
10.8	16.875	105	-10.0	-9.6	4.0
10.8	20.625	130	-10.0	-6.5	35.0
37.2	1.875	16	-5.0	-5.0	0.0
37.2	5.625	41	-5.0	-5.0	0.0
37.2	9.375	66	-5.0	-5.2	-4.0
37.2	13.125	91	-5.0	-6.1	-22.0

Figure 8.61 depicts the damage localization results and Figure 8.62 shows the damage severity estimates for Damage Case DB 3 using the damage indicator Elasticity β_j^V (Eq. (8.53)). Table 8.22 tabulates the percent error in severity estimation.

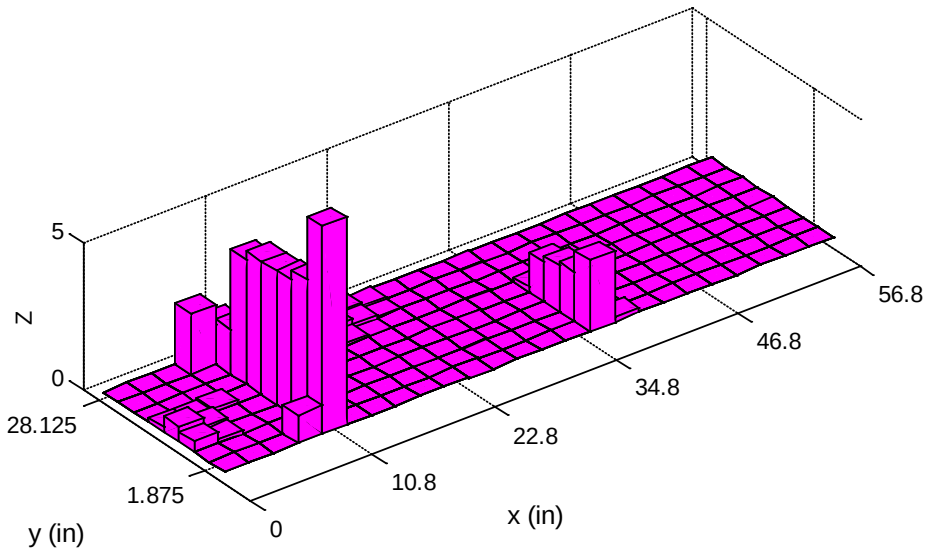

Figure 8.61 Damage Localization Result for Damage Case DB 3 Using Elasticity β_j^V

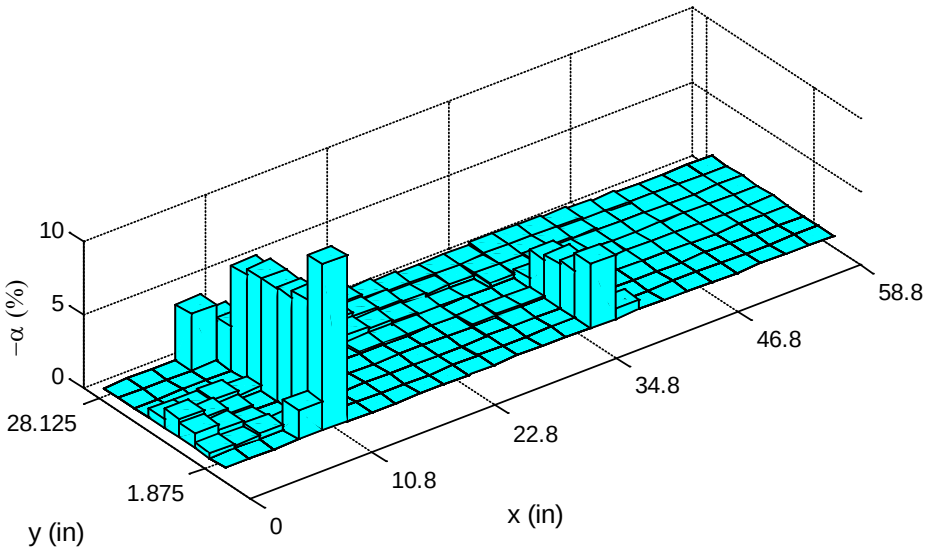

Figure 8.62 Damage Severity Estimates for Damage Case DB 3 Using Elasticity β_j^V

Table 8.22 Percent Error in Severity Estimates for Damage Case DB 3 Using Elasticity β_j^{V}

Damage Location		Damaged Element	Damage Severity (%)		Error (%)
x (in)	y (in)		Inflicted	Predicted	
10.8	1.875	5	-8.3	-11.2	-34.9
10.8	5.625	30	-8.3	-8.2	1.2
10.8	9.375	55	-8.3	-7.7	7.2
10.8	13.125	80	-8.3	-7.6	8.4
10.8	16.875	105	-8.3	-7.6	8.4
10.8	20.625	130	-8.3	-7.2	13.3
37.2	1.875	16	-3.4	-4.4	-29.4
37.2	5.625	41	-3.4	-3.2	5.9
37.2	9.375	66	-3.4	-3.0	11.8
37.2	13.125	91	-3.4	-2.6	23.5

Figure 8.63 depicts the damage localization results and Figure 8.64 shows the damage severity estimates for Damage Case DB 3 using the damage indicator Elasticity β_j^{V} (Eq. (8.54)). Table 8.23 tabulates the percent error in severity estimation.

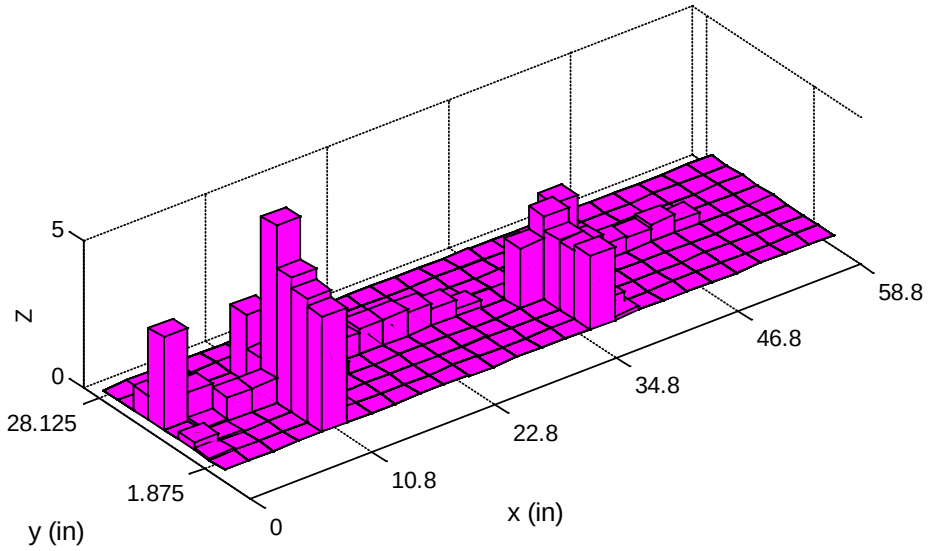

Figure 8.63 Damage Localization Result for Damage Case DB 3 Using Elasticity β_j^{ν}

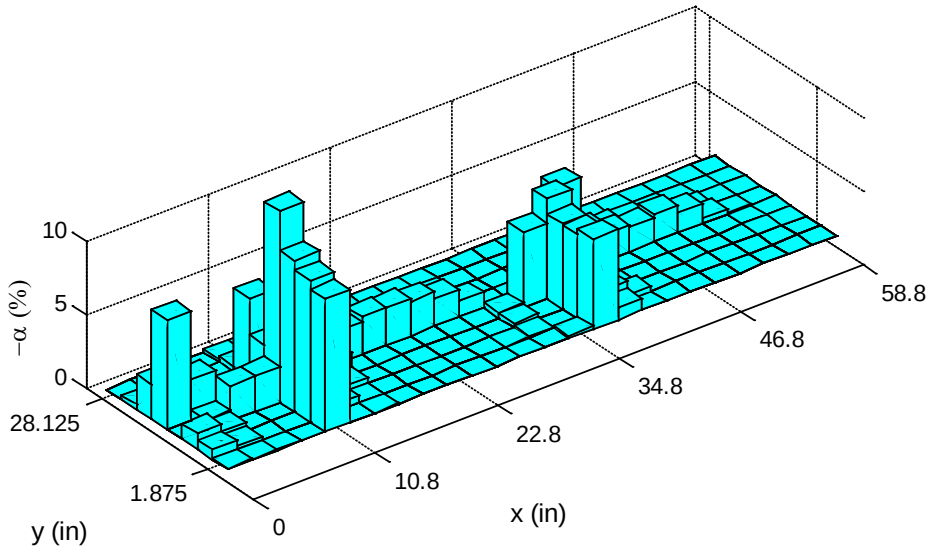

Figure 8.64 Damage Severity Estimates for Damage Case DB 3 Using Elasticity β_j^{ν}

Table 8.23 Percent Error in Severity Estimates for Damage Case DB 3 Using Elasticity β_j^{ν}

Damage Location		Damaged Element	Damage Severity (%)		Error (%)
x (in)	y (in)		Inflicted	Predicted	
10.8	1.875	5	-8.0	-9.0	-12.5
10.8	5.625	30	-8.0	-9.5	-18.8
10.8	9.375	55	-8.0	-10.2	-27.5
10.8	13.125	80	-8.0	-12.9	-61.3
10.8	16.875	105	-8.0	-3.2	60.0
10.8	20.625	130	-8.0	-5.7	28.8
37.2	1.875	16	-7.0	-6.1	12.9
37.2	5.625	41	-7.0	-5.7	18.6
37.2	9.375	66	-7.0	-5.7	18.6
37.2	13.125	91	-7.0	-6.8	2.9

Damage Case DB 4

Figure 8.65 shows the schematic representation of Damage Case DB 4 on the FE mesh of the deep beam. Figure 8.66 depicts the damage localization results and Figure 8.67 shows the damage severity estimates for Damage Case DB 4 using the damage indicator Elasticity β_j^{M} . Table 8.24 tabulates the percent error in severity estimation.

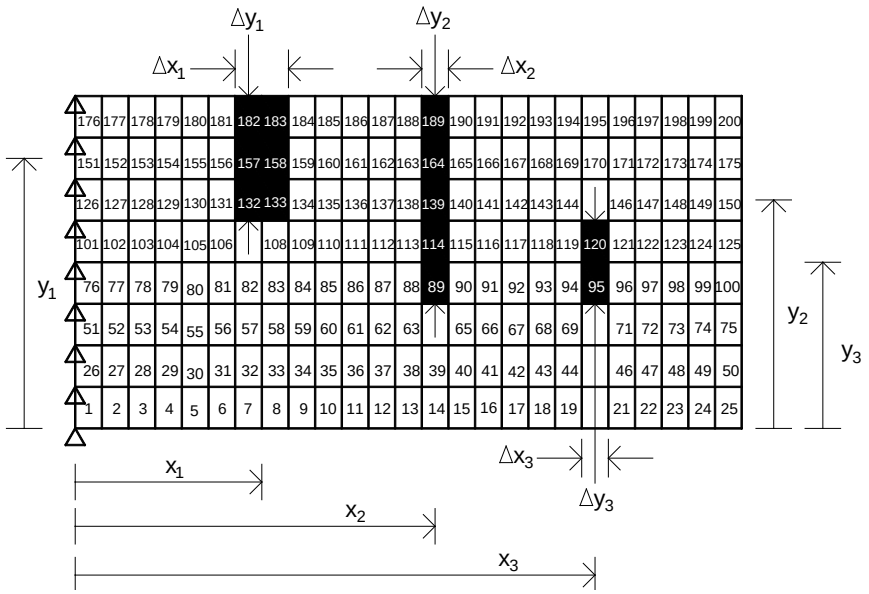

Figure 8.65 Schematic Representation of Damage Case DB 4

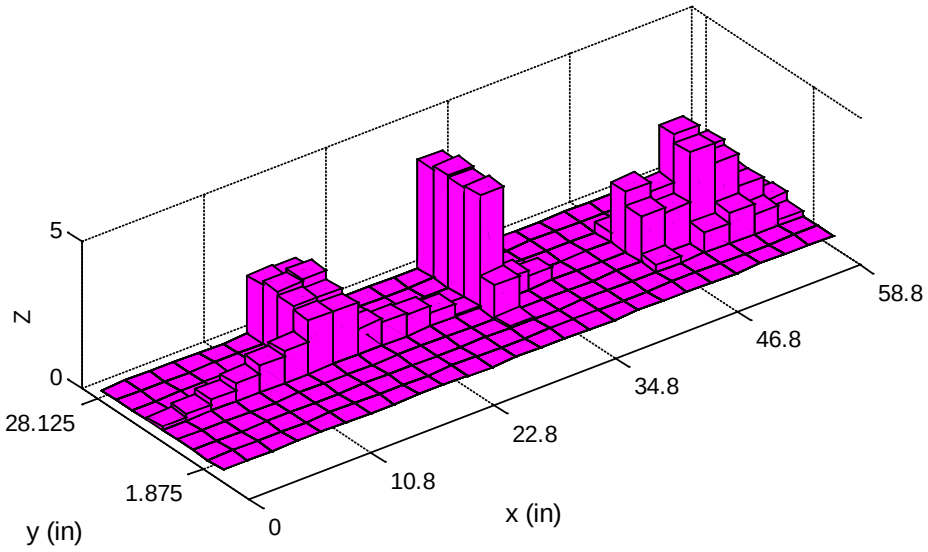

Figure 8.66 Damage Localization Result for Damage Case DB 4 Using Elasticity β_j^M

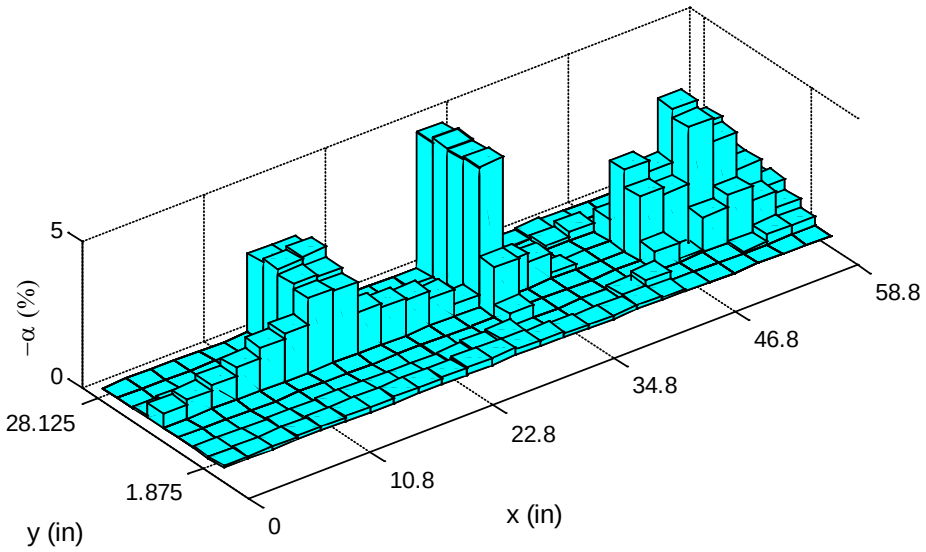

Figure 8.67 Damage Severity Estimates for Damage Case DB 4 Using Elasticity β_j^M

Table 8.24 Percent Error in Severity Estimates for Damage Case DB 4 Using Elasticity β_j^M

Damage Location		Damaged Element	Damage Severity (%)		Error (%)
x (in)	y (in)		Inflicted	Predicted	
15.6	20.625	132	-3.0	-2.7	10.0
15.6	24.375	133	-3.0	-2.6	13.3
15.6	28.125	157	-3.0	-2.8	6.7
18	20.625	158	-3.0	-2.9	3.3
18	24.375	182	-3.0	-2.7	10.0
18	28.125	183	-3.0	-2.7	10.0
32.4	13.125	89	-5.0	-1.7	66.0
32.4	16.875	114	-5.0	-4.7	6.0
32.4	20.625	139	-5.0	-4.7	6.0
32.4	24.375	164	-5.0	-4.7	6.0
32.4	28.125	189	-5.0	-4.6	8.0
46.8	13.125	95	-6.0	-2.1	65.0
46.8	16.875	120	-6.0	-2.7	55.0

Damage Case DB 5

Figure 8.68 shows the schematic representation of Damage Case DB 5 on the FE mesh of the deep beam. Figure 8.69 depicts the damage localization results and Figure 8.70 shows the damage severity estimates for Damage Case DB 5 using the damage indicator Elasticity β_j^M. Table 8.25 tabulates the percent error in severity estimation.

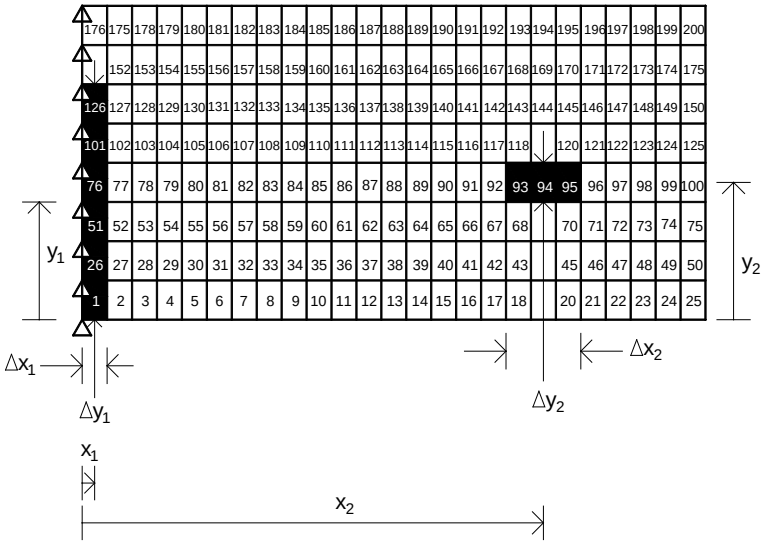

Figure 8.68 Schematic Representation of Damage Case DB 5

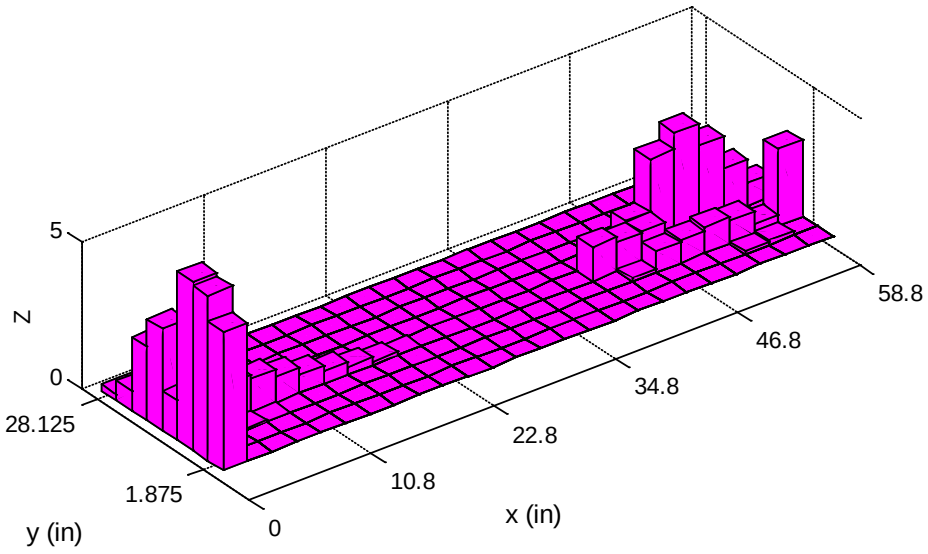

Figure 8.69 Damage Localization Result for Damage Case DB 5 Using Elasticity β_j^M

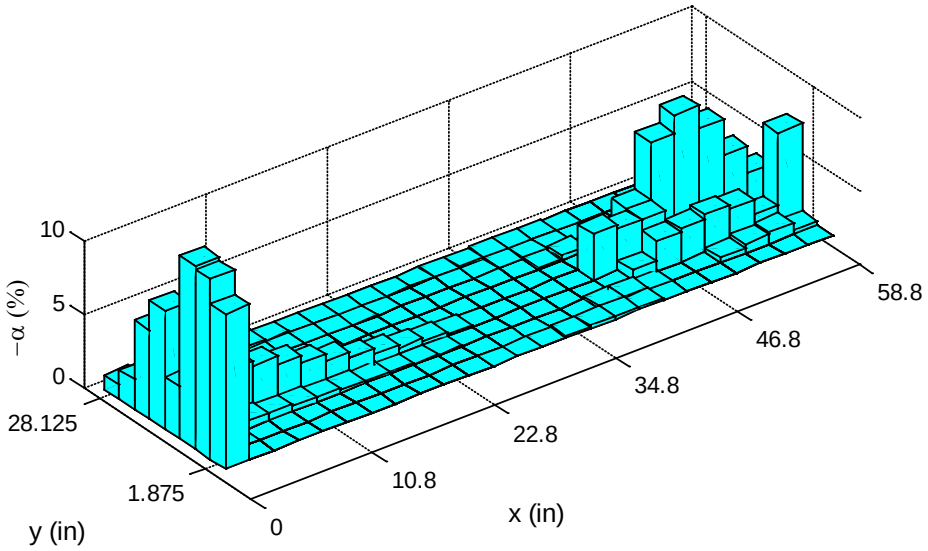

Figure 8.70 Damage Severity Estimates for Damage Case DB 5 Using Elasticity β_j^M

Table 8.25 Percent Error in Severity Estimates for Damage Case DB 5 Using Elasticity β_j^M

Damage Location		Damaged Element	Damage Severity (%)		Error (%)
x (in)	y (in)		Inflicted	Predicted	
1.2	1.875	1	-11.0	-10.5	4.5
1.2	5.625	26	-11.0	-12.1	-10.0
1.2	9.375	51	-11.0	-12.4	-12.7
1.2	13.125	76	-11.0	-3.5	68.2
1.2	16.875	101	-11.0	-8.0	27.3
1.2	20.625	126	-11.0	-6.0	45.5
42	13.125	93	-7.0	-3.1	55.7
44.4	13.125	94	-7.0	-2.8	60.0
46.8	13.125	95	-7.0	-2.8	60.0

Figure 8.71 depicts the damage localization results and Figure 8.72 shows the damage severity estimates for Damage Case DB 5 using the damage indicator Elasticity β_j^V (Eq. (8.53)). Table 8.26 tabulates the percent error in severity estimation.

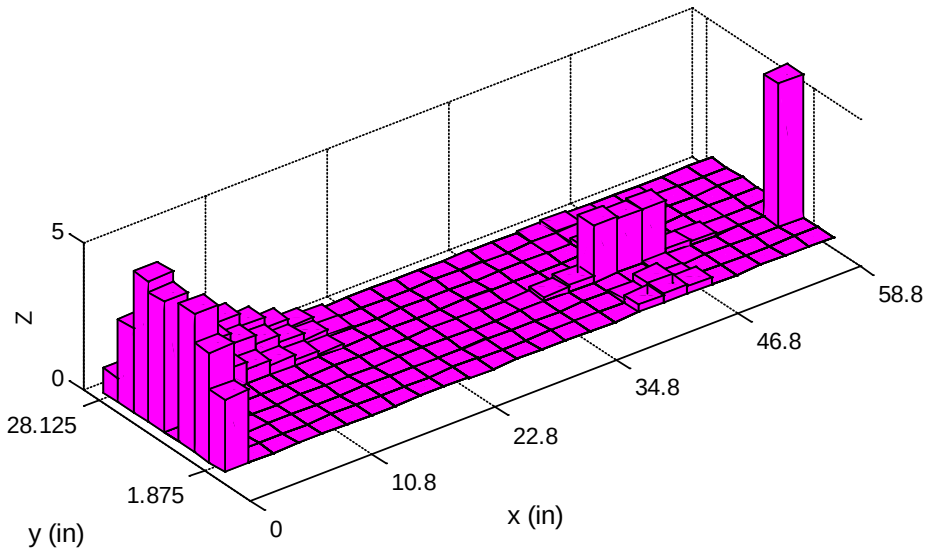

Figure 8.71 Damage Localization Result for Damage Case DB 5 Using Elasticity β_j^V

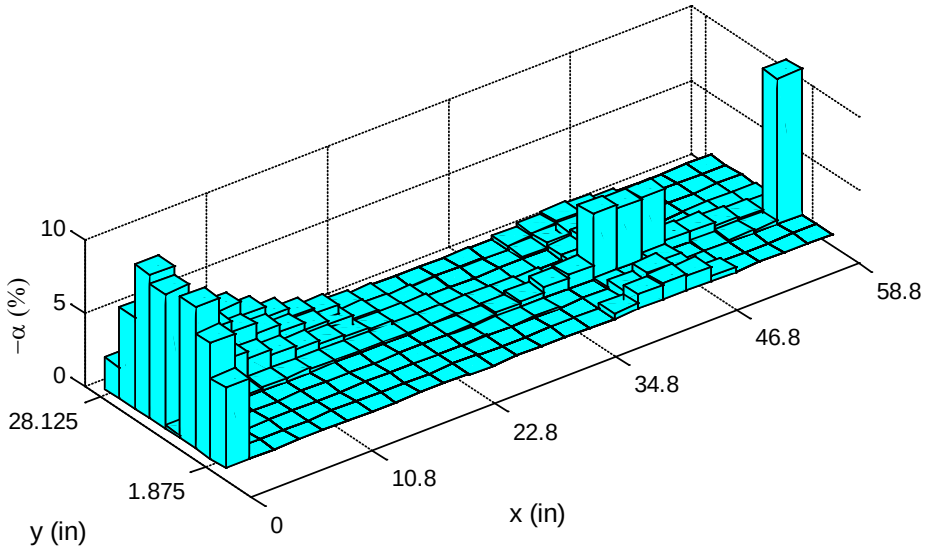

Figure 8.72 Damage Severity Estimates for Damage Case DB 5 Using Elasticity β_j^V

Table 8.26 Percent Error in Severity Estimates for Damage Case DB 5 Using Elasticity β_j^V

Damage Location		Damaged Element	Damage Severity (%)		Error (%)
x (in)	y (in)		Inflicted	Predicted	
1.2	1.875	1	-9.8	-5.5	43.9
1.2	5.625	26	-9.8	-7.8	20.4
1.2	9.375	51	-9.8	-9.6	2.0
1.2	13.125	76	-9.8	-0.2	98.0
1.2	16.875	101	-9.8	-9.1	7.1
1.2	20.625	126	-9.8	-9.8	0.0
42	13.125	93	-5.9	-4.4	25.4
44.4	13.125	94	-5.9	-4.2	28.8
46.8	13.125	95	-5.9	-4.3	27.1

Figure 8.73 depicts the damage localization results and Figure 8.74 shows the damage severity estimates for Damage Case DB 5 using the damage indicator Elasticity β_j^{ν} (Eq. (8.54)). Table 8.27 tabulates the percent error in severity estimation.

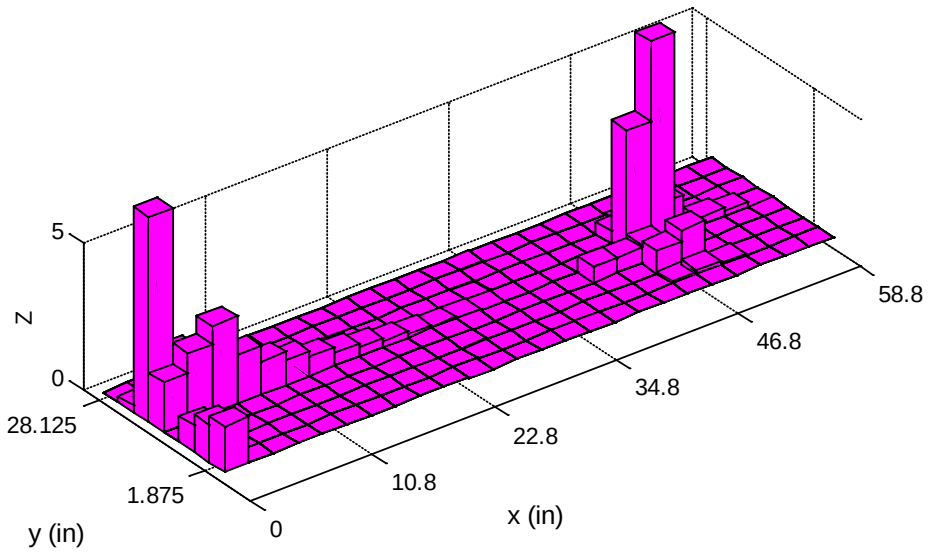

Figure 8.73 Damage Localization Result for Damage Case DB 5 Using Elasticity β_j^{ν}

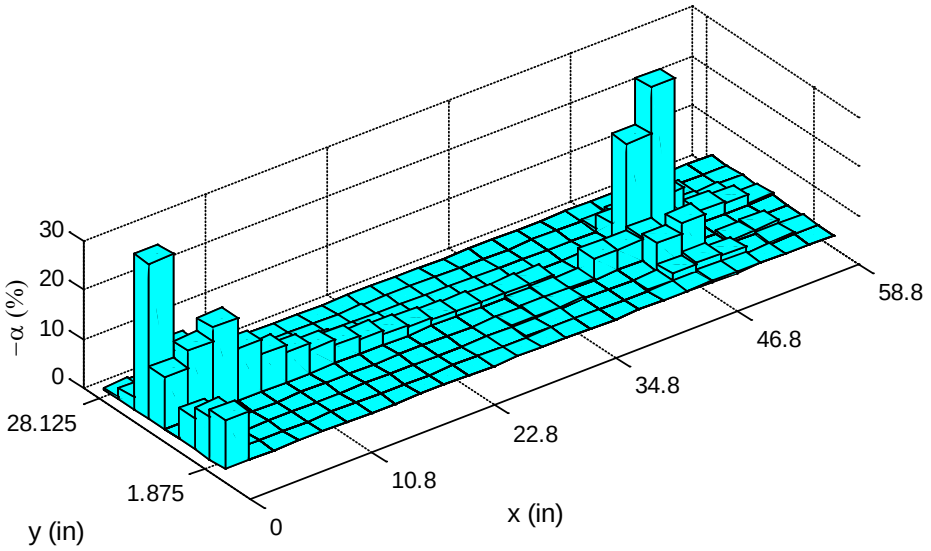

Figure 8.74 Damage Severity Estimates for Damage Case DB 5 Using Elasticity β_j^{ν}

Table 8.27 Percent Error in Severity Estimates for Damage Case DB 5 Using Elasticity β_j^{ν}

Damage Location		Damaged Element	Damage Severity (%)		Error (%)
x (in)	y (in)		Inflicted	Predicted	
1.2	1.875	1	-6.0	-9.9	-65.0
1.2	5.625	26	-6.0	-8.5	-41.7
1.2	9.375	51	-6.0	-6.3	-5.0
1.2	13.125	76	-6.0	0.0	100.0
1.2	16.875	101	-6.0	-10.5	-75.0
1.2	20.625	126	-6.0	-31.5	-425.0
42	13.125	93	-5.0	-4.3	14.0
44.4	13.125	94	-5.0	-4.3	14.0
46.8	13.125	95	-5.0	-4.8	4.0

DISCUSSION OF RESULTS

Based on the damage prediction results, the following observations can be made regarding the performance of the Elasticity Method:

Damage indicators Elasticity β_j^M and Elasticity β_j^ν successfully localized and quantified damage in scenarios SB 1 through SB 5. One false negative (FN) prediction was recorded in Damage Case SB 5 while utilizing Elasticity β_j^M for damage prediction. Note that, this corresponds to a single plane element located in the vicinity of the clamped-end. Certain deviations from the elastic solution are expected near boundaries, since the support conditions of FEM do not precisely match the ones utilized in the theoretical solution. The error between the true and the predicted damage severities ranged from a minimum of 0% for Damage Case SB 1 to a maximum of 100% for Damage Case SB 5. As expected, Elasticity β_j^V performed poorly in the case studies of the slender beam since shear deformations are likely to be significant only for the deep beam.

Damage scenarios IB 1 through IB 5 offered similar damage prediction results to the ones obtained for the slender beam. Damage indicators Elasticity β_j^M and Elasticity β_j^ν perform exceptionally well for the case studies of the intermediate beam also. The error between the true damage severity and the predicted damage severity, ranged from a minimum of 0% in Damage Case IB 3 to a maximum of 100 % in Damage Case IB 5. The location of FN prediction is analogous to the one given in the results of SB Damage Cases.

In damage scenarios DB 1 through DB 5, damage was successfully narrowed down to the vicinity of the inflicted damaged regions. Damage Case DB 1 offered the best damage detection results by correctly identifying the true damage locations and providing a maximum of 6.0% error for the damage severity estimate when Elasticity

β_j^M was utilized for damage detection. Damage Case DB 2 and DB 3 also performed equally well in identifying the location of damage, but presented a slight increase in the error between the true damage severity and the predicted damage severity. As the aspect ratio of the beam increased, damage indicator, Elasticity β_j^V, began to produce better damage prediction results than Elasticity β_j^v. Damage Cases DB 4 and DB 5 provided ambiguous damage prediction results at the elements located in the vicinity of the free end. This might be due to reaching diminutive strain data as the measurements are taken closer to the free end of the beam.

It is imperative to note that the damage indices utilized above are derived from linear elasticity solutions and are only exact if the test structure precisely matches the assumptions used in deriving the damage indices. Deviations from the elasticity solution are always expected especially within the proximity of supports.

SUMMARY AND CONCLUSIONS

Explicit damage indices were developed using the Theory of Linear Elasticity and the principle of identical external load distribution before and after damage in this chapter. It was shown that local changes in the structural and material properties of beam-type structural elements could be expressed in terms of the pre-damage and post-damage strain distributions. Damage in the flexural and shear stiffness distributions, as well as local changes in the Poisson's ratio due to damage may be investigated by utilizing such techniques. Proposed damage detection methodologies produced two-dimensional damage indicators, which were able to perform nondestructive damage evaluation through the length and the depth of the beam. Finally, it was shown that the damage indices developed for the tip-loaded cantilever beam also holds for other loading conditions and beam types (such as the simply supported beam subjected to uniform loading) under certain assumptions.

CHAPTER IX

DAMAGE DETECTION RESULTS USING FIELD MEASUREMENTS

INTRODUCTION

The objective of this chapter is to evaluate the performance of the proposed NDD methodologies using field measurements. Experimental modal data collected from the Interstate 40 (I-40) Bridge will be utilized to accomplish the stated objective. Experimental results include the pre-damage and post-damage translational mode shapes and eigenfrequencies of the structure. Since point deflections and rotations are required, employing the damage detection methodologies based on the Timoshenko beam theory is not possible with the given set of modal information. For this reason, NDD methods based on the Euler-Bernoulli beam theory will be used for damage prediction.

This chapter is divided into five sections: a section describing the structure and the inflicted damage scenarios; a section describing the structural response parameters utilized for damage detection; a section summarizing the previous NDD algorithms utilized for damage detection; a section evaluating the performance of the NDD methodology chosen for damage prediction; and a section discussing the outcomes of the performed case studies.

DESCRIPTION OF THE STRUCTURE

The I-40 Bridges located over Rio Grande in Albuquerque, NM were demolished in the summer of 1993 and were replaced by a new bridge. Prior to the replacement, researchers were able to introduce incremental levels of damage on the bridge and performed experimental modal analyses at each damage stage. The results of the experiments were utilized to evaluate the performance of five previously published non-destructive damage identification methods.

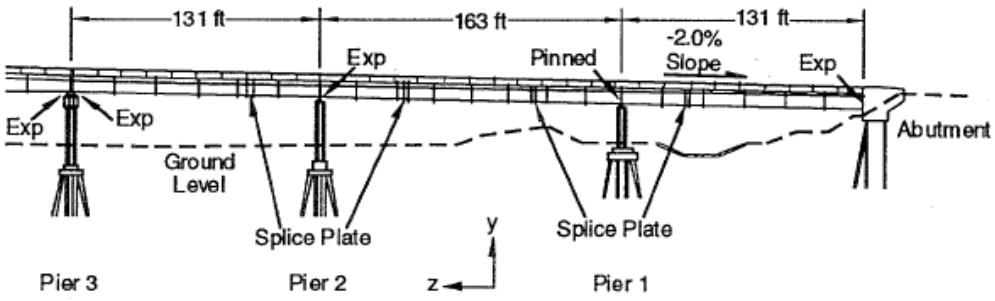

Figure 9.1 Elevation View of the Portion of the Bridge that was Tested

(Taken from: Farrar and Jauregui (1996))

The I-40 Bridge consisted of twin spans for each traffic direction. Each span was made up of a concrete deck, which was supported by two welded-steel plate girders and three steel stringers. Each bridge was made up of three identical sections. The sections were structurally independent. A single section had three spans; the two end spans were of equal length with approximately 131 ft., and the center span was approximately 163 ft. long. Detailed description of the structure may be found in Farrar et al. (1994). Elevation view and a typical cross-section of the bridge are given in Figures 9.1 and 9.2 respectively.

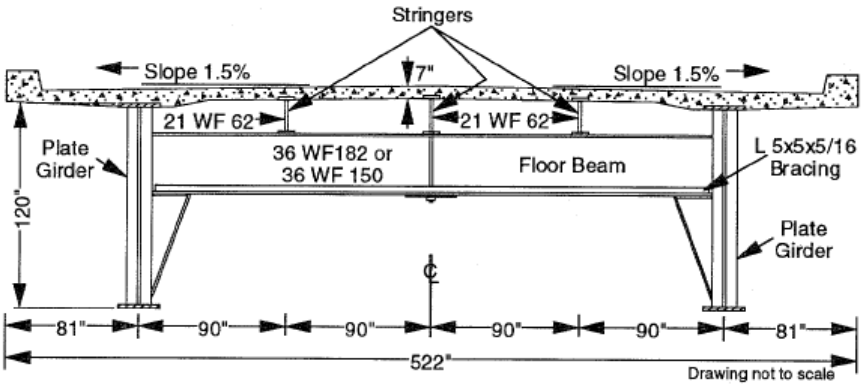

Figure 9.2 Typical Cross-section of the Bridge

(Taken from: Farrar and Jauregui (1996))

Inflicted Damage Scenarios

Four incremental levels of damage were inflicted at the mid-span of the north plate girder by making various torch cuts in the web and flange of the girder. These damage scenarios are intended to simulate fatigue cracking in the girder.

The first damage scenario was a two-foot long, 3/8 in. wide web cut centered vertically at the mid-height of the girder. In the second damage scenario, initial cut was extended to include the bottom of the web. In the third damage scenario, in addition to the 6ft web, the bottom flange was cut halfway in from either side below the web. Finally, the 6 ft web and full bottom flange were removed in the fourth damage scenario. Figure 9.3 depicts the torch cuts made at various portions of the north girder for simulating the sequential damage. Letters A to D represent damage scenarios 1 to 4 consecutively.

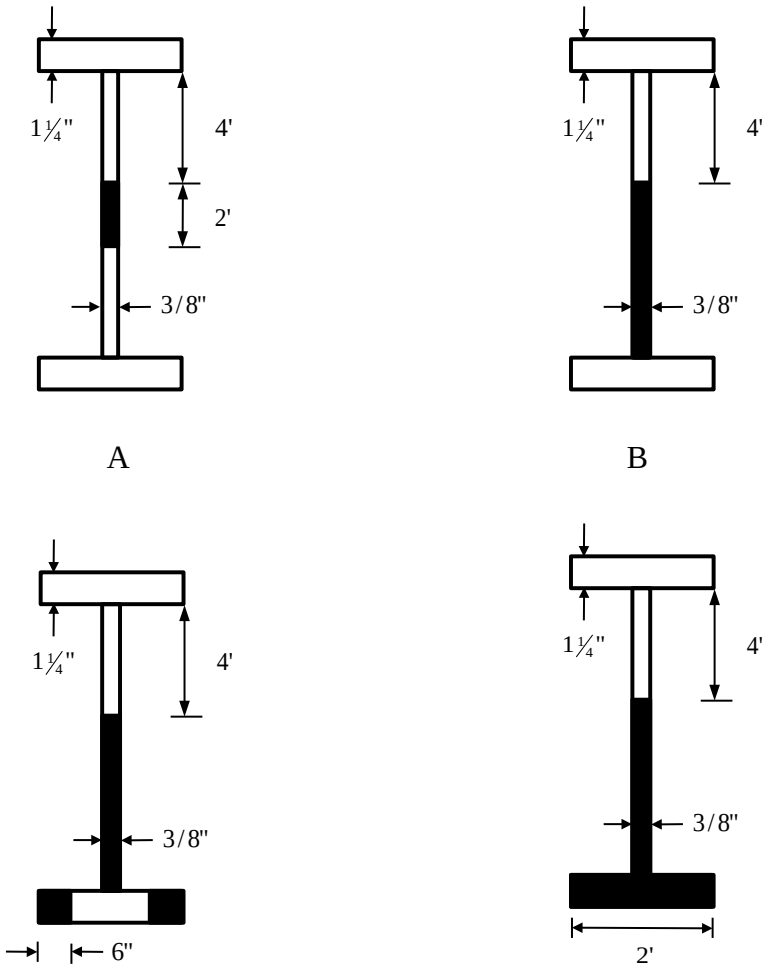

Figure 9.3 Damage Scenarios Inflicted on the North Plate Girder

A: Damage Scenario 1 (D1), B: Damage Scenario 2 (D2),

C: Damage Scenario 3 (D3), D: Damage Scenario 4 (D4).

RESPONSE PARAMETERS UTILIZED FOR DAMAGE DETECTION

Forced vibration tests were performed on the undamaged bridge. These tests were repeated after each incremental damage scenario had been introduced. Three sets of modal data were used for damage detection. SET 1 represented the experimental modal data obtained from the cross spectra analysis utilizing the refined set of sensor measurements collected from the mid-span of the north girder. The input signal was not monitored in this set of data and vertical accelerations were measured at the mid-height of the plate girder. Figure 9.4 depicts the locations of the accelerometers within the mid-span of the north girder. The first two bending modes for the undamaged structure and for four sequentially damaged structures are shown in Figure 9.5 A and B. Resonant frequencies for these modes are listed in Table 9.1. These modal data are taken from Farrar and Jauregui (1996).

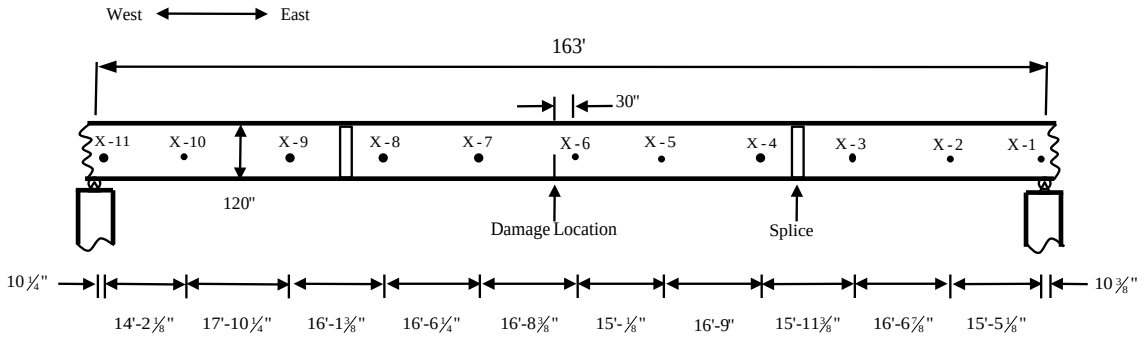

Figure 9.4 Sensor Layout for the North Plate Girder

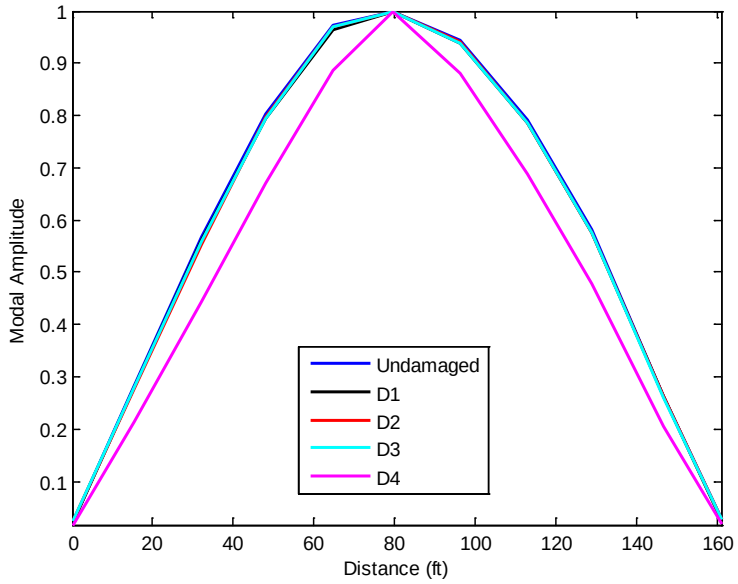

A

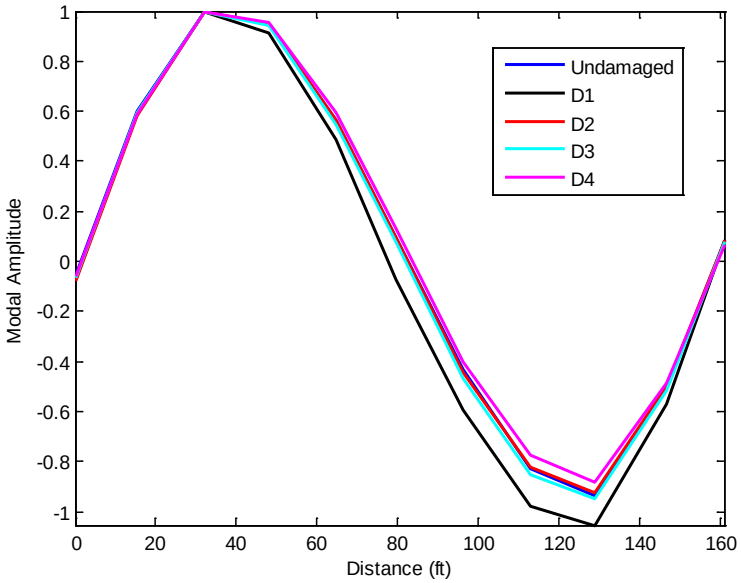

B

Figure 9.5 Unit-normalized Mode Shapes

A: The First Bending Mode, B: The Second Bending Mode.

Table 9.1 Resonant Frequencies for the First Two Bending Modes

Mode	Ref. (Hz)	D1 (Hz)	D2 (Hz)	D3 (Hz)	D4 (Hz)
1st Bending	2.500	2.531	2.531	2.469	2.312
2nd Bending	3.562	3.594	3.531	3.500	3.500

SUMMARY OF THE PREVIOUS NDD ALGORITHMS UTILIZED FOR DAMAGE DETECTION

Five damage detection algorithms were employed to locate the inflicted damage in the bridge. These include:

(1) The Damage Index Method (Stubbs et al. (1992));

(2) The Mode Shape Curvature Method (Pandey et al. (1991));

(3) The Change in Flexibility Method (Pandey and Biswas (1994))

(4) The Change in Uniform Load Surface Curvature Method (Zhang and Aktan (1995));

(5) The Change in Stiffness Method (Zimmerman and Kaouk (1994))

Detailed descriptions of these methods are available in literature. Only a brief summary is provided here.

The Damage Index Method

The damage indicator for the i^{th} mode and the j^{th} element, β_{ij}, is given by (Stubbs et. al. (1992)):

$$\beta_{ij} = \frac{s_j}{s_j^*} \tag{9.1}$$

where the scalars s_j and s_j^* are parameters that represent the bending stiffnesses of the undamaged and damaged j^{th} element of the damage detection model. Assuming Euler-Bernoulli beam behavior, the damage index was approximated by the expression:

$$\beta_{ij} = \frac{\sum_{i=1}^{NM}\left(\int_j [\{\phi_i^*\}''(x)]^2\,dx + \int_L [\{\phi_i^*\}''(x)]^2\,dx\right) / \int_L [\{\phi_i^*\}''(x)]^2\,dx}{\sum_{i=1}^{NM}\left(\int_j [\{\phi_i\}''(x)]^2\,dx + \int_L [\{\phi_i\}''(x)]^2\,dx\right) / \int_L [\{\phi_i\}''(x)]^2\,dx} \tag{9.2}$$

where NM denotes the number of modes that are being used. The i^{th} bending mode shape measured along the spatial coordinate x is represented by $\phi_i(x)$, and the asterisk (*) stands for the quantities associated with the damaged structure.

Note that if $\beta \le 1$, no damage exists in the member; if $\beta > 1$, then damage may exist in the member; and if $\beta = \infty$ then the member j would have lost all of its stiffness capacity.

A normalized damage indicator for each location denoted by Z_j is computed using the equation:

$$Z_j = \frac{(\beta_j - \overline{\beta})}{\sigma_\beta} \tag{9.3}$$

where $\overline{\beta}$ and σ_β represent the mean and standard deviation for the collection of damage indicators for all locations.

The Mode Shape Curvature Method

The relationship between the modal moment and the mode shape curvature is given by the following expression in beam-type structures:

$$\phi''(x) = \frac{M(x)}{EI} \tag{9.4}$$

where x is the spatial coordinate along the length of the beam and EI represents the flexural rigidity of a section in the beam. Due to this relationship, the absolute difference between the curvature mode shapes of the intact and damaged beam increases as the stiffness of the damaged zone is reduced. This difference may then be used to predict the location of the inflicted damage.

The Change in Flexibility Method

Utilizing mass-normalized mode shapes, the flexibility matrix F can be obtained from the modal data as follows:

$$F \approx \sum_{i=1}^{NM} \frac{1}{\omega_i^2} \Phi_i \Phi_i^T \tag{9.5}$$

where NM denotes the number of modes that are measured, ω_i represents the i^{th} natural frequency and Φ_i is the mass-normalized i^{th} mode shape vector.

Flexibility matrix of the damaged structure can be computed in a similar fashion. Utilizing the pre-damage and post-damage flexibility matrices, the change in flexibility due to damage may be calculated as follows:

$$\Delta F = F - F^* \tag{9.6}$$

For each column of ΔF, a damage indicator δ_j is defined to be the absolute maximum value of the elements in that column. Namely:

$$\delta_j = \max\left|\delta_{ij}\right|, \text{ for } i = 1..NM \tag{9.7}$$

The column of the flexibility matrix corresponding to the largest δ_j indicates the degree of freedom where damage is located.

The Change in Uniform Load Surface Curvature Method (Uniform Flexibility)

Utilizing certain characteristics of the Change Mode Shape Curvature Method and the Change in Flexibility Method, Zhang and Aktan (1995) proposed an alternative damage indicator. The sum of the unit load flexibilities (the sum of all columns of the flexibility matrix) represents the deformed shape of the structure loaded at all the degrees of freedom. This deformed shape is referred to as the uniform load surface. The absolute change in the curvatures of the uniform load surfaces before and after damage is an indicator of damage location. This difference is formulated as:

$$\Delta F'' = \left| \{F^*\}'' - \{F\}'' \right| \tag{9.8}$$

The Change in Stiffness Method

Utilizing mass-normalized mode shapes, the stiffness matrix K can be approximated from the modal data as follows:

$$K \approx \sum_{i=1}^{NM} \omega_i{}^2 \Phi_i \Phi_i{}^T \tag{9.9}$$

where NM denotes the number of modes that are measured, ω_i represents the i^{th} natural frequency and Φ_i is the mass-normalized i^{th} mode shape vector.

Similarly, for the damaged structure, the corresponding stiffness matrix can be approximated by:

$$K^* \approx \sum_{i=1}^{NM} \omega_i{}^{*2} \Phi_i{}^* \Phi_i{}^{*T} \tag{9.10}$$

where asterisk indicates the damaged modal parameters.

Utilizing the pre- and post-damage stiffness matrices, the change in stiffness due to damage may be calculated by:

$$\Delta K = K - K^{*} \tag{9.11}$$

A damage vector D_i, which should indicate the location of damage for the i^{th} mode is defined as:

$$D_i = \Delta K \Phi_i \tag{9.12}$$

Table 9.2 Summary of Damage Detection Results Using SET 1 Modal Data

(Adapted from: Farrar and Jauregui (1996))

Damage Scenario	Damage Index	Mode Shape Curvature	Change in Flexibility	Change in Uniform Flexibility	Change in Stiffness
D1	●	●●●	○	○	○
D2	●	●●	○	●●●	○
D3	●	●	○	●	○
D4	●	●	●	●	●
●	Damage Located				
●●	Damage Narrowed Down to Two Locations				
●●●	Damage Narrowed Down to Three Locations				
○	Damage Not Located				

Table 9.2 summarizes the performance of each damage detection algorithm described above by utilizing SET 1 modal data. The location of the most severe damage scenario (D4) has been identified by all methods. Clearly, standard modal properties such as resonant frequencies and mode shapes are poor indicators of damage. The Damage Index Method outperformed all other NDD algorithms by identifying the true location of damage in all scenarios. No information was provided regarding the damage severity estimates in the study.

PERFORMANCE OF THE EB PSEUDO METHOD ON LOS ALAMOS DATA

The performance of the EB Pseudo Method using the experimental modal data of the I-40 Bridge is evaluated in this section. The performance of the method is based on accurately identifying the location and the severity of the damage. SET 1 sensor readings are utilized for damage prediction.

Damage Scenario 1

Figures 9.6 and 9.7 depict the damage prediction results for Damage Scenario 1 using the damage indicator EB Pseudo β_j (Eq. (5.17)). Table 9.3 and 9.4 tabulate the performance of the damage detection methodology for the damage scenario.

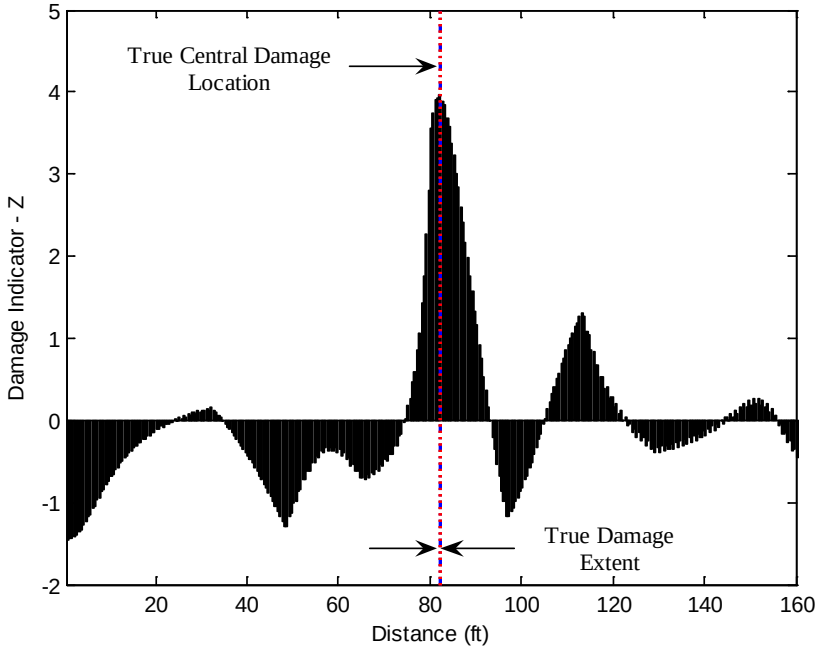

Figure 9.6 Damage Localization Result for Damage Scenario 1 Using EB Pseudo β_j

Table 9.3 Assessment of the Damage Localization Accuracy for Damage Scenario 1 Using EB Pseudo β_j

Damage Central Location (ft)		Error (%)	$P(T \subset P)$
True	Predicted		
82.2	82.0	0.1	100%

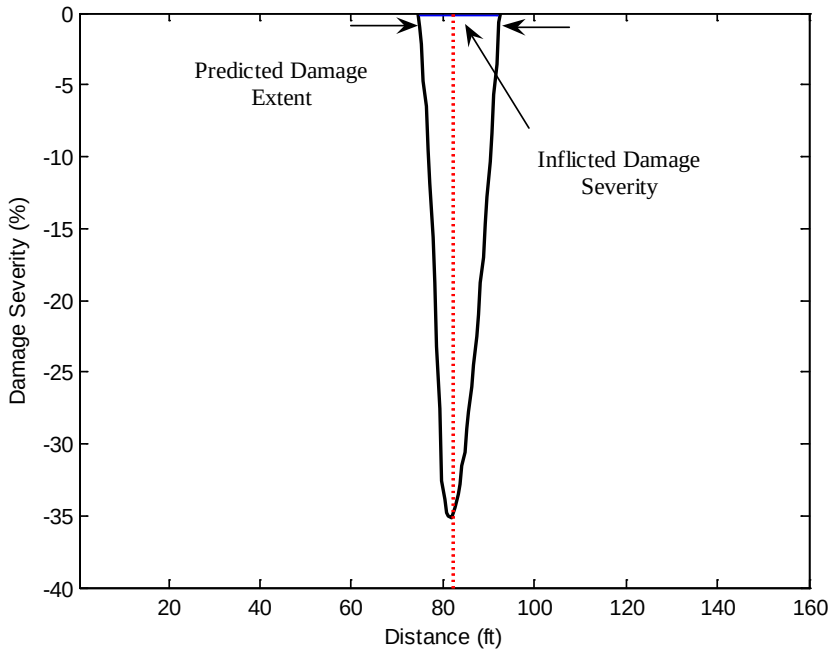

Figure 9.7 Damage Severity Estimate for Damage Scenario 1 Using EB Pseudo β_j

Table 9.4 Assessment of the Damage Severity Accuracy for Damage Scenario 1 Using EB Pseudo β_j

Damage Severity (%)		Error (%)
True	Predicted Lower Bound/Upper Bound	
-0.2	-22.0/-35.2	$(-11/-18)10^3$

Damage Scenario 2

Figures 9.8 and 9.9 depict the damage prediction results for Damage Scenario 2 using the damage indicator EB Pseudo β_j. Table 9.5 and 9.6 tabulate the performance of the damage detection methodology for the damage scenario.

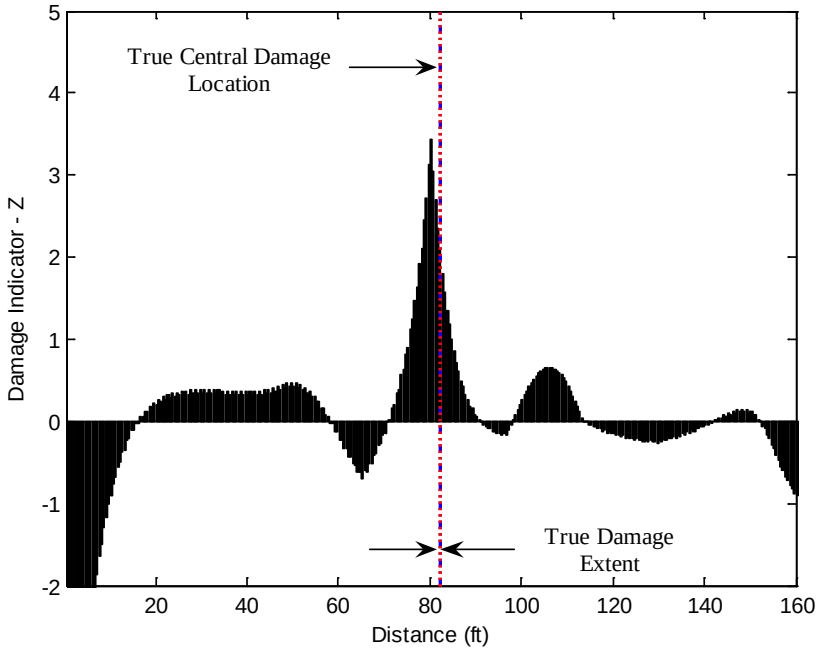

Figure 9.8 Damage Localization Result for Damage Scenario 2 Using EB Pseudo β_j

Table 9.5 Assessment of the Damage Localization Accuracy for Damage Scenario 2 Using EB Pseudo β_j

Damage Central Location (ft)		Error (%)	$P(T \subset P)$
True	Predicted		
82.2	80.3	1.2	100%

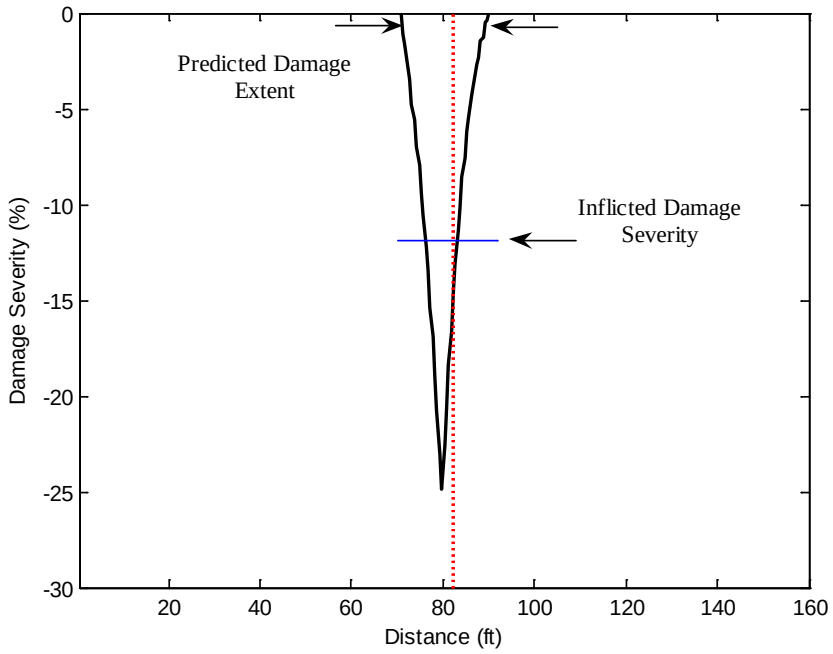

Figure 9.9 Damage Severity Estimate for Damage Scenario 2 Using EB Pseudo β_j

Table 9.6 Assessment of the Damage Severity Accuracy for Damage Scenario 2 Using EB Pseudo β_j

Damage Severity (%)		Error (%)
True	Predicted Lower Bound/Upper Bound	
-11.9	-10.4/-24.9	12.6/-109.2

Damage Scenario 3

Figures 9.10 and 9.11 depict the damage prediction results for Damage Scenario 3 using the damage indicator EB Pseudo β_j. Table 9.7 and 9.8 tabulate the performance of the damage detection methodology for the damage scenario.

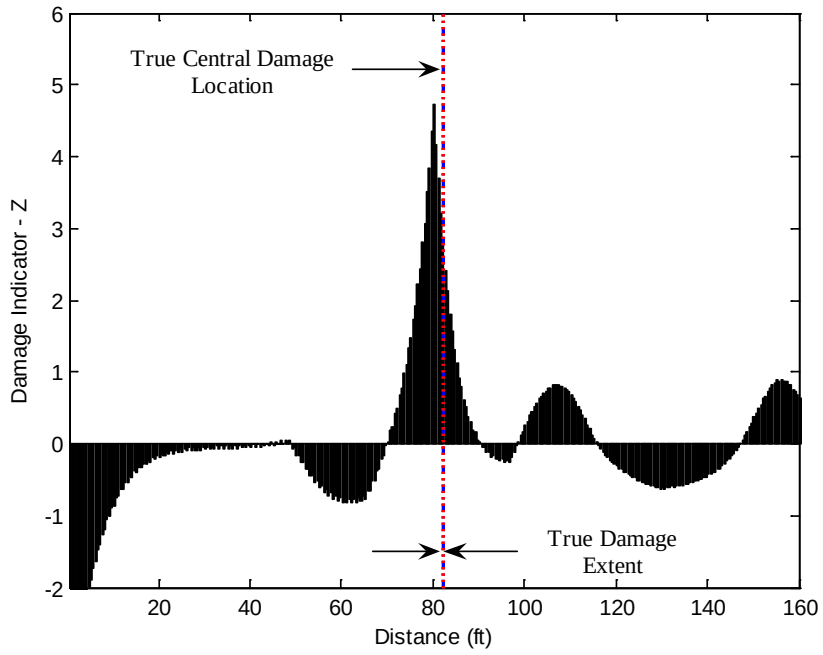

Figure 9.10 Damage Localization Result for Damage Scenario 3 Using EB Pseudo β_j

Table 9.7 Assessment of the Damage Localization Accuracy for Damage Scenario 3 Using EB Pseudo β_j

Damage Central Location (ft)		Error (%)	$P(T \subset P)$
True	Predicted		
82.2	80.3	1.2	100%

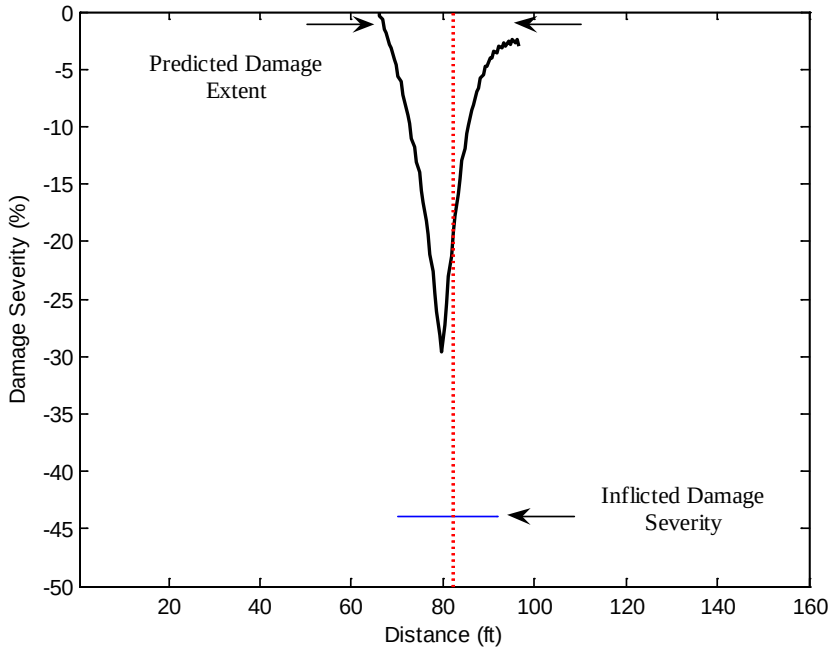

Figure 9.11 Damage Severity Estimate for Damage Scenario 3 Using EB Pseudo β_j

Table 9.8 Assessment of the Damage Severity Accuracy for Damage Scenario 3 Using EB Pseudo β_j

Damage Severity (%)		Error (%)
True	Predicted Lower Bound/Upper Bound	
-44.0	-11.1/-29.7	74.8/32.5

Damage Scenario 4

Figures 9.12 and 9.13 depict the damage prediction results for Damage Scenario 4 using the damage indicator EB Pseudo β_j. Table 9.9 and 9.10 tabulate the performance of the damage detection methodology for the damage scenario.

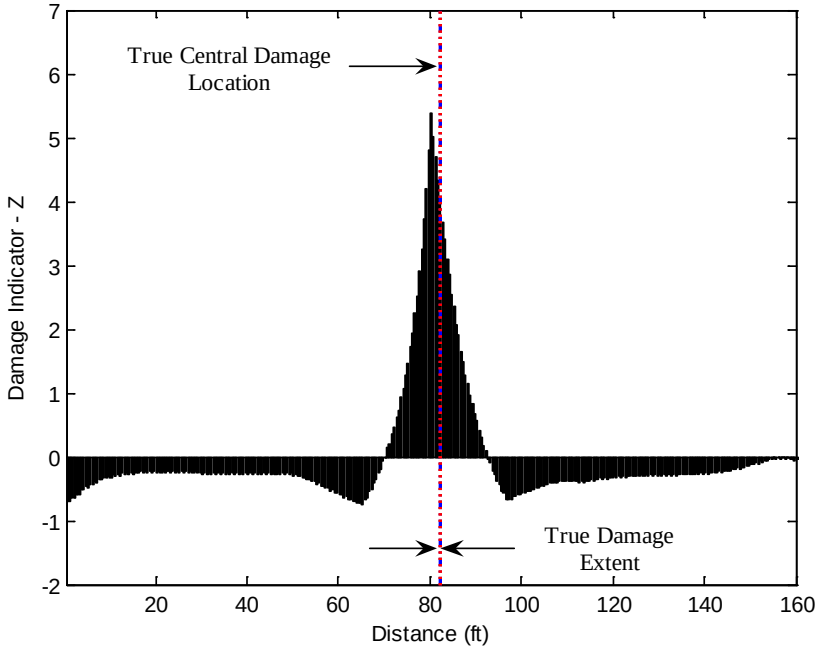

Figure 9.12 Damage Localization Result for Damage Scenario 4

Using EB Pseudo β_j

Table 9.9 Assessment of the Damage Localization Accuracy for Damage Scenario 4

Using EB Pseudo β_j

Damage Central Location (ft)		Error (%)	$P(T \subset P)$
True	Predicted		
82.2	80.3	1.2	100%

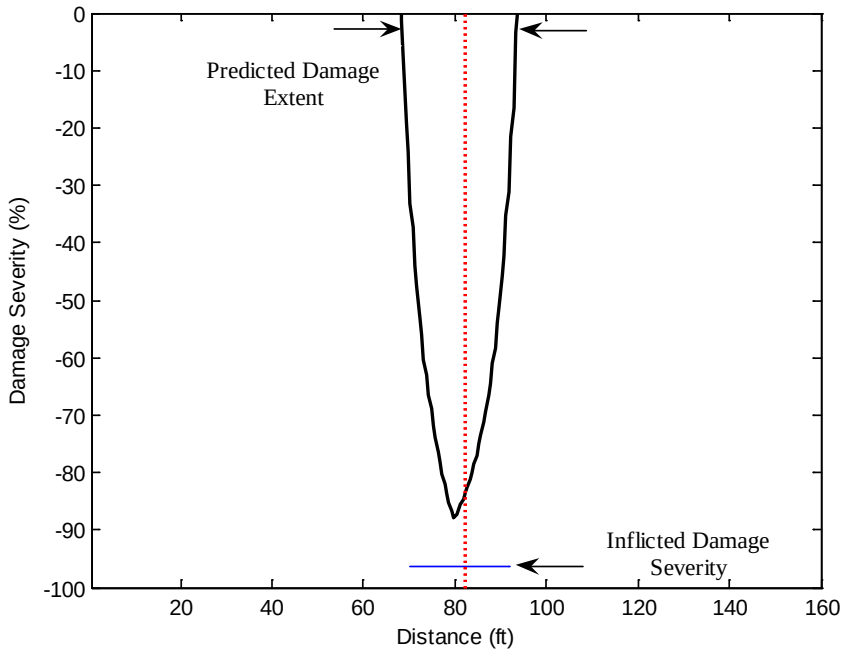

Figure 9.13 Damage Severity Estimate for Damage Scenario 4 Using EB Pseudo β_j

Table 9.10 Assessment of the Damage Severity Accuracy for Damage Scenario 4 Using EB Pseudo β_j

Damage Severity (%)		Error (%)
True	Predicted Lower Bound/Upper Bound	
-96.3	-72.0/-88.0	25.2/8.6

DISCUSSION OF RESULTS

Based on the results of the case studies, the following observations can be made regarding the performance of the EB Pseudo Method on Los Alamos Data:

Damage was successfully localized in all damage scenarios. The error between the central location of the true and the predicted damages, e_L, is as low as 0.2% for Damage Scenario 1. Damage Scenarios 2, 3 and 4 consistently indicated a localization error of 1.2%. These small localization errors are significant considering that the Damage Index Method was the only NDE algorithm that had the capability of locating damage in all damage scenarios in the Los Alamos Study (Farrar and Jauregui (1996)). Therefore, the EB Pseudo Method performed just as well as the Damage Index Method considering damage localization, and better than the other NDE algorithms listed in Table 9.2.

As far as the error between the true and the predicted damage severity is concerned, the performance of the EB Pseudo Method appears to vary depending on the damage scenario. The large error in severity estimation for Damage Scenario 1 may be linked to possible measurement errors. Note that the resonant frequencies increased in Damage Scenarios 1 and 2, whereas a stiffness reduction should have caused a decrease in the frequency content. The upper bound severity estimates were lower than the inflicted damage severities for Damage Scenarios 3 and 4. Note that these are significant stiffness reductions, which might have violated the principle of invariant stress resultants. Nonetheless, the estimated damage severity appeared to be reasonable for Damage Scenarios 3 and 4 considering the dictated sensor layout. A finer sensor layout within the localized damage region could improve these results.

Finally, note that the extent of the inflicted damage (localized torch cuts) may not correspond to the predicted damage extents in this study. Although torch cuts seemingly provide very local defects, it should be noted that the stress concentrations tend to spread out as the severity of the damage becomes significant. Farrar and Jauregui (1996) reported that the web on either side of the cut bent out of plane approximately 1 in. after imposing the second damage scenario defined above. This might be the cause of significant spillovers seen in damage extent estimates. Therefore, damage extent was not quantified in this study.

SUMMARY AND CONCLUSIONS

Experimental modal data collected from the Interstate 40 (I-40) Bridge were utilized to evaluate the performance of the EB Pseudo Method in this chapter. Experimental results included the pre-damage and post-damage translational mode shapes and eigenfrequencies of the structure. Four incremental levels of damage were inflicted at the mid-span of the north plate girder by making various torch cuts in the web and flange of the girder. Damage was successfully localized in all damage scenarios. Regarding the accuracy of damage severity results, the EB Pseudo Method provided satisfactory estimates in Damage Scenarios 3 and 4. Large errors in the severity estimations of Damage Scenarios 1 and 2 were linked to possible measurement errors.

CHAPTER X

SUMMARY AND CONCLUSIONS

SUMMARY AND MAJOR FINDINGS

The objective of this dissertation was to develop Level III damage detection algorithms, which utilize fundamental theories of mechanics to relate physical properties of the undamaged and damaged structure to measurable response quantities. The scope of this dissertation was limited to general beams that may be grouped under three main categories, namely: slender, intermediate and deep beams.

In Chapter II, the governing equations of equilibrium and the stress-displacement relations of the Euler-Bernoulli and the Timoshenko beam theories were introduced. The concept of flexural discontinuity in beam-type structures was discussed and equivalent flexural stiffness formulations at the point of flexural discontinuity were developed by utilizing the fundamental equations of the Euler-Bernoulli and the Timoshenko beam models.

In Chapter III, the numerical experiments utilized to evaluate the performances of the individual damage detection algorithms were introduced. Fifteen damage scenarios involving slender, intermediate and deep beams were designed.

In Chapter IV, an explicit damage index methodology (the EB Direct Method) based on the principle of invariant stress resultants and the Euler-Bernoulli beam theory was developed. The performance of the methodology was evaluated through the numerical experiments introduced in Chapter III. The following major findings were made in Chapter IV:

1. The proposed damage detection methodology was verified using the numerical experiments defined in Chapter III;

2. The proposed methodology produced satisfactory damage localization results in all types of beams (slender, intermediate, or deep) although it is based on the Euler-Bernoulli beam theory, which is pertinent only in the case of slender beams;

3. It was observed that the probability of correctly locating the extent of the damage decreased with the depth to length (aspect) ratio of the beam when using a damage detection theory that is developed on the basis of the Euler-Bernoulli assumption; and

4. The range and magnitude of the error in damage severity estimation increased as the aspect ratio of the beam increased.

In Chapter V, damage index methodologies (the EB Pseudo Methods) based on the singularities in the flexural stiffness distribution of the beam and the stress-displacement relations of the Euler-Bernoulli beam theory were developed. The performance of the methodologies was evaluated through the numerical experiments introduced in Chapter III. The major findings include:

1. The proposed damage detection methodologies were verified using the numerical experiments defined in Chapter III;

2. The proposed damage indicators, EB Pseudo β_j and EB Pseudo γ_j, provided almost identical damage prediction results;

3. Damage prediction results closely correlated to the damage prediction results presented in Chapter IV;

4. The proposed methodologies performed the best for slender beams; and

5. The results of the case studies indicated that local inspection is possible with the proposed methodologies through reducing the size of the system of linear equations.

In Chapter VI, the so-called TB Direct Method was developed. The method was based on the principle of invariant stress resultants of the Timoshenko beam theory. Local decreases in the bending and shear stiffnesses of structural members were investigated by the proposed indices. The performance of the methodology was evaluated through the numerical experiments introduced in Chapter III. The following major findings were made:

1. The proposed damage detection methodologies were verified using the numerical experiments defined in Chapter III;

2. On the basis of the damage prediction results obtained through using TB Direct β_j^M, it was concluded that the accuracy of damage detection is not function of the aspect ratio and remains fairly the same for any type of beam (slender, intermediate, or deep) when using an NDE methodology that is developed on the basis of the Timoshenko beam theory;

3. TB Direct β_j^M provided no FP damage predictions in any of the case studies;

4. Excluding the two FN predictions in Damage Cases 4 and 5, for any type of beam, the probability of zooming in on the damage was 100% when TB Direct β_j^M is utilized for damage detection;

5. It was examined that the damage indicator TB Direct β_j^M produced upper and lower bound damage severity ranges, which always contain the true inflicted damage severity; and

6. TB Direct β_j^V provides better damage prediction results for deeper beams (as the aspect ratio of the beam increases). However, damage severity estimates are not as accurate as damage localization results.

In Chapter VII, the concept of discontinuity was utilized, in conjunction with the derivatives of cross sectional rotation, in order to formulate the TB Pseudo Methods. The performance of the methodologies was evaluated using the numerical experiments developed in Chapter III. The major findings include:

1. The proposed damage detection methodology was verified using the numerical experiments defined in Chapter III;

2. Damage prediction results closely correlated to the damage prediction results presented in Chapter VI;

3. It was observed that the accuracy of damage detection is not function of the beam's aspect ratio when using the proposed methodology for damage detection; and

4. The results of the case studies indicated that local inspection is possible with the proposed methodology through reducing the size of the system of linear equations.

In Chapter VIII, explicit damage indices were developed using the Theory of Linear Elasticity and the principle of identical external load distribution before and after damage. The pre-damage and post-damage strain distributions were utilized to formulate damage indices for a cantilever beam and a simply supported beam. It was shown that damage in the bending and shear stiffnesses, as well as local changes in the Poisson's ratio due to damage, can be investigated utilizing such techniques. Proposed damage detection methodologies produced two-dimensional damage indicators, which were able to perform nondestructive damage evaluation through the length and the depth of the

beam. As always, the performance of the proposed methodology was evaluated through the numerical experiments introduced in Chapter III. The following major findings were made in Chapter VIII:

1. The proposed damage detection methodologies were verified using the numerical experiments defined in Chapter III.

2. Damage indicator Elasticity β_j^M performed exceptionally well in all case studies;

3. Damage indicator Elasticity β_j^V performed exceptionally well in the case studies of the slender and intermediate beams;

4. Elasticity β_j^V performed poorly in the case studies of the slender and intermediate beams since shear deformations are likely to be significant only for the deep beam; and

5. It was shown that the damage indices developed for the tip-loaded cantilever beam also holds for other loading conditions and beam types (such as the simply supported beam subjected to uniform loading) under certain assumptions.

In Chapter IX, the performance of the EB Pseudo Method was evaluated using the experimental modal data collected by personnel from Los Alamos National Laboratory from the Interstate 40 (I-40) Bridge. The major findings include:

1. Damage was successfully localized in all damage scenarios;

2. The proposed methodology provided satisfactory estimates of damage severity in Damage Scenarios 3 and 4;

3. Large errors in the severity estimations of Damage Scenarios 1 and 2 were linked to possible measurement errors.

ORIGINALITY OF THE WORK

There are at least ten original aspects of this study, which include:

1. True Level III damage detection algorithms have been developed;
2. More accurate damage localization, damage extent and damage severity estimations have been proposed;
3. Damage indices based on the Timoshenko Beam Theory have been developed;
4. Damage indices for intermediate and deep beams have been proposed;
5. Damage indices to predict changes in the shear stiffness and Poisson's ratio have been developed;
6. More realistic 2-D damage scenarios and accurate 2-D damage detection algorithms have been proposed;
7. Damage detection algorithms derived from linear elasticity theory have been proposed;
8. How to develop damage detection methodologies applicable to specific types of beams (such as tip-loaded cantilever or uniformly distributed simple beam) have been demonstrated;
9. How to utilize response parameters (ranging from static to dynamic data which may include translations, rotations or strains) for damage detection have been demonstrated; and
10. The discipline of global NDE has been established on the basis of fundamental mechanics.

CONCLUSIONS

Based on the results of the performed case studies, the following conclusions are drawn:

1. The performance of damage detection theories that are developed on the basis of the Euler-Bernoulli assumption is inversely proportional to the depth to length (aspect) ratio of the beam.

2. The performance of damage detection theories that are developed on the basis of the Timoshenko Beam theory is not a function of the beam's aspect ratio.

3. Damage detection methodologies derived from Linear Elasticity theory in conjunction with the principle of identical external load distribution before and after damage, produced two-dimensional damage indicators, which are able to perform nondestructive damage evaluation through the length and the depth of the beam.

FUTURE WORK

On the basis of the findings of this work, the following set of problems should be addressed in near future:

1. Develop Level IV damage detection algorithms based on the results of this study;

2. Extend the capability of the proposed methods to analyze 2D frames and trusses;

3. Extend the capability of the proposed methods to analyze 3-D structures (isotropic and/or anisotropic plates and shells); and

4. Extend the capability of the proposed methods to analyze arbitrary structures (pressure vessels, beams on elastic foundations, curved beams, etc.).

REFERENCES

Adams, R.D., Cawley, P., Pye, C.J., and Stone, B.J. (1978). "A vibration technique for non-destructively assessing the integrity of structures." *J. Mech. Engr. Science,* 20(2), 93-100.

Biondi, B. and Caddemi, S. (2005). "Closed form solutions of Euler-Bernoulli beams with singularities" *International. J. Solids and Structures,* 42, 3027-3044.

Biondi, B. and Caddemi, S. (2007). "Euler-Bernoulli beams with multiple singularities in the flexural stiffness" *European. J. of Mechanics and Solids,* 26, 789-809.

Cawley, P., and Adams, R.D. (1979). "The locations of defects in structures from measurements of natural frequencies." *J. Strain Analysis,* 14(2), 49-57.

Choi, S.H. (1999). "Evaluation of relative performance of classification algorithms for NDD combining multiple damage algorithms." Ph.D. Dissertation, Texas A&M University, College Station, Texas.

Cook, R.D., Malkus, D.S., Plesha M.E., Witt, R.J. (2002). *Concepts and applications of finite element analysis,* Wiley, New York, NY.

Cowper, G.R. (1966). "The shear coefficient in Timoshenko's beam theory." *Comput. J. Applied Mechanics,* 33, 335-340.

Doebling, S.W., Farrar, C.R., Prime, M.B., and Shevitz, D.W. (1996). "Damage identification and health monitoring of structural and mechanical systems from changes in their vibration characteristics: A literature review." Report No. LA-13070-MS. Los Alamos National Laboratory, Los Alamos, New Mexico.

Farrar, C. R., Baker, W. E., Bell, T. M., Cone, K. M., Darling, T.W., Duffey, T.A., Eklund, A., Migliori, A. (1994). "Dynamic characterization and damage detection in the I-40 bridge over the Rio Grande." Report No. LA-12767-MS. Los Alamos National Laboratory, Los Alamos, New Mexico.

Farrar, C. and Jauregui, D. (1996). "Damage detection algorithms applied to experimental modal data from the I-40 bridge." Report No. LA-13074-MS. Los Alamos National Laboratory, Los Alamos, New Mexico.

Fox, C.H.J. (1992). "The location of defects in structures: A comparison of the use of natural frequency and mode shape data." *Proc. 10th International Modal Analysis Conference,* San Diego, California, 522-528.

Gudmundson, P. (1982). "Eigenfrequency changes of structures due to cracks, notches or other geometrical changes." *J. Mechanics and Physics of Solids*, 30(5), 339-359.

Guan, H., and Karbhari, V.M. (2008). "Improved damage detection method based on element modal strain damage index using sparse measurement." *J. Sound and Vibration*, 309, 465-494.

Hajela, P. and Soeiro, F.J. (1990). "Structural damage detection based on static and modal analysis." *AIAA J.*, 28(6), 1110-1115.

Hjelmstad, K.D., and Shin, S. (1997). "Damage detection and assessment of structures from static response." *J. Engineering Mechanics*, 123(6), 568-576.

Hutchinson, J.R. (2001). "Shear coefficients for Timoshenko beam theory." *J. Applied Mechanics*, 68, 87-92.

Hyung, S. (2007). "Simultaneous identification of stiffness and damping." Ph.D. Dissertation, Texas A&M University, College Station, Texas.

Jensen, J.J. (1983). "On the shear coefficient in Timoshenko's beam theory." *J. Sound and Vibration*, 87(4), 621-635.

Kaneko, T. (1975). "On Timoshenko's correction for shear in vibrating beams." *J. Physics D: Applied Physics*, 8, 1927-1936.

Kim, B.H. (2002). "Local damage detection using modal flexibility." Ph.D. Dissertation, Texas A&M University, College Station, Texas.

Kim, B.H., Stubbs, N., and T. Park (2005). "A new method to extract modal parameters using output-only responses." *J. Sound and Vibration*, 282(1-2), 215-230.

Kim, J.T. (1993). "Assessment of relative impact of model uncertainty on the accuracy of nondestructive damage detection in structures." Ph.D. Dissertation, Texas A&M University, College Station, Texas.

Kim, J.T., and Stubbs, N. (2002). "Improved damage identification method based on modal information." *J. Sound and Vibration*, 252(2), 223-238.

Kim, J.T., and Stubbs, N. (2003). "Crack detection in beam-type structures using frequency data." *J. Sound and Vibration*, 259(1), 145-160.

Kim, J.T., Ryu, Y-S., Cho, H-M, and Stubbs, N. (2003). "Damage identification in beam-type structures: Frequency-based method vs. mode-shape-based method." *J. Engineering Structures*, 25, 57-67.

Maduakolam, M.N. (1995). "Global non-destructive detection of structural and mass damage to floating structures." Ph.D. Dissertation, Texas A&M University, College Station, Texas.

Mazurek, D. F. and DeWolf J. T. (1990). "Experimental study of bridge monitoring technique." *J. Structural Engineering,* 116(9), 2532-2549.

Nam, D.H. (2001). "Improvements in the accuracy of system identification and nondestructive damage evaluation in civil engineering structures." Ph.D. Dissertation, Texas A&M University, College Station, Texas.

Nicholson, D.W., and Alnefaie, K.A. (2000). "Modal moment index for damage detection in beam structures." *Acta Mechanica,* 144, 155-167.

Osegueda, R. A., DSouza, P. D., Qiang, Y. (1992). "Damage evaluation of offshore structures using resonant frequency shifts." *Serviceability of Petroleum, Process, and Power Equipment, ASME* PVP 239/MPC 33, 31-37.

Osegueda, R. A., Revilla, A., Pereyra, L., Moguel, O. (1999). "Fusion of modal strain energy differences for localization of damage." *Proc. SPIE Vol. 3586,* Newport Beach, California, 189-199.

Pandey, A.K., Biswas, M., and Samman, M.M. (1991). "Damage detection from changes in curvature mode shapes." *J. Sound and Vibration,* 145(2), 321-332.

Pandey, A.K., Biswas, M., (1994). "Damage detection in structures using changes in flexibility." *J. Sound and Vibration,* 169(1), 3-17.

Pandey, A.K., Biswas, M., (1995). "Experimental verification of flexibility difference method for locating damage in structures." *J. Sound and Vibration,* 184(2), 311-328.

Park, S. (1997). "Development of a methodology to continuously monitor the safety of complex structures." Ph.D. Dissertation, Texas A&M University, College Station, Texas.

Park, S., Bolton, R.W., Stubbs, N. (2006). "Blind test Results for nondestructive damage detection in a steel frame." *J. Structural Engineering,* 132(5), 800-809.

Petro, S.H., Chen S.-E., GangaRao, H.V.S., and Venkatappa, S. (1997). "Damage detection using vibration measurements." *Proc. 13th International Modal Analysis Conference,* Orlando, Florida, 113-119.

Reddy, J.N. (1997). "On locking-free shear deformable beam finite elements." *Comput. Methods Appl. Mech. Engrg.,* 149, 113-132.

Reddy, J.N. (1999). "On the dynamic behavior of the Timoshenko beam finite elements." *Sadhana*, 24(3), 175-198.

Rytter, A. (1993). "Vibrational based inspection of civil engineering structures." Ph.D. Dissertation, University of Aalborg, Aalborg, Denmark.

Salawu, O.S. (1997). "Detection of structural damage through changes in frequency: A review." *Engineering Sciences*, 19(9), 718-723.

Sanayei, M. and Saletnik, M.J., (1996). "Parameter estimation of structures from static strain measurements, I: Formulation." *J. Structural Engineering*, 122(5), 555-562.

Shi, Z.Y., Law, S.S., and Zhang, L.M. (1998). "Structural damage localization from modal strain energy change." *J. Sound and Vibration*, 218(5), 825-844.

Shi, Z.Y., Law, S.S., and Zhang, L.M. (2000). "Structural damage detection from modal strain energy change." *J. Engineering Mechanics*, 126(12), 1216-1223.

Shi, Z.Y., Law, S.S., and Zhang, L.M. (2002). "Improved damage quantification from elemental modal strain energy change." *J. Engineering Mechanics*, 128(5), 521-529.

Shull, P.J. (2002). *Nondestructive evaluation: Theory, techniques, and applications*, Marcel Dekker, New York, NY.

Stubbs, N. (1985). "A general theory of non-destructive damage detection in structures." *Structural Control*, H.H.H. Leipholz, ed., Martinus Nijhoff Publishers, Dordrecht, The Netherlands, 694-713.

Stubbs, N., Broome, T.H., Osegueda R. (1990). "Nondestructive construction error detection in large space structures," *AIAA J.*, 28(1), 146-152.

Stubbs, N. and Osegueda R. (1990a). "Global non-destructive damage evaluation in solids." *The Int. J. Analytical and Experimental Modal Analysis*, 5(2), 67-79.

Stubbs, N. and Osegueda, R. (1990b). "Global damage detection in solids-experimental verification." *The Int. J. Analytical and Experimental Modal Analysis*, 5(2), 81-97.

Stubbs, N., and Kim, J.T., and Topole, K. (1992). "An efficient and robust algorithm for damage localization in offshore platforms." *ASCE 10th Structures Congress*, San Antonio, Texas, 543-546.

Stubbs, N., Kim, J.T., and Farrar, C.R. (1995). "Field verification of a nondestructive damage localization in offshore platforms." *Proc. 13th International Modal Analysis Conference*, Nashville, Tennessee, 210-218.

Stubbs, N. and Kim, J.T. (1996). "Global damage detection in solids-experimental verification." *AIAA J.*, 34(8), 1644-1649.

Southwell, R.V. (1936). *An introduction to the theory of elasticity for engineers and physicists,* Clarendon Press, Oxford, Great Britain.

Timoshenko, S.P. and Goodier, J.N. (1951). *Theory of elasticity,* McGraw-Hill Book Company, New York, NY.

Toksoy, T., and Aktan, A.E. (1994). "Bridge-condition assessment by modal flexibility." *Experimental Mechanics,* 34(3), 271-278.

Topole, K.G. (1993). "Nondestructive damage evaluation in nonlinear structures." Ph.D. Dissertation, Texas A&M University, College Station, Texas.

Ugural, A.C. and Fenster, S.K. (2003). *Advanced strength and applied elasticity,* Prentice Hall, Upper Saddle River, NJ.

Wahab, M.M.A., and Roeck, G.D. (1999). "Damage detection in bridges using modal curvature: Application to a real damage scenario." *J. Sound and Vibration,* 226(2), 217-235.

West, W.M. (1984). "Illustration of the use of modal assurance criterion to detect structural changes in an orbiter test specimen." *Proc. Air Force Conference on Aircraft Structural Integrity,* 1-6.

Zhang, Z., and Aktan, A.E. (1995). "The damage indices for constructed facilities." *Proc. 13th International Modal Analysis Conference,* Nashville, Tennessee, 1520-1529.

Zimmerman, D.C., and Kaouk, M. (1994). "Structural damage detection using minimum rank update theory." *J. Vibration and Acoustics,* 116, 222-231.

APPENDIX A

APPROXIMATION OF THE DEFLECTION PROFILES USING MODAL FLEXIBILITY

The flexibility matrix is the inverse of the stiffness matrix and relates the applied static loads to the resulting structural displacements. Each row of the flexibility matrix may be interpreted as the deformed shape of a structure due to a unit load applied at the corresponding degree of freedom (DOF). The modal approximation of the flexibility matrix is the dynamically measured flexibility or simply, the modal flexibility.

The modal flexibility matrix can be accurately created from a few of the lower modes. This makes the modal flexibility particularly attractive since modal data is mostly limited to the first few mode shapes and eigenfrequencies in practical applications.

The flexibility matrix may be formulated as:

$$u_j = \sum_{i=1}^{r} \frac{\phi_{ji}}{\lambda_i m_i} \phi_i \tag{A.1}$$

where m_i, ϕ_i, and λ_i denote the i^{th} modal mass, mode shape, and eigenvalue, respectively. The j^{th} component of the i^{th} modal vector is denoted by ϕ_{ji}. The vector u_j represents the deflection profile due to a unit load applied at the j^{th} DOF.

A more generalized form of the above equation may be formulated by including rotational DOFs to the modal flexibility matrix. In this case, vector u_j may also represent the rotation of a structure if rotational degrees of freedom are utilized in computing Eq. (A.1).

A certain drawback of the dynamically measured flexibility is the uncertainty in modal mass. Mass-normalized mode shapes are necessary to construct the modal flexibility matrix, which requires the use of forced vibration tests instead of output-only modal analysis techniques. However, ambient modal analysis techniques, which oblige output-only modal tests, are becoming more popular due to their nonintrusive and inexpensive nature (Kim et al. (2005)). In such cases, numerical approximations of modal mass are necessary in order to build the modal flexibility correctly. An extension to the numerical approximation scheme proposed by Kim (2002) is presented here.

If the density, cross-sectional area and moment of inertia of a beam-like structure are known, and translational and rotational modal amplitudes are measured by an output-only modal analysis method, then the i^{th} modal mass, m_i, may be approximated by

$$m_i = \int_0^L \rho A \phi_i(x)\phi_i(x)dx + \int_0^L \rho I \varphi_i(x)\varphi_i(x)dx \tag{A.2}$$

where ρ, A, and I are the density, cross-sectional area and moment of inertia of the beam. The functions $\phi_i(x)$ and $\varphi_i(x)$ denote the translational and rotational profiles of the i^{th} bending mode.

The numerical approximation scheme given in Eq. (A.2) is the general form of the mass matrix given in Reddy (1999) where the dynamic behavior of the Timoshenko beam finite elements were discussed. However, $\phi_i(x)$ and $\varphi_i(x)$ denote the shape functions utilized to build the FEM of the Timoshenko beams, instead of the translational and rotational modal amplitudes as expressed above. Reddy (1999) showed that when shear deformations are negligible, ϕ_i reduces to usual Hermite interpolation functions and $\varphi_i(x)$ reduces to $-\frac{d\phi_i}{dx}$. Using modal translations and rotations in lieu of $\varphi_i(x)$ and $\phi_i(x)$ yields acceptable modal mass estimates for the lower modes, however

larger deviations from exact values are expected for higher modes. Fortunately, modal flexibility's lower mode dependency makes the numerical approximation scheme feasible.

In order to construct the flexibility matrix from the modal data, it is assumed that an output-only modal testing is performed for each of the test beam utilized in this study. The outcomes of these tests are the first three natural frequencies and transverse as well as rotational degrees of freedom of the mode shapes measured at the centerline of each beam. The first three bending modes of the undamaged slender, intermediate and deep beam are depicted in Figure A.1, Figure A.2 and Figure A.3, respectively.

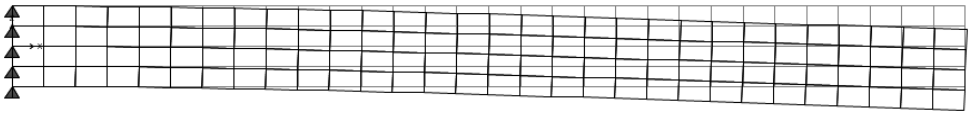

(a) The First Bending Mode (18.43 Hz)

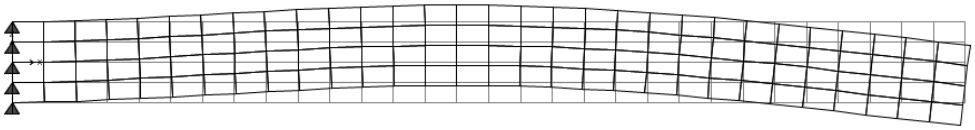

(b) The Second Bending Mode (112.0 Hz)

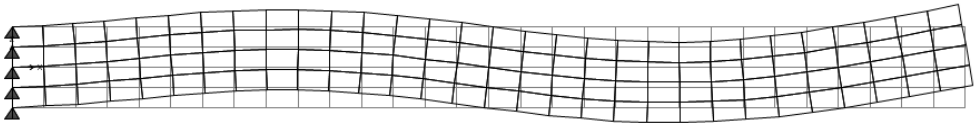

(c) The Third Bending Mode (300.1 Hz)

Figure A.1 The First Three Bending Modes of the Undamaged Slender Beam

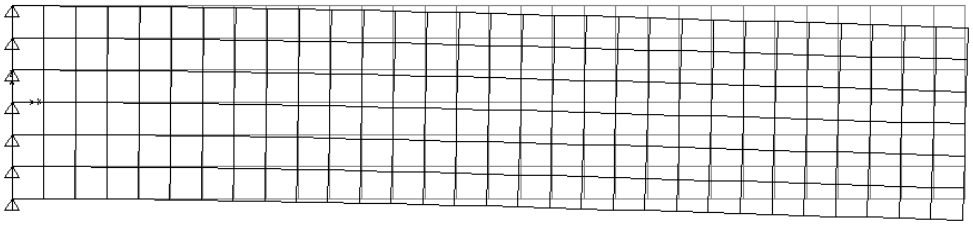

(a) The First Bending Mode (52.03 Hz)

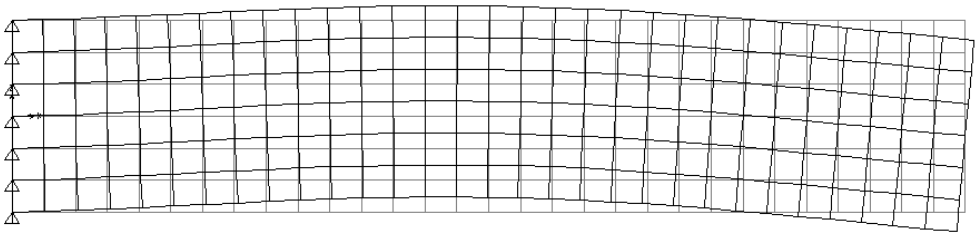

(b) The Second Bending Mode (281.08 Hz)

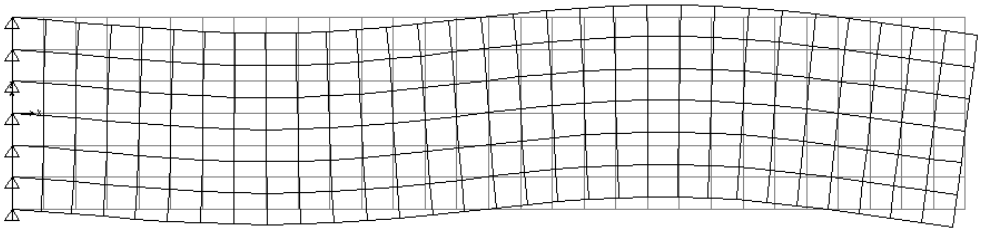

(c) The Third Bending Mode (671.07 Hz)

Figure A.2 The First Three Bending Modes of the Undamaged Intermediate Beam

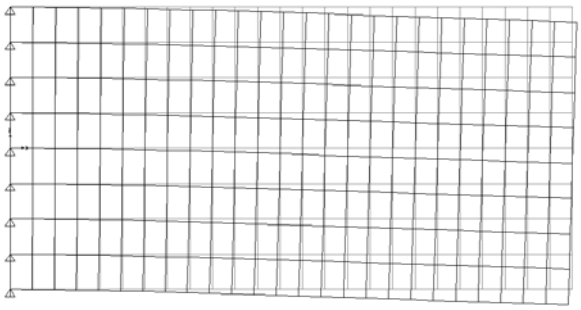

(a) The First Bending Mode (229.23 Hz)

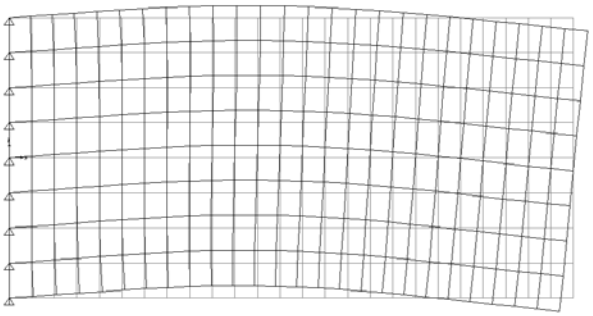

(b) The Second Bending Mode (873.07 Hz)

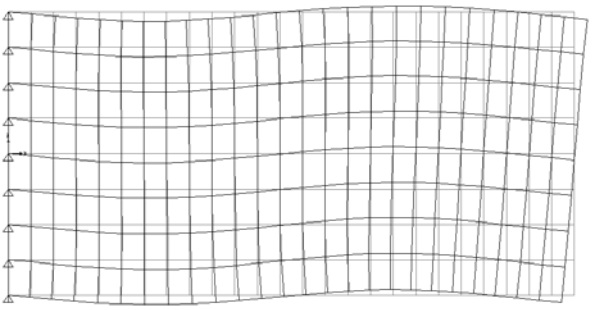

(c) The Third Bending Mode (1825.75 Hz)

Figure A.3 The First Three Bending Modes of the Undamaged Deep Beam

Firstly, modal mass must be approximated by using the numerical approximation scheme given in Eq. (A.2). Upon utilizing the transverse and rotational degrees of freedom of the mode shapes measured at the centerline of the test beams and assuming that the density and geometry of the beams are readily available, modal mass for the first three bending modes of the beam can be approximated. Tables A.1 and A.2 tabulate the percentile error in modal mass approximation by including and excluding the contribution of the rotary inertia, respectively.

Table A.1 Percentile Error in Modal Mass Approximation (with rotary inertia)

Mode	Slender Beam	Intermediate Beam	Deep Beam
1st Bending Mode	0.032%	0.097%	0.380%
2nd Bending Mode	0.494%	1.346%	3.352%
3rd Bending Mode	1.626%	3.583%	3.432%

Table A.2 Percentile Error in Modal Mass Approximation (without rotary inertia)

Mode	Slender Beam	Intermediate Beam	Deep Beam
1st Bending Mode	0.298%	1.531%	6.792%
2nd Bending Mode	1.253%	6.453%	25.200%
3rd Bending Mode	2.046%	8.772%	32.775%

It is clear that including the rotary terms in modal mass calculations significantly improves the results, specifically in higher modes of vibration.

Once the modal mass is found, Eq. (A.1) can be used to compute the modal flexibility matrix. For instance, assume that the deformed shape of the beam under the unit load applied at the tip is to be approximated. Following results can be obtained upon utilizing the translational and rotational modal amplitudes measured at the centerline of each test beam. The subsequent figures show the comparison of the deflections approximated by the modal flexibility with the static deflection profiles caused by a unit load at the tip of the beam. Figures A.4, A.5 and A.6 depict the vertical displacement and rotation of the beam axis for the slender, intermediate and deep beams, respectively. It is clear that the modal flexibility provides remarkably good estimates of the static displacement and rotation profiles by utilizing as few as three bending modes.

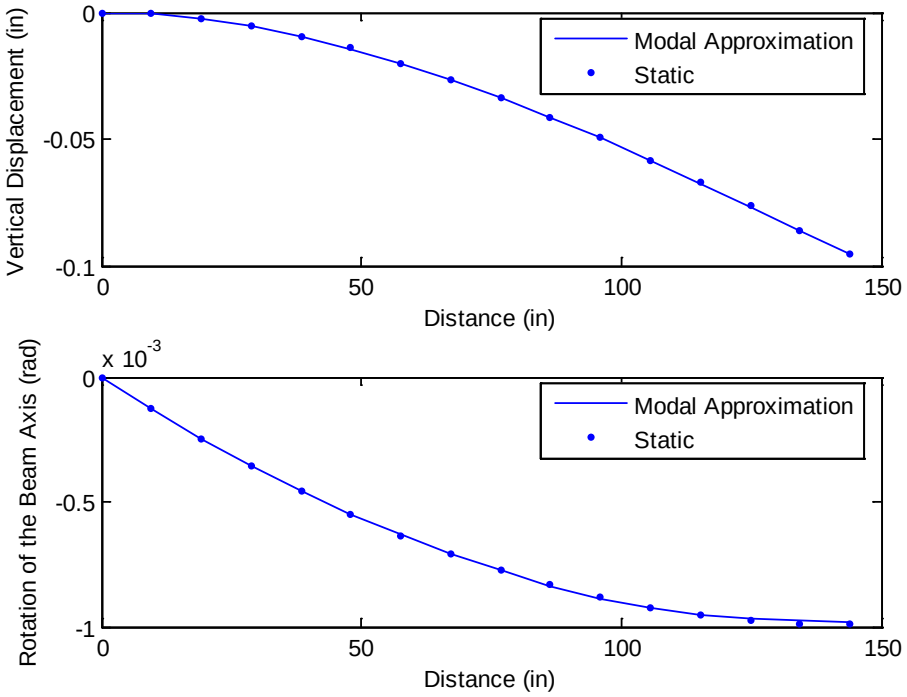

.

Figure A.4 Comparison of the Deflections Approximated by the Modal Flexibility with the Static Deflection Profile of the Slender Beam

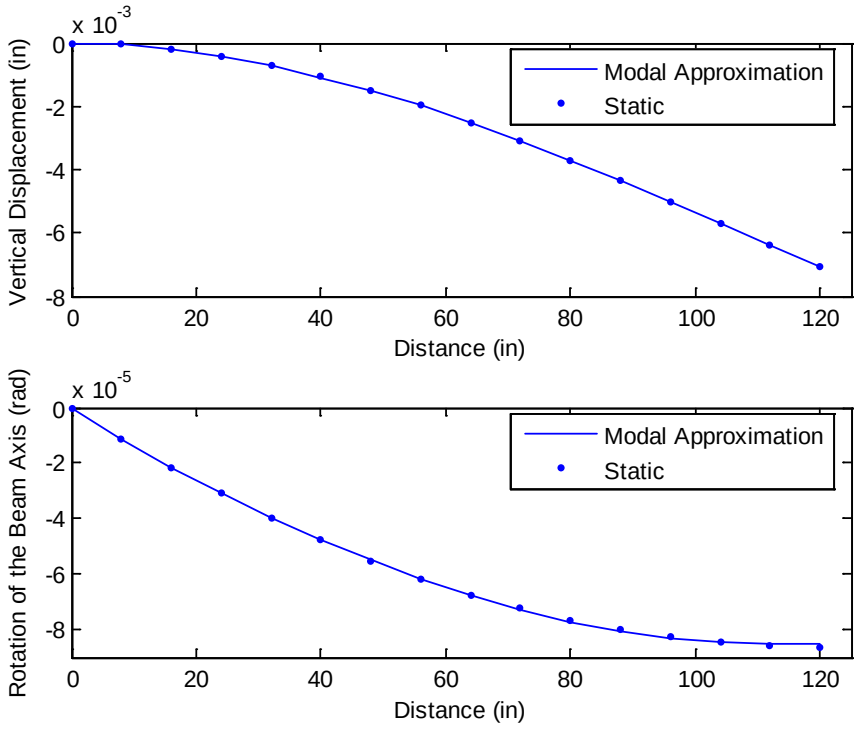

Figure A.5 Comparison of the Deflections Approximated by the Modal Flexibility with the Static Deflection Profile of the Intermediate Beam

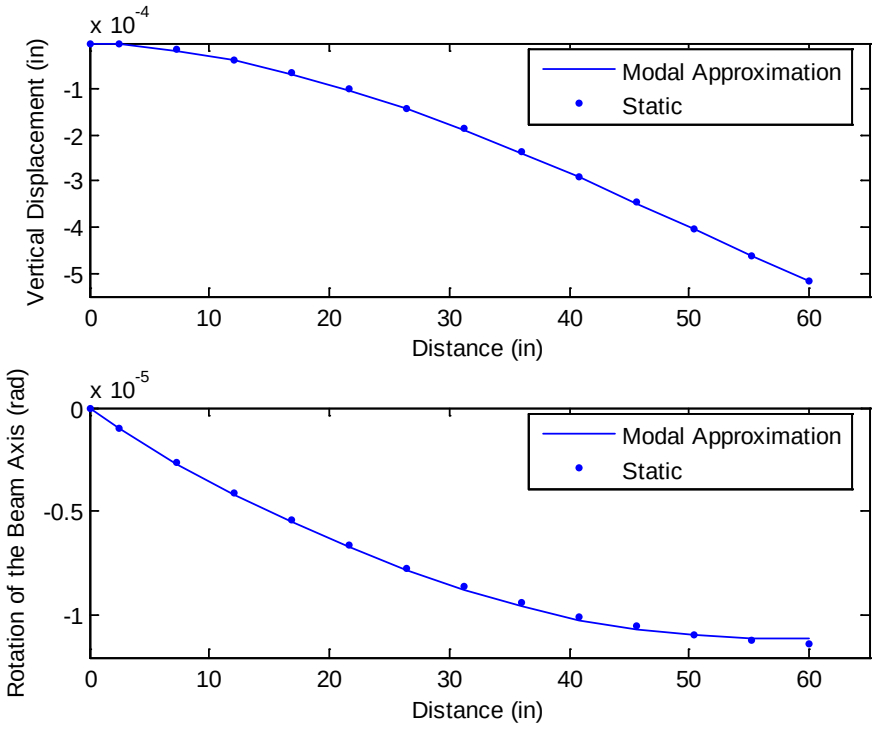

Figure A.6 Comparison of the Deflections Approximated by the Modal Flexibility with the Static Deflection Profile of the Deep Beam

VITA

Selcuk Dincal finished high school at Bursa Erkek Lisesi in 1998 and attended Eskisehir Osmangazi University immediately after, where he received a Bachelor of Science degree in civil engineering in 2002. In the fall of 2003, he enrolled to the Master's of Science program in the Civil Engineering Department at Texas A&M University, with structural engineering specialization. He started his doctoral studies immediately after receiving his M.S. degree on December 2005. He has worked as a graduate teaching assistant at the Student Learning Center (formerly known as Center for Academic Enhancement) and at Zachry Department of Civil Engineering during his studies at Texas A&M University. His research interests include solid mechanics, dynamic analysis and health monitoring of civil engineering structures, and finite element modeling. His contact address is Zachry Department of Civil Engineering, Texas A&M University, CE/TTI Building, 3136 TAMU, College Station, TX 77843, USA. His e-mail address is selcukdincal@gmail.com.